Structural Characterization of Macromolecular Complexes Within Thick Specimens Using Cryo-Focused-Ion-Beam Scanning Electron Microscopy (cryo-FIB-SEM) and Cryo-Electron-Tomography (cryo-ET)

Dissertation

zur Erlangung der naturwissenschaftlichen Doktorwürde

(Dr. sc. nat.)

vorgelegt der

Mathematisch-naturwissenschaftlichen Fakultät der Universität Zürich

von

Jan Harapin

aus Kroatien

…

Promotionskomission

Prof. Dr. Ohad Medalia (Vorsitz, Leiter)

Prof. Dr. Damian Brunner

Prof. Dr. Henning Stahlberg

Zürich, 2017

Table of Contents

Table of figures

Summary

Structural characterization of macromolecules in their native surroundings is a challenging task that allows us to describe fundamental processes in molecular and structural biology. Cryo-electron tomography (cryo-ET) is a fast evolving field where the continuous development of computational tools enables the study of macromolecular assemblies at a resolution of a few nanometers. Novel thinning procedures allow the application of cryo-ET to the reconstruction of intracellular structures normally found in thick regions of vitrified cells and tissues. In as much, it has established itself as a leading tool for structural studies in various sub disciplines of biology.

In the second chapter, I describe a novel method that encompasses sample vitrification, cryo-FIB-SEM milling, and application of surface fiducial markers after milling, and tomographic imaging of thinned multicellular specimens. I have vitrified embryos of *C. elegans* and entire *C. elegans* worms on EM grids that enabled homogenous vitrification throughout and unrestricted cryo-FIB-SEM milling. The application of surface fiducial markers onto the thin lamellae, under cryogenic conditions, allowed the application of cryo electron tomography (CET) under various imaging conditions. I was then able to reconstruct tomograms showing cellular interiors at close-to-focus conditions. This approach is general and enables many down-stream applications for further data processing.

In the third chapter, I describe the application of cryo-FIB-SEM milling and native cryo-ET imaging of spherical phenylalanine-glycine repeat-rich particles (FG particles) formed by the *T. thermophila* MacNup98A nucleoporin. The MacNup98A protein is used as a good in vitro model for the central channel of the nuclear pore complex (NPC) and was used in this study to determine whether any higher order structural organization occurs within a densely crowded FG particle environment. Here, the local protein concentration is estimated to be proportional to that found in the central channel of the NPC. I am showing that FG particles have higher order structural organization characterized by filamentous-like densities of various length and thickness. The very crowded atmosphere found within the FG repeat structures did not allow testing whether the binding of nuclear transport factors, such as Importin-β fragment (45-462) and GFP variant 3b7 altered the internal organization of the particles.

In summary, we have shown the applicability of the cryo-FIB-SEM platform to various biologically relevant samples that could ultimately allow high-resolution reconstructions of intra- and extracellular macromolecular complexes and protein networks at specific and defined developmental stages or physiological states.

Zusammenfassung

Die strukturelle Analyse von Makromolekülen in ihrer natürlichen Umgebung ist eine herausfordernde Aufgabe und trägt zum besseren Verständnis grundlegender molekular- und strukturbiologischer Prozesse bei. Die sich sehr schnell entwickelnde Technologie der Kryo-Elektronentomographie sowie computerbasierender Methoden erlauben die Untersuchung von Makromolekülen in einer Auflösung von einigen Nanometern. Darüberhinaus erlauben Techniken, die sich zur Herstellung sehr dünner Präparate eignen, intrazelluläre Strukturen zu rekonstruieren, die sich normalerweise in sehr dicken Regionen vitrifizierter Zellen oder Geweben befinden. Somit stellt die Kombination dieser Techniken eine mittlerweile sehr etablierte Methode dar, strukturelle Fragestellungen in der Biologie zu adressieren.

Im zweiten Kapitel beschreibe ich eine neue Methode der Vitrifizierung von Präparaten, die Herstellung von Kryo-FIB Schnitten, die Applikation von Referenzmarkern nach der Herstellung der vitrifizierten Schnitte, sowie die tomographische Analyse multizellulärer Proben. Anhand der Analyse von *C. elegans* Embryos und entwickelter Würmer konnte so eine Methode etabliert werden, den zellulären Aufbau auf molekularer Ebene unter nahezu nativen Bedingungen zu visualisieren – ein Verfahren welches der weiterführenden Untersuchung und Prozessierung zellulärer Strukturen dient.

Im dritten Kapitel beschreibe ich die Herstellung von Kryo-FIB Schnitten und die Kryo-Elektronentomographie kugelförmiger Partikel bestehend aus sich wiederholenden Phenylalanin-Glycin-reichen Aminosäresequenzen (FG-Partikel) des Kernporenproteins MacNup98A von *T. thermophila*. Das Kernporenprotein MacNup98 stellt ein repräsentatives in vitro Modell für den zentralen Kanal des Kernporenkomplexes dar und diente in meiner Arbeit der Untersuchung der Organisation und Formation potentieller Sekundärstrukturen innerhalb eines dicht gepackten FG-Partikels und wurde in vergleichbaren Konzentrationen verwendet, wie sie in vivo im zentralen Kanal des Kernporenkoplexes vorzufinden sind. Ich konnte zeigen, dass die FG-Partikel durch die Präsenz filamentöser Strukturen unterschiedlicher Länge und Dicke charackterisiert sind. Aufgrund der hohen Dichte der Strukturen innerhalb des FG-Partikels war es leider nicht möglich weiterführende Studien zur Interaktion dieser Filamente mit nukleären Transportfaktoren wie z.B. eines Importin-b Fragments (45-462) oder des GFP Fusionsproteins 3b7 durchzuführen.

Zusammenfassend erläutern wir die Anwendbarkeit der Kryo-FIB Technik zur Herstellung dünner Präparate verschiedener biologisch relevanter Modelle, sowie die Analyse und Rekonstruktion hoch-aufgelöster intra- und extramolekularer Proteinstrukturen in unterschiedlichen Entwicklungsstadien eines Organismus bzw. unter verschiedenen physiologischen Bedingungen.

Acknowledgements

I would like to acknowledge my supervisor, Prof. Ohad Medalia, for giving me the wonderful opportunity to work in his lab on such an exciting project. It has been a long and fun journey full of learning and personal development that has shaped me professionally.

A big thank you to all the members of the ZMB facility, especially Dr. Andres Kaech for being a true mentor and friend throughout the duration of my thesis. I could not have done it without you.

I would also like to thank all the past and current members of that Medalia group that have each in their own way left a significant mark on my professional development and, in some case, become dear friends. Here, I would like to particularly thank Dr. Monika Zwerger for being and awesome mentor, office companion, and a dear friend; Dr. Noah Medalia, whom I have shared not only office space but also many fun moments; Dr. Heidi Roschitzki-Voser, for her scientific support and comfort in times of stress; and Dr. Matthias Eibauer, for teaching me all I know about electron microcopy and image analysis. I also want to acknowledge my lab colleagues for providing a fun and engaging environment to work in; in particular Simona, Anna, Rebecca, Mauro, Bruno, Rossi, Yagmur, Tanuj, and Raja.

I would most of all like to thank my family (Zlatko, Snjezana, and Dora), to whom I dedicate this work, for their unwavering support and belief in my abilities, especially in times of doubt. You have given me all the tools needed to succeed in life and have been there right next to me, pushing me, and cheering for me every step of the way. I cannot imagine having a better support structure or better people around me to share my life experiences with.

I would like to thanks my close friends Noam, Lana, Iva, Antonija, Sarah, Martin, Jeppe, David, Sinisa, Camille, and Emil for many fun times together that have enriched my life in incredible ways.

Finally yet importantly, I would like to acknowledge some people who have had a tremendous impact on my life and stood by my side at my strongest and weakest moments. My dearest friends Ivana and Tamara, whom I have known for so many years and been through countless experiences with. My wonderful boyfriend Willy, who has been a stable and happy pillar of support for me, especially in my most irrational moments. To my darling flat mate and

adopted sister Annik, I can only say that fate alone has brought us together to love and support each other in all of life's most interesting adventures.

There have been other great and important people going in and out of my life over the past 6 years to whom I would also like to express gratitude for a wonderful time spent together. You are all fondly remembered and appreciated, but too many to be specifically named here. I thank you all for the fun times together.

Chapter 1

Introduction

Electron microscopy

A microscope (from the Ancient Greek: μικρός, mikrós, "small" and σκοπεῖν, skopeîn, "to look" or "see") is an instrument used to see objects that are far too small for the naked eye to observe. An optical microscope, i.e. light microscope, is a type of microscope that uses visible light and a system of lenses to magnify images of small objects. An electron microscope essentially does the same but uses a beam of electrons, instead of photons, as well as specialized lenses to illuminate the sample. The wavelength of an electron is approximately 100 000 times smaller than that of a photon, therefore the obtainable resolution (i.e. the ability to see two spatially independent features as separate entities) of an electron microscope is significantly higher than that of the light microscope (law of Abbé). From the construction of the first working prototype, by Ernst Ruska and Max Knoll in 1931, this feature has been extensively exploited in order to elucidate the ultrastructures of a wide range of biological and inorganic specimens. These include microorganisms, large molecules, macromolecular complexes, entire cells, tissue biopsy samples, metals, and crystal, as well as samples from materials industry for quality control and failure analysis (Harris, 2015).

The two most widespread electron microscopy techniques relevant to imaging biological samples are transmission electron microscopy (TEM) and scanning electron microscopy (SEM). They both operate under similar basic physical principles but vary greatly in their application. Both make use of high-speed electrons emanating from an electron gun as a source of illumination that are accelerated, focused, and guided to the sample through a set of electromagnetic lenses. The key difference lies in the way the signals generated by the interaction of the electron beam with the solid sample are produced and detected.

In SEM the electron beam scans across a rectangular area of the specimen (i.e. raster scanning) and the electrons lose energy upon interacting with the thick sample. This produces a variety of secondary effects such as heat, emission of low-energy secondary electrons and high-energy backscattered electrons, light emission (cathodoluminescence), and X-ray emission (***Figure 1***, top half). All these signals can be detected, recorded, and used for reconstructing

the image of the specimen. They carry within them all the information about the properties of the specimen surface, e.g. its topography and composition (Williams and Carter).

In TEM the electron beam penetrates a suitably thin sample and for some electrons scattering will occur whereas for others it will not. These two types of electron beams exiting the sample are known as the scattered and unscattered beams, respectively, and are both important for the generation of contrast in the TEM (***Figure 1***, bottom half). The amount of scattering (change of direction) experienced by an incident electron when interacting with a solid sample in TEM is proportional to the atomic mass of the atom/electron with which it interacted (collided). The exiting beam is finally magnified by the objective lens and projected through a set of projection lenses onto a fluorescent screen or some type of electronic detector for direct recording of the signal (Williams and Carter).

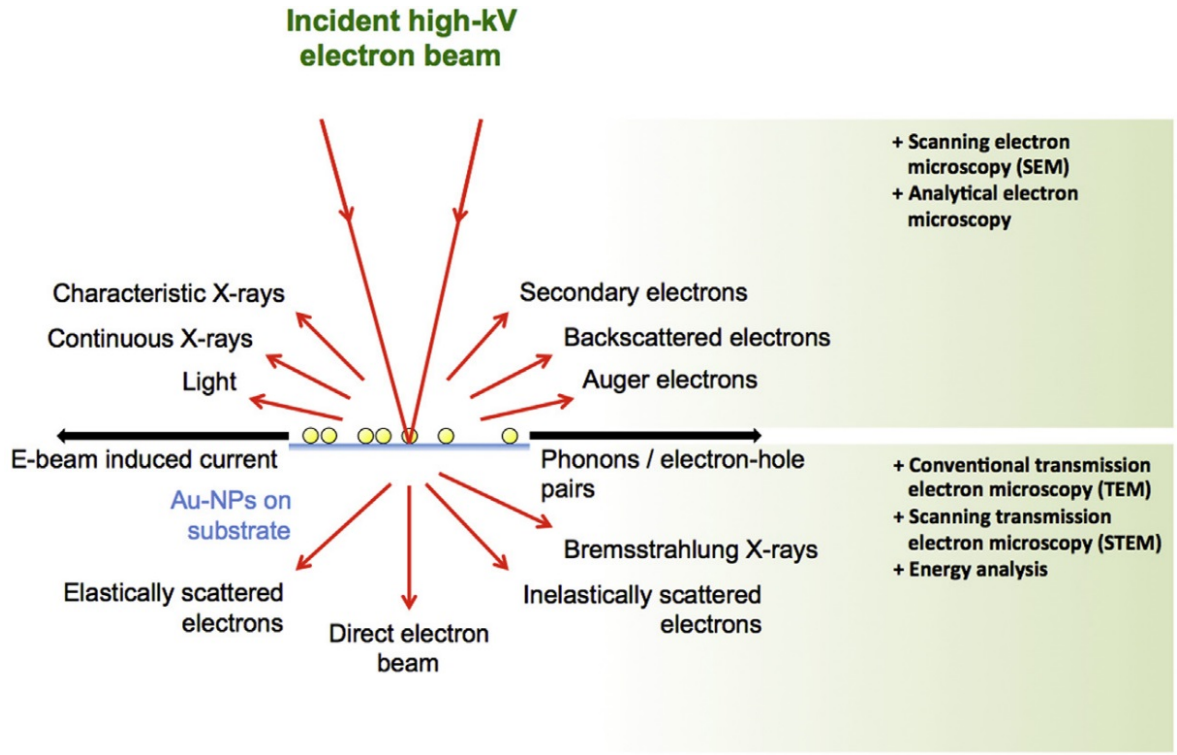

Figure 1: Electron beam interacting with the sample in SEM and TEM.

Defocus phase contrast

Vitrified or "cryogenically fixed" biological samples generate only weak contrast in the TEM. Electron micrographs of these samples recorded close-to-focus on these samples suffer from

poor contrast due to the contrast transfer function remaining at low spatial frequencies (Frank). Using the objective lens to apply an underfocus of approximately 5–10 µm can compensate for the damping of low frequencies. It can also help overcome difficulties in identifying the objects under scrutiny. Such an approach, termed 'defocus phase contrast', is the most routinely used phase contrasting method in cryo-EM (Dai et al.) (***Figure 2***, left panel). Defocusing the objective lens improves the contrast transfer of low frequency information; however, the envelope function of the CTF shows a continuous weakening of amplitudes towards higher spatial frequencies, which leads to a loss of high-resolution information (Zhu et al.). The CTF is a sinusoidal function that oscillates between positive and negative contrast transfer bands. It also forms nodes at places where it passes zero, i.e. there is no transfer of information, and data is lost at these frequencies (Danev et al.). This hindrance can be overcome to some extent by combining images recorded at several different defocus values. The idea behind such an approach is that their CTFs will have nodes at different spatial frequencies and will compensate for each other's areas of lost information.

To extract information beyond the first destructive electron interference (typically referred as ''the first zero''), a computational CTF correction can be applied to the electron micrographs (Fernandez et al.; Zanetti et al.). This becomes quite challenging when applied to tomographic data. The precise value of applied defocus is often hard to determine because of the low electron-dose imaging conditions as well as the gradients of the CTF values present throughout each projection due to the geometry of tilting (Zanetti et al.) (Eibauer et al.; Philippsen et al.; Winkler et al.). The use of defocus phase contrast mandates a trade-off between contrast and resolution, where higher defocus values lead to an increase in image contrast at the expense of the resolution, and vice versa.

Phase plates for cryo-ET

An alternative way to boost the contrast of low-resolution information, without sacrificing the high-resolution information in an image, is by adding a phase-shift-inducing device to the optical system (Zernike). There are several different kinds of such devices, and they are commonly referred to as ''phase plates'' (Danev et al.). Their routine use in TEM was held back for a long time by numerous technical issues such as charging, contamination, design, production, and required technical modifications to the microscope (Danev and Nagayama). The first phase plate useful for cryo-ET was the Zernike phase plate (Dai et al.; Danev and

Nagayama; Fukuda and Nagayama; Murata et al.). It is a thin amorphous carbon film (20-30 nm thick) with a submicron diameter hole (<1 μm) in its center, and is placed in the back focal plane of the TEM (***Figure 2***, middle panel). The unscattered electron beams passes unmodified through the central hole of the plate, while the diffracted beam hits the carbon layer experiencing a phase shift of about π/2 (Dai et al.). This phase shift changes the CTF from a sine to a cosine function that exhibits maximum contrast transfer at low frequencies. Images can be recorded in focus or at close-to-focus, thereby avoiding loss of information due to CTF oscillations (Murata 2010). Moreover, there is no need to correct the CTF as the information is uniformly transferred over a wide range of spatial frequencies (Danev et al.). ZPP was initially used for imaging small specimens such as purified protein complexes due to the restrictions imposed by the size of the central hole that limited the recoverable amount low resolution information (attributed to the 'cut-on frequency' of the plate (Danev et al.; Danev and Nagayama; Murata et al.) (Nagayama and Danev). ZPPs present a number of issues that have thus far prevented their widespread use. These include the rapid aging of the plate, which demands weekly exchange (Danev et al.), necessity for precise alignment and centering of the hole with respect to the path of the unscattered beam, and the artifacts introduced into the images by the edges of the hole, e.g. fringes around high-contrasting objects. A smaller hole-size allows imaging of large specimens but introduces alignment and centering difficulties (Danev and Nagayama; Fukuda et al.). The Volta phase plate (VPP), offers solutions to the above-mentioned issues. Similarly to the ZPP, a VPP can be placed in the back focal plane of the objective lens (***Figure 2***, right panel), and generates a phase shift of about π/2 when operated in-plane (Danev et al.). Unlike the ZPP, a does not have a hole and the unscattered beam passes through a continuous carbon film which produces the phase shift due differences between the inner and surface potentials generated by pre-irradiating (pre-charging) it with the central diffraction beam (Danev et al.). The VPP is easier to operate and has a longer life span.

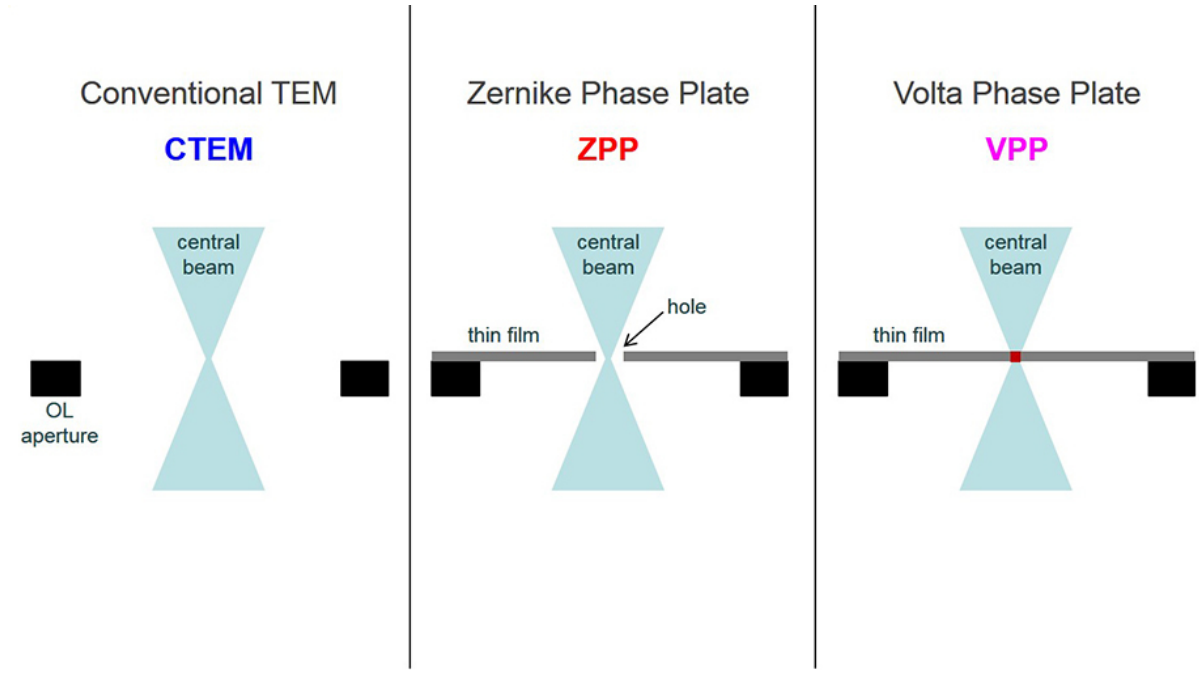

Figure 2. Schematic comparison between different phase contrast techniques.

Conventional TEM with the objective lens on the left, Zernike phase plate in the middle and the Volta phase plate on the right.

Imaging with direct electron detectors (DEDs)

The commonly used charge-coupled device (CCD) detectors are being replaced by a new generation of detectors that are based on complementary metal-oxide-semiconductor (CMOS) technology. DEDs possess neither a scintillator nor optical coupling and are designed to directly record the primary electrons, thereby dramatically improving both the detection sensitivity and the SNR (Faruqi and Henderson). One of the key advantages of DEDs over CCDs is that they show a significantly improved detective quantum efficiency (DQE) and modulation transfer function (MTF), particularly at high spatial frequencies (Bammes et al.; Clough et al.; Jin et al.; Ruskin et al.), and at 300 keV (McMullan et al.). Stage drift arising from the instability of the sample holder and beam induced sample motion, normally generated upon the interaction of the electron beam with the sample, both cause blurring of the images and are detrimental to resolution (Brilot et al.; Li et al.; Ramachandra et al.). DEDs offer a huge advantage in this respect by making use of a fast frame rate (10–40 fps) and a fast readout rate in order to correct for those motions. This is accomplished by subdividing each exposure into several frames, yielding a 'frame-stack'. The individual exposures within each frame-stack can then be computationally processed in order to align them with respect to each other ('motion correction') and projected into a single image that now possesses a significantly

enhanced contrast (Li et al.). Due to the recording of individual electrons, the Landau noise (noise arising from the statistical variations in the signal deposited by the incident electrons) and the readout noise are eliminated (Li et al.), increasing the DQE at low spatial frequencies (McMullan et al.). Correcting for drift and beam-induced movements (Li et al.; Ramachandra et al.) is of great importance for cryo-ET where the increasing sample thickness, stage tilt and longer exposure times at high tilts significantly start to affect the image quality. Owing to both an improved DQE and MTF, the DEDs have had a profound impact on the quality of high-resolution reconstructions in both the single-particle cryo-EM (Li et al.; Scheres) and cryo-ET (Asano et al.; Pfeffer et al.).

Principles of cryo electron-tomography (cryo-ET)

With cryo-ET, one can observe electronic densities *in situ* due to the phase contrast generated between the biological material and the surrounding vitrified ice. The initial step in the preparation of biological samples for cryo-ET is vitrification, which allows one to circumvent the use of chemical fixatives and contrasting agents such as heavy metal salts (Dubochet et al., 1988). Tomographic data acquisition is carried out within a TEM on vitrified samples of suitable thickness (< 1 µm). The samples are rotated around a defined tilt axis in pre-defined increments using a precisely controlled stage. The most commonly used scheme covers a maximal angular range of 140°, between -70° in one direction and +70° in the other (Frank, 1992) (**Figure 3**). A series of 2D projections, termed a 'tilt-series', is collected under 'low electron dose' conditions (typically <80 $e^-/Å^2$) in order to avoid excessive exposure of the sample the electron beam, which could lead to radiation damage (Dierksen et al., 1993). The acquired 2D projections are then aligned to a common frame using either fiducial surface markers, i.e. colloidal gold of approximately 10-15 nm in diameter (Amat et al.) or cross-correlation-based techniques (Castano-Diez et al.; Sorzano et al.). The aligned stack of 2D images is then used to reconstruct the 3D volume of the specimen, namely a 'tomogram' (Frank, 1992). The quality of the final tomogram depends directly on the value of the angular increments and the number of recorded two-dimensional images (Horowitz et al.). The lack of coverage in the high-tilt range (i.e. above -70° and +70°), however, inevitably creates an area of missing information termed 'the missing wedge'. It was named after its appearance in Fourier space, which leads to feature elongation and reduced resolution in the direction of the electron beam (Frank, 1992). A potential remedy for the effect of the missing wedge on

data quality is to acquire a second tilt-series orthogonal in direction to the first one, i.e. 'dual-axis tilting' (Mastronarde). This reduces the total area of the missing wedge to < 10%, however aligning the two perpendicular sets of projections remains a challenging task (Iancu et al.). Cryo-ET has had an instrumental role in several biological sub-disciplines including cellular biology (Al-Amoudi et al.; Maimon et al.; Patla et al.), and microbiology (Abrusci et al.; Bharat et al., 2012; Briegel et al.; Dobro et al.; Kurner et al.; Lieber et al.; Meyerson et al.; Swulius et al.). It can describe a particular cellular scene and provide a 3D structural map of a sample in a close-to-physiological state (Fridman et al.; Lucic et al.; Yahav et al.).

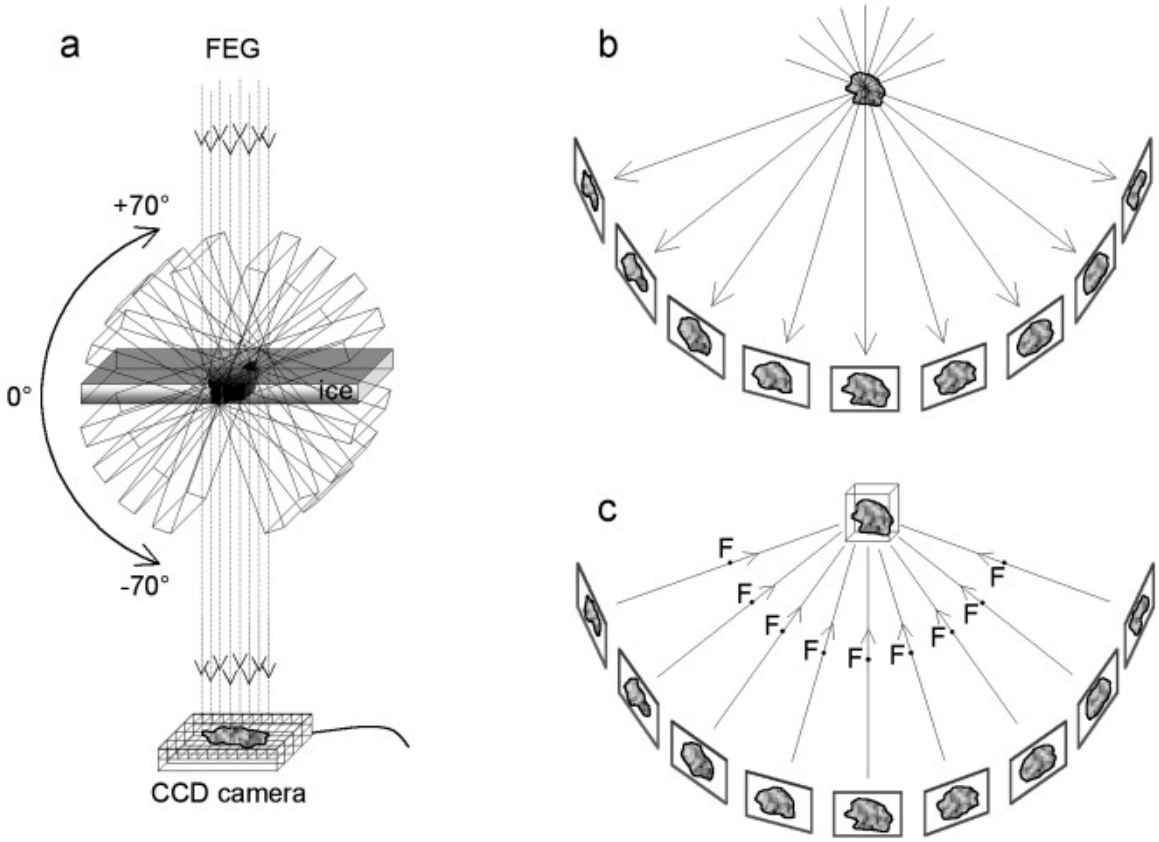

Figure 3. Schematic illustration of the tomographic imaging procedure and 3D volume reconstruction

(a) Tomographic acquisition scheme showing the tilting of the sample around a defined axis inside the TEM. (b) Collection of a series of 2D projection images. (c) Computational reconstruction of the 3D volume from the 2D projections. Adapted from (Grunewald et al., 2003).

Short introduction to subtomogram averaging

Particular intracellular structures and protein complexes (actin cytoskeleton, nuclear lamina, nuclear pore complexes (NPCs), and ribosomes) can be imaged in the context of the intact cell by using cryo-ET. The recorded images can subsequently be analyzed by specialized image processing methods (Frangakis and Forster). Tomograms containing macromolecular assemblies present in multiple copies can be further processed by 'subtomogram averaging' (Bartesaghi and Subramaniam; Briggs; Forster et al., 2005). The key idea behind subtomogram averaging is to combine the subtomograms (subvolumes of tomograms) containing the repeating structures in order to produce an average (final structure) with a higher resolution and SNR compared to the initial tomograms. In order to successfully apply subtomogram averaging to a biological complexes, they must must first be clearly identifiable within the sample, structurally homogenous (in as few conformations as possible, preferably one), and occur in many different orientations.

The first step in the subtomogram averaging procedure is to fill up the missing wedge in the tomographic data in order to generate a subtomogram average with isotropic resolution (Forster et al.). First, the subtomograms are aligned with respect to a common reference (***Figure 4***, left panel). The rotational part of the alignment is performed by an exhaustive search over a set of equally distributed Euler angles (Stolken et al.). The reference is rotated and convoluted with the missing wedge before a cross-correlation comparison with the sub volumes is carried out. These steps are performed successively for all desired angles (***Figure 4***, middle panel). This part is computationally and time exhausting, and therefore opens the opportunity for new software development that aim at accelerating the process (Bartesaghi et al., 2008; Castano-Diez et al.; Chen et al.; Hrabe et al.; Scheres et al.; Xu et al.). A unique rotation (indicated by the maximum cross-correlation value) and translation (given by the position of the cross-correlation peak) can be assigned to each subtomogram (Frangakis et al.; Frank). The subtomograms are then transformed according to the calculated parameters, and the aligned stack of volumes is averaged and ultimately serves as the reference for the next step. This iterative procedure is carried out until the structure no longer changes with subsequent iterations and no more significant rotations and translations are occurring. The iteratively refined transformations are used to generate the final subtomogram average (Walz

et al.) (***Figure 4***, right panel). Due to a high value of defocus usually applied in cellular cryo-ET, typically in the range of -6 to -15 µm, the maximal achievable resolution of a subtomogram average is around 3-5 nm. In order to extend the information beyond the first destructive electron interference, a contrast transfer function (CTF) correction can be applied to the projection images (van Heel et al.). Here, the resulting CTF-corrected tomograms serve as input data for subtomogram averaging. The CTF correction in combination with subtomogram averaging allows the reconstruction of images of macromolecular complexes in their native context, and will facilitate reaching resolutions close to 1 nm in the near future.

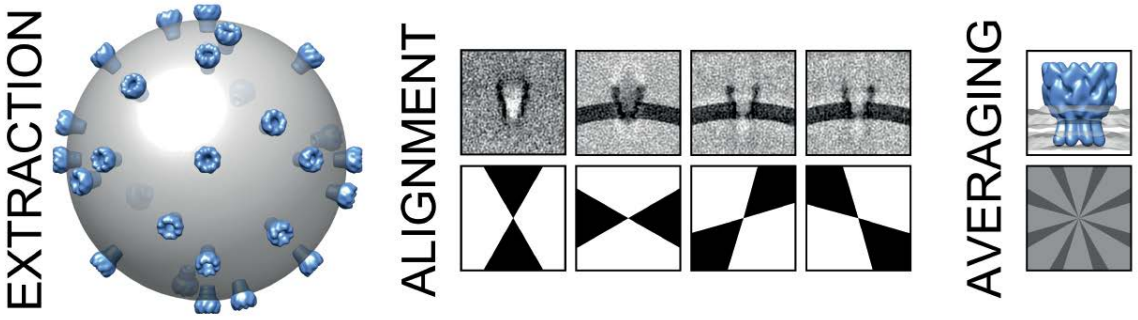

Figure 4. Schematic representation of the major steps involved in a subtomogram averaging procedure.

Introduction to cryo focused-ion-beam (cryo-FIB)

FIB technology is routinely used in the field of material sciences in order to manipulate sample thickness and access the interiors of complex materials (MoberlyChan). In biological sciences, it is conducive to a broad range of applications for the sequential imaging of plastic embedded samples at room temperature (Bennett et al.; Bushby et al.; Heymann et al.) It provides highly-resolved views of membranes up to 5 nm (Kreshuk et al.), however, the three-dimensional details of macromolecular complexes cannot be fully reconstructed due to fixation, dehydration, staining with heavy metal salts, and embedding of the specimen into resins (Bushby et al.).

Cryo-FIB is the technique of choice for the production of thin, vitrified specimens for the subsequent cryo-ET analysis (Marko et al.; Marko et al.; Rigort et al.; Wang et al.). EM grids containing vitrified samples can be directly transferred to the cryo-FIB without further processing or use of chemical fixatives and stains. The sample is thinned by a beam of Ga^+ ions

travelling at a velocity sufficiently high to overcome the surface binding energies of the sample upon collision. This interaction causes the displacement of atoms and leaves a thinned surface (Giannuzzi). Cryo-lamellae of various tomography-suitable thicknesses can be readily produced (***Figure 5***). Upon completion of the milling, the EM grid is transferred into TEM for tomographic analysis. High quality tomograms of biological samples (Rigort et al.), irrespective of the original cellular thickness, can be acquired opening up a plethora of directions for studying the structural and functional organization of both cells and tissues, e.g. human cells and embryos of *C. elegans* (Harapin et al., 2013). The quality of these tomograms makes possible the application of subtomogram averaging techniques (Rigort et al.) and the reconstruction of macromolecular complexes in tissues.

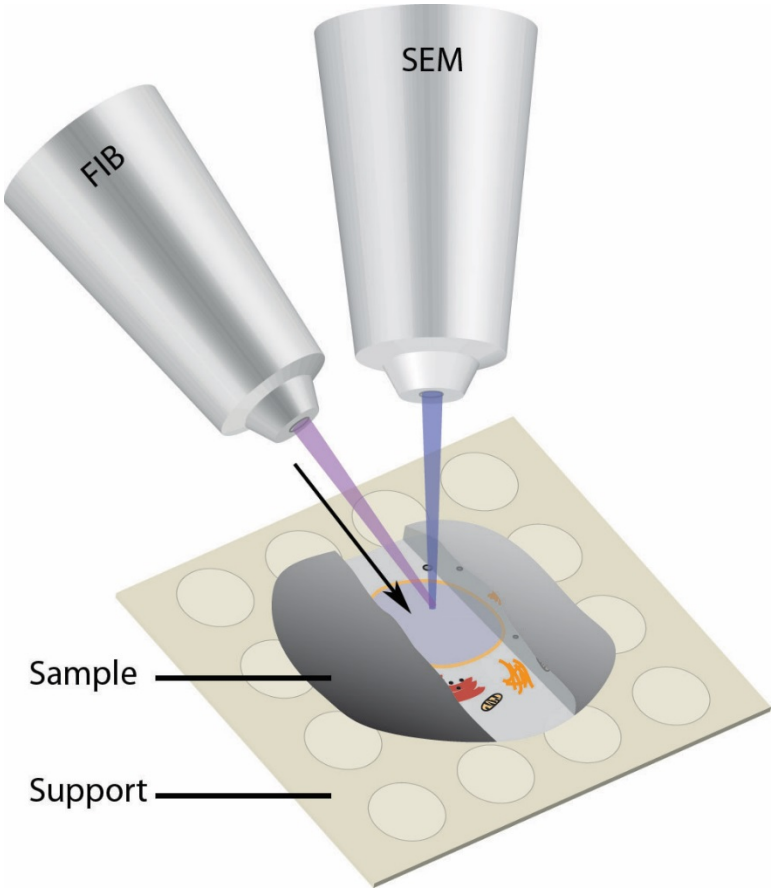

Figure 5. Schematic representation of the cryo-FIB milling procedure.

Chapter 2

Structural analysis of multicellular organisms with cryo-ET

Introduction

CET has over the recent years evolved into the method of choice for the structural studies and characterization of intracellular landscapes and macromolecular complexes contained therein (Dubrovsky et al.; Fridman et al.; Gan and Jensen; Lucic et al.; Yahav et al.). This was mostly accomplished through its unique combination of snap-freezing of the samples, which allows water to be vitrified and biological processes momentarily arrested, and tilting of the specimen inside the electron microscope, which allows one to ultimately achieve much better sampling in terms of the total amount of obtainable information. A series of 2D projection images of a vitrified sample is routinely collected by tilting the sample around a defined axis, aligning the projections to a common reference using surface fiducial gold markers, and ultimately back-projecting them to reconstruct the sample volume (Frank; Lucic et al.). Three-dimensional tomographic reconstructions obtained from suitably thin (i.e. < 1µm) regions of intact biological samples (e.g. peripheral regions of fibroblasts, and viruses) have already yielded detailed insights into many cellular processes (Ben-Harush et al.), while thick specimens (i.e. > 1µm) such as most eukaryotic cells or tissues cannot be imaged without previously applying some form of a thinning procedure (Al-Amoudi et al.; Harapin et al.). Various sectioning methods, making use of diamond knives for cutting the specimens, have been routinely applied in order to make whole-mount biological samples transparent to the electron beam. However, many drawbacks remained inherently associated with such crude physical cutting methods. These include, (i) artifacts that arise from the use of chemical fixatives, which can have detrimental effects on the molecular structures and local organization, (ii) sectioning with diamond knives, which often produce visible clefts and crevices on the surface of the sections, (ii) and staining with heavy-metal salts, which gives rise to issues in the correct interpretation of what is being visualized (Dubochet et al.).

Vitreous samples for CET analysis are usually prepared using the so-called snap-freezing methods by which heat is drained from the sample at very high rates. This occurs when the sample is immersed into a liquid with a very high specific heat capacity that is actively cooled by liquid nitrogen and therefore kept at close to liquid nitrogen temperatures (i.e. -196°C)

(Dubochet et al., 1988; Luyet and Gehenio, 1940). Despite being a fast coolant on its own, liquid nitrogen does not possess a specific heat capacity high enough to allow the water contained inside biological samples to transition into amorphous (i.e. vitreous) solid (i.e. ice) when frozen, but rather stays in a crystalline solid state (Dubochet and Mcdowall, 1981). This inevitably leads to the inability to execute cryo-ET on such samples. Therefore, biological samples are most often vitrified by plunge freezing or by high-pressure freezing (HPF). Both methods allow the water in biological samples to become vitrified either by plunging the samples into liquid nitrogen-cooled liquid ethane, which acts through its very high specific heat capacity to swiftly drain the heat from the sample, or by using various organic solvents as freezing media, such as hexadecane, under very high pressure to achieve the same. Both techniques result in a sample in which the water content is in a vitreous state and the sample itself has been fixed physically, rather than chemically. The outcome on the cellular and subcellular levels is the momentary arrest of all biological processes as well as the preservation of the ultrastructural details of macromolecules and macromolecular complexes in their native physiological environment (Dobro et al.; Dubochet and Sartori Blanc). Several factors influence the successful outcome of vitrification as well as its uniformity throughout the sample, most notably the thickness of the material, which predetermines the method to be used, and the presence of naturally occurring intracellular cryoprotectants (Gilkey and Staehelin), which largely facilitate it. Samples that are up to a few tens of μm in thickness can be successfully vitrified by plunge freezing while much thicker ones, such as whole-mount biological specimens, require the application of high-pressure freezing (Hunziker et al.).

Cryogenic focused-ion-beam scanning electron microscopy (cryo-FIB-SEM) has been developed relatively recently and has since been successfully applied in order to reduce regions of interest within a vitrified biological sample to thin lamellae suitable for imaging with cryo-ET as well as further down-stream structural analyses (Hsieh et al.; Marko et al.; Rigort et al.; Wang et al.). Sample thinning proceeds in multiple rounds via a surface sputtering process. This involves aiming a focused beam of Ga^+ ions at the region of interest wherein the accelerated heavy ions cause the ejection of atoms from the sample surface upon colliding with them. The process is non-detrimental to the residual sample surface and any implantation of Ga^+ ions, as well as surface heating, is normally restricted to the first 10 nm of the surface when working with low currents and under room temperature conditions (Giannuzzi and Stevie). However, the milling procedure ultimately leaves the thin lamellae,

destined for imaging in the electron microscope, devoid of surface fiducial markers. This makes the process of tomographic imaging and the subsequent alignment of the 2D projections challenging due to the poor signal-to-noise ratio of the images recorded from specimens thicker than 200 nm (Grimm et al.). For samples that are <200 nm thick, feature-tracking methods have been used to successfully align and subsequently reconstruct the 3D volume when images were recorded at high values of defocus (Rigort et al.). However, for thicker samples as well as for close-to-focus imaging, fiducial markers remain an indispensable prerequisite for high-resolution tomographic reconstructions that can be used for further image processing.

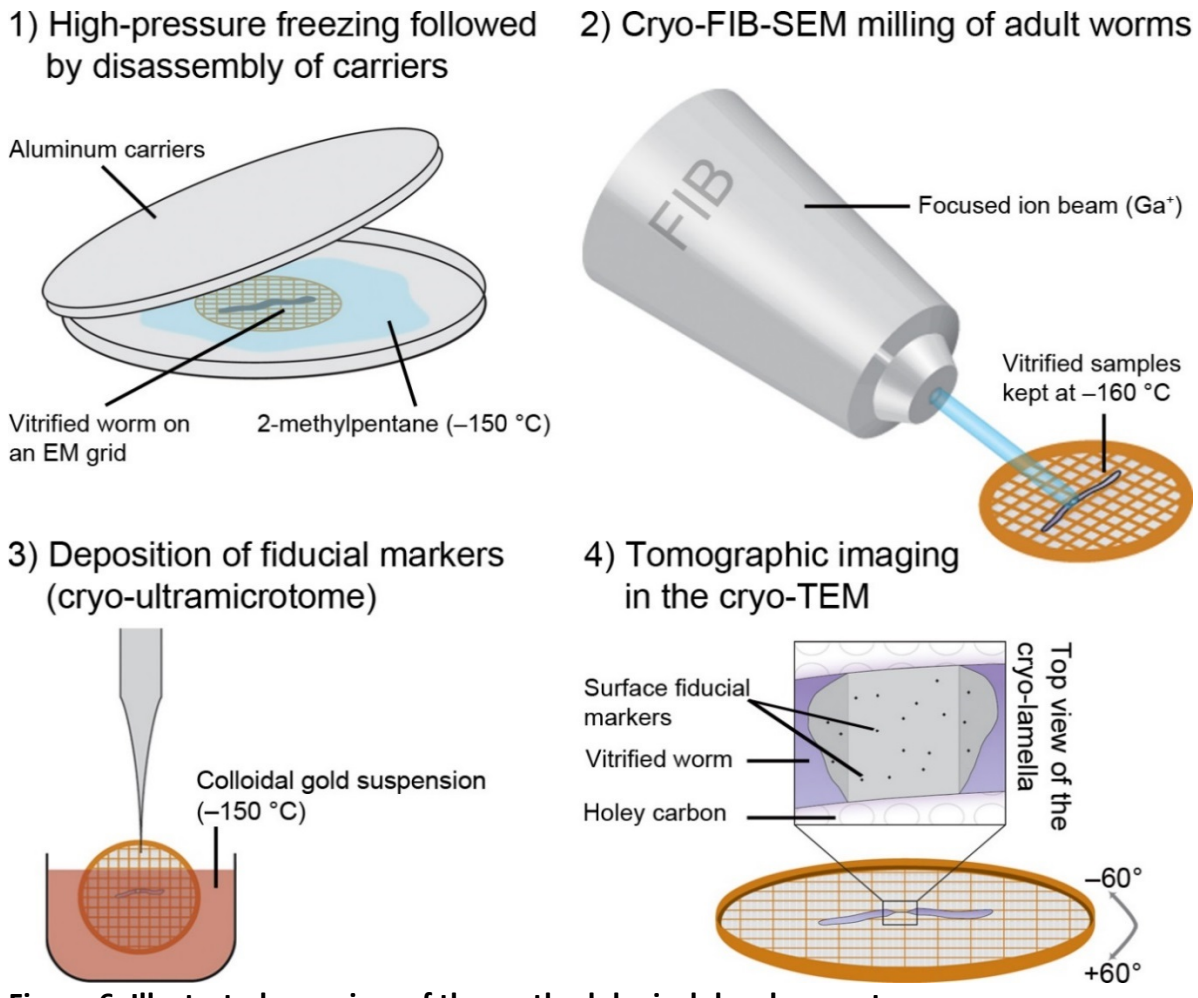

Figure 6. Illustrated overview of the methodological developments.

(1) HPF freezing of whole-body *C. elegans*, (2) cryo-FIB-SEM milling, (3) deposition of colloidal gold markers on top of the vitreous cryo-lamellae, (4) and tomographic imaging.

Materials, methods, and developments

Cryo holder and shutter design

The prototype cryo holder of the VCT100 cryo-transfer system (Leica Microsystem, Vienna, Austria) was obtained from Leica Microsystems as part of an ongoing collaboration to improve its design through dedicated user feedback. The prototype holder was equipped with a slit that could take in two EM grids at a time and the opening and closing of the slit was regulated via two separate screws located just underneath each of the slits. The prototype was designed to hold the grids at an angle of approximately 45° with reference to the horizontal baseline, and the depth of the slits was created such that almost one half of the grid surface would fall into the slit (***Figure 7***, panel a). This posed two potential issues for our future usage and applications. The first problem was the geometrical constraint during the movement of the SEM stage inside the FIB-SEM device. It could not be moved nor tilted to cover a full angular range in the direction of the FIB column but was limited to only a few degrees. This meant that we needed to make sure that our grids were held inside the slits at an angle that would require minimal adjusting with respect to the FIB column. The second issue was that we wanted to have access to as much of the grid surface as possible. During the process of sample vitrification, irrespective of the freezing method of choice, one cannot control where the samples will physically be positioned on the surface of the holey carbon layer after freezing. Due to the nature of plunge freezing, embryos of *C. elegans* would often end up clustering slightly more on the bottom of the grid hanging from the guillotine-like plunge freezer due to gravity. In addition, grids would often suffer from breakage of the holey carbon layer as well as well as poor spreading on the grid. In terms of cryo-FIB-SEM milling, this could lead to the user spending significantly more time screening through many grids and having to constantly take out old ones and insert new ones in order to find those with the most optimal conditions. Therefore, we chose to create the most optimal conditions we could before starting the cryo-FIB milling procedure. We modified the prototype holder in order to accommodate standard EM grids (Quantifoil Micro tools, GmbH) at a 30° preset angle with respect to the horizontal base line (***Figure 7***, panel b, white arrowhead), which translates into a 6° angle pre-tilt between the sample and the FIB column in the Auriga cross-beam system (Carl Zeiss Microscopy GmbH, Oberkochen, Germany). The attachment slit for EM grids is now composed of two aluminum pieces (***Figure 7***, panel b, green and red arrowheads). Opening and closing

is regulated via a screw located on the top part (Figure 7, panel b, black arrowhead); clock-wise rotation to open, and counter clock-wise to close, while the base is freely movable (Figure 7, panel b, green arrowhead). The shutter was redesigned as an aluminum box that completely envelops the cryo-holder and facilitates contamination-free specimen transfer from liquid nitrogen to high-vacuum conditions and back (***Figure 7***, panel c). The shutter is kept firmly attached under cryogenic conditions to the tip of the manipulator of the VCT100 cryo transfer shuttle (Leica Microsystems) by means of a freely rotatable Teflon ring. A 90° clockwise rotation of the VCT rods fastens the holder onto the desired stage and the shutter retracts with the inward movement of the rod, thus leaving the EM grids carrying the specimens exposed in the high-vacuum cryo-devices (***Figure 7***, panel d). A 90° counterclockwise motion releases the holder from the desired stage and while at the same time keeping the shutter firmly in place, thereby ensuring that the EM grid is completely shielded from any atmospheric disturbances during transfer.

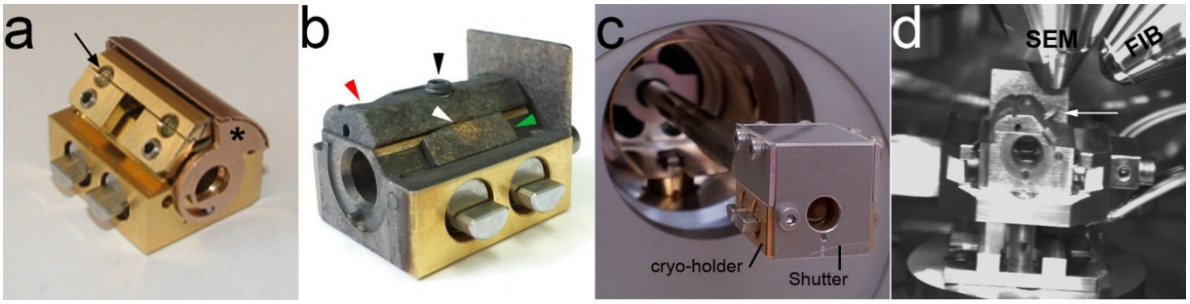

Figure 7. Cryo-holder and shutter design.

Panel (a) shows the Leica prototype cryo-holder before modifications were carried out to accommodate EM grids at a specific pre-tilt with respect to the FIB beam (b. Panel (c) shows the cryo-shutter attached to the holder at the tip of the VCT system. Panel (d) shows the whole setup on the cryo-stage within the Auriga dual-beam device.

Cultivation of *Ceanorhabditis elegans*

Worms were kept in continuous culture on NGM plates supplemented with the OP50 bacterial strain (obtained from Caenorhabditis Genetics Center, University of Minnesota, Minneapolis, USA) according to a well-established protocol (Brenner). Fresh culture plates were prepared either by transferring a piece of agar from an old plate (i.e. chunking) onto a new one or by bleaching the plates. This was done at least once a week, and every two to three weeks fresh L1 worms were awoken from the -80°C storage and new stocks were regularly frozen. Bleaching was mostly performed in order to temporarily synchronize the growing worm population and, occasionally, to get rid of contamination (Brenner; Strange et al., 2007).

Modified Tokuyasu cryo-sectioning of *C. elegans*

A plate comprising a mixed population of *C. elegans* worms was used to pick worms from. Worms were transferred into a droplet of Levamisole and left for a minute until they were fully paralyzed. The droplet of Levamisole (Sigma-Aldrich, Switzerland) was then replaced by a chemical fixative and the worms were cut into three equally-sized pieces with a scalpel. Several worms at a time were processes this way and left in the fixative for an hour. Many fixed pieces were collected by pipetting (the tip of the pipette was shortened by trimming) into a 1.5 mL Eppendorf tube. Once the worms had pelleted onto the bottom of the tube, excess liquid was pipetted away and a small amount of molten gelatin was added such as to cover the bottom of the tube. Once the tube had cooled and the gelatin solidified, the bottom of the tube was cut off by a scalpel and the gelatin was squeezed out and placed onto a chilled glass slide under a binocular. It was then assessed for the presence of the worm fragments, which were normally found in a concentrated spot on the very bottom. This part was sliced into roughly 1 mm^3 cubes and each of those was glued onto a cryo-sectioning aluminum pin using a droplet of 2.3 M sucrose. These pins were then flash-frozen in liquid nitrogen and stored in a dewar at -80°C.

Pins containing the frozen samples were attached to the cryo-sectioning motor and trimming was performed at -75°C with a 50mm/s feed and in 100 nm thick slices. Trimming was carried out such that the resulting shape on the sample surface was a pyramid with a flat top. The flat top was shaped as a rectangle and fine sectioning was carried out along the longer side of it. Fine sectioning was done at -105°C with a 0.3 mm/s feed and in 200-300 nm slices. Cryo-sections were collected in ribbons of 5 and picked up with the help of a specially-designed loop in a droplet of 2.3 M sucrose (Tokuyasu). The drop was taken out of the cryogenic environment, thawed for 10s, and applied onto an EM grid. The EM grid was subsequently placed onto a drop of sterile water with the sample facing downward. Re-hydration was carried out for 2-3 hours in order remove sucrose remnants and re-hydrate the sample as much as possible. Cryo-sections were then vitrified by plunge freezing.

The procedure was essentially the same for U2Os cells, differing only in the very beginning. The cells were trypsinized from cell culture dishes, collected into tubes, gently pelleted, and embedded into gelatin.

Plunge freezing of *C. elegans* embryos

Mixed populations of adult worms were synchronized by bleaching and embryos were isolated on a large scale and collected in 1.5 mL Eppendorf tubes in M9 buffer (Brenner). Approximately 40 embryos were applied onto plasma-cleaned, holey carbon, copper grids (Quantifoil, Germany) in a 3 µL droplet using siliconized pipette tips and inspected under a binocular. Grids showing a satisfactory amount and distribution of embryos were then blotted 3-6s, plunged into liquid nitrogen-cooled liquid ethane, and stored in liquid nitrogen storage dewars.

High-pressure freezing (HPF) of intact worms

Worms were washed off plates with M9 buffer (at either a particular stage of development or a mixed population) and a desired dilution was pipetted onto plasma-cleaned, carbon-coated, copper grids using siliconized pipette tips. An approximately 2 µL droplet of worm suspension was applied directly onto the center of the EM grid to avoid the worms spreading towards the edges. Grids were then blotted on filter paper in order to remove the bulk of the liquid and subsequently air-dried briefly (up to 5 s). Grids were then quickly transferred into the 100 µm cavity of an acetone-cleaned, 6 mm aluminum carrier (Wohlwend Engineering, Sennwald, Switzerland), which had been pre-moisturized with a small droplet of 2-methylpentane (Sigma). After the grid had stuck to the carrier, the compartment was filled with 2-methylpentane, applied with the help of a Hamilton syringe, until the sample was completely covered. A flat, 6 mm, aluminum carrier was placed on top causing the excess solution to drain into the surrounding filter paper. The sandwiched assembly was then quickly transferred into the middle plate setup at the loading station of the HPM100 high-pressure freezing machine (Leica Microsystems). Samples were frozen without using ethanol as synchronization fluid. Aluminum carriers were inspected for pressure-induced deformation (bends and kinks) after the freezing process and bent carriers were discarded. Straight carriers were transferred into the FC6 cryo-ultramicrotome chamber (Leica Microsystems) at -150°C, causing 2-methylpentane to thaw (melting point at -160°C), and taken apart after ~10 minutes. Grids were inspected under the binocular and only those containing physically undamaged worms were retrieved with tweezers and stored in grid boxes in liquid nitrogen.

Freezing of Drosophila melanogaster embryos

Drosophila melanogaster embryos (w1118) of varying developmental stages were collected on apple agar plates and dechorionated. Various substrates were tested for the stable attachment of fly embryos onto plasma-cleaned, 200 mesh, holey carbon, copper EM grids (Quantifoil) prior to cryo fixation. The use of poly-L-lysine turned out to be the most successful. In this approach, glow-discharged grids were first coated by incubation on droplets of poly-L-lysine within a humidified chamber. Embryos were subsequently added, excessive liquid removed with a filter paper, and the set-up was air-dried for 10 min.

Many other conditions were also tested. (i) A thin layer of silicon grease (Baysilone-paste, Bayer) was applied onto the EM grid and the embryos placed on top with a fine paintbrush. (ii) Grids were floated on a droplet of 20% BSA in a humidity chamber, embyos placed on top and the excess liquid blotted after 10 min of air-drying. (iii) The waxy layer of the vitelline membrane removed in order to alter the chemical composition of the embryo's surface according to Rand and colleagues (Rand et al.). To this end, the embryos were incubated in a 1:10 solution of 90% R-limone (Fluka), 5% cocamide DEA (Ninol 11 CM, Stepan Chemical), and 5% ethoxylated alcohol (Imbentin U/070, Kolb) for 2 min. After treatment with the embryo permeabilization solvent, embryos were washed 4x in PBS and placed onto an EM grid coated with poly-L-lysine. (iv) A heptane-glue mixture, otherwise routinely used in the positioning of embryos on imaging dishes for spinning disc confocal microscopy, was applied as a fine film between EM grid and fly embryos. (v) EM grids were incubated on droplets of either lectin concanavalin A (Calbiochem) or lectin from Bandeiraea simplicifolia (Sigma-Aldrich) within a humidified chamber and subsequently air-dried on the EM grid prior to being high-pressure-frozen (HPF). (vi) Dechorionated embryos were attached to a poly-L-lysine coated grid and dried for 3 to 4 min in a silica gel chamber (Roth). (vii) Finally, a east paste (baking yeast) was tested in order to glue the embryo to the grid. None of these approaches yielded a satisfactory outcome.

Preparation for cryo-FIB-SEM milling

Grids containing vitrified worms were attached under liquid nitrogen to the slit of the modified cryo-holder at the cryo working station (Leica Microsystems). Afterwards, they were transferred with the VCT100 shuttle onto the cryo-stage of the BAF060 freeze-fracturing device (Leica Microsystems) held at -170°C. After app. 15 minutes, 2-methylpentane had

completely sublimed under high-vacuum conditions (app. 10^{-7} mbar), leaving the surface of the EM grid free of embedding material and the sample fully exposed. App. 20 nm of carbon were deposited onto the surface of the grids by electron beam evaporation under standard conditions (acceleration voltage 1.78 kV, emission voltage 0.78 V, steady evaporation rate of 0.2 nm/s) in order to facilitate subsequent SEM imaging and cryo-FIB-SEM milling. Grids were then transferred with the VCT100 shuttle system from the BAF device onto the cryo-stage of the Auriga crossbeam system, which was actively cooled by an external dewar and kept at -156°C.

Grids containing embryos that had been vitrified by plunge freezing were processed in a similar fashion with a few modifications. They were coated with 10 nm of carbon coat inside the BAF060 before being transferred to the Auriga crossbeam without additional processing or modification being carried out.

Grids containing the chorionated embryos attached via poly-L-lysine interaction, were placed into the 150 µm deep indentation of an acetone-cleaned 6 mm aluminum platelet carrier (Wohlwend Engineering), which was premoisturized with a small droplet of 2-methylpentane (Sigma). The cavity of the carrier was further filled with the freezing medium using a Hamilton syringe, covering the embryos completely. The HPF-sandwich was closed with the flat side of a 6 mm B-type carrier, draining excess solution into the surrounding filter paper. Vitrification was performed using the Leica HPM100 (Leica Microsystems) without ethanol spraying. Grids with vitrified fly embryos were retrieved from the sandwich by placing the assembly for 10 minutes into a cryo-chamber (Leica EM FC6) set to -150°C, causing 2-methylpentane to thaw. After a visual inspection of vitrified embryos for physical damages, such as cracks with the built-in stereomicroscope, the EM grids were stored in liquid nitrogen. Attaching the grid to the modified cryo holder was performed in a dedicated cryo station (Leica Microsystems). Transfer steps were carried out using a VCT100 shuttle. Sublimation of 2-methylpentane was performed under high vacuum conditions within less than 30 min in a BAF060 device (Leica Microsystems), cooled to -150°C. A layer of carbon (15-20 nm) was applied by electron beam evaporation while rotating the sample and turning the carbon source to avoid charging problems complicating the SEM imaging.

Cryo-FIB-SEM milling

The FIB column of the Zeiss Auriga crossbeam system used in this study was regularly heated, and the apertures for the different milling current strengths were fully aligned once per week. It remained stable throughout the duration of the entire procedure. After the sample was inserted, the stage was mechanically manipulated into the final position for imaging and milling. The eucentric axis of the stage was set to 13 mm, after which the stage was brought to very close proximity of the SEM column. The working distance (i.e. point of intersection of the SEM and FIB beams) was then set to 4.95 mm and the area of interest brought into focus by adjusting the Z-height of the stage. After centering the features of interest, the stage was left to rest for about 10 minutes. This eliminated drift-related imaging issues, and from this point onward the beam shift dials were used to center the features of interest on the screen.

We chose the lamella-type milling approach, which entails gradual reduction of total sample surface from above and below the horizontal mid plane. Intact worms are up to 1 mm in length and 60 µm in diameter. Rough milling was performed in several rounds, first using a 4 nA probe, followed by a 240 pA probe to reduce the thickness around the area of interest in the mid plane of the worm. Once the thickness was ~2 µm, fine milling was performed at 50 pA leaving an approximately 660 nm thick lamella. In this case the penetration depth of the Ga^+ beam was set to 8 µm, due to the huge diameter of the animal, and the whole procedure took ~30 hours (milling was carried out in multiple steps that individually took 1-3 hours, depending on the beam current strength and penetration depth used). After milling was completed, the cryo-holder was retrieved from the Auriga, and the grids were disassembled from it in the cryo-working station under liquid nitrogen and stored in grid boxes in liquid nitrogen dewars.

C. elegans embryos are approximately 40x20 µm in size. First rounds of so-called rough milling ware performed using a 240 pA probe. This was used to reduce either the middle of the sample or one of the edges to a 2 µm thick layer. Fine milling was then performed using a 50 pA probe, leaving an approximately 330 nm thick lamella. The Ga^+ beam was set to a penetration depth of 3 µm and the whole procedure took ~4 hours per embryo. All the FIB apertures used here were operated at 30kV of acceleration voltage and SEM imaging, when needed, was carried out very quickly with an electron acceleration voltage of 5 kV in order to minimize detrimental effects of electron on the sample surface.

Cryo-FIB-SEM milling of *D. melanogaster* embryos was performed with the Auriga cross-beam system (Zeiss, Germany), which was actively cooled to -156°C through a self-refillable liquid nitrogen dewar. Within subsequent rounds of material ablation from below and above the region of interest, a thin cryo-lamella was created. Coarse milling was performed using a 16 nA probe, followed by semi-fine milling with a 240 pA probe and further thinning with a 50 pA probe. This generated a 200-300 nm thick lamella within 3-4 days of milling. The milling depth was set to 7-13 µm depth, using 2-3 layers. The generated lamellae were transferred and stored in liquid nitrogen dewars.

After the milling was completed, the surfaces of the lamellae exhibited typical FIB-related artifacts. These included curtaining (due to irregularities on the sample's surface first encountered by the FIB beam), some Ga ion deposition at the edges of the lamellae (due to the nature of the interaction of the Ga ions with solid surfaces), and a slight increase in thickness of the area on the lamella where the beam exits the sample (due to defocusing of the Ga ion beam). We have found that curtaining as well as big variations in thickness can be circumvented by setting the penetration depth of the beam to approximately twice more than what is needed.

Synthesis and application of fiducial gold markers for the cryo lamellae

We modified a toluene-based synthesis of suspensions of colloidal gold particles similar to the procedure described by Hiramatsu and Osterloh in 2004(Hiramatsu and Osterloh, 2004). A solution containing 50 mg of tetrachloroauric acid (Sigma) in 1.0 g (1.2 mL) of oleylamine (Acros Organics, Geel, Belgium) and 1.0 ml of toluene was quickly injected into a solution containing 1.7 g (2.9 mL) of oleylamine in 49 mL of toluene at 110°C. The reaction was carried out for 2 h at this temperature, after which the products were precipitated by the addition of 100 mL of ice-cold methanol. Particles ∼10 nm in diameter were isolated by centrifugation at 500g, methanol was decanted, and the tubes were left to air-dry in order to evaporate residual methanol. Finally, the gold particles were resuspended in 1 mL in 2-methylpentane. Where needed, the gold particles were further diluted to a desired concentration with 2-methylpentane. Gold was applied to the lamellae in the cryo-ultramicrotome chamber held at -150°C, inside 0.5 mL wells of an aluminum box (produced by our in-house workshop). Grids were briefly immersed into the gold suspension (2-3s), rinsed twice by immersion into liquid

ethane in adjacent wells, blotted extensively (>20s) with filter papers until no residual liquid could be observed on the tweezers or the grids, and stored in grid boxes.

Cryo-ET and annotations

Specimens were analyzed in a 300 kV FEG FEI Polara transmission electron microscope (FEI, Eindhoven, the Netherlands) equipped with a Gatan post-column GIF 2002 energy filter. Tilt series were acquired, covering either an angular range of +60° to -60°, unless otherwise indicated, with 2° tilt increments and defocus values ranging from -6 µm to -16 µm, for both the embryos and intact worms. Primary magnifications of 41,000x and 50,000x were used and this resulted in a 4.08 nm and 3.36 nm pixel size, respectively. Projection images (2048 × 2048 pixels) were aligned using 10 nm fiducial gold markers, and reconstructed by means of a weighted back-projection algorithm, as implemented by the TOM toolbox software package33. Width of the energy slit used for tomographic imaging was 20 eV. Images were collected on a Gatan Ultrascan 4000 CCD camera. Three-dimensional rendering and annotating was carried out using the Amira 3.0 software.

Correlative light and electron microscopy

EM grids containing cryo-FIB processed embryos of *C. elegans* have been detached from the cryo-holder inside the cryo-working station and directly transferred (i.e. dipped) into a solution of 4% PFA in M9 buffer. After 15s the grids were removed from the fixative, rinsed gently in M9, and placed in a small droplet of M9 on a petri dish with a microscopy coverslip built into the bottom. Bright-field and fluorescent images were acquired on a Leica upright microscope (Leica, microsystems, Germany).

Results

A. Establishing sample preparation techniques for the imaging of the nuclear lamina in its native context in *C. elegans* and mammalian cells (U2Os)

Cryo-sectioning of whole-body *C. elegans* worms

In order to assess the initial quality of the sample preparation procedure, cryo-sections were transferred onto standard EM grids and placed in a droplet of 2% uranylacetate for 1 minute. The negatively stained sections showed remarkable structural preservation and most of the tissue as well as intracellular features could readily be observed. The cuticle, gut, and many lipid vesicles were clearly discernable in all images (**Figure 8**, panel, a). Upon closer inspection of selected cells, one could easily observe the nuclear envelope barring a single NPC, as well as many typical cytoplasmic features (**Figure 8**, panel b). Subsequent rehydration of snap-frozen cryo-sections and their examination with cryo-EM revealed the interiors of the cuticle and muscle layers (**Figure 8**, panel c), as well as that of the gastrointestinal tract, where many microvilli could be seen projecting into the intestinal interior (**Figure 8**, panel d).

CET was carried out on the sections and revealed the intracellular milieu in detail. The nuclear envelope, NPCs (**Figure 8**, panel f, black arrowheads), mitochondria, and the Golgi network were all clearly detectable (**Figure 8**, panels e and f). The goal of this approach was to visualize the nuclear lamina in its native context within the worms. A more clear view of it was unfortunately obstructed by the nature of the sample preparation procedure, additional contrast electron densities emanating from the sucrose infiltration procedure and the chemical aldehyde fixation, as well as the presence of heterochromatin at the nuclear periphery (**Figure 8**, panel f, white arrows).

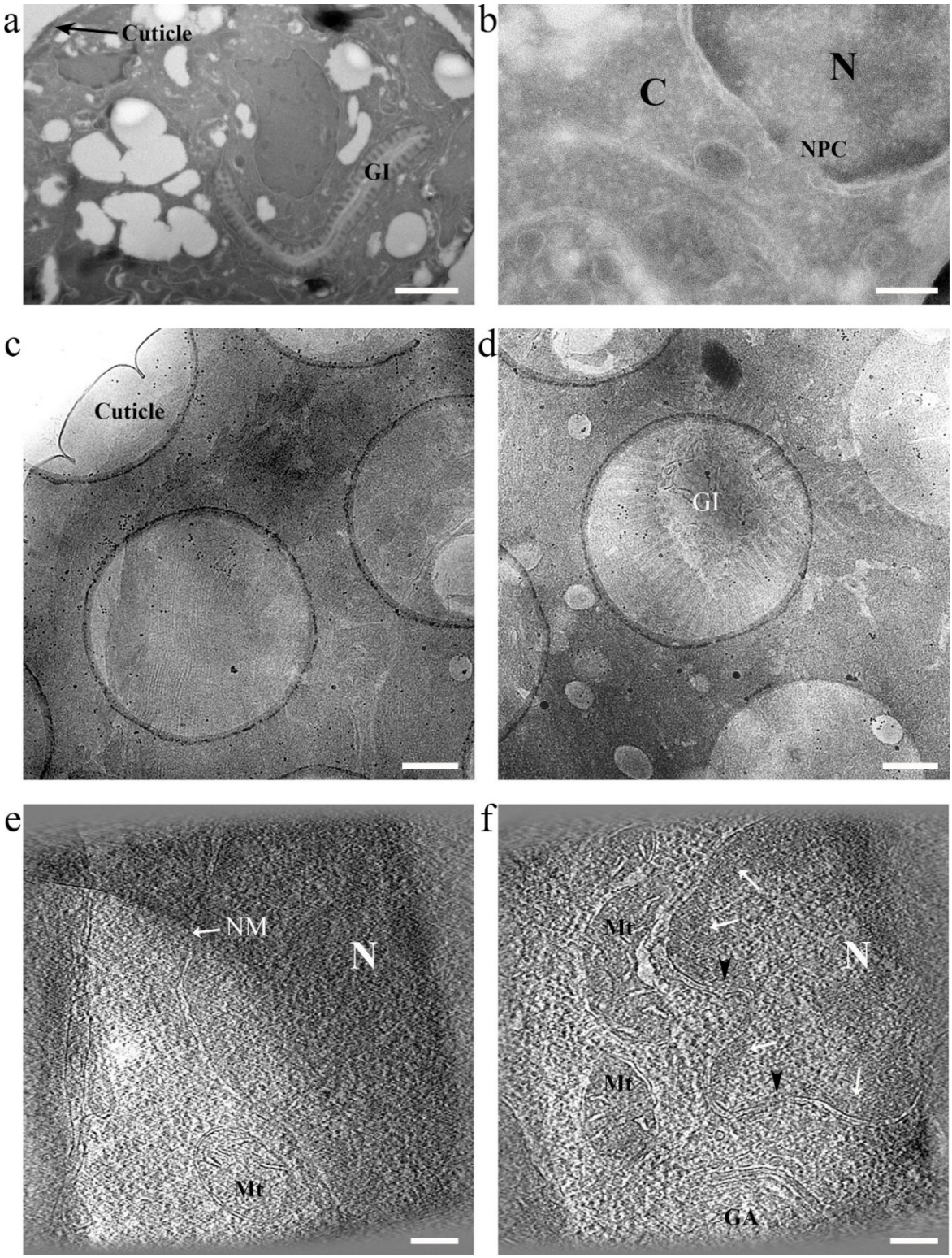

Figure 8. Cryo-sectioning and EM/ET evaluation of cryo-sections of whole-body *C. elegans*.

Panels (a,b) show 300 nm thick cryo-sections negatively stained with 2% uranylacetate. Panels (c,d) show cryo-EM images taken on 300 nm sections. Panels (e,f) show slices from representative tomograms acquired on 300 nm sections. Scale bar values: a (1 µm), b (100 nm), c and d (500 nm), e and f (200 nm).

Cryo-sectioning of sucrose-shocked U2Os cell

The inability to expose the nuclear lamina in *C. elegans*, due to the limitations of sample preparation as well as its close association with heterochromatin at the nuclear periphery (Richter et al., 2008), prompted us to try an approach previously described by Richter and colleagues in 2007. According to their results, we used 320 mM sucrose in the cell culture medium in order to osmotically shock human U2Os cells, leading to a reversible withdrawal of heterochromatin from the nuclear periphery (Richter et al., 2007). We were also interested in setting up the cryo-FIB conditions for the milling of fibroblasts from patients barring various different laminopathic mutations in their lamin A genes as well as cell lines artificially expressing them (Camozzi et al., 2014).

U2Os cells were shocked for 20 and 40 minutes according to the published protocol (Richter et al., 2007). The cells were then fixed in 4% PFA for 10 minutes and examined under a confocal microscope. Staining was carried out with antibodies against lamins A/C and B1 (Sigma-Aldrich, Switzerland) according to standard immunofluorescence protocols (Sambrook et al.). Lamins A/C and B1 showed that they were fully retained at the nuclear envelope in the control and both of the sucrose-shock treatments. Additional Hoechst staining (Sigma-Aldrich, Switzerland) confirmed that the heterochromatin was uniformly spread out throughout the nucleoplasm and the nuclear periphery. Upon treating the cells with sucrose in the extracellular milieu, the heterochromatin showed signs of retractions from the nuclear periphery. There was no clearly observable difference between the 20 minutes and 40 minutes treatment. In both cases the heterochromatin had retracted, leaving the lamins more exposed, and the nucleoplasmic DNA started to look holey (***Figure 9***, panel a). The cells were processed for Tokuyasu cryo-sectioning as described in the materials and methods sections, cut into 300 nm cryo-sections, and examined with cryo-ET. Representative tomographic slices show the nucleo-cytoplasmic interface with clearly discernable cytoplasmic features, such as actin and ribosomes (***Figure 9***, panels b and c). Despite the confocal microscopy showing promising results for the unveiling of the nuclear lamina, the cryo-ET did not support such a finding. The expected position of the nuclear lamina at the envelope was uniformly covered by heterochromatin, precluding its direct observation (***Figure 9***, panels b and c, yellow arrowheads). This was most likely because the osmotic shock was transmitted to the cells via the feeding medium. This medium had to be aspirated and the cells washed quickly before they were switched into the fixation solution. In this small window of several minutes, the

osmotic shock could have been released long enough for the heterochromatin to assume its previous place at the nuclear periphery.

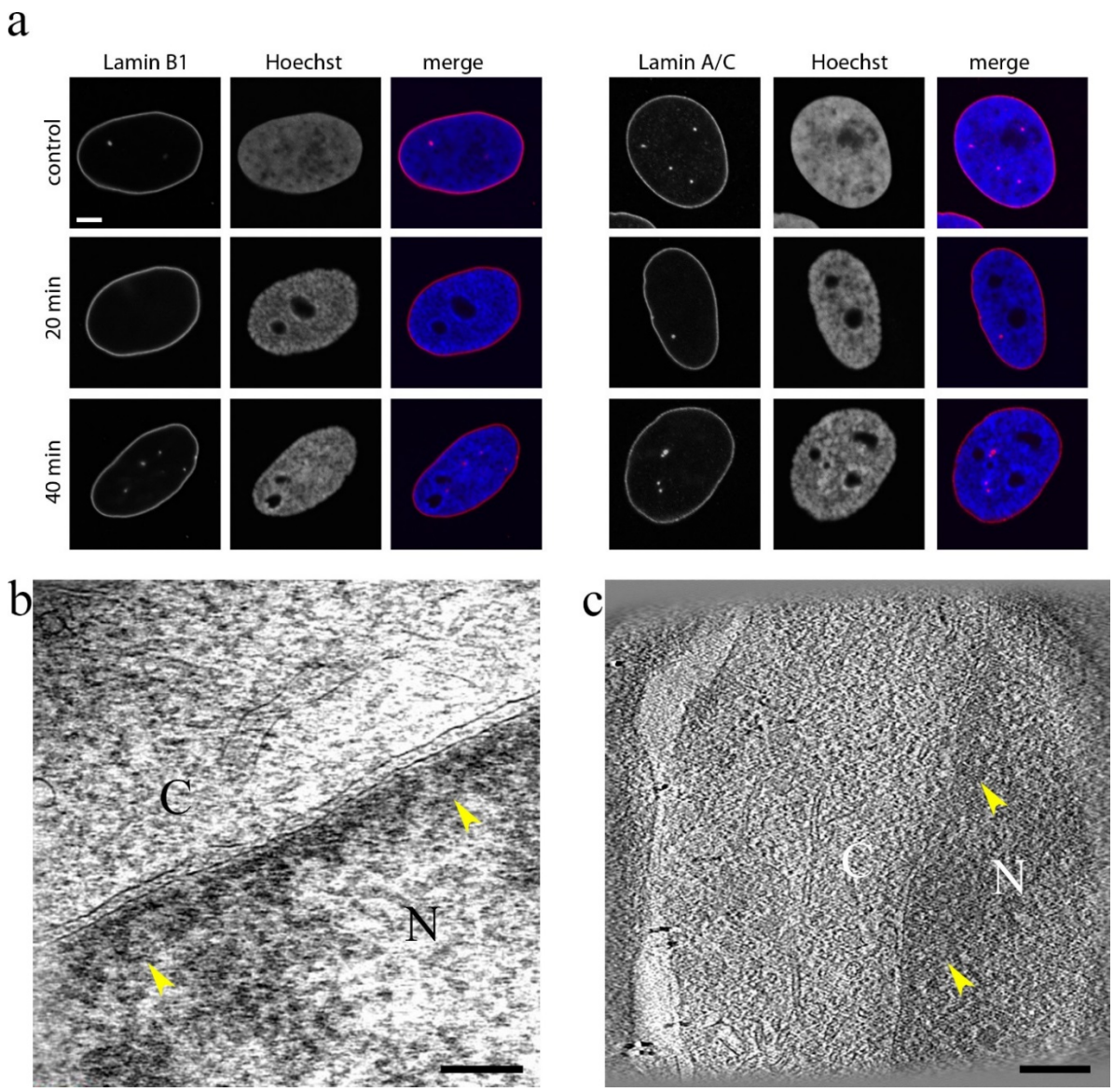

Figure 9. Cryo-sectioning of sucrose-shocked U2Os cells.

(a) Confocal microscopy of cells control, 20 min sucrose-shocked, and 40 min sucrose-shocked cells. Scale bar indicates 2 µm. (b,c) Tomographic slices showing the nucleoplasmic periphery of a sucrose-shocked cell. Scale bars indicate 200 nm.

Cryo-FIB-SEM and EM on U2Os cells

U2Os cells were grown in culture, trypsinized, and directly seeded onto glow-discharged carbon-coated EM grids. The grids were blotted for several seconds and vitrified by plunge freezing. The final concentration as well as distribution on the grids were estimated via SEM imaging and found to be optimal for further processing (**Figure 10**, panel a). They were milled from above and below using a parallelogram milling object and a 50 pA probe. The procedure

resulted in a 200 nm thick cryo-lamella (**Figure 10**, panel b) that was subsequently investigated by cryo-EM and cryo-ET (results for cryo-ET not shown here). EM images acquired on the lamella showed that the first attempt at creating a satisfactory milled surface was successful. The lamella appeared very flat, with minimal curtaining, and a clear difference could be observed between the milled and non-milled parts at the very edge (**Figure 10**, panel c, asterisk). The lamella showed the routinely observed black sports at the point where the FIB beam exited the sample, which are most likely due to Ga^+ ion implantation at the edges (**Figure 10**, panel d, black arrowheads). The most interesting observations came from a close-up view of the lamella interior. It showed a very material-dense intracellular environment with a nucleus filled with dense heterochromatin, baring a single NPC (white arrow), and a cytoplasm crowded with differently shaped vesicles, actin cables and ribosomes (**Figure 10**, panel e).

The goal of this approach was to establish cryo-FIB milling methods for mammalian cells in order to visualize the nuclear lamina in its native environment and as close-to-physiological conditions as possible. At this point, we did not yet develop the method for the post-milling application of fiducial markers on the cryo-lamella surface so the tomography data was reconstructed using feature tracking in order to align the projection images. This yielded a tomogram that was uninformative and not representable; therefore, the data is not included here.

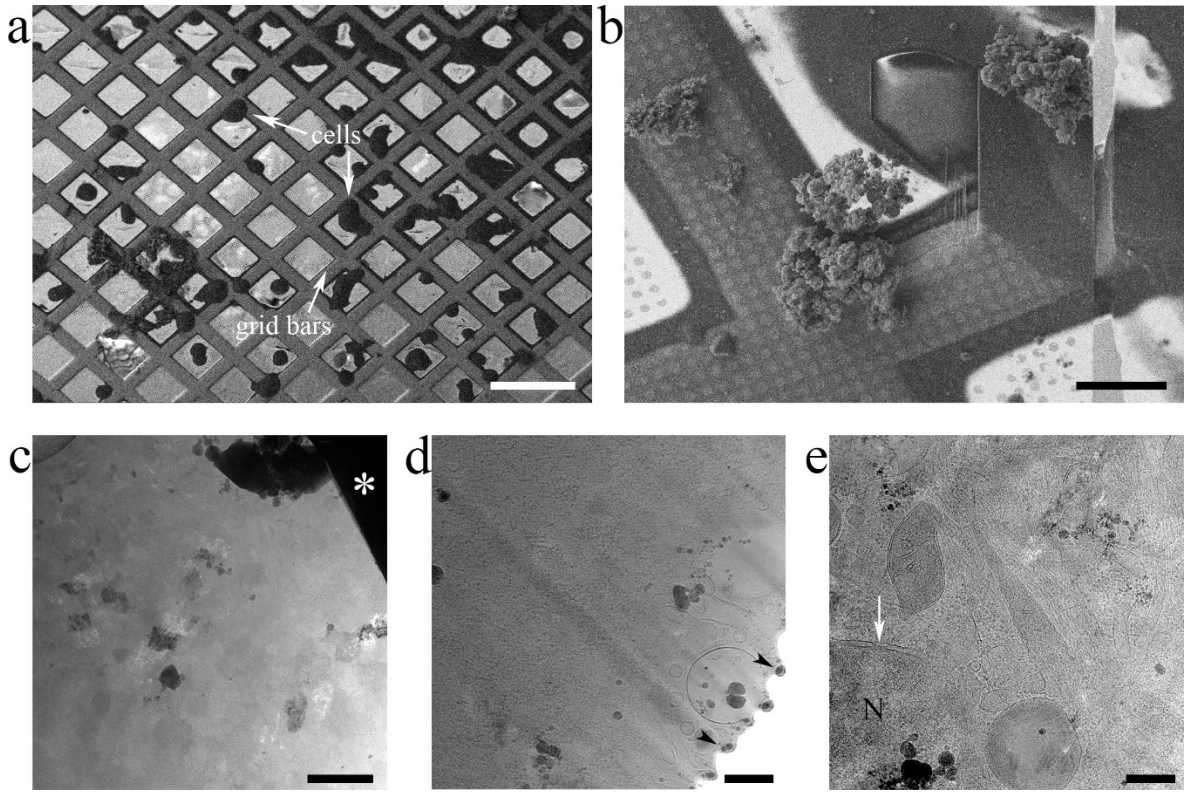

Figure 10. Cryo-FIB-SEM and EM on U2Os cells.

(a) SEM top-view of an EM with vitrified U2Os cells. (b) SEM top-view of the site of the future cryo-lamella. (c-e) Cryo-EM images taken on the cryo-lamella. White sterisk indicated non-milled sides, and black arrowheads indicate places of putative Ga ion implantation. Scale bars indicate 200 µm (a), 20 µm (b), 1 µm (c), and 200 nm (d and e).

B. Establishing the sample vitrification and cryo-FIB-SEM procedures for the milling of bulk multicellular specimen

Direct vitrification of *C. elegans* on EM grids

Adult worms need to be high-pressure-frozen in order to ensure a reliable and uniform vitrification throughout the entire body of the animal. Traditionally used cryoprotectants (e.g. dextrane, 1-hexadecene) (Dahl and Staehelin) often lead to the sample becoming indistinguishable from the surrounding freezing medium post-freezing (**Figure 11**, panel a). In order to resolve this issue, 2-methylpentane was used as a filler (i.e. cryoprotecting, freezing medium). 2-methylpentane is liquid in the range of -146°C to -160°C, which allows disassembly of the HPF aluminum carriers inside a cryo-ultramicrotome chamber without cracking the samples or dislodging them from EM grids. Moreover, it can be sublimed within this temperature range under high-vacuum conditions. This ensures that the sample is fully

exposed during milling as well as fully vitrified (**Figure 11**, panel b). Grids containing specimens were attached to the specially designed cryo-holder following HPF and transferred to a freeze-fracturing device. Within approximately 10 minutes at -150°C, 2-methylpentane was completely sublimed under high-vacuum conditions. This facilitated the subsequent cryo-FIB milling of the areas of interest.

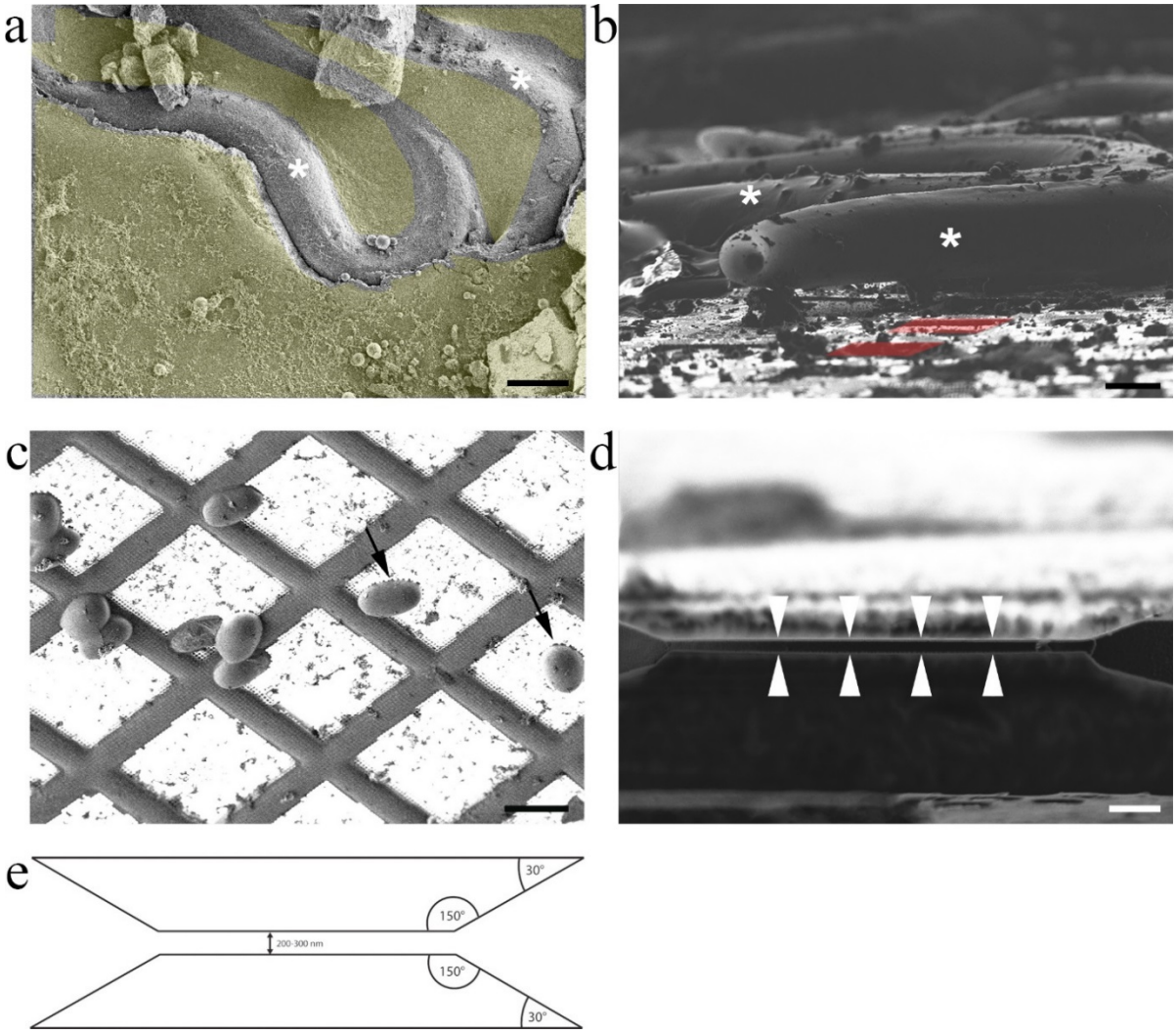

Figure 11. HPF of whole-body worms and cryo-FIB of *C. elegans*.

(a) HPF of adult *C. elegans* worms using 1-hexadecene as freezing medium. Layer of solidified medium (yellow) surrounding the worms (asterisk). (b) HPF using 2-methylpentane as freezing medium. Visible grid squares (red) and fully exposed worms (asterisk). (c) Plunge-frozen embryos of *C. elegans* (black arrows) fully exposed on the EM grid. (d) Exemplary cryo-lamella (area in-between white arrows) after cryo-FIB milling. (e) Parallelogram shape used for creating the thin cryo-lamella. Scale bars: 40 µm (a-c), 2 µm (d).

Cryo-FIB milling of intact worms and embryos

The shape of the milling object used for thinning high-pressure frozen *C. elegans* worms (**Figure 12**, panel a, white arrows) and plunge-frozen embryos, was a parallelogram (**Figure 11**, panel e), which left a 150° internal angle between the lamella and the non-milled material in the immediate surroundings (**Figure 12**, panel c, area marked by black arrows). For a large specimen such as a worm we chose a milling site and started removing material with a 4 nA probe until the sample was thinned to an ~5 µm thick lamella. The advantage of starting out with rough and fast milling is that it reduced the overall milling time; however, significant amounts of heat are transferred to the sample during this process. The quality of vitrification can also be assessed at this point by checking for the presence of cracks in the sample after the first round of milling. In order to avoid tissue damage arising from heat transfer, samples were further semi-fine-milled with a weaker current. The amount of heat transferred by the 240 pA aperture was found to be tolerated by the sample, since no evident morphological distortions of the lamella could be visibly detected (**Figure 12**, panel b, arrowheads, and panel c, area marked by white arrows). The quality of the milling procedure can be evaluated by observing the shape of the cryo-lamella that can change from a flat to bent appearance due to excessive heat transfer. The semi-fine milling step left a ~1 µm thick lamella that was further fine-milled using a 50 pA probe. This resulted in ~660 nm thick, fully vitrified cryo-lamellae, which had a relatively smooth surface and were stable for the subsequent CET analysis (**Figure 12**, panels b and c).

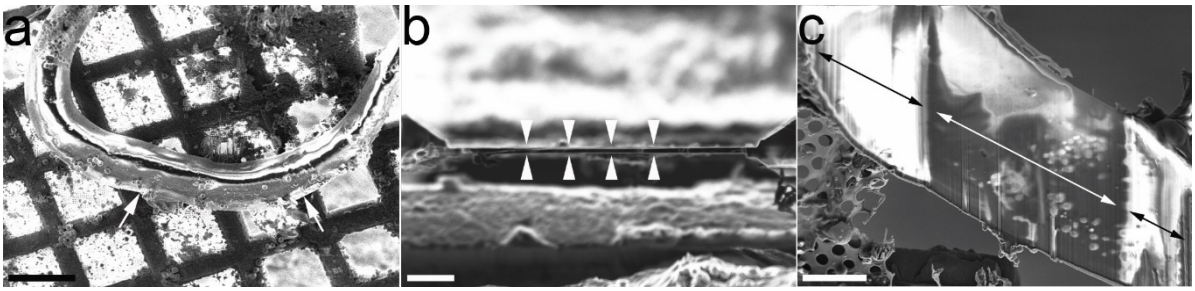

Figure 12. Cryo-FIB-SEM on adult whole-body *C. elegans*.

(a) SEM top-view of an adult worm (white arrows) vitrified on an EM grid. (b) FIB side-view of the cryo-lamella (area in-between arrowheads). (c) SEM top-view of the cryo-lamella. Scale bars indicate 100 µm (a), 5 µm (b), and 10 µm (c).

Areas of interest in embryos of *C. elegans* were milled to an average thickness of ~330 nm. The smaller overall size of the embryos gave rise to shorter milling time compared to that of whole worms (it takes about 4 hours to complete one embryo). Before starting the milling procedure embryos were visually assessed for structural integrity, meaning that no cracks were present on the surface or the interior (**Figure 13**, panel b, white arrowheads). Semi-fine milling was applied from above and below the region of interest with a 240 pA probe, followed by a fine-milling step using a 50 pA probe (**Figure 13**, panel a). As mentioned above, the shape of the lamellae was designed to minimize potential down-stream difficulties during tilt-series acquisition. Under these conditions, the lamellae are on average very flat, and stable for imaging in the TEM (**Figure 13**, panel c).

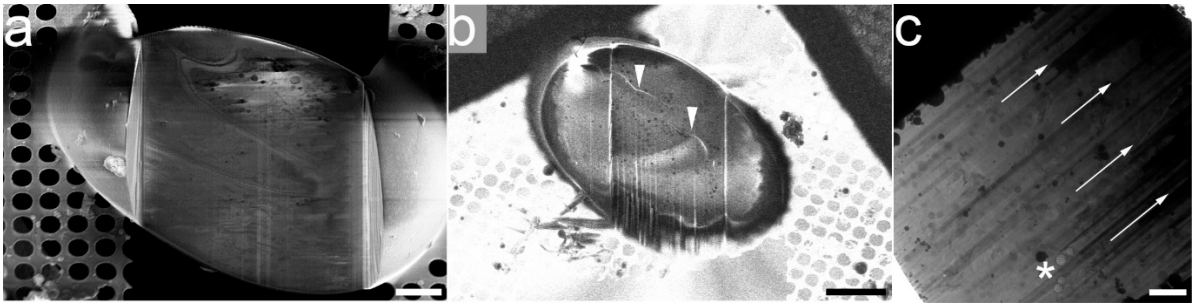

Figure 13. Cryo-FIB-SEM milling of *C. elegans* embryos.

(a) SEM top-view of a suitable cryo-lamella. (b) SEM top-view of an unsuitable cryo-lamella. (c) TEM micrograph of the cryo-lamella with the direction of the FIB beam (white arrows), and the sites damaged through the use for focusing and tracking (asterisk) indicated. Scale bars indicate 5 µm (a), 10 µm (b), and 2 µm (c).

We routinely milled embryos down to a 20x40 µm lamella and the worms to a 30x60 µm lamella at a desired site due to time constraints (it takes up to three full working days to complete such a procedure). Several such thinned regions could potentially be introduced into the worms at different sites but this would prolong the total procedure significantly. It is crucial to keep in mind that the width of the lamellae should be kept at a minimum in order to avoid mechanical breaks during the various transfer steps (in our experience regions of up to 30 µm in width were found to be optimally stable for further handling and processing).

Deposition of fiducial gold markers onto the lamellae under cryogenic conditions

Fiducial gold markers are routinely used in CET for the initial alignment of the tilt-series projections to a common plane. 7-15nm gold nanoparticles are commonly added to samples

prior to vitrification. However, when using cryo-FIB they should be added after the lamella is formed to ensure a spatial proximity between the sample and markers. Gold nanocrystals measuring on average 10 nm in diameter were synthesized in an organic solvent, as described by Hiramatsu and Osterloh in 2004 and deposited onto the lamellae as described in Gruska and coworkers in 2008 (Gruska et al., 2008; Hiramatsu and Osterloh, 2004) (**Figure 14**, panel a,b). We resuspended the gold nanoparticles in 2-methylpentane (**Figure 14**, panel c)and cooled them inside a cryo-ultramicrotome chamber (**Figure 14**, panel d), where grids containing thinned samples were immersed into the gold nanoparticles suspension (Materials and Methods section). Our setup inside the cryo-ultramicrotome chamber included an aluminum block with several 500 µL wells. One was filled with the gold suspension and two were filled with liquid ethane. Cryo-EM imaging was initially carried out to establish the blotting times necessary to get grids devoid of surface contamination as well as to test the effect of using toluene and 2-MP as solvents. The fiducial markers dissolved in 2-MP exhibited an even distribution along the surface of empty test grids (**Figure 14**, panel e) and the lamellae (***Figure 15***, panel a), allowing unhindered reconstructions of cellular interiors. Furthermore, grids prepared using this approach were free of toluene and other ice-related surface contamination whereas others were completely covered in thick ice clusters and the gold was clumped (**Figure 14**, panel f)

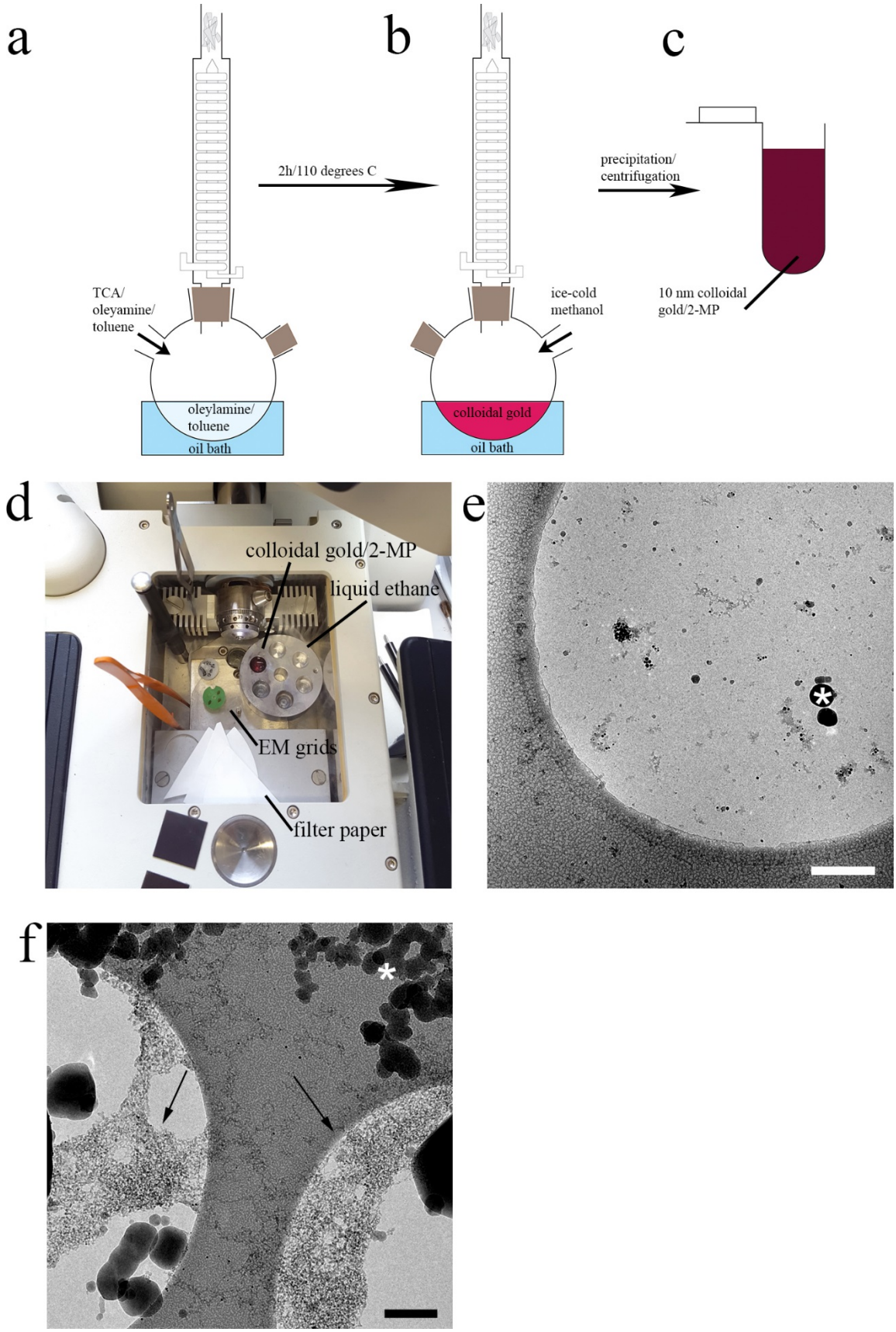

Figure 14. Synthesis and quality control of fiducial gold markers for cryo application.

(a-c) Schematic overview of the synthesis steps. (d) Setup and application of the fiducial markers inside the cryo-ultramicrotome chamber. (e,f) Cryo-EM images of the gold markers with 2-methylpentan and toluene as solvents, respectively. Scale bars indicate 250 nm.

CET of C. elegans embryos and adult worms

We acquired tomograms at different focus values on cryo-lamellae in which we could detect the various macromolecular complex typically found in the cellular interior of both embryos and worms. The images shown in ***Figure 15***, represent a typical nucleo-cytoplasmic border of interphase cells. The cytoplasms are rich in free and membrane-bound ribosome assemblies, which are clearly detectable. These reconstructions reveal typical intracellular components such as mitochondria and a plethora of vesicles, which are clearly discernable. In particular, we were interested in visualizing the nuclear lamina, a filamentous protein layer underlying the nuclear envelope (Burke and Stewart, 2013b; Ho and Lammerding, 2012). Ce-lamin was previously analyzed both in vitro and by ectopical expression in *Xenopus laevis* oocytes (Ben-Harush et al., 2009; Grossman et al., 2012a). However, due to technical limitations, nuclei from *C. elegans* could not be investigated in a sufficiently high resolution. Therefore, we applied the cryo-FIB-SEM technique to embryos and worms, either wild type or overexpressing the ce-lamin labelled with GFP (**Figure 16**, panels b and d), and, as expected, ~6-8 nm thick filamentous structures were detected at the nuclear periphery indicated by green arrow heads. However, a specific labeling approach would be required to verify unambiguously the identity of these structures within a crowded environment such as the nucleus.

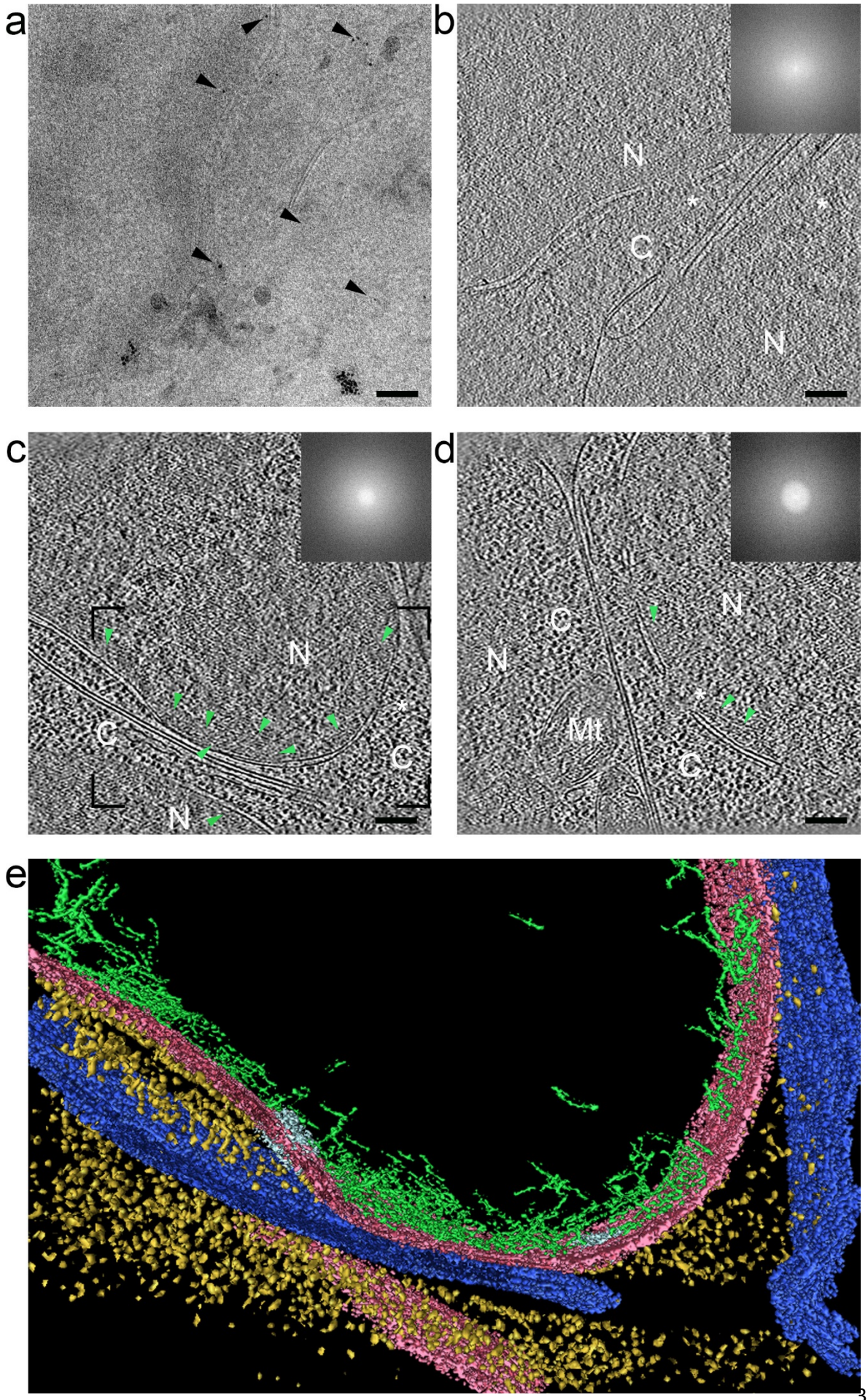
a
b
N
C
N
c
N
C
C
N
d
C
N
N
Mt
C
e

Figure 15. CET of *C. elegans* embryos.

(a) Cryo-TEM image of a 0°-tilt projection showing individual fiducial gold markers (arrowheads) on the lamellar surface. (b) 4-nm tomographic slice recorded on an embryo overexpressing the native ce-lamin, at a defocus value of −6 µm. The final resolution was determined from the first zero of the contrast transfer function (CTF) and calculated to be 3.4 nm. (c,d) Tomographic slices (4 nm and 3.4 nm, respectively) acquired on embryos overexpressing the native ce-lamin (green arrowheads), with a defocus value of −16 µm. The final resolution was determined from the first zero of the CTF and calculated to be 5.6 nm for both tomograms. The power spectra for tomograms b–d were generated using the 0°-tilt projection images and are shown as insets. N, nucleus; C, cytoplasm; Mt, mitochondrion; asterisks indicate nuclear pore complexes. (e) Surface rendered view, generated using Amira 5.4.2, corresponding to the black-framed area in c. Dark blue, plasma membrane; pink, nuclear membrane; gold, ribosomes; light blue, nuclear pore complexes; green, filamentous structures adjacent to the inner nuclear membrane. Scale bars, 200 nm.

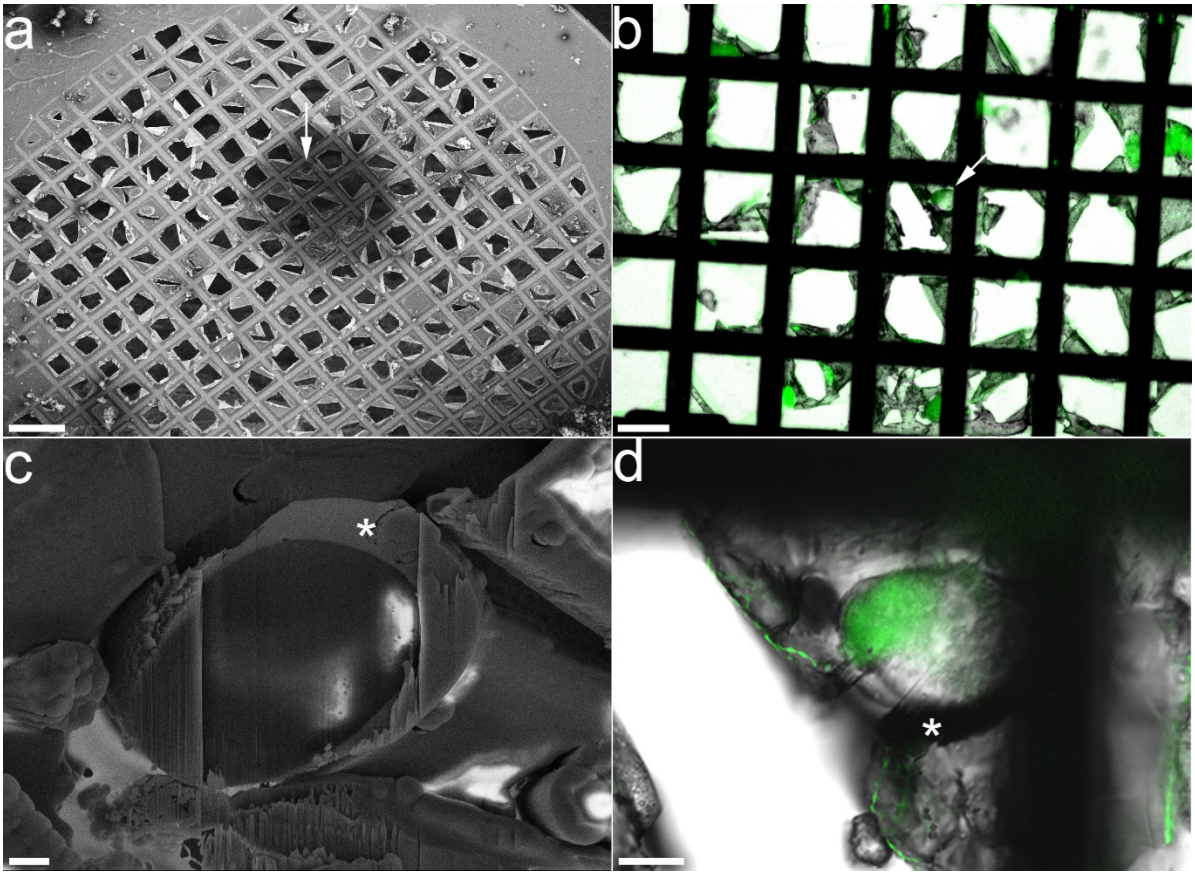

Figure 16. CLEM on *C. elegans* embryos.

(a) SEM top-view of the EM grid indicating the site of the milled embryo (white arrow). (b) BF fluorescence image of the milled embryo from panel a (white arrow). (c) SEM top-view of the cryo-lamella with the surrounding platinum coating (asterisk). (d) BF fluorescence image of the same cryo-lamella from panel c, rotated by 180°.

Tissue interiors of vitrified, milled, adult worms were imaged with -16 µm of defocus on ~660 nm thick lamellae. These cellular volumes, considered thick by CET standards, could easily be aligned using fiducial markers. Figure 17b shows a cytoplasmic interface of three cells (**Figure 17**, panel b) as well as the nucleus of a single cell within the adult worm (**Figure 17**, panel a). Despite the slightly lower signal-to-noise ratio in comparison with the tomograms acquired on thinner lamellae, this data shows a high level of structural detail in terms of both intra- and intercellular processes. One example is the plasma membrane budding event between two adjacent cells (**Figure 17**, panel a, white arrow). Intracellular structures were accessible for CET analysis, revealing features such as NPCs (**Figure 17**, panel a, white asterisks) and filamentous structures adjacent to the inner nuclear membrane (**Figure 17**, panel a, green arrowheads) as well as a ribosome-rich cytoplasmic environment.

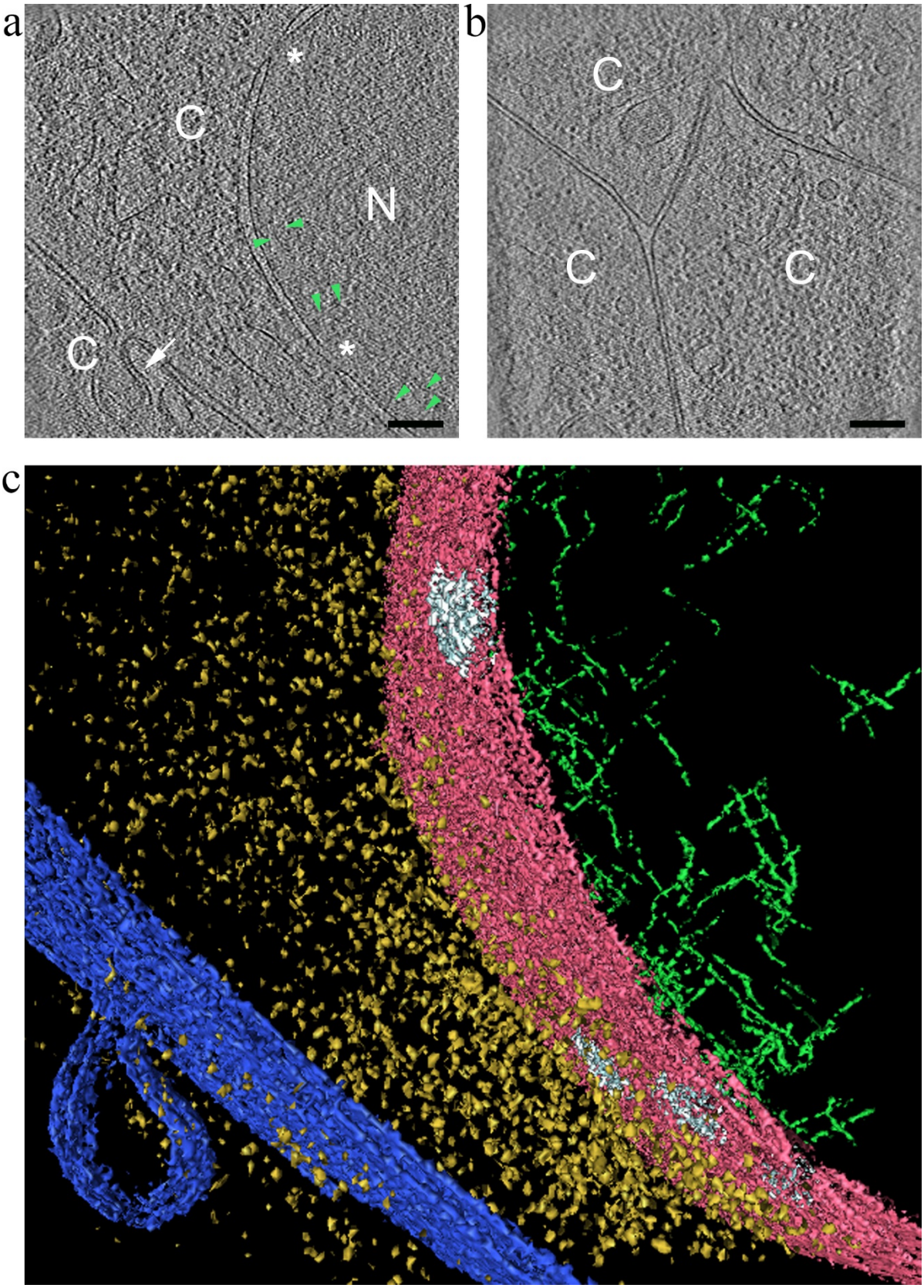

Figure 17. CET of whole-body worms.

(a,b) 3.4 nm thick tomographic slices acquired with a –16 µm defocus on a worm cryo-lamella. Green arrowheads point towards filamentous structures adjacent to the INM, the black arrow points to a plasma membrane protrusion and the white asterisks indicate the position of NPCs. (N – nucleus, C – Cytoplasm). (c) A surface rendered view corresponding

to the black-framed area in panel a. Plasma membrane – dark blue, nuclear membrane – pink, ribosomes – gold, NPCs – light blue, and filamentous structures adjacent to the INM – green. Final resolution of both tomograms was estimated from the first zero of the CTF and calculated to be 5.4 nm. Scale bars represent 200 nm (a,b).

Cryo-FIB-SEM of *Drosophila melanogaster* embryos

D. melanogaster embryos were attached to the EM grids using poly-L-lysine. This provided a permanent attachment of the embryos, resisting the disassembly of the aluminum carrier sandwich after high-pressure freezing and transfer to the cryo-electron microscope. The embryos were not obscured by the poly-L-lysine after sublimation of 2-methylpentane (**Figure 18**, panel a). Several lamellae were produced via cryo-FIB milling and within successive rounds of milling material was removed from below and above the region of interest. A high milling current of 16 nA was applied, followed by coarse milling down to a < 10 µm thick lamella (**Figure 18**, panel b). Several rounds of coarse milling removed material adjacent to the lamella (figure 18, panel c). Since rough milling introduced a substantial amount of heat to the sample, the lamella was further thinned with a 240 pA probe yielding a 3 µm lamella (**Figure 18**, panel d). Finally, fine milling with a 50 pA probe reduced the lamella thickness to approximately 200-300 nm. Reducing the sample thickness to a few hundreds of nanometers took approximately 3-4 days, with ablation time windows of 0.5-3 hours, producing a lamella of 300 nm x 20 µm x 80 µm. Running the cryo-FIB for this long was accomplished by using a self-refillable liquid nitrogen dewar.

Several attempts of creating a thin lamella via FIB-ablation and subsequent cryo-ET were undertaken. The created lamellae appeared thin enough in SEM after milling (not shown here). The embryo and the generated lamella were successfully transferred into the cryo-electron microscope, as both were still recognizable (data not shown). Nevertheless, it was not possible to record tomograms or 2D electron micrographs of the lamella. One possible explanation was the presence of a grid bar right underneath the lamella, blocking the electron beam. Therefore, the grid bar underneath one generated lamella was removed in successive rounds of coarse milling within 6 hours (**Figure 18**, d). Although the lamella appeared thin enough for electron tomography and although the electron beam should not have been obscured, a tomogram of the lamella could not be recorded (**Figure 18**, panel d, area indicated by white double arrow). Most likely, the very long milling procedures over several days, and /

or the transfer of the grid caused severe ice contamination and stability problems. Twelve lamellae within 12 independent samples were generated in total. Unfortunately, none gave any structural insight.

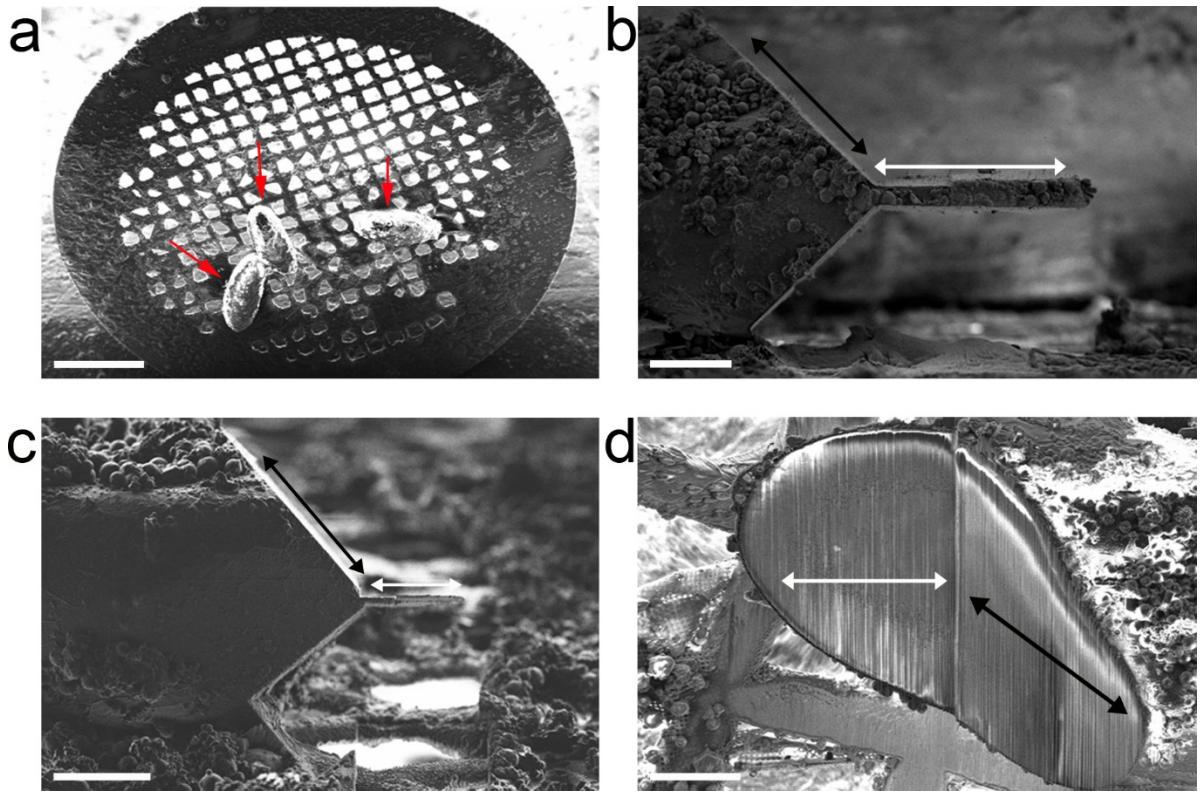

Figure 18. Cryo-FIB-SEM of *D. melanogaster* embryos.

(a) SEM overview image of the EM grid bearing 3 embryos (red arrows). (b) FIB side view of the edge of the embryo after several rounds of milling with high currents. (c) FIB side view of the thin lamella after successive rounds of course and fine milling. The area underneath the lamella is also cleared in order to facilitate tomographic imaging. (d) SEM top view of the lamella after milling. Black double arrows indicate the non-milled slopes surrounding the lamella and the white double arrows indicate the lamella itself. Scale bars indicate 500 µm (a) and 50 µm (b–d).

Discussion

The ability to vitrify multicellular samples using HPF directly on EM grids, without frozen material surrounding the specimen, is a substantial improvement. It increases the accessibility of the object under scrutiny to the cryo-FIB-SEM and enables the targeting of specific areas of interest. The absence of fiducial markers on top of the cryo-FIB-milled lamellae has been a limiting factor to the application of CET and most of the studied samples had to be relatively

thin, i.e. <200 nm, as well as acquired at relatively high defocus values in order to increase contrast for feature tracking alignment procedures (Villa et al., 2014). Our protocol for the introduction of surface fiducial markers under cryogenic conditions is simple, non-detrimental, and enables the successful alignment and reconstruction of tomograms acquired on "thick" regions (250-350 nm) within biological specimens. Moreover, we were able to demonstrate the successful alignment and reconstruction of 3D volumes acquired on ~660 nm thick lamellae. This would have been impossible without the use of high-contrasting fiducial markers. The cryo-FIB-SEM approach has already successfully been employed to describe the organization of protein networks and macromolecular complexes contained within cells (Engel et al., 2015; Hsieh et al., 2014; Mahamid et al., 2016; Rigort et al., 2012a). Together with the improvements described here, it opens-up different venues for extracting high-resolution information from cellular interiors and, for example, from otherwise intact tissues.

Despite being a well-established and much-used model organism (Kipreos, 2005; Koreth and van den Heuvel, 2005), the entire *C. elegans* worm and its embryos have so far not been studied in a vitreous (i.e. close to physiological) state with three-dimensional structural approaches. In addition to showing the applicability of the cryo-FIB-SEM to worms, we were also able to show that it can be used to generate cryo-lamella within embryos of *D. melanogaster*, another well-studied model organism (Roberts, 2006). These embryos, measuring 200x500 µm, proved challenging to mill due to their shear huge size. Many technical limitations stood in the way of obtaining good cryo-ET data from them, such as the use of glues to fix the embryos on the surface of the EM grid, the necessity to mill away grid bars that were often encountered underneath the potentially interesting milling sites, to name a few. However, if technical limitations (e.g. keeping samples at cryogenic temperatures over longer periods and using pre-thinning techniques for bulk specimens before milling) could be overcome, this would open up exciting new possibilities for the structural investigation of this organism at discrete moments in its life cycle. Together these results reveal the great potential of using the cryo-FIB technique for studying tissue morphology and physiology at particular developmental stages and across model organisms.

This work targeted both the adult worms and embryos, and allowed us to look into the intracellular organization and nuclear architecture of this organism. Furthermore, we have

indicated the presence of filament-like structures at the nuclear periphery in the immediate vicinity of the inner nuclear membrane. These most likely represent the *C. elegans* nuclear lamina, which is composed of a single ce-lamin protein. We have also shown, in the form of a simple correlation with light microscopy, the retention of the fluorescence signal post cry-FIB-SEM milling (Figure 16). The overall morphology and organization of these elements, as well as their prevalence in the wt vs. the GFP-fused overexpression state, were found to be consistent with previously published data (Ben-Harush et al., 2009; Mattout et al., 2011). Further analyses are needed in order to thoroughly and unambiguously characterize the organization of these structures in 3D. However, the data at present suggests that they may form non-conventional IF-like filaments (Grossman et al., 2012a).

CET can be used together with three-dimensional averaging procedures in order to describe the structural make-up of macromolecular complexes in situ. Thinning of samples with non-detrimental procedures such as the cryo-FIB allows one to extend the application of CET to studying intrinsic aspects of cellular physiology and developmental processes from a structural perspective. Big macromolecular assemblies, cellular machineries, and physiological processes can now be reconstructed at specific stages of development. This will give exciting and new insights about the macromolecular remodeling taking place within complex organisms on the cellular and systemic levels.

Chapter 3

Structural investigation of FG-repeat hydrogels and particles as *in vitro* models for the central channel of the NPC

Introduction

NPCs are composed of approximately 30 different proteins collectively called nucleoporins (Nups). Each one is present in multiple copies throughout the macromolecular complex (Alber et al.; Cronshaw et al.; Ori et al.; Terry and Wente). The overall architecture of the NPC is mostly conserved between lower and higher eukaryotes. It generally possesses a pseudo-eightfold symmetrical central framework termed the spoke complex, a central pore, and filamentous structures on the cytoplasmic and nuclear sides of the complex (Elad et al.). On the nucleoplasmic face, the NPC is in close interaction with the nuclear lamina, a meshwork of filamentous protein structures, and other associated proteins (Burke and Stewart). This gigantic macromolecular complex is over 120 MDa in molecular weight and brings together the outer and the inner nuclear membranes to form aqueous translocation channels. The permeability barrier of the NPC allows passive diffusion of small molecules as well as receptor-dependent translocation of large proteins and ribo-nucleoproteins (Adams and Wente; Grossman et al.). The limit is a molecular weight of about 30 KDa or a diameter of approximately 5 nm (Mohr et al.). Macromolecular cargo usually harbors a specific nuclear localization signal (NLS) or nuclear export signal (NES) that are recognized by transport receptors that mediate cargo passage through the NPC. Nuclear transport receptors (NTRs), referred to as karyopherins, accompany cargo during transport processes across the NPC by means of hydrophobic interactions with phenylalanine-glycine-rich nucleoporin repeat domains (FG-repeats) (Stewart; Suntharalingam and Wente). There are several categories of NTRs and these include most notably importins (importin-α and importin-β), exportins, NTF2, and Hikeshi. The first three are driven by the RanGTP/GDP system while the Hikeshi is powered by the Hsp70 ATPase (Kose et al.; Ribbeck et al.).

The overall architecture of the *X. laevis* NPC was recently resolved to a final resolution of approximately 20 Å by Eibauer and colleagues (**Figure 19**). This was achieved by combining clever sample preparation, cryo-ET, direct electron detectors, and subtomogram averaging without the use of chemical fixatives (Eibauer et al.). It showed a complex that is 71 nm high with an outer diameter of 126 nm and an inner diameter of 90 nm with well-preserved structural motifs – the cytoplasmic ring (CPR), the spoke ring (SR), and the nucleoplasmic ring (NPR) (Frenkiel-Krispin et al.). One of the most interesting results that came out of this work was an ordered structure occupying the central channel of the NPC, forming a ring-like assembly attached to the SR by a porous interface, and located at a distance of 23 nm from the channel center. It is now clear that these densities belong most likely to cargo being transported through the pore channel as well as to the different Nups occupying these regions at the time of transport as described before (Beck et al.; Beck et al.). The major structural differences were found, with respect to the human NPC, in the NPR and the central channel. The authors went further on to compare two biochemically distinct states of the frog NPC, a native or non-treated one, and one treated with the transcription blocker actynomycin D (ActD). The native NPC showed the highest amount of structural variability at the nucleoplasmic entrance to the CCR, which was coupled to an increase in filamentous entities in the ActD-treated NPC. Furthermore, when viewed as a central x-y section, the two states of the NPC start to exhibit a different amount of equally spaced 2-6 nm channels, which implies that the inner pore ring indeed contributes to the formation of a structural barrier that opens or closes this gateway (Eibauer et al.).

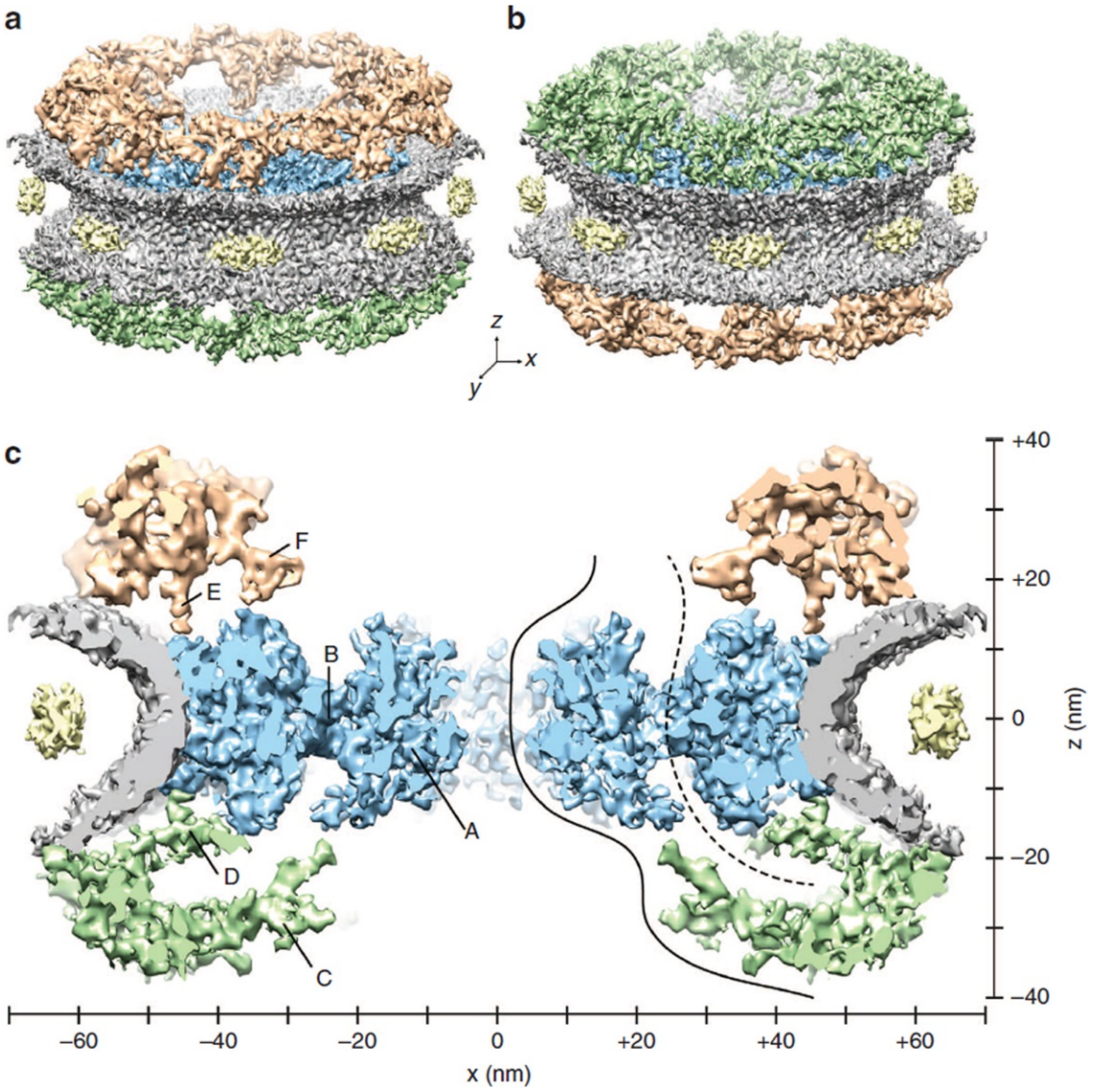

Figure 19. The structure of the native *X. laevis* NPC.

(a,b) Surface-rendered grazing views of the NPC. The NE is depicted in grey, the luminal densities in yellow, and the SR in blue. (a) Upper side of the CPR is shown in golden color. (b) Top of the NPR is shown in green color. (c) View of the central nucleocytoplasmic section (25-nm thick) through the NPC structure; CCR (A) and SR-CCR interface (B). The axes show the dimensions of the NPC in the x- and y-direction. Reproduced with permission (Eibauer et al., 2015).

FG Nups are critical for the function of the NPC and have up to 50 FG dipeptide motifs in their FG domains (Strawn et al.). The mammalian Nup98 possesses about 500 residues in its FG domain and has been estimated to occur in approximately 48 per NPC (Ori et al.). FG motifs are critical for the protein interactions in the central channel of the NPC. They provide binding sites for the NTRs (Iovine et al.), they bind parts of the NPC scaffold (Patel et al.; Schrader et al.), and they engage in cohesive interactions driven primarily by their hydrophobicity (Frey et

al.; Ribbeck and Gorlich). FG-repeat-rich Nups are assumed to fill the space of the central channel of the NPC (Brohawn and Schwartz; Hoelz et al.; Rout et al.) and are considered to be intrinsically disordered, i.e. having no higher order structural organization. If this would be the case, they would not appear in the final averaged map due to being averaged out during the averaging procedure.

Of the many different Nups, Nup98 is of importance to this structural study. It is not only directly involved in transporting proteins and mRNAs (Blevins et al.), but also predominantly asymmetrically localized to the nuclear face of the NPC (Frosst et al.; Radu et al.), while a fraction of it is found on the cytoplasmic side of NPC (Griffis et al.). The MacNup98A is nucleoporin found in the macronucleus of the single cell eukaryote *Tetrahymena thermophila* that possesses GLFG repeats in its N-terminus (Iwamoto et al.). The importin-β (45-462) mutant used in this study can actively bind FxFG repeat Nups (such as Nup98) but cannot release them upon binding, thus accumulating at the nuclear rim (Kutay et al.; Schmidt and Gorlich, 2015). It has also been found to phase separate and stable near-spherical FG particles (Schmidt and Gorlich, 2015). This observation is further supported by unpublished results from our lab showing a significant increase in electron densities in and around the central channel of the *X. laevis* NPC, predominantly at the sites of FG-repeat domains of FG-repeat-containing Nups (**Figure 20**, panel b).

The recognition of the CCR by Eibauer and colleagues in their averaged final maps of the NPC goes one-step further in showing that these proteins do exhibit some degree of structural order. This can be further explained by the fact that Nups are able to interact with each other in a crowded environment such as the one present in the center of the central channel of the NPC. Here, they could even be envisioned to form assemblies such as hydrogels when present in a high enough local concertation (Frey and Gorlich), and these structures can be imaged by electron microscopy (Estroff et al.; Milles and Lemke).

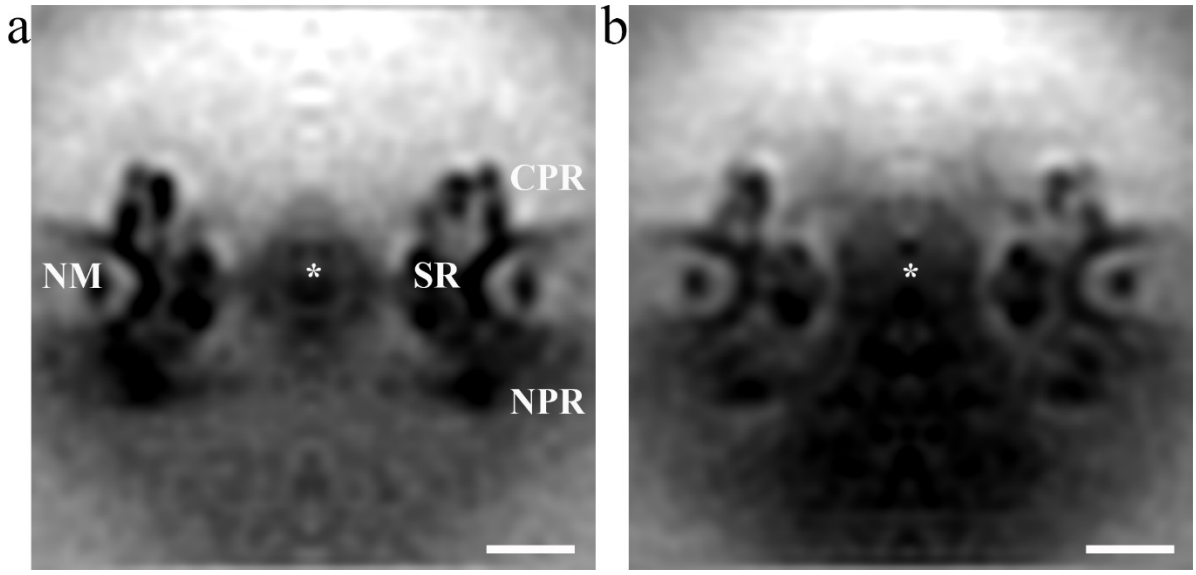

Figure 20. Comparison of the final averaged structures of *X. laevis* NPC.

(a) Central slice through the a full wt *X. laevis* NPC at low resolution (~6nm) with key organizational motifs indicated. (b) Central slice through the full *X. laevis* NPC treated with Importin-β fragment (45-462). Asterisks indicate the putative center of the central channel in both structures. NM – nuclear membrane, SR – spoke ring, CPR – cytoplasmic ring, NPR – nucleoplasmic ring. Scale bars indicate 50 nm. (These unpublished results were kindly provided by Dr. Matthias Eibauer.)

Project aim

In this work we aimed to (i) investigate whether the FG-particles formed by the *Tetrahymena thermophila* Nup98 FG-repeat domains possess any higher order internal structural organizational elements. (ii) In a second step, we aimed to elucidate how the internal structural organization could be affected by diffusing nuclear transport receptors and cargo through them.

Materials and methods

Preparation of yNup100 protein hydrogels

Carbon-coated copper R2/1 200 mesh EM grids (Quantifoil GmBH, Germany) were coated with an additional layer of 10 nm carbon, glow discharged for 30 s, and placed into a humidity chamber while suspended in air with tweezers. Yeast Nup100 was provided to us as a lyophylisate by the lab of Prof. Dirk Goerlich. A small amount of protein was weighed and transferred from the -20°C storage tube into a fresh tube and 0.2% TFA (trifluoroacetic acid) prepared in H2O was added to achieve a final protein concentration of 200 mg/mL (e.g. 3 mg of protein powder covered with 15 µL of 0.2% TFA). The mixture was spun in a tabletop

centrifuge for approximately 1 minute. At this point, the sample started jellifying so it was resuspended a few times and, subsequently, handled with haste. A small amount of protein was applied to the grid surface with a fine pipette tip and left to solidify overnight, approximately 12-16h. Grids were subsequently plunge-frozen into liquid ethane. For this purpose, the EM grids were coated with an additional layer of 10 nm carbon coat in a sputter coater (manufacturer, model).

Isolation and purification of MacNup98

FG domains were purified using Ni(II) chelate chromatography under denaturing conditions (100 mM Tris pH 8, 8 M GuHCl, 10 mM DTT). Elution was with imidazole in 100 mM Tris pH 8, 20% formamide. If necessary, they were further purified by covalent chromatography, whereby an engineered C-terminal cysteine was allowed to form a disulfide bond with a 2-thiopyridine-activated SH-silica matrix (described below) and elution was achieved by reducing the disulfides with DTT. FG domains were finally re-buffered to 20% acetonitrile, 0.08% TFA and lyophilised. O-GlcNAc modification of FG domains was performed as previously described (Labokha, 2013).

Expression, purification and validation of Imp-β fragment (45-462)

Imp-β fragment (45-462) was provided to us on a pSF-type plasmid by the laboratory of Prof. Dirk Goerlich. The plasmid was amplified in a BL-21 strain through the standard heat-shock transformation protocol (Sambrook et al., 2006). Colonies containing the plasmid were picked the following day, plasmid DNA isolated with a miniprep kit (Quiagen, Germany), and the 2 best preps confirmed by sequencing (Microsynth, Switzerland). A small scale expression test was conducted in LOBSTR (*E. coli* B F- ompT hsdS (rB-mB-) dcm+ Tetr E. coli gal λ (DE3) endA Hte [argU ileY leuW Camr]) and Rosetta (F- ompT hsdSB (rB- mB-) gal dcm (DE3) pRARE2 (CamR)) strains of *E. coli* that were grown overnight in TB medium supplemented with 2% glucose and Kan/Cam. Overnight cultures were diluted 1:1 with the same medium indicated above and split between 2 tubes each totaling 2mL. For each strain, one set of six was left growing non-induced, and subsequently used to make glycerol stocks, while the other set was induced with 0.5 mM IPTG. Both sets were left growing for approximately 5h at 37°C with 170 rpm shaking. Glycerol stocks were made from the non-induced samples by mixing 0.5 mL of sample with 0.5 mL of sterile 87% glycerol, vortexed before flash freezing in liquid nitrogen, and stored at -80°C.

Two best clones were chosen for proper protein expression that induced at OD600=0.8 with 0.5 M freshly prepared IPTG (1 mM stock) and the cultures switched to an 18°C incubator with 110 rpm rotation for overnight induction. In the morning, freshly prepared PMSF was added to the cultures to a final concentration of 2 mM (added up to 5 mL of 200 mM stock in pure ethanol). 500 mL of both clones was distributed between two centrifugation bottles (2x250 mL) and spun down in the Sorvall centrifuge for an hour at 8000 rpm and 4°C. The procedure was repeated for the other 500 mL and the bacteria were pelleted for 20 min on top of the existing pellet. The supernatant was discarded in a beaker and kept for resuspending the pellet. The pellets were collected off the bottom with a spatula and the remaining material was dissolved in supernatant with a pipette and transferred into a 50 mL falcon tube. Altogether 4 falcon tubes, corresponding to each of the 4 expression flasks, were put into the table top centrifuge and spun down for 15 min at 4000 g at 4°C. The supernatant was discarded and the pellets were stored in the -80°C fridge. Cell pellets of clone R1 were opened with sonication and run over a benchtop Ni-NTA purification scheme. Three elution gractions were collected with three different concentrations on imidazole (150 mM, 250 mM, and 350 mM, respectively). Fractions E2 and E3 were concentrated separately using Amicon Ultra 4 concentrators with a 30 KDa cut-off, and run separately on the SEC. Fractions D12-E12 from elution 2 were pooled together and concentrated on an Amicon ultra 4, 30 kDa cut-off concentrator. Fractions D13-E12 were pooled together and concentrated on an Amicon ultra 4, 30 kDa cut-off concentrator. Final concentration of the protein was measured on the nanodrop and determined to be 1.2 mg/mL, and the presence of the His tag was checked by western blotting with an anti-His antibody.

Preparation of near-spherical-like MacNup98A particles

Scheme 1: 12 mg of lyophilised Mac98A was dissolved in 180 µL of 4M GdmHCl to a final concentration of 1mM. A 280 mM stock solution of MacNup98A:Alexa647 was diluted to a final concentration of 10 µM. 38 µL of unlabeled MacNup98A were mixed with 2 µL of Alexa647-labeled protein and the solution was flash frozen in liquid nitrogen in small aliquots. 2 µL of this mixture were then diluted with 98 µL of assay buffer (20 mM Tris-HCl, 130 mM NaCl, 2 mM MgCl2, 5 mM DTT, 250 mM sucrose, pH 7.5) to a final MacNup98A concentration of 20 µM. 3 µL drops of sample were applied to reinforced carbon-coated copper grids, blotted for approximately 8 sec, and plunge-frozen into liquid-nitrogen-cooled liquid ethane.

Scheme 2: 38 µL of MacNup98A (1.5 mM stock solution dissolved in 6 M GdmHCl) was mixed with 2 µL of Alexa647-labeled protein (1 mM solution dissolved in 4 M GdmHCl) and small aliquots of this solution were snap-frozen in liquid nitrogen and stored at -80°C. 1.4 µL of this solution were mixed with 98.6 µL of assay buffer (20 mM Tris-HCl, 150 mM NaCl, 2 mM MgCl2, pH 8) to yield a 20 µM final concentration of FG particles. This solution was used for further infusion experiments.

Infusion of spheres with transport receptors and cargo

The tetrameric variant of GFP, labelled 3b7 was received as a 120 µM stock solution and was diluted with assay buffer (50mM Tris-HCl pH8, 300 mM NaCl) to a 10 µM concentration, aliquoted into 6 µL aliquots, snap-frozen in liquid nitrogen, and stored at -80°C until further use. FG particles of MacNup98A were prepared according to scheme 2, as described in the previous section. For the infusion experiments, 5 µL of 3b7 were added to 45 µL of FG particles' mixture and left for several minutes to mix on ice. 40 µL this mixture was added to 20 µL of an undiluted BSA-coated solution of 10 nm colloidal gold, thus achieving the optimal 1:3 dilution of the fiducial markers for cryo-ET, and kept on ice until vitrification.

Importin-β fragment (45-462) (Kutay and Goerlich, 1997) was prepared according to the procedure described in the Materials and Methods section. To achieve a final working concentration of 1 µM, 5 µL of the protein were mixed with 35 µL of the FG particle mixture, and left for several minutes to mix on ice. All 40 µL were then mixed with 20 µL of BSA-coated colloidal gold and kept on ice until vitrified.

Vitrification of FG particle samples

Holey carbon copper grids R2/1, 200 mesh (Quantifoil, Germany) were additionally coated with a 10 nm carbon layer in a sputter coater (Safematic CCU-010, Germany). These reinforced grids were then glow discharged for 30s (Harrick, USA). 20 µL of the FG particle suspension was mixed with 10 µL of BSA-coated gold tracers measuring 10 nm in diameter (Aurion, Germany) and the mixture was applied to the EM grids in 3 µL volumes. The grids were blotted in the range of 6–8 s with a Whatman number 1 filter paper (Whatman, Germany), and plunged into liquid-nitrogen-cooled liquid ethane in a custom-built manual plunger. Samples were stored in grid boxes in a liquid-nitrogen-cooled container until further processing.

Cryo-FIB-SEM milling of protein hydrogels and spherical particles

EM grids containing vitrified FG particles were loaded into the Auriga cryo-FIBSEM device as previously described in Chapter 2. Samples were thinned using a 20 pA aperture at an acceleration of 30 kV. The thinning steps took approximately 10 minutes or less per spherical particles. Samples were thinned in a ramping fashion using a parallelogram-shaped milling object provided by the Smart-SEM software (Carl-Zeiss, Germany).

Cryo-ET imaging of FG particles with the objective aperture

Samples were imaged with a 300 kV electron microscope (Titan, FEI) equipped with a FEG. Imaging conditions were as follows: C1 aperture (2000 µm), C2 aperture (70 µm), objective aperture (100 µm), spot size 6, illuminated area of 2.8 µm and a nominal magnification of 64000x, which yielded a pixel size of 0.22 nm at the camera level. Projection images of the sample were collected using the SerialEM software (Mastronarde 2005) covering the full angular range (-60° to +60°) with 2° increments. The slit of the energy filter (Gatan) was set to 20 eV. Projection images were acquired in stacks on a direct electron detector (K2 Summit, Gatan) keeping the flux at around 10 e^-/px/s in the counted mode, with individual exposures of 0.2s. The total applied dose was around 80 $e^-/Å^2$ for the entire tomogram. Images were acquired at a nominal defocus of -6 µm.

Image processing and tomogram reconstruction

Specimen drift was compensated for using customized software (Li 2013). Tomograms were reconstructed using the TomToolbox package (Nickel 2005) and customized matlab scripts.

Cryo-ET imaging of FG particles with the Volta phase plate

Phase plate calibrations were performed according to the manufacturer's instructions (FEI, Eindhoven, The Netherlands). Same imaging settings were used for imaging with the phase plate as for the imaging with the objective aperture. Projection images were acquired using the SerialEM software. The phase plate was charged according to previously established calibration curves for the spot size and magnification used (spot size 6 and nominal magnification of 64000x). The position on the phase plate was changed for every tomogram and the carbon plate was recharged anew.

Confocal light microscopy imaging

Two-channel fluorescence images were acquired on a Leica SP5 Mid-UV-VIS microscope using a HCX PlanApo 40x, NA 1.25 or HCX PlanApo. 63x, NA 1.4 oil immersion lens. Multi colored samples were analyzed in the sequential scan mode, using different laser lines for detection of the specific dyes. Excitation of Alexa647 was carried out using the 647 nm line of the He/Ne laser. An Argon laser was used for the excitation of the 488 nm GFP.

Integrated Results and Discussion

Structural characterization of the internal organization of hydrogels formed by yNup100

Hydrogels formed by yNup100 were assembled according to scheme 1 (see Materials and Methods section) and left to settle overnight in a hydration chamber. They were subsequently plunge-frozen without blotting and transferred into the cryo-FIB-SEM for milling. The resulting hydrogels measure 500-1000 µm in diameter and were relatively flat, with thicknesses in the range of several hundred micrometers (**Figure 21**, panels a and b). Cryo-FIB-SEM milling was applied according to the scheme described for the whole-body *C. elegans* and *D. melanogaster* embryos. Milling was carried out starting with high-energy probes (20 nA), and gradually lowered to 240 pA as the material was progressively ablated. For the fine polishing step, the 120 pA aperture was used in order to generate a lamella approximately 250 nm thick (**Figure 21**, panels c and d, Figure 22, panels c and d). The successful application of cryo-FIB-SEM usually resulted in lamellae that were around 25 µm wide (**Figure 21**, panels c and d, white arrow), suspended between sloped non-milled sides (**Figure 21**, panels c and d, white asterisk) and appearing very flat. An example of an unsuccessfully milled area of the hydrogel is indicated by black arrows (**Figure 21**, e and f). In this case, the vast majority of sample material remained non-milled directly below the sire of the future cryo-lamella.

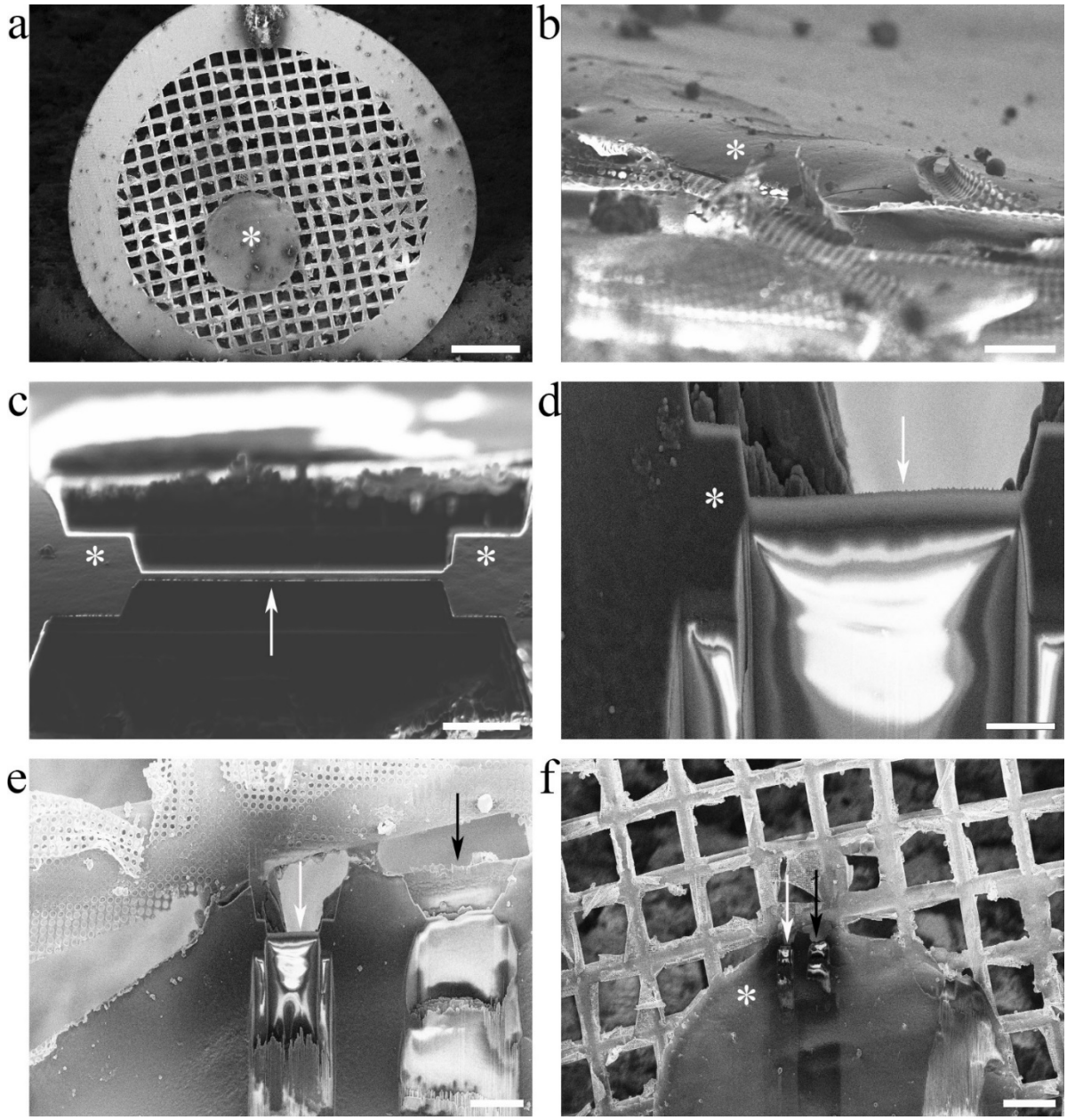

Figure 21. Cryo-FIB-SEM on hydrogels formed by yNup100.

(a) SEM top-view of the yNup100 hydrogel (asterisk) on an EM grid. (b) FIB side-view of the yNup100 hydrogel (asterisk). (c) FIB side-view of the thin cryo-lamella (white arrow) and the non-milled sides (asterisk). (d) SEM top-view of the thin cryo-lamella (white arrow) and the non-milled sides (asterisk) from panel c. (e) SEM top-view close-up of a successfully milled cryo-lamella (white arrow) and an unsuccessful attempt at milling (black arrow). (f) SEM top-view of the location of the two milling sites (black and white arrows) on the hydrogel surface (asterisk). Scale bars indicate 500 µm (a), 100 µm (b), 5 µm (c and d), 20 µm (e), and 100 µm (f).

Grids containing cryo-lamellae were taken to the TEM after surface fiducial markers were applied. The lamellae were often cracked and found barring clusters of ice contamination (**Figure 22**, panels a, b). This was still good enough to perform cryo-ET on them and the sites

selected for tomographic imaging are highlighted with a dotted black rectangle (**Figure 22**, panel b). Representative tomographic slices are displayed in Figure 22 and show that no internal structural organization could be detected. This is most likely due insufficient tilt coverage, alignment issues, and a lack of structured features within the particular area chosen for imaging. The hydrogels were previously tested *in vitro* for the presence and distribution of the FG-repeat-rich regions with confocal microscopy (Frey and Gorlich, 2007), but the average size of the field of view varies greatly between light and electron microscopy. It is very likely that the FG-repeat-rich fragments clusters in discreet areas of the hydrogel and are spaced by surrounding buffer, resulting in the inability to reliably target such areas with cryo-ET without precisely knowing their position. It is also possible that yNup100 simply does not form higher order structures of the kind that would be readily detectable by cryo-ET.

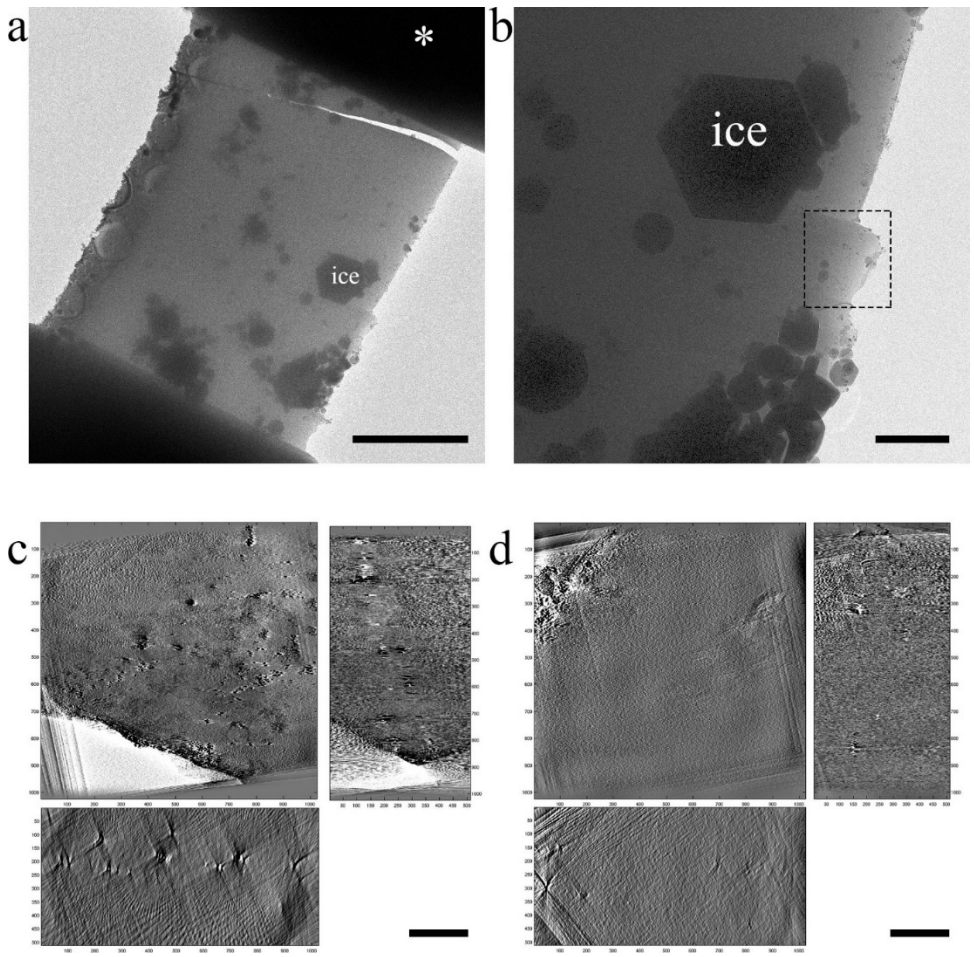

Figure 22. Cryo-EM and cryo-ET of hydrogels formed by yNup100.

(a) TEM top-view of the cryo-lamella with the non-milled side indicated (asterisk). (b) Close-up of the cryo-lamella showing a region of tomography data acquisition (black box). (c,d)

Slices from tomograms acquired on the cryo-lamella from panels a and b. Tomographic slices are 1.68 nm thick. Scale bars indicate 10 µm (a), 1 µm (b), and 200 nm (c,d).

Structural analysis of the FG-repeat-rich near-spherical particles formed by the *T. thermophila* MacNup98A

FG particles were assembled according to scheme 1 (see Materials and Methods section) and inspected for fluoresce signal under a confocal microscope. The particles showed a very even distribution in solution and an almost perfectly spherical shape, as well as homogenous staining with the Alexa647 fluorophore (**Figure 23**, panels a,b). After quality inspection, the particles were blotted extensively, plunge-frozen, and transferred into the cryo-FIB-SEM device. In the SEM images the particles appear spherical, dome-shaped, very clearly identifiable on the carbon support film (**Figure 23**, panels c,d) measuring on average between 2 and 6 µm in diameter. The milling approach chosen here was to create cryo-lamellae, which meant that the sample material was ablated from above and below the area where the future lamella would lie (**Figure 23**, e, blue square). Initially a 50 pA probe was used but this was found to deliver to much heat to the sample because the lamellae appeared collapsed of physically distorted (data not shown). This immediately prompted us to switch to a much lower probe and from that moment onward, only the 20 pA probe was used in processing the FG particles (**Figure 23**, f, blue square). Fiducial markers were then added as described previously, and the samples were transferred into the TEM. The surface of the cryo-lamellae was smooth (**Figure 24**), with very little curtaining, and almost devoid of any ice contamination (**Figure 24**, panels a,b). However, all of the lamellae were cracked (**Figure 24**). This posed a problem for normal data acquisition at these locations because it would happen that the two sides of the crack were superimposed on each other. Unfortunately, this did not become apparent until tomography was initiated and the sample reached higher tilt angles. Other problems followed from this lack of mechanical integrity. For example, the lamellae were mechanically much less stable, due to not being fully suspended between two non-milled sides, which often lead to blurring of the images during data acquisition, becoming more prominent at higher tilts.

The issue of mechanical instability, emanating from cracked cryo-lamellae was resolved by changing the milling strategy. The particles were from this point onward milled in a “ramp-

like" fashion. This means that the samples were milled only from the top and under a shallow incident angle (Rigort et al., 2012b). This produces an area of transparency (sample thickness much less than 500 µm), the length of which is directly related to the incident angle of the FIB beam. In other words, the shallower the incident angle, the longer the transparency area for tomographic imaging. This approach yielded satisfactory results. The particles were thinned in such that they could be easily imaged on the edges where the FIB beam exited the sample (**Figure 25**, panels b-d, blue circles). The major advantage of this approach was in the fact that a single milling window could now be used in order to create areas available for data collection. On average, a single milling window would last app. 20 minutes and one could process a great number of particles per milling session (**Figure 25**, panels b-d, yellow dots). All the transparency regions yielded tomograms of high quality, two of which are shown here as representative (**Figure 25**, panels e,f). The tomographic slices show a very clearly defined particle edge at the interface with the surrounding buffer. The most exciting part is the clear presence of higher order structural organization within the particles. It appears that MacNup98A organizes into filamentous-like structures within the particles. The structures can be seen in the x-y view as strongly contrasting dots (**Figure 25**, panels e,f, red circles) that run through a sizeable portion of the volume, as seen in the x-z and y-z views. Apart from the black dots, potentially representing putative filaments present in the z-direction, filamentous-like densities can be observed running in the x-y direction as well (**Figure 25**, panels e,f, green arrowheads). The contrast difference observed between the filamentous-like densities and the strongly contrasting globular-like ones could also arise from the fact that the globular-like ones represent areas where the Alexa647 dye is bound to an FG repeat. These structures appear to be on average 4-6 nm in diameter, but without subtomogram averaging one cannot establish these values with outmost precision. A very interesting point that has to be made here is that the FIB beam does not seem to incur any structural damage or alteration to the FG particles themselves or their internal structural components. Comparing a tomographic slice from a tomogram acquired on a milled particle (**Figure 25**, panel f) to a tomogram of a non-particle (**Figure 25**, panel e), imaged on its very thin edge, one can appreciate that there are no obvious differences in the general appearance of the filamentous-like structural elements. In both cases, the particles have the same general shape and form, and the internal organization appears to be the same. This was very encouraging for future experiments using the cryo-FIB-SEM approach to study the structural organization of MacNup98A FG particles.

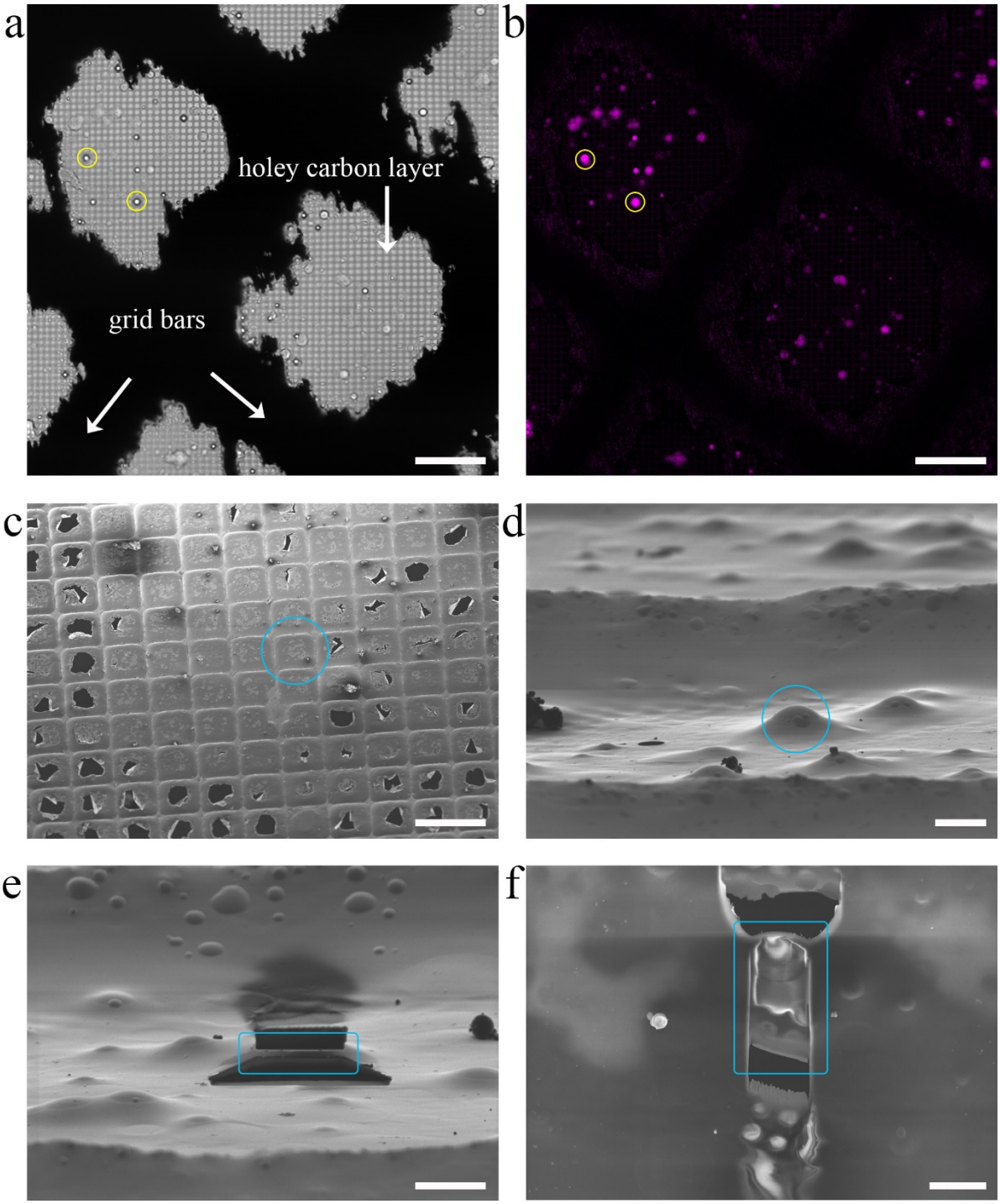

Figure 23. FG particles formed by MacNup98A.

(a) BF image taken of an EM grid barring a droplet of FG particles (highlighted in yellow circles). Fluorescence confocal image of the same area as in panel a, showing the particles (highlighted in yellow circles) internally stained with the Alexa647 dye (purple color). (c) SEM top-view of the EM grid mesh selected for FIB milling (blue circle). (d) FIB side-view of the FG particle selected for FIB milling (blue circle). (e) FIB side-view showing the FG-particle post milling and the site of the cryo-lamella (blue box). (f) SEM top view close-up of the milled particle indicating the cryo-lamella (blue box). Scale bars indicate 1 µm (f), 5 µm (d,e), 30 µm (a,b), 200 µm (c).

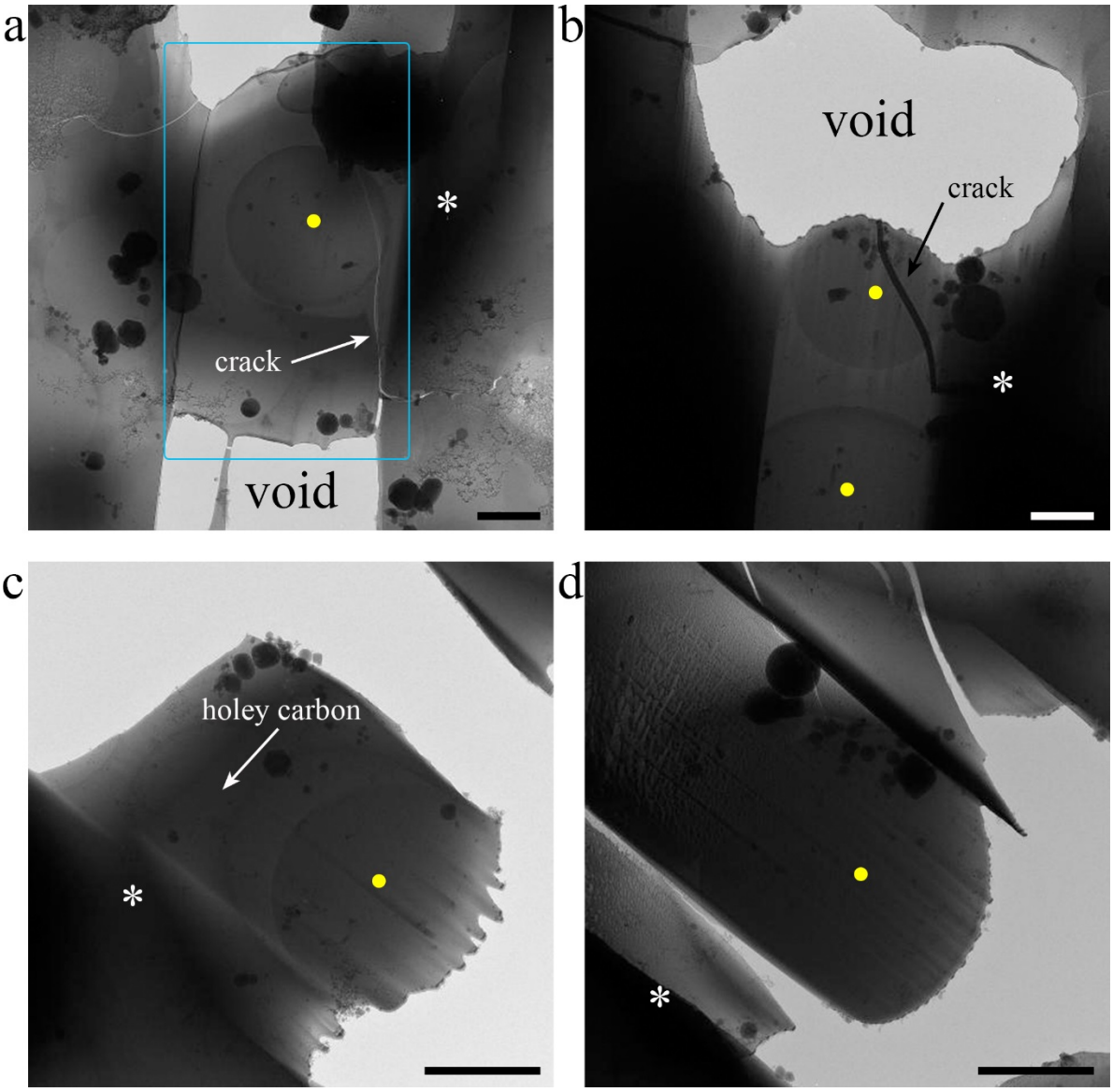

Figure 24. Cryo-TEM imaging of the FG particle cryo-lamellae.

(a-d) TEM images showing the mechanically damaged cryo-lamellae (blue box in panel a) containing the milled FG particles (yellow circle). White asterisk indicates non-milled sides. Scale bars indicate 1 µm.

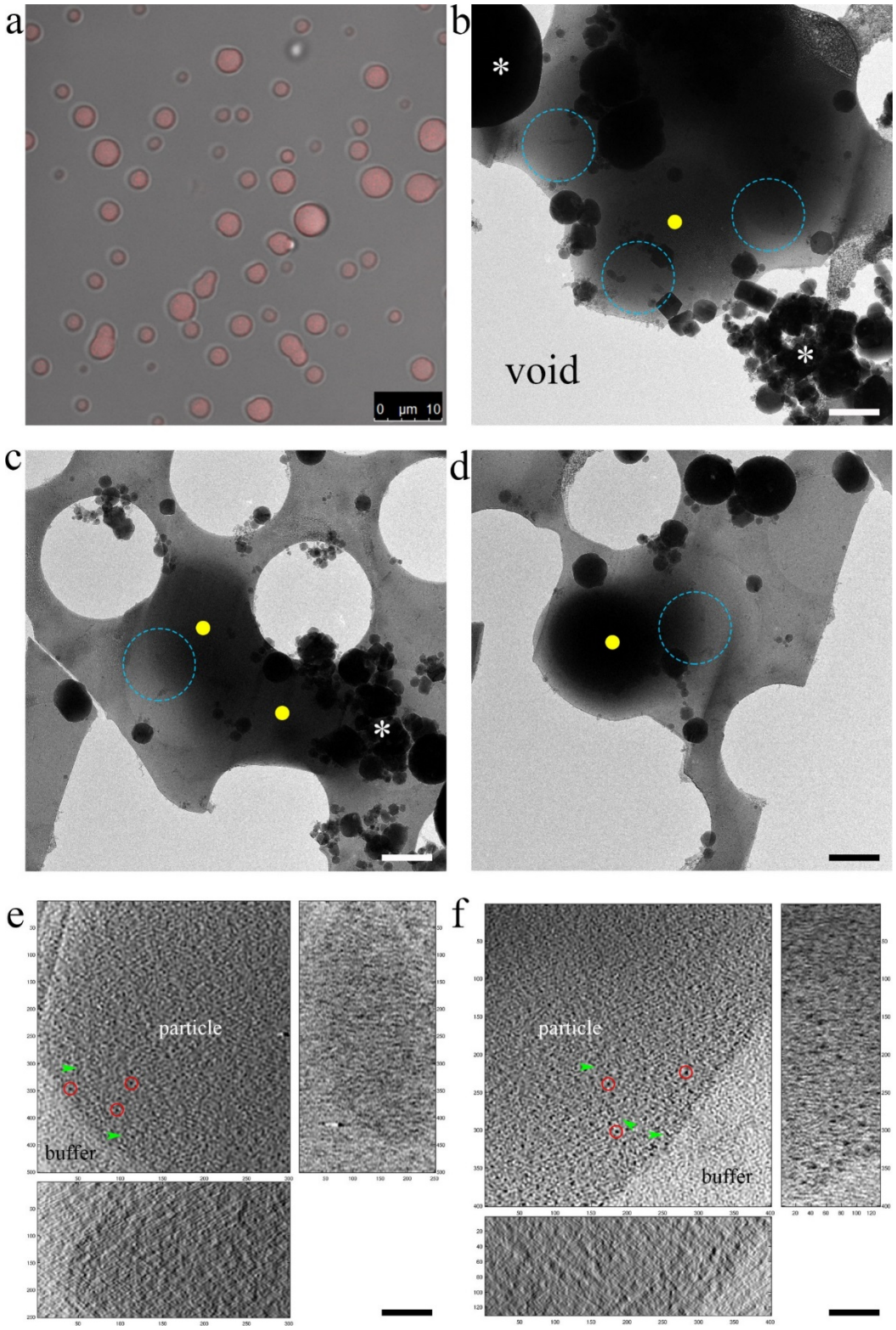

Figure 25. Structural analysis of FG particles using the ramp milling approach.

(a) Confocal image showing the shape of the FG particles in solution (Alexa647). (b-d) TEM images showing the FG particles (yellow circles) milled with a ramp approach. Blue circles indicate sites on with tomographic data was collected. (e) Tomographic slice from a non-milled particle with filamentous-like densities running in the x,y-direction (green arrowheads) and globular-like densities (red circles). (f) Tomographic slice of a milled particle with filamentous-like densities running in the x,y-direction (green arrowheads) and

globular-like densities (red circles). Tomographic slices are 0.88 nm thick. Scale bars indicate 1 µm (b-d), and 200 nm (e,f).

We then set out to see if we could use image-processing methods to enhance the contrast of the filaments running in the x-y direction in order to facilitate further data analysis. The idea was to render a defined volume of the particle and use this mask to do a network analysis in order to calculate the average diameter and sizes of the porous space in-between the filamentous-like densities as well to better under the sizes of the putative filaments. We decided to apply a nonlinear anisotropy diffusion filter (Perona and Malik, 1990) to our tomographic data and the outcome is shown in Figure 26. This filter is especially useful in cases where edges and line-like structures want to be enhanced. The overall contrast of the tomogram was indeed significantly enhanced. This is especially apparent in the case of globuloar-like densities (**Figure 26**, panels a,b, red circles). One immediately observes that the black dots seen in the x-y views of the two tomograms are more strongly contrasted in both the x-y (red circles) as well as the x-z and y-z views (blue boxes) when comparing the same positions. The main differences stem from the fact that their edges are much more clearly defined. However, a different issue arises upon closer inspection of the filamentous-like densities running in the x-y direction in the x-y views of both tomographic slices (**Figure 26**, panels a,b, white arrows). The densities running in the x-y direction do not match at the same position between the unfiltered and filtered tomograms. The ones observed in the unfiltered one are no longer present in the filtered one and the ones observed as strongly contrasting in the filtered tomogram are not present in the unfiltered tomogram. This is a known artifact that could result from applying a nonlinear anisotropy diffusion filter, where filament-like features can be introduced in the images due to the very nature of how the feature edges are processed and how discernable they are in the original data (Weickert, 1994).

Overall, the strategy employed here to studying the internal structural organization has yielded satisfactory results. We have established the cryo-FIB-SEM conditions needed to produce stable cryo-lamellae that can be used for the collection of tomographic data. Furthermore, we have shown that the interaction of the FIB beam with the FG particles is non-detrimental under the described experimental condition and that the structures we observe inside the milled particles completely match those observed in a non-milled particle. We have also shown that higher order structural organization is not only present but can readily be

detected in the FG particles interior. The artifact-prone anisotropy filtering approach was shown to not be applicable in our data so has been omitted from further analysis.

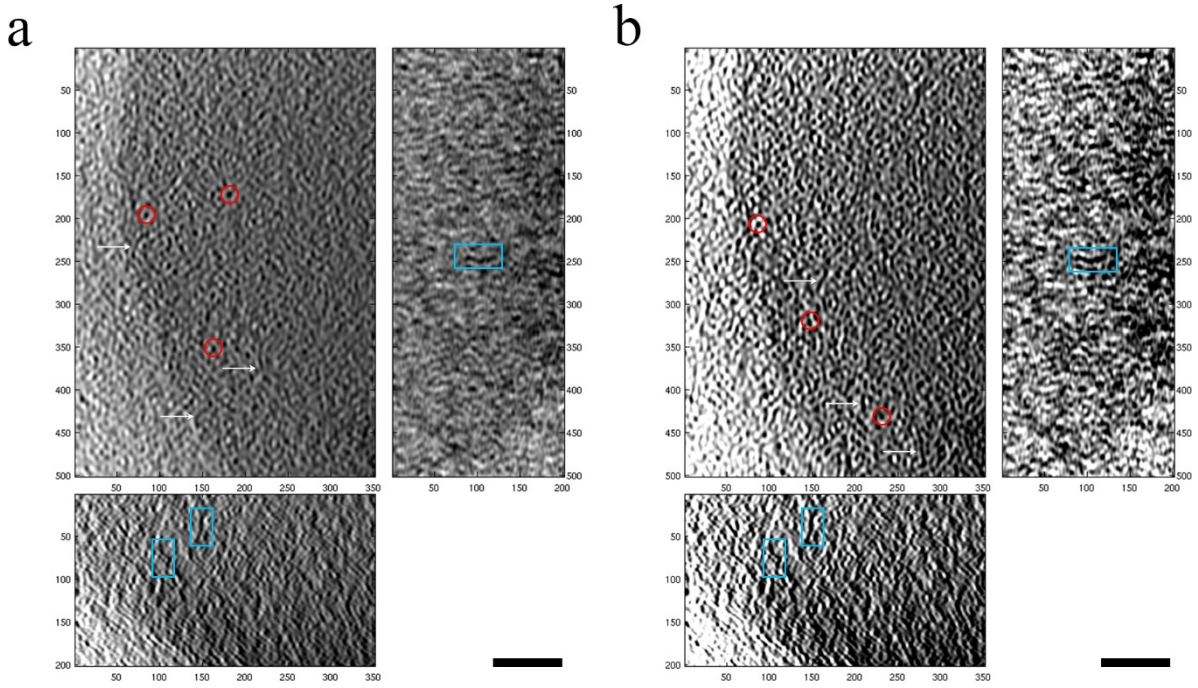

Figure 26. Comparison of the effect of applying a linear anisotropy filter to tomographic data obtained from FG particles.

(a) Tomographic slice showing the internal organization of the FG particle without anisotropy filtering. (b) The same tomographic slice, as shown in panel a, but with anisotropy filtering applied. White arrows indicate putative filaments running in the x,y-direction, red circles indicate putative filaments running in the z-direction, and blue boxes indicate the same putative filament densities in the x,z and y,z-views of the non-filtered (a) and filtered tomogram (b). Tomographic slices are 0.88 nm thick. Scale bars indicate 200 nm.

Testing the robustness of MacNup98A FG particles

After the conditions for the assembly, imaging and processing of the data acquired on FG particles had been established, we sought out to continue with further experiments. However, we first encountered an unexpected issue. The FG particles assembled according to scheme 1 were no longer behaving as previously seen. After inserting the particles into cryo-FIB-SEM, we noticed a change in their overall morphology. The particles that used to appear like well-defined spherical domes (**Figure 23**, panel d, blue circle) now had a completely flattened appearance (**Figure 27**, panels a,e), yellow arrowheads). Additionally, they showed no trace of any detectable structures in TEM images either (data not shown). We decided to address this issue in several ways. (i) All the buffers used in the assembly process were exchanged and

freshly prepared prior to particle assembly. (ii) Several different sucrose concentrations in the buffer were tested to see if the osmotic pressure has any effect, e.g. no sucrose, 125 mM, 250 mM, and 500 mM (**Figure 27**, panels e,f). (iii) 2% glutaraldehyde was added to the particles after assembly to test if blotting might be causing structural alteration to the particles (**Figure 27**, panel c,d). (iv) A range of several pH values were used to determine if this has any effect on the particle assembly and stability, e.g. pH6.5-8 (data not shown). (v) Different concentrations of sodium chloride were used in order to determine whether the ionic strength of the buffer plays any role, e.g. 100 mM, 150 mM, 200 mM, and 250 mM (data not shown). Figure 27 summarizes and highlights the most important experimental step carried out in order to tackle this problem. All SEM and TEM images acquired on the samples prepared with the described modifications essentially followed the same pattern. The particles were completely flattened and without observable internal structural organization, except in the case of glutaraldehyde fixation where at least in the SEM the particles regained their spherical appearance (**Figure 27**).

The issue of altered FG particle morphology was ultimately resolved together with our collaborator. The root cause of it seemed to have been a biochemical/structural instability due to long-term storage at -80°C as well as the use of an insufficient concentration of guanidine hydrochloride in the storage buffer. From this point onward, the protein fragments were kept in 6 M guanidine hydrochloride and assembled according to the scheme two (see Materials and Methods section). This included some salt concentration adjustments, omission of certain salts, as well as a modified pH value. FG particles assembled according to scheme 2 were extensively tested with confocal microscopy, SEM, and TEM. In confocal microscopy, they again showed a spherical appearance (**Figure 29**, panels c and d); however, in SEM they looked flattened. When imaged in the TEM, sharp edges could be clearly observed as well as internal structural features, in contrast to before. This was in itself a breakthrough because from this point onward, we could do all tomographic imaging on the particles without having to process them first with the cryo-FIB-SEM.

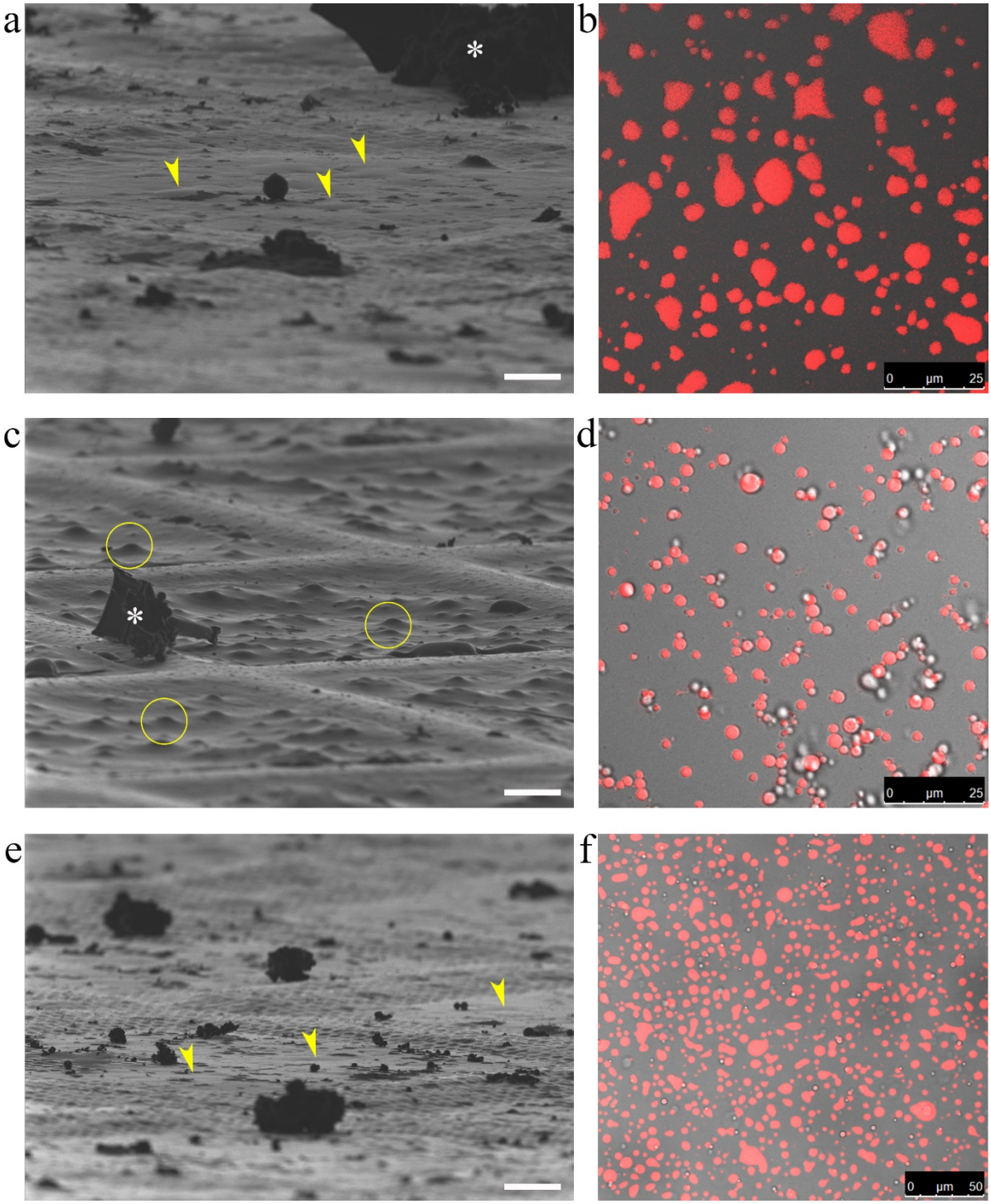

Figure 27. Probing the changing morphology of the MacNup98A FG particles.

(a) FIB side-view of the FG particles prepared according to scheme 1 (see materials and methods section) with the corresponding confocal image (Alexa647) (b). (c) FIB side-view of the FG particles chemically fixed with 2% GA and the corresponding confocal image (Alexa647) (d). (e) FIB side-view of the FG particles prepared without sucrose in the assembly buffer and the corresponding confocal image (Alexa647) (f). Scale bars indicate 10 µm (a,c,e).

Testing the effects of diffusing cargo (quadruple GFP construct) and special forms of import factors (Imp-β fragment) on the Nup98 FG particles

Once all the issues of particle morphology and quality had been resolved, we proceeded with further experiments. We wanted to examine more closely what the internal structural organization of the FG-repeat domains of Nup98 look like inside the FG particles. Additionally, we wanted to see if diffusing cargo or transport receptors would have any visible effect on the overall internal structural organization within the particles themselves.

We expressed and purified a dominant negative mutant of Importin-β, more specifically the fragment 45-462. It was previously shown not only to strongly bind the FG repeats, but also to accumulate at the nuclear rim due to the inability of being released (Kutay et al., 1997). Imp-β fragment was obtained in a highly pure form with Ni-NTA beads and SEC, concentrated (**Figure 28**), and confirmed by a western blot against the His-tag (data not shown). It was ultimately added to the FG particle in a final concentration of 1 μM, as was previously shown to be in the physiological range (Kutay et al., 1997).

To test another transport with cargo-like properties we used a variant of GFP baring the FG-binding domain of the nuclear transport factor NTF2. This construct is a functional analogue of NTF2 and was provided to us by the laboratory of Prof. Dirk Goerlich. It has been experimentally observed that it forms stable tetrameric complexes and passes the NPC barrier significantly faster than NTF2, and the partitioning coefficient between the buffer and particles is very high (personal communication from the Goerlich lab). We have added it to a final concentration of 1 μM, which ensured full particle saturation. Figure 29 schematically shows the expected localization and mixing modalities between the Imp-β fragment, 3b7 construct, and FG particles. Our hypothesis was that, due its size and affinity for FG repeats, Imp-β fragment should not be able to penetrate the particles completely but rather accumulate at the periphery or in the outermost layer (**Figure 29**, panel b). In the case of the 3b7 construct, it infused the FG particles completely with no signal detectable in the surrounding buffer (**Figure 29**, panel a).

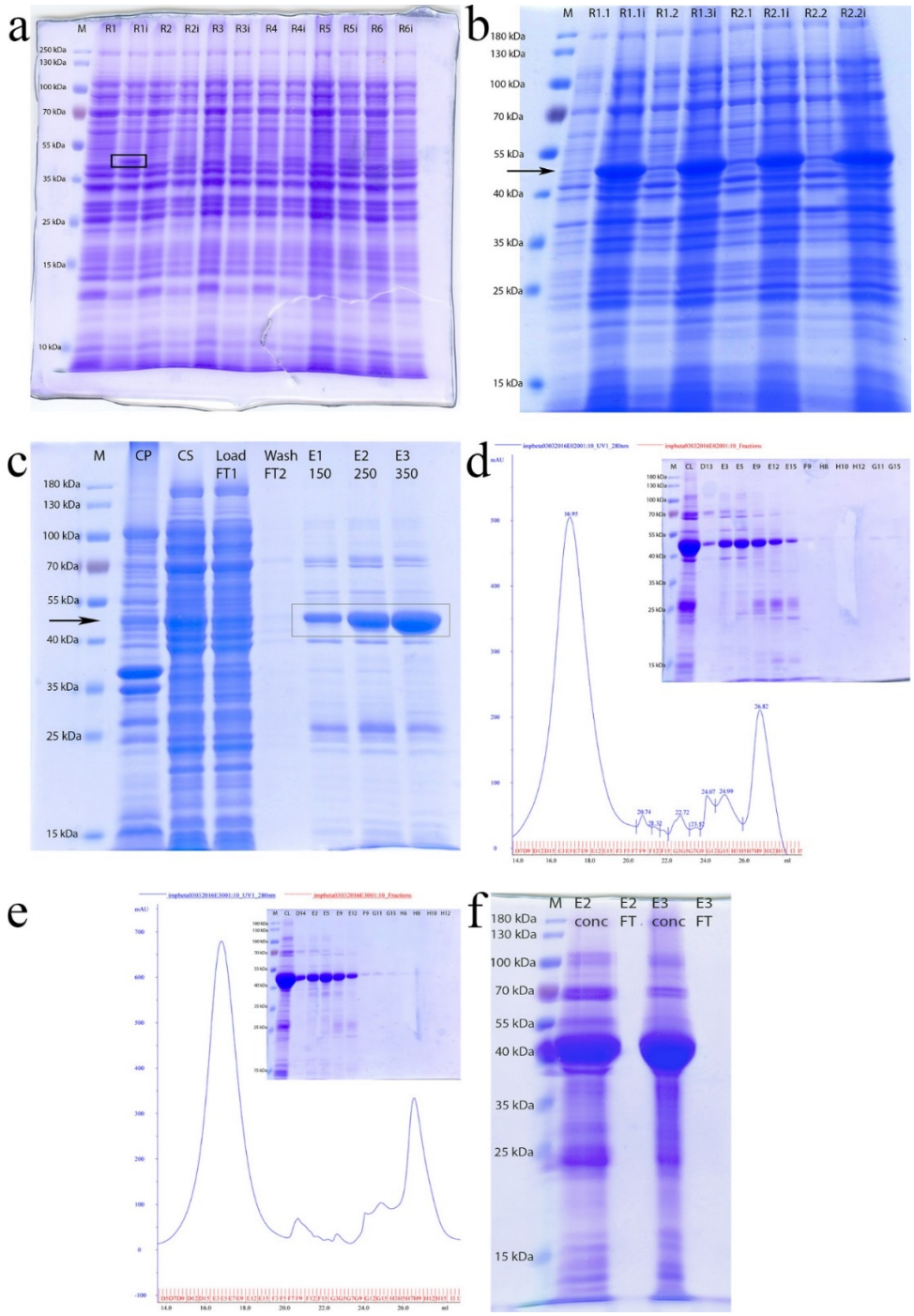

Figure 28. Expression and purification of Importin-β fragment (45-462).

(a,b) SDS-PAGE gels showing the mini-scale expression trial for Imp-β fragment. Black box indicates the band corresponding to Imp-β fragment post-induction and black arrow points to its molecular weight height. (c) SDS-PAGE gel showing the optimized expression and purification of the Imp-β fragment on Ni-NTA beads. Black arrow indicated the height of Imp-β fragment. M – marker, CP – pellet, CS – supernatant, load FT1 – first flow through after the entire cell extract was loaded, wash FT2 – flow through of the wash step after binding of protein to the beads, E1-E3 – elution fractions with different concentrations of imidazole (numbers shown in mM). (d,e) SEC elution profiles showing the fraction peaks and the corresponding SDS-PAGE gels in the insets. (f) SDS-PAGE gel showing the pooled

and concentrated fractions. M – marker, E2 and E3 – concentrated elution fractions, FT – concentrator flow through.

FG particles infused with the Imp-β fragment assumed the expected near-spherical shape as seen by the confocal microscope images (**Figure 29**, panel d). Imp-β fragment was not fluorescently labelled in our experiments so its presence could not be confirmed by fluorescent imaging (it was confirmed by western blotting against the His-tag, data not shown). The color of the FG particles in Figure 29d comes from the Alexa-647-labelled FG-repeat domains. A representative tomographic slice is shown in Figure 29f. The particles show a clearly defined edge, i.e. phase separation between the particle interior and the surrounding buffer, with no discernable electron densities in the buffer. Along the particle edge one can distinguish either filamentous-like densities running in the x-y direction (green arrowheads) or strongly contrasted black dots (red dots), which presumably belong to rod-like densities running in the z-direction (only the x-y view is shown in the figure) (**Figure 29**, panel f). FG particles infused with the 3b7 construct showed the same overall internal and external organization with densities running in all three directions. Between the two tomograms it is very easy to identify the filamentous-like densities running in the z-direction (red circles); however, the densities running in the x-y direction were generally more clearly visible in the case of Imp-β fragment (**Figure 29**, panels e,f). A comparison of tomographic slices from the three different experimental states is shown in Figure 30. All slices come from tomograms that were acquired on particles of similar thickness and under the same imaging conditions. Furthermore, the images were processed in Matlab and Photoshop using the same bandpass filtering setting as well as image tuning parameters. All three experimental conditions show the same overall particle geometry and organization with some subtle and interesting differences. One can clearly notice an increase in the overall contrast, especially at the particle rim, in the case of the Imp-β fragment treatment (**Figure 30**, panel c). Moreover, there is a striking difference in the general detectability of the filamentous-like densities running in the x-y direction in the Imp-β fragment tomograms. On top of that, one can also observe a slight increase in the visibility of the filamentous-like densities running in the z-direction in the 3b7 tomograms (**Figure 30**, panel b).

These results suggest that there is indeed a very highly structured environment within the FG particles, and that diffusing different types of complexes through them could ultimately allow

one to either track their trajectories or visualize them in complex with the FG repeats. Tomograms of the particles treated with Imp-β fragment show that rendering such data in 3D using Amira might provide data of quality sufficiently high for a network analysis, from which the crowdedness, porosity, and putative filament lengths could be extracted. Tomograms showing the 3b7-treated FG particles show an enrichment in electron densities in the buffer surrounding the particle in discrete locations (**Figure 29**, panel e, Figure 30 panel b) as well as having highlighted filamentous-like densities running in the x-y direction, at least in comparison to the untreated state (**Figure 30**, panel a). This prompted us to try a different imaging approach for studying the infused FG particles that would allow us to discern more clearly the diffusing cargo from the FG repeat-associated structures.

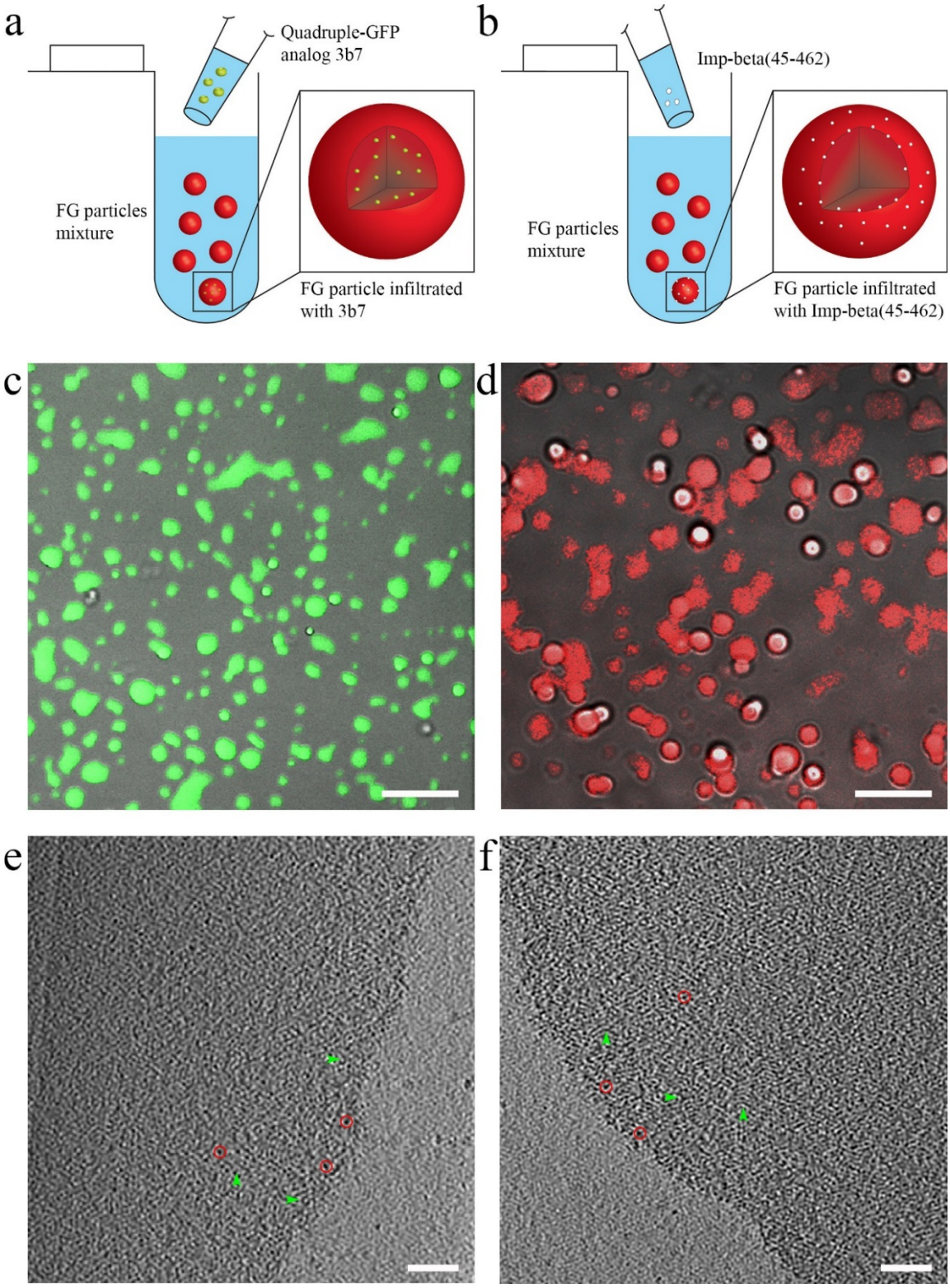

Figure 29. Infusion of FG particles with Importin-β (45-642) and 3b7 GFP analogue.

(a,b) Illustration of the expected interaction of 3b7 analogue and Imp-β fragment with FG particles, respectively. (c,d) Confocal images on FG particles infused with 3b7 (GFP signal) and Imp-β fragment (Alexa647 indicates the FG particle), respectively. (e,f) Representative tomographic slices (0.88 nm) of the FG particles infused with 3b7 and Imp-β mutant, respectively. Red circles indicate putative filaments running in the z-direction, and green

arrowheads indicate putative filaments running in the x,y-direction. Scale bars indicate 10 µm (c,d) and 100 nm (e,f).

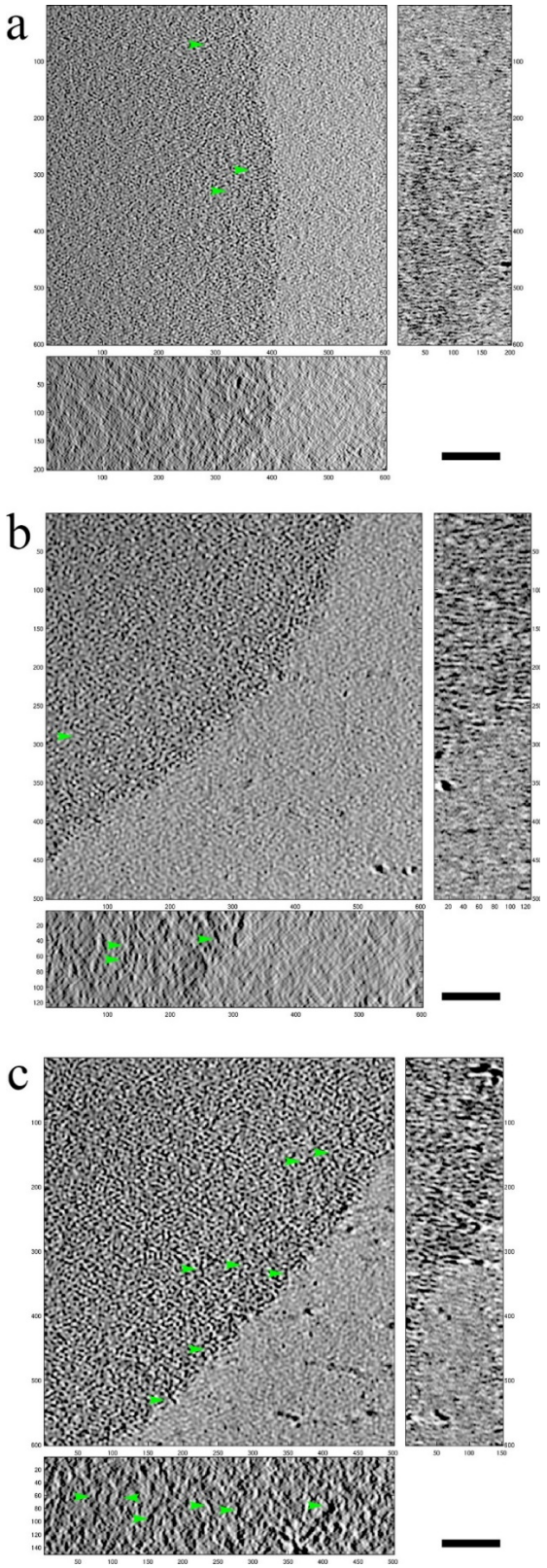

Figure 30. Comparison of the three experimental states of FG particles.

(a) Representative tomographic slice showing a non-treated FG particle. (b) Representative tomographic slice showing an FG particle infused with 3b7. (c) Representative tomographic slice showing an FG particle infused with Importin-β fragment (45-462). Green arrowheads indicate presence of filamentous-like structures in the different views. All tomographic slices are 0.88 nm thick. Scale bars indicate 100 nm.

Imaging FG particles infused with the 3b7 GFP variant with the Volta phase plate

We decided to image our FG particles infused with the 3b7 GFP variant with the Volta phase plate instead of the objective aperture (**Figure 31**, panel a). As mentioned in the introduction, the phase plate enhances the contrast of very small particles allowing the user to distinguish them more clearly. It also enables for the use of in-focus imaging, allowing better retention of high-resolution information while preserving strong contrast. Our aim was to see if we could enhance the contrast of the FG filaments running in the x-y direction as well as the 3b7 particles in the buffer and inside the particle. The goal was to try to catch the 3b7 construct interacting with the FG-repeat domains.

We first did a test trial with the phase plate in order to establish the optimal imaging conditions for tomography. A plot of the interdependence of the applied dose and the amount of phase shift the electrons experienced because of "pre-charging" the phase plate is shown in panel b (**Figure 31**, panel b). From this, we calculated the amount of exposure, i.e. pre-charge, needed for the phase plate in order to carry out tomographic imaging. We chose to pre-charge the phase plate with a dose of app. 70 $e^-/Å^2$. Figure 31 compares two representative tomographic slices from tomograms acquired on FG particles infused with the 3b7 construct. In the tomograms acquired with the phase plate one can clearly distinguish electron densities in the buffer surrounding the particles, which are app. 4-6 nm in diameter (**Figure 31**, panels d,f). There is also a noticeable enrichment in these in the phase plate tomograms (**Figure 31**, panels d,f) in comparison to the ones acquired with the objective aperture (**Figure 31**, panels c,e).

Despite the increased detection of globular densities in the buffer surrounding the FG particles, the phase plate tomograms did not yield a contrast enhancement that was dramatically superior to the tomograms acquired with the objective aperture. The same overall FG particle organization is seen in both cases, both in terms of the particle edge as well

interior. Furthermore, the 3b7 GFP variant has an estimated diameter of app. 4-6 nm, which roughly corresponds to the average diameter of the observed filamentous-like densities running in the z-direction. In other words, we could clearly discern the densities potentially belonging 3b7 outside the particle, but not inside where it blended with the FG-repeat surroundings. Since subtomogram averaging is a time-consuming and lengthy procedure, we did not want to proceed with it under these circumstances. The overcrowded FG-repeat environment inside the FG particles in combination with the inability to distinguish clearly the 3b7 from the rod-like FG repeats would make it very hard to conduct subtomogram averaging in any reasonable form.

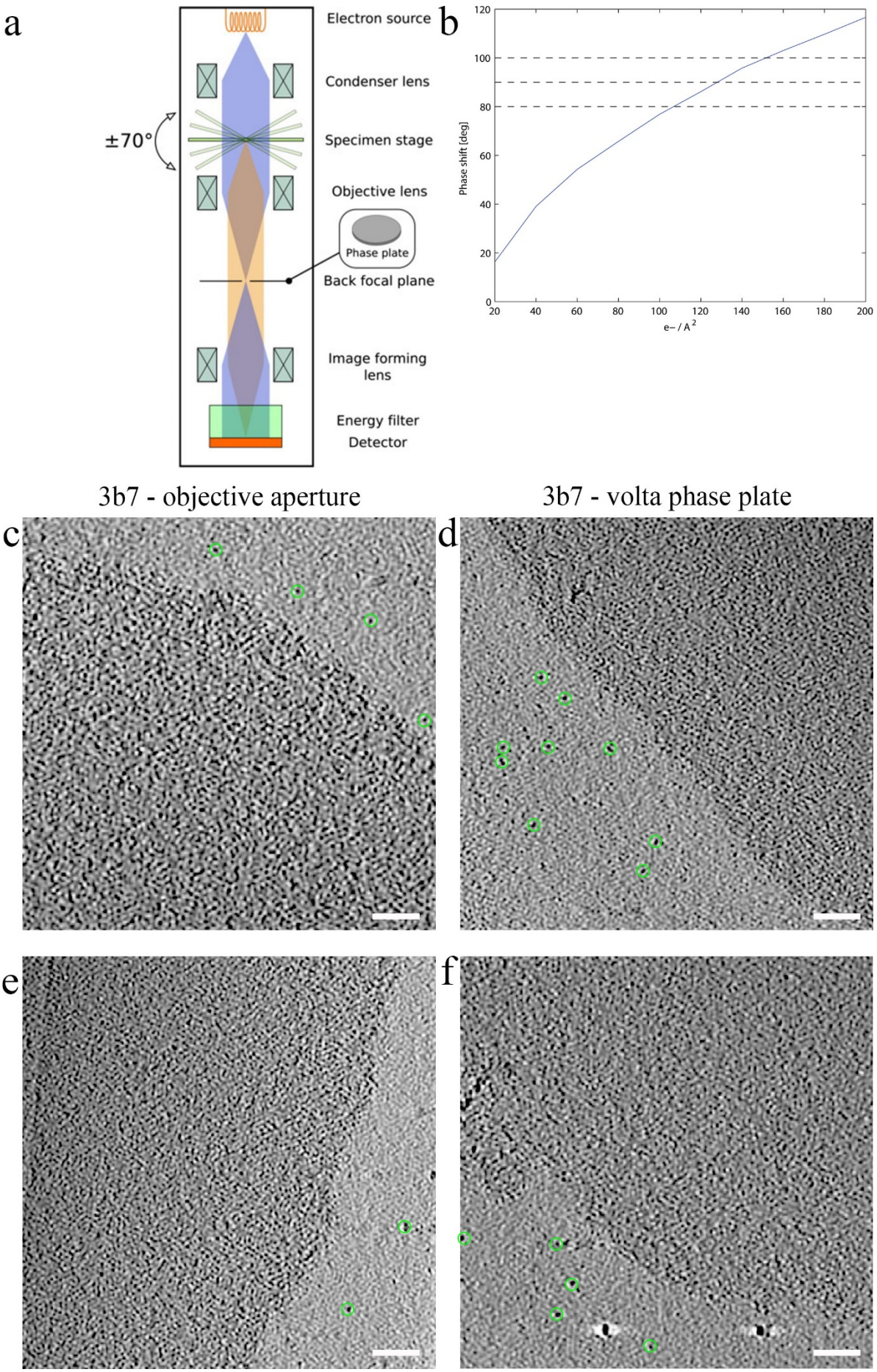
a
Electron source
Condenser lens
±70°
Specimen stage
Objective lens
Phase plate
Back focal plane
Image forming lens
Energy filter
Detector
b
Phase shift [deg]
e– / A 2
3b7 - objective aperture
3b7 - volta phase plate
c
d
e
f

Figure 31. Comparison of the tomograms acquired with the objective aperture and the Volta phase plate on FG particles infused with 3b7.

(a) Schematic comparison of the objective aperture and Volta phase plate inside a TEM. (b) Plot showing a calibration curve for imaging with the phase plate and the relationship between the applied dose and the amount of phase shift obtained. (c,e) Representative tomographic slices (0.88 nm) from tomograms acquired with the objective aperture and an underfocus of -5 µm. (d,f) Representative tomographic slices from tomograms acquired with the phase plate and an underfocus of -1µm. Green circle indicate the suspected presence of the 3b7 protein in the buffer surrounding the particles. Scale bars indicate 100 nm.

Summary and perspectives:

We have demonstrated that hydrogels formed by the isolated FG-repeat regions of the MacNup98A protein possess higher order internal structural organization. We have detected and highlighted the presence of filamentous-like densities of various length and size throughout the tomograms. Taken together, these observations potentially hint at different modalities of assembly. We aim to understand better the network formed by these proteins and analyze it in the presence of cargo and cargo receptors diffusing through it in order to shed some light on the basis for its structural organization as well as the different modes of nuclear transport.

References

Abrusci, P., Vergara-Irigaray, M., Johnson, S., Beeby, M.D., Hendrixson, D.R., Roversi, P., Friede, M.E., Deane, J.E., Jensen, G.J., Tang, C.M.*, et al.* (2013). Architecture of the major component of the type III secretion system export apparatus. Nat Struct Mol Biol *20*, 99-104.

Adams, R.L., and Wente, S.R. (2013). Uncovering nuclear pore complexity with innovation. Cell *152*, 1218-1221.

Al-Amoudi, A., Diez, D.C., Betts, M.J., and Frangakis, A.S. (2007). The molecular architecture of cadherins in native epidermal desmosomes. Nature *450*, 832-837.

Alber, F., Dokudovskaya, S., Veenhoff, L.M., Zhang, W., Kipper, J., Devos, D., Suprapto, A., Karni-Schmidt, O., Williams, R., Chait, B.T.*, et al.* (2007). The molecular architecture of the nuclear pore complex. Nature *450*, 695-701.

Amat, F., Moussavi, F., Comolli, L.R., Elidan, G., Downing, K.H., and Horowitz, M. (2008). Markov random field based automatic image alignment for electron tomography. Journal of structural biology *161*, 260-275.

Asano, S., Fukuda, Y., Beck, F., Aufderheide, A., Forster, F., Danev, R., and Baumeister, W. (2015). Proteasomes. A molecular census of 26S proteasomes in intact neurons. Science *347*, 439-442.

Bammes, B.E., Rochat, R.H., Jakana, J., Chen, D.H., and Chiu, W. (2012). Direct electron detection yields cryo-EM reconstructions at resolutions beyond 3/4 Nyquist frequency. Journal of structural biology *177*, 589-601.

Bartesaghi, A., Sprechmann, P., Liu, J., Randall, G., Sapiro, G., and Subramaniam, S. (2008). Classification and 3D averaging with missing wedge correction in biological electron tomography. Journal of structural biology *162*, 436-450.

Bartesaghi, A., and Subramaniam, S. (2009). Membrane protein structure determination using cryo-electron tomography and 3D image averaging. Current opinion in structural biology *19*, 402-407.

Beck, M., Forster, F., Ecke, M., Plitzko, J.M., Melchior, F., Gerisch, G., Baumeister, W., and Medalia, O. (2004). Nuclear pore complex structure and dynamics revealed by cryoelectron tomography. Science *306*, 1387-1390.

Beck, M., Lucic, V., Forster, F., Baumeister, W., and Medalia, O. (2007). Snapshots of nuclear pore complexes in action captured by cryo-electron tomography. Nature *449*, 611-615.

Ben-Harush, K., Maimon, T., Patla, I., Villa, E., and Medalia, O. (2010). Visualizing cellular processes at the molecular level by cryo-electron tomography. Journal of cell science *123*, 7-12.

Ben-Harush, K., Wiesel, N., Frenkiel-Krispin, D., Moeller, D., Soreq, E., Aebi, U., Herrmann, H., Gruenbaum, Y., and Medalia, O. (2009). The supramolecular organization of the C. elegans nuclear lamin filament. Journal of molecular biology *386*, 1392-1402.

Bennett, A.E., Narayan, K., Shi, D., Hartnell, L.M., Gousset, K., He, H., Lowekamp, B.C., Yoo, T.S., Bliss, D., Freed, E.O.*, et al.* (2009). Ion-abrasion scanning electron microscopy reveals surface-connected tubular conduits in HIV-infected macrophages. PLoS Pathog *5*, e1000591.

Bharat, T.A., Davey, N.E., Ulbrich, P., Riches, J.D., de Marco, A., Rumlova, M., Sachse, C., Ruml, T., and Briggs, J.A. (2012). Structure of the immature retroviral capsid at 8 A resolution by cryo-electron microscopy. Nature *487*, 385-389.

Blevins, M.B., Smith, A.M., Phillips, E.M., and Powers, M.A. (2003). Complex formation among the RNA export proteins Nup98, Rae1/Gle2, and TAP. Journal of Biological Chemistry *278*, 20979-20988.

Brenner, S. (1974). The genetics of Caenorhabditis elegans. Genetics *77*, 71-94.

Briegel, A., Li, X., Bilwes, A.M., Hughes, K.T., Jensen, G.J., and Crane, B.R. (2012). Bacterial chemoreceptor arrays are hexagonally packed trimers of receptor dimers networked by rings of kinase and coupling proteins. Proceedings of the National Academy of Sciences of the United States of America *109*, 3766-3771.
Briggs, J.A. (2013). Structural biology in situ-the potential of subtomogram averaging. Current opinion in structural biology *23*, 261-267.
Brilot, A.F., Chen, J.Z., Cheng, A.C., Pan, J.H., Harrison, S.C., Potter, C.S., Carragher, B., Henderson, R., and Grigorieff, N. (2012). Beam-induced motion of vitrified specimen on holey carbon film. Journal of structural biology *177*, 630-637.
Brohawn, S.G., and Schwartz, T.U. (2009). Molecular architecture of the Nup84-Nup145C-Sec13 edge element in the nuclear pore complex lattice. Nat Struct Mol Biol *16*, 1173-U1178.
Burke, B., and Stewart, C.L. (2013a). The nuclear lamins: flexibility in function. Nature reviews Molecular cell biology *14*, 13-24.
Burke, B., and Stewart, C.L. (2013b). The nuclear lamins: flexibility in function. Nature reviews Molecular cell biology *14*, 13-24.
Bushby, A.J., P'Ng K, M., Young, R.D., Pinali, C., Knupp, C., and Quantock, A.J. (2011). Imaging three-dimensional tissue architectures by focused ion beam scanning electron microscopy. Nature protocols *6*, 845-858.
Camozzi, D., Capanni, C., Cenni, V., Mattioli, E., Columbaro, M., Squarzoni, S., and Lattanzi, G. (2014). Diverse lamin-dependent mechanisms interact to control chromatin dynamics. Focus on laminopathies. Nucleus *5*, 427-440.
Castano-Diez, D., Kudryashev, M., Arheit, M., and Stahlberg, H. (2012). Dynamo: a flexible, user-friendly development tool for subtomogram averaging of cryo-EM data in high-performance computing environments. Journal of structural biology *178*, 139-151.
Castano-Diez, D., Scheffer, M., Al-Amoudi, A., and Frangakis, A.S. (2010). Alignator: A GPU powered software package for robust fiducial-less alignment of cryo tilt-series. Journal of structural biology *170*, 117-126.
Chen, Y., Pfeffer, S., Hrabe, T., Schuller, J.M., and Forster, F. (2013). Fast and accurate reference-free alignment of subtomograms. Journal of structural biology.
Clough, R.N., Moldovan, G., and Kirkland, A.I. (2014). Direct Detectors for Electron Microscopy. J Phys Conf Ser *522*.
Cronshaw, J.M., Krutchinsky, A.N., Zhang, W., Chait, B.T., and Matunis, M.J. (2002). Proteomic analysis of the mammalian nuclear pore complex. The Journal of cell biology *158*, 915-927.
Dahl, R., and Staehelin, L.A. (1989). High-pressure freezing for the preservation of biological structure: theory and practice. Journal of electron microscopy technique *13*, 165-174.
Dai, W., Fu, C., Khant, H.A., Ludtke, S.J., Schmid, M.F., and Chiu, W. (2014). Zernike phase-contrast electron cryotomography applied to marine cyanobacteria infected with cyanophages. Nature protocols *9*, 2630-2642.
Danev, R., Buijsse, B., Khoshouei, M., Plitzko, J.M., and Baumeister, W. (2014). Volta potential phase plate for in-focus phase contrast transmission electron microscopy. Proceedings of the National Academy of Sciences of the United States of America *111*, 15635-15640.
Danev, R., Glaeser, R.M., and Nagayama, K. (2009). Practical factors affecting the performance of a thin-film phase plate for transmission electron microscopy. Ultramicroscopy *109*, 312-325.
Danev, R., Kanamaru, S., Marko, M., and Nagayama, K. (2010). Zernike phase contrast cryo-electron tomography. Journal of structural biology *171*, 174-181.
Danev, R., and Nagayama, K. (2008). Single particle analysis based on Zernike phase contrast transmission electron microscopy. Journal of structural biology *161*, 211-218.

Danev, R., and Nagayama, K. (2010). Phase plates for transmission electron microscopy. Methods in enzymology *481*, 343-369.
Danev, R., and Nagayama, K. (2011). Optimizing the phase shift and the cut-on periodicity of phase plates for TEM. Ultramicroscopy *111*, 1305-1315.
Dierksen, K., Typke, D., Hegerl, R., and Baumeister, W. (1993). Towards Automatic Electron Tomography .2. Implementation of Autofocus and Low-Dose Procedures. Ultramicroscopy *49*, 109-120.
Dobro, M.J., Melanson, L.A., Jensen, G.J., and McDowall, A.W. (2010). Plunge freezing for electron cryomicroscopy. Methods in enzymology *481*, 63-82.
Dobro, M.J., Samson, R.Y., Yu, Z., McCullough, J., Ding, H.J., Chong, P.L., Bell, S.D., and Jensen, G.J. (2013). Electron cryotomography of ESCRT assemblies and dividing Sulfolobus cells suggest spiraling filaments are involved in membrane scission. Mol Biol Cell.
Dubochet, J., Adrian, M., Chang, J.J., Homo, J.C., Lepault, J., McDowall, A.W., and Schultz, P. (1988). Cryo-electron microscopy of vitrified specimens. Quarterly reviews of biophysics *21*, 129-228.
Dubochet, J., and Mcdowall, A.W. (1981). Vitrification of Pure Water for Electron-Microscopy. J Microsc-Oxford *124*, Rp3-Rp4.
Dubochet, J., and Sartori Blanc, N. (2001). The cell in absence of aggregation artifacts. Micron *32*, 91-99.
Dubrovsky, A., Sorrentino, S., Harapin, J., Sapra, K.T., and Medalia, O. (2015). Developments in cryo-electron tomography for in situ structural analysis. Archives of biochemistry and biophysics *581*, 78-85.
Eibauer, M., Hoffmann, C., Plitzko, J.M., Baumeister, W., Nickell, S., and Engelhardt, H. (2012). Unraveling the structure of membrane proteins in situ by transfer function corrected cryo-electron tomography. Journal of structural biology *180*, 488-496.
Eibauer, M., Pellanda, M., Turgay, Y., Dubrovsky, A., Wild, A., and Medalia, O. (2015). Structure and gating of the nuclear pore complex. Nature communications *6*.
Elad, N., Maimon, T., Frenkiel-Krispin, D., Lim, R.Y., and Medalia, O. (2009). Structural analysis of the nuclear pore complex by integrated approaches. Current opinion in structural biology *19*, 226-232.
Engel, B.D., Schaffer, M., Cuellar, L.K., Villa, E., Plitzko, J.M., and Baumeister, W. (2015). Native architecture of the Chlamydomonas chloroplast revealed by in situ cryo-electron tomography. eLife *4*.
Estroff, L.A., Leiserowitz, L., Addadi, L., Weiner, S., and Hamilton, A.D. (2003). Characterization of an organic hydrogel: A cryo-transmission electron microscopy and X-ray diffraction study. Adv Mater *15*, 38-+.
Faruqi, A.R., and Henderson, R. (2007). Electronic detectors for electron microscopy. Current opinion in structural biology *17*, 549-555.
Fernandez, J.J., Li, S., and Crowther, R.A. (2006). CTF determination and correction in electron cryotomography. Ultramicroscopy *106*, 587-596.
Forster, F., Medalia, O., Zauberman, N., Baumeister, W., and Fass, D. (2005). Retrovirus envelope protein complex structure in situ studied by cryo-electron tomography. Proceedings of the National Academy of Sciences of the United States of America *102*, 4729-4734.
Frangakis, A.S., Bohm, J., Forster, F., Nickell, S., Nicastro, D., Typke, D., Hegerl, R., and Baumeister, W. (2002). Identification of macromolecular complexes in cryoelectron tomograms of phantom cells. Proceedings of the National Academy of Sciences of the United States of America *99*, 14153-14158.

Frangakis, A.S., and Forster, F. (2004). Computational exploration of structural information from cryo-electron tomograms. Current opinion in structural biology *14*, 325-331.
Frank, J. (1992). Electron tomography : three-dimensional imaging with the transmission electron microscope (New York: Plenum Press).
Frank, J. (2006). Three-Dimensional Electron Microscopy of Macromolecular Assemblies: Visualization of Biological Molecules in Their Native State, 2nd edn (Oxford University Press).
Frenkiel-Krispin, D., Maco, B., Aebi, U., and Medalia, O. (2010). Structural analysis of a metazoan nuclear pore complex reveals a fused concentric ring architecture. Journal of molecular biology *395*, 578-586.
Frey, S., and Gorlich, D. (2007). A saturated FG-repeat hydrogel can reproduce the permeability properties of nuclear pore complexes. Cell *130*, 512-523.
Frey, S., Richter, R.P., and Goerlich, D. (2006). FG-rich repeats of nuclear pore proteins form a three-dimensional meshwork with hydrogel-like properties. Science *314*, 815-817.
Fridman, K., Mader, A., Zwerger, M., Elia, N., and Medalia, O. (2012). Advances in tomography: probing the molecular architecture of cells. Nature reviews Molecular cell biology *13*, 736-742.
Frosst, P., Guan, T., Subauste, C., Hahn, K., and Gerace, L. (2002). Tpr is localized within the nuclear basket of the pore complex and has a role in nuclear protein export. Journal of Cell Biology *156*, 617-630.
Fukuda, Y., Fukazawa, Y., Danev, R., Shigemoto, R., and Nagayama, K. (2009). Tuning of the Zernike phase-plate for visualization of detailed ultrastructure in complex biological specimens. Journal of structural biology *168*, 476-484.
Fukuda, Y., and Nagayama, K. (2012). Zernike phase contrast cryo-electron tomography of whole mounted frozen cells. Journal of structural biology *177*, 484-489.
Gan, L., and Jensen, G.J. (2012). Electron tomography of cells. Quarterly reviews of biophysics *45*, 27-56.
Giannuzzi, L.A. (2005). Introduction to Focused Ion Beams: Instrumentation, Theory, Techniques and Practice (Springer).
Giannuzzi, L.A., and Stevie, F.A. (2005). Introduction to focused ion beams : instrumentation, theory, techniques, and practice (New York: Springer).
Gilkey, J.C., and Staehelin, L.A. (1986). Advances in Ultra-Rapid Freezing for the Preservation of Cellular Ultrastructure. J Electron Micr Tech *3*, 177-210.
Griffis, E.R., Xu, S.L., and Powers, M.A. (2003). Nup98 localizes to both nuclear and cytoplasmic sides of the nuclear pore and binds to two distinct nucleoporin subcomplexes. Mol Biol Cell *14*, 600-610.
Grimm, R., Typke, D., Barmann, M., and Baumeister, W. (1996). Determination of the inelastic mean free path in ice by examination of tilted vesicles and automated most probable loss imaging. Ultramicroscopy *63*, 169-179.
Grossman, E., Dahan, I., Stick, R., Goldberg, M.W., Gruenbaum, Y., and Medalia, O. (2012a). Filaments assembly of ectopically expressed Caenorhabditis elegans lamin within Xenopus oocytes. Journal of structural biology *177*, 113-118.
Grossman, E., Medalia, O., and Zwerger, M. (2012b). Functional architecture of the nuclear pore complex. Annu Rev Biophys *41*, 557-584.
Grunewald, K., Medalia, O., Gross, A., Steven, A.C., and Baumeister, W. (2003). Prospects of electron cryotomography to visualize macromolecular complexes inside cellular compartments: implications of crowding. Biophys Chem *100*, 577-591.
Gruska, M., Medalia, O., Baumeister, W., and Leis, A. (2008). Electron tomography of vitreous sections from cultured mammalian cells. Journal of structural biology *161*, 384-392.

Harapin, J., Eibauer, M., and Medalia, O. (2013). Structural analysis of supramolecular assemblies by cryo-electron tomography. Structure *21*, 1522-1530.
Harris, J.R. (2015). Transmission electron microscopy in molecular structural biology: A historical survey. Archives of biochemistry and biophysics *581*, 3-18.
Heymann, J.A., Hayles, M., Gestmann, I., Giannuzzi, L.A., Lich, B., and Subramaniam, S. (2006). Site-specific 3D imaging of cells and tissues with a dual beam microscope. Journal of structural biology *155*, 63-73.
Hiramatsu, H., and Osterloh, F.E. (2004). A simple large-scale synthesis of nearly monodisperse gold and silver nanoparticles with adjustable sizes and with exchangeable surfactants. Chem Mater *16*, 2509-2511.
Ho, C.Y., and Lammerding, J. (2012). Lamins at a glance. Journal of cell science *125*, 2087-2093.
Hoelz, A., Debler, E.W., and Blobel, G. (2011). The Structure of the Nuclear Pore Complex. Annual Review of Biochemistry, Vol 80 *80*, 613-643.
Horowitz, R.A., Koster, A.J., Walz, J., and Woodcock, C.L. (1997). Automated electron microscope tomography of frozen-hydrated chromatin: the irregular three-dimensional zigzag architecture persists in compact, isolated fibers. Journal of structural biology *120*, 353-362.
Hrabe, T., Chen, Y., Pfeffer, S., Cuellar, L.K., Mangold, A.V., and Forster, F. (2012). PyTom: a python-based toolbox for localization of macromolecules in cryo-electron tomograms and subtomogram analysis. Journal of structural biology *178*, 177-188.
Hsieh, C., Schmelzer, T., Kishchenko, G., Wagenknecht, T., and Marko, M. (2014). Practical workflow for cryo focused-ion-beam milling of tissues and cells for cryo-TEM tomography. Journal of structural biology *185*, 32-41.
Hunziker, E.B., Herrmann, W., Schenk, R.K., Mueller, M., and Moor, H. (1984). Cartilage ultrastructure after high pressure freezing, freeze substitution, and low temperature embedding. I. Chondrocyte ultrastructure--implications for the theories of mineralization and vascular invasion. The Journal of cell biology *98*, 267-276.
Iancu, C.V., Wright, E.R., Benjamin, J., Tivol, W.F., Dias, D.P., Murphy, G.E., Morrison, R.C., Heymann, J.B., and Jensen, G.J. (2005). A "flip-flop" rotation stage for routine dual-axis electron cryotomography. Journal of structural biology *151*, 288-297.
Iovine, M.K., Murphy, R., Watkins, J., and Wente, S.R. (1995). Essential Function of the Glfg Region of Nup116 in Nuclear Transport. Mol Biol Cell *6*, 1155-1155.
Iwamoto, M., Koujin, T., Osakada, H., Mori, C., Kojidani, T., Matsuda, A., Asakawa, H., Hiraoka, Y., and Haraguchi, T. (2015). Biased assembly of the nuclear pore complex is required for somatic and germline nuclear differentiation in Tetrahymena. Journal of cell science *128*, 1812-1823.
Jin, L., Milazzo, A.C., Kleinfelder, S., Li, S.D., Leblanc, P., Duttweiler, F., Bouwer, J.C., Peltier, S.T., Ellisman, M.H., and Xuong, N.H. (2008). Applications of direct detection device in transmission electron microscopy. Journal of structural biology *161*, 352-358.
Kipreos, E.T. (2005). C. elegans cell cycles: invariance and stem cell divisions. Nature reviews Molecular cell biology *6*, 766-776.
Koreth, J., and van den Heuvel, S. (2005). Cell-cycle control in Caenorhabditis elegans: how the worm moves from G1 to S. Oncogene *24*, 2756-2764.
Kose, S., Furuta, M., and Imamoto, N. (2012). Hikeshi, a nuclear import carrier for Hsp70s, protects cells from heat shock-induced nuclear damage. Cell *149*, 578-589.
Kreshuk, A., Straehle, C.N., Sommer, C., Koethe, U., Cantoni, M., Knott, G., and Hamprecht, F.A. (2011). Automated detection and segmentation of synaptic contacts in nearly isotropic serial electron microscopy images. PLoS One *6*, e24899.

Kurner, J., Frangakis, A.S., and Baumeister, W. (2005). Cryo-electron tomography reveals the cytoskeletal structure of Spiroplasma melliferum. Science *307*, 436-438.
Kutay, U., Izaurralde, E., Bischoff, F.R., Mattaj, I.W., and Gorlich, D. (1997). Dominant-negative mutants of importin-beta block multiple pathways of import and export through the nuclear pore complex. Embo Journal *16*, 1153-1163.
Li, X.M., Mooney, P., Zheng, S., Booth, C.R., Braunfeld, M.B., Gubbens, S., Agard, D.A., and Cheng, Y.F. (2013). Electron counting and beam-induced motion correction enable near-atomic-resolution single-particle cryo-EM. Nature methods *10*, 584-+.
Lieber, A., Leis, A., Kushmaro, A., Minsky, A., and Medalia, O. (2009). Chromatin organization and radio resistance in the bacterium Gemmata obscuriglobus. Journal of bacteriology *191*, 1439-1445.
Lucic, V., Forster, F., and Baumeister, W. (2005). Structural studies by electron tomography: from cells to molecules. Annu Rev Biochem *74*, 833-865.
Lucic, V., Leis, A., and Baumeister, W. (2008). Cryo-electron tomography of cells: connecting structure and function. Histochemistry and cell biology *130*, 185-196.
Lucic, V., Rigort, A., and Baumeister, W. (2013). Cryo-electron tomography: the challenge of doing structural biology in situ. The Journal of cell biology *202*, 407-419.
Luyet, B.J., and Gehenio, M.P. (1940). Life and death at low temperatures (Normandy, Mo.,: Biodynamica).
Mahamid, J., Pfeffer, S., Schaffer, M., Villa, E., Danev, R., Cuellar, L.K., Forster, F., Hyman, A.A., Plitzko, J.M., and Baumeister, W. (2016). Visualizing the molecular sociology at the HeLa cell nuclear periphery. Science *351*, 969-972.
Maimon, T., Elad, N., Dahan, I., and Medalia, O. (2012). The human nuclear pore complex as revealed by cryo-electron tomography. Structure *20*, 998-1006.
Marko, M., Hsieh, C., Moberlychan, W., Mannella, C.A., and Frank, J. (2006). Focused ion beam milling of vitreous water: prospects for an alternative to cryo-ultramicrotomy of frozen-hydrated biological samples. Journal of microscopy *222*, 42-47.
Marko, M., Hsieh, C., Schalek, R., Frank, J., and Mannella, C. (2007). Focused-ion-beam thinning of frozen-hydrated biological specimens for cryo-electron microscopy. Nature methods *4*, 215-217.
Mastronarde, D.N. (1997). Dual-axis tomography: an approach with alignment methods that preserve resolution. Journal of structural biology *120*, 343-352.
Mattout, A., Pike, B.L., Towbin, B.D., Bank, E.M., Gonzalez-Sandoval, A., Stadler, M.B., Meister, P., Gruenbaum, Y., and Gasser, S.M. (2011). An EDMD mutation in C. elegans lamin blocks muscle-specific gene relocation and compromises muscle integrity. Current biology : CB *21*, 1603-1614.
McMullan, G., Faruqi, A.R., Clare, D., and Henderson, R. (2014). Comparison of optimal performance at 300 keV of three direct electron detectors for use in low dose electron microscopy. Ultramicroscopy *147*, 156-163.
Meyerson, J.R., White, T.A., Bliss, D., Moran, A., Bartesaghi, A., Borgnia, M.J., de la Cruz, M.J., Schauder, D., Hartnell, L.M., Nandwani, R*., et al.* (2011). Determination of molecular structures of HIV envelope glycoproteins using cryo-electron tomography and automated sub-tomogram averaging. Journal of visualized experiments : JoVE.
Milles, S., and Lemke, E.A. (2013). Nup153 in Nuclear Transport: Plasticity of Nucleoporin/Transport-Receptor Complexes. Biophys J *104*, 30a-30a.
MoberlyChan, W.J.S., R. (2007). Ion Beam Induced Surface Modulations from Nano to Pico: Optimizing Deposition During Erosion and Erosion During Deposition. MRS Proceedings *1059/2007*.

Mohr, D., Frey, S., Fischer, T., Guttler, T., and Gorlich, D. (2009). Characterisation of the passive permeability barrier of nuclear pore complexes. The EMBO journal *28*, 2541-2553.
Murata, K., Liu, X., Danev, R., Jakana, J., Schmid, M.F., King, J., Nagayama, K., and Chiu, W. (2010). Zernike phase contrast cryo-electron microscopy and tomography for structure determination at nanometer and subnanometer resolutions. Structure *18*, 903-912.
Nagayama, K., and Danev, R. (2009). Phase-plate electron microscopy: a novel imaging tool to reveal close-to-life nano-structures. Biophysical reviews *1*, 37-42.
Ori, A., Banterle, N., Iskar, M., Andres-Pons, A., Escher, C., Khanh Bui, H., Sparks, L., Solis-Mezarino, V., Rinner, O., Bork, P*., et al.* (2013). Cell type-specific nuclear pores: a case in point for context-dependent stoichiometry of molecular machines. Mol Syst Biol *9*, 648.
Patel, S.S., Belmont, B.J., Sante, J.M., and Rexach, M.F. (2007). Natively unfolded nucleoporins gate protein diffusion across the nuclear pore complex. Cell *129*, 83-96.
Patla, I., Volberg, T., Elad, N., Hirschfeld-Warneken, V., Grashoff, C., Fassler, R., Spatz, J.P., Geiger, B., and Medalia, O. (2010). Dissecting the molecular architecture of integrin adhesion sites by cryo-electron tomography. Nature cell biology *12*, 909-915.
Perona, P., and Malik, J. (1990). Scale-Space and Edge-Detection Using Anisotropic Diffusion. Ieee T Pattern Anal *12*, 629-639.
Pfeffer, S., Woellhaf, M.W., Herrmann, J.M., and Forster, F. (2015). Organization of the mitochondrial translation machinery studied in situ by cryoelectron tomography. Nature communications *6*.
Philippsen, A., Engel, H.A., and Engel, A. (2007). The contrast-imaging function for tilted specimens. Ultramicroscopy *107*, 202-212.
Radu, A., Moore, M.S., and Blobel, G. (1995). The Peptide Repeat Domain of Nucleoporin Nup98 Functions as a Docking Site in Transport across the Nuclear-Pore Complex. Cell *81*, 215-222.
Ramachandra, R., Bouwer, J.C., Mackey, M.R., Bushong, E., Peltier, S.T., Xuong, N.H., and Ellisman, M.H. (2014). Improving Signal to Noise in Labeled Biological Specimens Using Energy-Filtered TEM of Sections with a Drift Correction Strategy and a Direct Detection Device. Microscopy and Microanalysis *20*, 706-714.
Rand, M.D., Kearney, A.L., Dao, J., and Clason, T. (2010). Permeabilization of Drosophila embryos for introduction of small molecules. Insect biochemistry and molecular biology *40*, 792-804.
Ribbeck, K., and Gorlich, D. (2001). Kinetic analysis of translocation through nuclear pore complexes. Embo Journal *20*, 1320-1330.
Ribbeck, K., Lipowsky, G., Kent, H.M., Stewart, M., and Gorlich, D. (1998). NTF2 mediates nuclear import of Ran. Embo Journal *17*, 6587-6598.
Richter, K., Nessling, M., and Lichter, P. (2007). Experimental evidence for the influence of molecular crowding on nuclear architecture. Journal of cell science *120*, 1673-1680.
Richter, K., Nessling, M., and Lichter, P. (2008). Macromolecular crowding and its potential impact on nuclear function. Biochimica et biophysica acta *1783*, 2100-2107.
Rigort, A., Bauerlein, F.J., Villa, E., Eibauer, M., Laugks, T., Baumeister, W., and Plitzko, J.M. (2012a). Focused ion beam micromachining of eukaryotic cells for cryoelectron tomography. Proceedings of the National Academy of Sciences of the United States of America *109*, 4449-4454.
Rigort, A., Bauerlein, F.J., Villa, E., Eibauer, M., Laugks, T., Baumeister, W., and Plitzko, J.M. (2012b). Focused ion beam micromachining of eukaryotic cells for cryoelectron tomography. Proceedings of the National Academy of Sciences of the United States of America *109*, 4449-4454.

Roberts, D.B. (2006). Drosophila melanogaster: the model organism. Entomol Exp Appl *121*, 93-103.
Rout, M.P., Aitchison, J.D., Suprapto, A., Hjertaas, K., Zhao, Y.M., and Chait, B.T. (2000). The yeast nuclear pore complex: Composition, architecture, and transport mechanism. Journal of Cell Biology *148*, 635-651.
Ruskin, R.S., Yu, Z.H., and Grigorieff, N. (2013). Quantitative characterization of electron detectors for transmission electron microscopy. Journal of structural biology *184*, 385-393.
Sambrook, J., Russell, D.W., and Sambrook, J. (2006). The condensed protocols from Molecular cloning : a laboratory manual (Cold Spring Harbor, N.Y.: Cold Spring Harbor Laboratory Press).
Scheres, S.H., Melero, R., Valle, M., and Carazo, J.M. (2009). Averaging of electron subtomograms and random conical tilt reconstructions through likelihood optimization. Structure *17*, 1563-1572.
Scheres, S.H.W. (2014). Beam-induced motion correction for sub-megadalton cryo-EM particles. eLife *3*.
Schmidt, H.B., and Gorlich, D. (2015). Nup98 FG domains from diverse species spontaneously phase-separate into particles with nuclear pore-like permselectivity. eLife *4*.
Schrader, N., Koerner, C., Koessmeier, K., Bangert, J.A., Wittinghofer, A., Stoll, R., and Vetter, I.R. (2008). The crystal structure of the Ran-Nup153ZnF2 complex: a general Ran docking site at the nuclear pore complex. Structure *16*, 1116-1125.
Sorzano, C.O., Messaoudi, C., Eibauer, M., Bilbao-Castro, J.R., Hegerl, R., Nickell, S., Marco, S., and Carazo, J.M. (2009). Marker-free image registration of electron tomography tilt-series. BMC Bioinformatics *10*, 124.
Stewart, M. (2006). Structural basis for the nuclear protein import cycle. Biochem Soc Trans *34*, 701-704.
Stolken, M., Beck, F., Haller, T., Hegerl, R., Gutsche, I., Carazo, J.M., Baumeister, W., Scheres, S.H., and Nickell, S. (2011). Maximum likelihood based classification of electron tomographic data. Journal of structural biology *173*, 77-85.
Strange, K., Christensen, M., and Morrison, R. (2007). Primary culture of Caenorhabditis elegans developing embryo cells for electrophysiological, cell biological and molecular studies. Nature protocols *2*, 1003-1012.
Strawn, L.A., Shen, T.X., Shulga, N., Goldfarb, D.S., and Wente, S.R. (2004). Minimal nuclear pore complexes define FG repeat domains essential for transport. Nature cell biology *6*, 197-206.
Suntharalingam, M., and Wente, S.R. (2003). Peering through the pore: nuclear pore complex structure, assembly, and function. Dev Cell *4*, 775-789.
Swulius, M.T., Chen, S., Jane Ding, H., Li, Z., Briegel, A., Pilhofer, M., Tocheva, E.I., Lybarger, S.R., Johnson, T.L., Sandkvist, M.*, et al.* (2011). Long helical filaments are not seen encircling cells in electron cryotomograms of rod-shaped bacteria. Biochem Biophys Res Commun *407*, 650-655.
Terry, L.J., and Wente, S.R. (2007). Nuclear mRNA export requires specific FG nucleoporins for translocation through the nuclear pore complex. Journal of Cell Biology *178*, 1121-1132.
Tokuyasu, K.T. (1973). A technique for ultracryotomy of cell suspensions and tissues. The Journal of cell biology *57*, 551-565.
van Heel, M., Gowen, B., Matadeen, R., Orlova, E.V., Finn, R., Pape, T., Cohen, D., Stark, H., Schmidt, R., Schatz, M.*, et al.* (2000). Single-particle electron cryo-microscopy: towards atomic resolution. Quarterly reviews of biophysics *33*, 307-369.
Villa, E., Schaffer, M., Plitzko, J.M., and Baumeister, W. (2014). Opening Windows into the Cell: Focused-Ion-Beam Milling for Cryo-Electron Tomography. Biophys J *106*, 600a-600a.

Walz, J., Typke, D., Nitsch, M., Koster, A.J., Hegerl, R., and Baumeister, W. (1997). Electron Tomography of Single Ice-Embedded Macromolecules: Three-Dimensional Alignment and Classification. Journal of structural biology *120*, 387-395.
Wang, K., Strunk, K., Zhao, G., Gray, J.L., and Zhang, P. (2012). 3D structure determination of native mammalian cells using cryo-FIB and cryo-electron tomography. Journal of structural biology *180*, 318-326.
Weickert, J. (1994). Anisotropic Diffusion Filters for Image-Processing Based Quality-Control. Eur Con Mat *9*, 355-362.
Williams, D.B., and Carter, C.B. (2008). Transmission electron microscopy : a textbook for materials science, 2nd edn (New York: Springer).
Winkler, H., Zhu, P., Liu, J., Ye, F., Roux, K.H., and Taylor, K.A. (2009). Tomographic subvolume alignment and subvolume classification applied to myosin V and SIV envelope spikes. Journal of structural biology *165*, 64-77.
Xu, M., Beck, M., and Alber, F. (2012). High-throughput subtomogram alignment and classification by Fourier space constrained fast volumetric matching. Journal of structural biology *178*, 152-164.
Yahav, T., Maimon, T., Grossman, E., Dahan, I., and Medalia, O. (2011). Cryo-electron tomography: gaining insight into cellular processes by structural approaches. Current opinion in structural biology *21*, 670-677.
Zanetti, G., Riches, J.D., Fuller, S.D., and Briggs, J.A. (2009). Contrast transfer function correction applied to cryo-electron tomography and sub-tomogram averaging. Journal of structural biology *168*, 305-312.
Zernike, F. (1942). Phase contrast, a new method for the microscopic observation of transparent objects Part II. Physica *9*, 974-986.
Zhu, J., Penczek, P.A., Schroder, R., and Frank, J. (1997). Three-dimensional reconstruction with contrast transfer function correction from energy-filtered cryoelectron micrographs: procedure and application to the 70S Escherichia coli ribosome. Journal of structural biology *118*, 197-219.

Structural analysis of multicellular organisms with cryo-electron tomography

Jan Harapin[1], Mandy Börmel[1,2], K Tanuj Sapra[1], Damian Brunner[2], Andres Kaech[3] & Ohad Medalia[1,4,5]

We developed a method for visualizing tissues from multicellular organisms using cryo-electron tomography. Our protocol involves vitrifying samples with high-pressure freezing, thinning them with cryo-FIB-SEM (focused-ion-beam scanning electron microscopy) and applying fiducial gold markers under cryogenic conditions to the lamellae post-milling. We applied this protocol to acquire tomograms of vitrified *Caenorhabditis elegans* embryos and worms, which showed the intracellular organization of selected tissues at particular developmental stages in otherwise intact specimens.

Cryo-electron tomography (CET) has become the method of choice for structural studies of cells, organelles and macromolecular complexes[1–4]. Vitrification is used to instantaneously arrest all biological processes in order to preserve samples in a frozen, hydrated, near-native state[5,6], thereby circumventing the unwanted side effects of chemical fixation[7]. However, CET is limited by the thickness of the specimen of interest. Cryo-FIB-SEM is a relatively new technique that incorporates sample vitrification and is an alternative to conventional sample-thinning methods. This technique produces thin lamellae of the regions of interest[8–11], which can then be imaged by CET. However, these lamellae are devoid of surface fiducial markers, which makes tomographic imaging and reconstruction challenging because of the inherently lower signal-to-noise ratio of images of specimens thicker than ~300 nm (ref. 12). Here we describe a protocol for high-pressure freezing (HPF) and cryo-FIB-SEM milling of multicellular specimens, addition of surface fiducial markers under cryogenic conditions post-milling and CET imaging (**Fig. 1e**).

We vitrified adult worms with HPF using 2-methylpentane because it is a liquid at −150 °C and can facilitate the disassembly of aluminum carriers without fracturing the specimens or dislodging them from the electron microscopy (EM) grids. Furthermore, 2-methylpentane could be sublimed within minutes at −150 °C and high vacuum, ensuring full exposure of the sample during milling (**Fig. 1b** and **Supplementary Fig. 1h**). This offers a substantial improvement over traditional cryoprotectants (for example, 1-hexadecene)[13], which make the sample indistinguishable from these chemicals after freezing (**Fig. 1a**).

In order to facilitate easy control over the milling procedure, we modified a Leica prototype cryo-holder such that the EM grids are attached at their rims (**Supplementary Fig. 1a–c**). This enabled us to spread samples over the entire surface of the grid and orient the grid in-plane with the FIB column, thereby increasing the overall throughput of the technique. Additionally, this makes it possible to remove the grid from the cryo-holder, add fiducial markers and insert it into any cryo-transmission electron microscope (cryo-TEM).

The shape of the milling object used for thinning worms and their embryos was a parallelogram (**Fig. 1f**) that left a 150° internal angle between the lamella and the nonmilled material (**Supplementary Fig. 1j**). This prevented the nonmilled sides from getting into the path of the beam and occluding the imaging area at high tilts during tilt-series acquisition.

Plunge-frozen *C. elegans* embryos (**Fig. 1c**) were semifinely milled above and below the region of interest with a 240-pA probe. This step was followed by a fine-milling step using a 50-pA probe. This resulted in ~330-nm-thick lamellae that were on average very flat and stable for imaging in a cryo-TEM (**Fig. 1d** and **Supplementary Fig. 1e**,**g**). Adult worms were rough milled with a 4-nA probe until the region of interest was reduced to ~5-µm-thick lamellae (**Supplementary Fig. 1h–j**).

High-current milling reduced the overall milling time; however, substantial amounts of heat were transferred to the sample. After the first round of milling, the quality of the vitrification could be assessed by checking for the presence of cracks in the sample (**Supplementary Fig. 1f**). Samples were then semifinely milled with a 240-pA probe to remove the heat-afflicted material. The amount of heat delivered by this probe was well tolerated by the sample, as there were no evident morphological distortions of the lamella such as changes in its shape from straight to bent (data not shown). The ~2-µm-thick lamellae from adult worms were finely milled using a 50-pA probe, and this resulted in ~660-nm-thick lamellae (**Supplementary Fig. 1i**). We thinned both embryos and worms to ~30-µm-wide lamellae (**Supplementary Fig. 1e**,**j**), covering the full diameter of the specimen. It took ~30 h to reduce an adult worm to a lamella, compared to the ~3 h it took per embryo. In our experience, 30-µm-wide lamellae are mechanically stable for further handling and processing.

[1]Department of Biochemistry, University of Zurich, Zurich, Switzerland. [2]Institute of Molecular Life Sciences, University of Zurich, Zurich, Switzerland. [3]Center for Microscopy and Image Analysis, University of Zurich, Zurich, Switzerland. [4]Department of Life Sciences in the Negev, Ben-Gurion University, Beer-Sheva, Israel. [5]National Institute for Biotechnology in the Negev, Ben-Gurion University, Beer-Sheva, Israel. Correspondence should be addressed to O.M. (omedalia@bioc.uzh.ch) or A.K. (andres.kaech@zmb.uzh.ch).

RECEIVED 10 SEPTEMBER 2014; ACCEPTED 16 MARCH 2015; PUBLISHED ONLINE 11 MAY 2015 ; DOI:10.1038/NMETH.3401

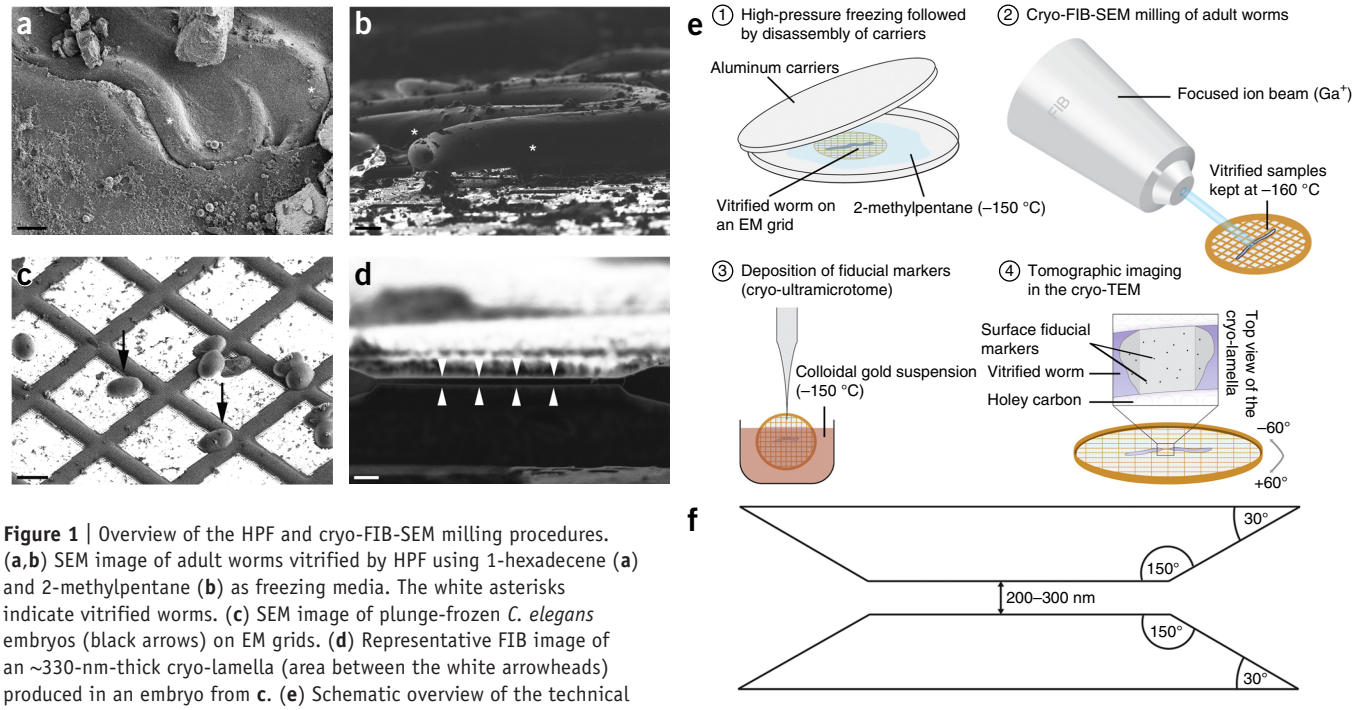

Figure 1 | Overview of the HPF and cryo-FIB-SEM milling procedures. (**a**,**b**) SEM image of adult worms vitrified by HPF using 1-hexadecene (**a**) and 2-methylpentane (**b**) as freezing media. The white asterisks indicate vitrified worms. (**c**) SEM image of plunge-frozen *C. elegans* embryos (black arrows) on EM grids. (**d**) Representative FIB image of an ~330-nm-thick cryo-lamella (area between the white arrowheads) produced in an embryo from **c**. (**e**) Schematic overview of the technical procedures for tomographic imaging of milled worms. (**f**) Drawing of the parallelogram shapes (i.e., milling objects) used for cryo-FIB-SEM thinning of embryos and worms above and below the region of interest. Scale bars, 40 µm (**a**–**c**) and 2 µm (**d**).

Owing to the nature of the cryo-FIB-SEM milling procedure, fiducial gold markers have to be added after milling to ensure spatial proximity between the sample and the markers. We synthesized 10-nm gold nanoparticles in 2-methylpentane and applied the nanoparticles to the surface of the lamellae (Online Methods). The distribution of gold markers along the surface of the grids and the lamella was even (**Fig. 2a**), enabling unhindered reconstructions of cellular interiors of both embryos and adult worms (**Fig. 2b**–**e** and **Supplementary Fig. 2c**–**e**, respectively). Furthermore, grids prepared using gold resuspended in 2-methylpentane were free of toluene and other surface contamination (**Supplementary Fig. 2b**); the gold particles that were resuspended in toluene were covered in ice contamination clusters and appeared clumped (**Supplementary Fig. 2a**).

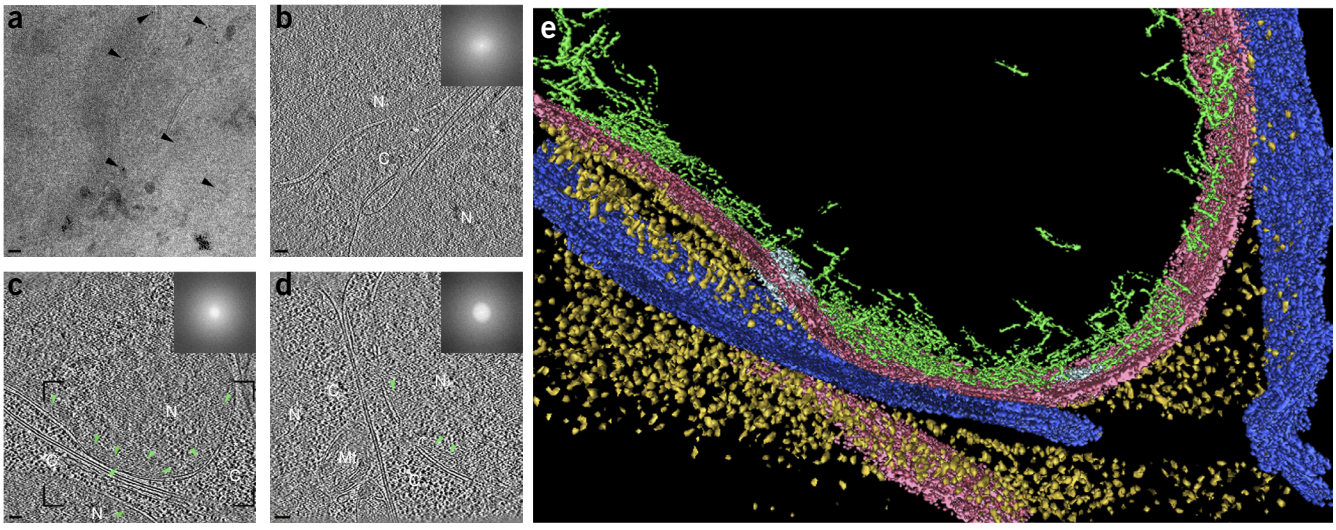

Figure 2 | CET of vitrified *C. elegans* embryos. (**a**) Cryo-TEM image of a 0°-tilt projection showing individual fiducial gold markers (arrowheads) on the lamellar surface. (**b**) 4-nm tomographic slice recorded on an embryo overexpressing the native ce-lamin, at a defocus value of –6 µm. The final resolution was determined from the first zero of the contrast transfer function (CTF) and calculated to be 3.4 nm. (**c**,**d**) Tomographic slices (4 nm and 3.4 nm, respectively) acquired on embryos overexpressing the native ce-lamin (green arrowheads), with a defocus value of –16 µm. The final resolution was determined from the first zero of the CTF and calculated to be 5.6 nm for both tomograms. The power spectra for tomograms **b**–**d** were generated using the 0°-tilt projection images and are shown as insets. N, nucleus; C, cytoplasm; Mt, mitochondrion; asterisks indicate nuclear pore complexes. (**e**) Surface rendered view, generated using Amira 5.4.2, corresponding to the black-framed area in **c**. Dark blue, plasma membrane; pink, nuclear membrane; gold, ribosomes; light blue, nuclear pore complexes; green, filamentous structures adjacent to the inner nuclear membrane. Scale bars, 200 nm.

We acquired tomograms with a moderate to high defocus (−6 µm to −16 µm) and detected structures and macromolecular complexes typically found in a eukaryotic cell, including free and membrane-bound cytoplasmic ribosome assemblies, mitochondria and vesicles (**Fig. 2c–e**, **Supplementary Fig. 2c–e** and **Supplementary Videos 1** and **2**). We were particularly interested in visualizing the nuclear lamina, a filamentous protein layer underlying the nuclear envelope[14,15]. Purified and ectopically expressed *C. elegans* lamins (ce-lamins) had previously been visualized by cryo-electron microscopy[16,17]. However, the low resolution limited the structural analysis of the nuclei. Therefore, we applied our procedure to wild-type embryos that overexpressed GFP-labeled ce-lamin (**Supplementary Fig. 3**). As expected, ~6- to 8-nm-thick filamentous structures were detected at the nuclear periphery (**Fig. 2c** and **Supplementary Fig. 2c**). However, specific labeling approaches will be required to unambiguously identify these structures within the crowded nuclear environment. The cryo-FIB–milled adult worms were imaged on ~660-nm-thick lamellae at −16-µm defocus (**Supplementary Fig. 2c**,**e**). Despite the low signal-to-noise ratio, these data could be aligned using fiducial markers, revealing many of the same features as the tomograms acquired on thinner embryo lamellae (**Fig. 2b–d**).

Our method enables the visualization of >200-nm-thick, vitrified multicellular specimens by cryo-FIB-SEM milling and deposition of fiducial markers onto the sample before CET. We were able to align and reconstruct three-dimensional volumes of ~660-nm-thick lamellae, which would have been impossible without the use of high-contrast fiducials. The cryo-FIB-SEM approach has already offered glimpses into the organization macromolecular complexes within cells[9,11], and together with the improvements described here, it opens up the possibility of acquiring high-resolution information from the cellular interiors of intact tissues. We were able to show the retention of the fluorescent signal post-thinning in *C. elegans* embryos. This will eventually enable the identification and localization of proteins of interest with high precision and accuracy on the surface of the thin cryo-lamellae using various forms of the correlative light and electron microscopy approach. Structural approaches using three-dimensional imaging techniques have so far not been used to study *C. elegans* in a near-native state in detail despite it being a well-established model system[18]. We also demonstrate the possibility of carrying out cryo-FIB-SEM milling on embryos of *Drosophila melanogaster*, another extensively studied model organism (**Supplementary Fig. 4**). Cryo-FIB-SEM in conjunction with CET and averaging procedures can be used to describe the structure of macromolecular complexes *in situ* and at specific stages of development, which will provide more detailed insights into the cellular and macromolecular remodeling taking place within complex organisms.

METHODS

Methods and any associated references are available in the online version of the paper.

Note: Any Supplementary Information and Source Data files are available in the online version of the paper.

ACKNOWLEDGMENTS

We thank Y. Gruenbaum (The Hebrew University of Jerusalem) for providing us with the strains of *C. elegans* used in this study. This work was supported by a European Research Council (ERC) Starting Grant (243047 INCEL) and the Swiss National Science Foundation (SNSF 31003A_141083/1).

AUTHOR CONTRIBUTIONS

J.H., A.K., K.T.S., D.B. and O.M. designed the experiments and wrote the manuscript. J.H. and M.B. carried out the experiments.

COMPETING FINANCIAL INTERESTS

The authors declare no competing financial interests.

1. Fridman, K., Mader, A., Zwerger, M., Elia, N. & Medalia, O. *Nat. Rev. Mol. Cell Biol.* **13**, 736–742 (2012).
2. Yahav, T., Maimon, T., Grossman, E., Dahan, I. & Medalia, O. *Curr. Opin. Struct. Biol.* **21**, 670–677 (2011).
3. Gan, L. & Jensen, G.J. *Q. Rev. Biophys.* **45**, 27–56 (2012).
4. Lučič, V., Rigort, A. & Baumeister, W. *J. Cell Biol.* **202**, 407–419 (2013).
5. Dobro, M.J., Melanson, L.A., Jensen, G.J. & McDowall, A.W. *Methods Enzymol.* **481**, 63–82 (2010).
6. Dubochet, J. & Sartori Blanc, N. *Micron* **32**, 91–99 (2001).
7. Dubochet, J. *et al. Q. Rev. Biophys.* **21**, 129–228 (1988).
8. Marko, M., Hsieh, C., Schalek, R., Frank, J. & Mannella, C. *Nat. Methods* **4**, 215–217 (2007).
9. Rigort, A. *et al. Proc. Natl. Acad. Sci. USA* **109**, 4449–4454 (2012).
10. Wang, K., Strunk, K., Zhao, G., Gray, J.L. & Zhang, P. *J. Struct. Biol.* **180**, 318–326 (2012).
11. Hsieh, C., Schmelzer, T., Kishchenko, G., Wagenknecht, T. & Marko, M. *J. Struct. Biol.* **185**, 32–41 (2014).
12. Grimm, R., Typke, D., Barmann, M. & Baumeister, W. *Ultramicroscopy* **63**, 169–179 (1996).
13. Dahl, R. & Staehelin, L.A. *J. Electron Microsc. Tech.* **13**, 165–174 (1989).
14. Burke, B. & Stewart, C.L. *Nat. Rev. Mol. Cell Biol.* **14**, 13–24 (2013).
15. Ho, C.Y. & Lammerding, J. *J. Cell Sci.* **125**, 2087–2093 (2012).
16. Ben-Harush, K. *et al. J. Mol. Biol.* **386**, 1392–1402 (2009).
17. Grossman, E. *et al. J. Struct. Biol.* **177**, 113–118 (2012).
18. Kipreos, E.T. *Nat. Rev. Mol. Cell Biol.* **6**, 766–776 (2005).

ONLINE METHODS

Cryo-holder and shutter design. The prototype cryo-holder (**Supplementary Fig. 1a**) of the VCT100 cryo-transfer system (Leica Microsystem) was modified in order to accommodate standard EM grids (Quantifoil Micro tools GmbH) at a 30° preset angle with respect to the horizontal base line, which translates into a 6° angle between the sample and the FIB column in the Auriga cross-beam system (Carl Zeiss Microscopy GmbH). The attachment slit for EM grids is composed of two aluminum pieces. Opening and closing is regulated via a screw located on the top part: clockwise rotation to open and counter clockwise to close; the base is freely movable (**Supplementary Fig. 1b**). The shutter was redesigned as an aluminum box that completely envelops the cryo-holder and facilitates contamination-free specimen transfer from liquid nitrogen to high-vacuum conditions and back (**Supplementary Fig. 1c**). The shutter is always attached to the tip of the manipulator of the VCT100 cryo-transfer-shuttle (Leica Microsystems) via a Teflon ring. This allowed us to rotate the tip of VCT100 in order to attach or detach the entire cryo-holder from the cryo-stages inside the various devices used throughout this procedure (**Supplementary Fig. 1d**).

Plunge freezing of *C. elegans* embryos. Mixed populations of adult worms were synchronized by bleaching, and embryos were isolated on a large scale and collected in 1.5-mL Eppendorf tubes in M9 buffer[19]. Approximately 40 embryos were applied onto plasma-cleaned, holey carbon, copper grids (Quantifoil) in a 3-µL droplet using siliconized pipette tips and inspected under a binocular. Grids were then blotted 3–6 s (**Fig. 1c**), plunged into liquid ethane and stored.

High-pressure freezing (HPF) of adult worms. Adult worms were washed off plates with M9 buffer (either at a particular stage of development or as a mixed population), and a desired dilution was pipetted onto plasma-cleaned C-coated copper grids using siliconized pipette tips. An approximately 2-µL droplet of worm suspension was applied directly onto the center of the EM grid to prevent the worms from spreading toward the edges. Grids were then blotted on filter paper to remove the bulk of the liquid and air-dried briefly (up to max. 5 s). Grids were then quickly transferred into the 100-µm-deep cavity of an acetone-cleaned 6-mm aluminum carrier (Wohlwend Engineering), which was premoisturized with a small droplet of 2-methylpentane (Sigma). After the grid stuck to the carrier, the compartment was filled with 2-methylpentane using a Hamilton syringe until the sample was completely covered. A flat 6-mm aluminum carrier was quickly placed on top, causing the excess solution to drain into the surrounding filter paper. The sandwiched assembly was then quickly transferred into the middle plate setup at the loading station of the HPM100 high-pressure freezing machine (Leica Microsystems). Samples were frozen without using ethanol as synchronization fluid in order to avoid surface contamination. Aluminum carriers were inspected for pressure-induced deformation after the freezing process, and bent carriers were discarded. Straight carriers were transferred into the FC6 cryo-ultramicrotome chamber (Leica Microsystems) at −150 °C, causing 2-methylpentane to thaw (melting point is −160 °C), and taken apart after ~10 min. Grids were inspected under a binocular, and only those containing physically intact worms were retrieved with tweezers and stored in grid boxes in liquid nitrogen.

Preparation for cryo-FIB-SEM. Grids containing vitrified worms were attached to the slit of the modified cryo-holder at the cryo-station (Leica Microsystems). They were transferred with the VCT100 shuttle to the cryo-stage of the BAF060 freeze-fracturing device (Leica Microsystems) cooled to −150 °C. After ~15 min, 2-methylpentane completely sublimed under high-vacuum (approximately 10^{-7} mbar), leaving the surface of the EM grid free of any embedding material and the sample fully exposed. We applied a layer of carbon ~20 nm thick to the surface of the grids by electron beam evaporation in order to facilitate subsequent SEM imaging and cryo-FIB-SEM milling. Grids were then transferred with the VCT100 onto the cryo-stage of the Auriga cross-beam system, which was actively kept at −156 °C. Grids containing vitrified embryos were coated with 10 nm of carbon coat and transferred to the Auriga without further processing.

Platinum deposition and correlative light and electron microscopy. We deposited platinum ~3 µm thick around the embryos from a distance of 3 mm using the built-in gas injection system (GIS) of the Auriga cross-beam platform according to a previously described protocol for cold deposition[20]. The GIS temperature was set to 25 °C and the deposition time was 4–6 s, resulting in platinum thicknesses of 1–3 µm. The deposition process was driven by the thermal gradient between the deposition gas and the cold specimen surface and no beams are used to assist it.

After milling was completed, the EM grid carrying the vitrified embryos was quickly thawed in 4% PFA at room temperature and left in the fixative for 10 min. Bright-field and fluorescence images were acquired on a Leica fluorescence microscope (DMI 4000B, Leica) and overlaid.

Cryo-FIB-SEM milling. The Zeiss Auriga cross-beam system used in this study was aligned once per week and remained stable throughout the duration of the entire milling procedure. After the sample was inserted, the stage was brought to the desired position and left to settle for about 15 min, which eliminated drift-related imaging issues. Features of interest were from that point onward centered using the beam shift dials in between rounds of milling. We chose the lamella-type milling approach, which entailed a gradual reduction of total sample volume above and below the horizontal midplane.

Intact worms are up to 1 mm in length and 60 µm in diameter. Rough milling was performed in several rounds, starting with a 4-nA probe and continuing with a 240-pA probe to reduce the thickness around the area of interest in the middle plane of the worm. Once the thickness was ~2 µm, fine milling was performed at 50 pA, leaving an ~660-nm-thick lamella. In this case the milling depth of the Ga^+ beam was set to 8 µm owing to the huge diameter of the worm, and the whole procedure took ~30 h (milling was carried out in multiple steps that individually took 1–3 h, depending on the beam current strength and milling depth set). After milling was completed, the cryo-holder was retrieved from the Auriga and the grids were stored in grid boxes.

Embryos of *C. elegans* are approximately 40 µm × 20 µm in size, so rough milling was performed using a 240-pA probe, reducing the middle of the sample to a 2-µm thick lamella. Fine milling was performed using a 50-pA probe, leaving an ~330-nm-thick lamella. The Ga^+ beam was set to a milling depth of 3 µm, and the whole procedure took ~3 h per embryo.

doi:10.1038/nmeth.3401

The surfaces of the lamellae initially exhibited typical FIB-related artifacts post-milling. These included curtaining, some gallium-ion deposition at the edges of the lamellae and a slight increase in thickness of the area on the lamella where the beam exits the sample (due to defocusing). We found that curtaining as well as big variations in thickness can be circumvented by setting the milling depth of the beam to approximately twice what was actually needed. The beam penetration depth on the Auriga can be calibrated to suit different kinds of materials. We routinely used the calibration for silicon as a reference and found the milling depth for frozen biological material to be approximately ten times less than that needed for silicon (setting the milling depth to 1 µm resulted in actual milling depth of approximately 10 µm for embryos and worms).

Fiducial markers for the cryo-lamellae. We modified a toluene-based synthesis of suspensions of colloidal gold particles similarly to a previously described procedure[21]. A solution containing 50 mg of tetrachloroauric acid (Sigma) in 1.0 g (1.2 mL) of oleylamine (Acros Organics) and 1.0 mL of toluene was quickly injected into a solution containing 1.7 g (2.9 mL) of oleylamine in 49 mL of toluene at 110 °C. The reaction was carried out for 2 h at this temperature, after which the products were precipitated by the addition of 100 mL of methanol. Particles ~10 nm in diameter were isolated by centrifugation at 500*g*, methanol was decanted and the tubes were left to air-dry in order to evaporate residual methanol. Finally, the gold particles were resuspended in 1 mL in 2-methylpentane. Where needed, the gold particles were further diluted to a desired concentration with 2-methylpentane. Gold was applied to the lamellae in the cryo-ultramicrotome chamber at −150 °C, inside 0.5 mL wells of an aluminum box (produced by our in-house workshop) similarly to in a previously described procedure[22]. Grids were briefly immersed in the gold suspension (2–3 s), rinsed twice by immersion into liquid ethane in adjacent wells, blotted extensively (>20 s) with filter papers until no residual liquid could be observed on the tweezers or the grids, and stored in grid boxes. The quality of the gold-particle synthesis, as well as the particle distribution, was assessed on empty plunge-frozen grids in the cryo-TEM (**Supplementary Fig. 2a**,**b**)

Cryo-electron tomography (CET) and annotations. Specimens were analyzed in a 300-kV FEG FEI Polara transmission electron microscope equipped with a Gatan post-column GIF 2002 energy filter. Tilt series were acquired—covering either an angular range of −54° to +60° (**Fig. 2c** and **Supplementary Fig. 2a**,**b**) or, in specific cases, −40° to +40° owing to spatial constraints (**Fig. 2b**,**d**)—with 2° tilt increments and defocus values ranging from −6 µm to −16 µm, for both the embryos and worms. Primary magnifications of 41,000× and 50,000× were used, and this resulted in a 4.08-nm and 3.36-nm pixel size, respectively. Projection images (2,048 × 2,048 pixels) were aligned using 10-nm fiducial gold markers and reconstructed by means of a weighted back-projection algorithm, as implemented by the TOM toolbox software package[23]. The width of the energy slit used for tomographic imaging was 20 eV. Images were collected on a Gatan Ultrascan 4000 CCD camera. Resolutions of tomograms were estimated from the first zero crossing over the CTF and are indicated in the figure panel. Power spectra demonstrating the absence of crystalline ice were generated using the 0°-tilt projections of each of the respective tomograms (**Fig. 2b**–**d** and **Supplementary Fig. 2c**,**e**). We acquired 18 tomograms from *C. elegans* embryos and 5 from adult worms. Slices from representative tomograms were displayed in the figure panels. Three-dimensional rendering and annotating was carried out using the Amira 5.4.2 software (FEI).

19. Strange, K., Christensen, M. & Morrison, R. *Nat. Protoc.* **2**, 1003–1012 (2007).
20. Hayles, M.F., Stokes, D.J., Phifer, D. & Findlay, K.C. *J. Microsc.* **226**, 263–269 (2007).
21. Hiramatsu, H. & Osterloh, F.E. *Chem. Mater.* **16**, 2509–2511 (2004).
22. Gruska, M., Medalia, O., Baumeister, W. & Leis, A. *J. Struct. Biol.* **161**, 384–392 (2008).
23. Nickell, S. *et al. J. Struct. Biol.* **149**, 227–234 (2005).

doi:10.1038/nmeth.3401

Structure
Review

Structural Analysis of Supramolecular Assemblies by Cryo-Electron Tomography

Jan Harapin,[1] Matthias Eibauer,[1] and Ohad Medalia[1,2,*]
[1]Department of Biochemistry, University of Zurich, Winterthurerstrasse 190, 8057 Zurich, Switzerland
[2]Department of Life Sciences and the National Institute for Biotechnology in the Negev, Ben-Gurion University, Beer-Sheva, 84105 Israel
*Correspondence: omedalia@bioc.uzh.ch
http://dx.doi.org/10.1016/j.str.2013.08.003

Structural analysis of macromolecular assemblies in their physiological environment is a challenging task that is instrumental in answering fundamental questions in cellular and molecular structural biology. The continuous development of computational and analytical tools for cryo-electron tomography (cryo-ET) enables the study of these assemblies at a resolution of a few nanometers. Through the implementation of thinning procedures, cryo-ET can now be applied to the reconstruction of macromolecular structures located inside thick regions of vitrified cells and tissues, thus becoming a central tool for structural determinations in various biological disciplines. Here, we focus on the successful in situ applications of cryo-ET to reveal structures of macromolecular complexes within eukaryotic cells.

Macromolecular assemblies are central players in many cellular processes that influence the dynamic intracellular architecture of cells. For instance, cytoskeletal processes occur within fractions of a second, resulting in major remodeling of the cytoplasm and the overall cellular morphology (Diez et al., 2005). Various experimental tools for analyzing multicomponent macromolecular structures inside cells have been developed in order to advance the current understanding of functional interactions and dynamic properties of different cellular processes. More specifically, advances in imaging and image analysis techniques have enabled the structural analysis of macromolecular assemblies to reach resolutions on the previously unattainable nanometer scale, thus providing novel insights into the local and global organization of functional modules and cellular networks (Fridman et al., 2012; Lučić et al., 2008).

Cryo-electron tomography (cryo-ET) has a pivotal role in cellular biology (Al-Amoudi et al., 2007; Maimon et al., 2012; Patla et al., 2010), microbiology (Dobro et al., 2013; Kürner et al., 2005; Lieber et al., 2009; Swulius et al., 2011) and virology (Bharat et al., 2012; Meyerson et al., 2011). It can depict a particular cellular scene and provide a three-dimensional (3D) structural map of an unperturbed, vitrified sample, i.e., in a close-to-physiological state (Fridman et al., 2012; Lučić et al., 2005; Yahav et al., 2011). Preserving fine and delicate structural details in a close-to-life state are made possible by the use of rapid freezing, which thus circumvents the deleterious effects of chemical fixatives and dehydration on cellular ultrastructures (Adrian et al., 1984; Dubochet et al., 1988).

In this review, we will focus on the principles and implementation of cryo-ET in the field of cellular and molecular structural biology and discuss the recent technical advances in reconstructing 3D structures of macromolecular complexes within intact cells and organelles. The combination of cryo-ET and single-particle analysis approaches will be discussed in detail with special emphasis on their potential for increasing the final resolution of reconstructed images. Finally, we will discuss complementary sample preparation procedures that enable the application of cryo-ET to large cells and tissues. Although we focus on the application of these techniques to eukaryotic systems, cryo-ET has proven itself instrumental for reconstructing molecular structures in prokaryotes, yielding impressive results (Abrusci et al., 2013; Briegel et al., 2012; Schlimpert et al., 2012; Swulius et al., 2011).

Cryo-ET: Basic Principles

The true power of cryo-ET lies in its ability to directly observe macromolecular densities in situ due to phase contrast between the biological material and the surrounding vitrified ice, bypassing the use of fixatives as well as commonly used contrasting agents such as heavy metal salts (Medalia et al., 2002). Thus, the initial step in preparing biological samples for cryo-ET is vitrification, which is typically performed by plunging into liquid-nitrogen-cooled liquid ethane or high-pressure freezing (HPF) to ensure full hydration and ultrastructure preservation.

During the process of tomographic acquisition, vitrified samples of suitable thickness (<1 μm) are rotated around a defined tilt axis in discrete increments inside the transmission electron microscope (TEM), covering a maximal range of 140°, between −70° and +70° (Frank, 1992). A series of two-dimensional projections, i.e., a "tilt-series," is collected under "low electron dose" conditions (typically <100 $e^{-}/Å^{2}$) to prevent radiation damage to the sample (Dierksen et al., 1992, 1993). The tilt-series is subsequently aligned to a common frame using fiducial markers, i.e., colloidal gold of 10-15 nm in diameter (Amat et al., 2008), or using cross-correlation-based strategies (Castaño-Díez et al., 2010; Sorzano et al., 2009). The aligned tilt-series is then used to reconstruct the 3D volume of the specimen, namely, a tomogram (Frank, 1992). Although the most commonly used algorithm for tomographic reconstruction is the weighted back projection (Radermacher, 1988), alternative algorithms, such as algebraic reconstruction technique (ART) (Gordon et al., 1970) and simultaneous iterative reconstruction technique (SIRT) (Gilbert, 1972), are also in use.

The quality of the final tomogram is directly dependent on the angular increments and the number of recorded two-dimensional images (Horowitz et al., 1997). However, the inherent

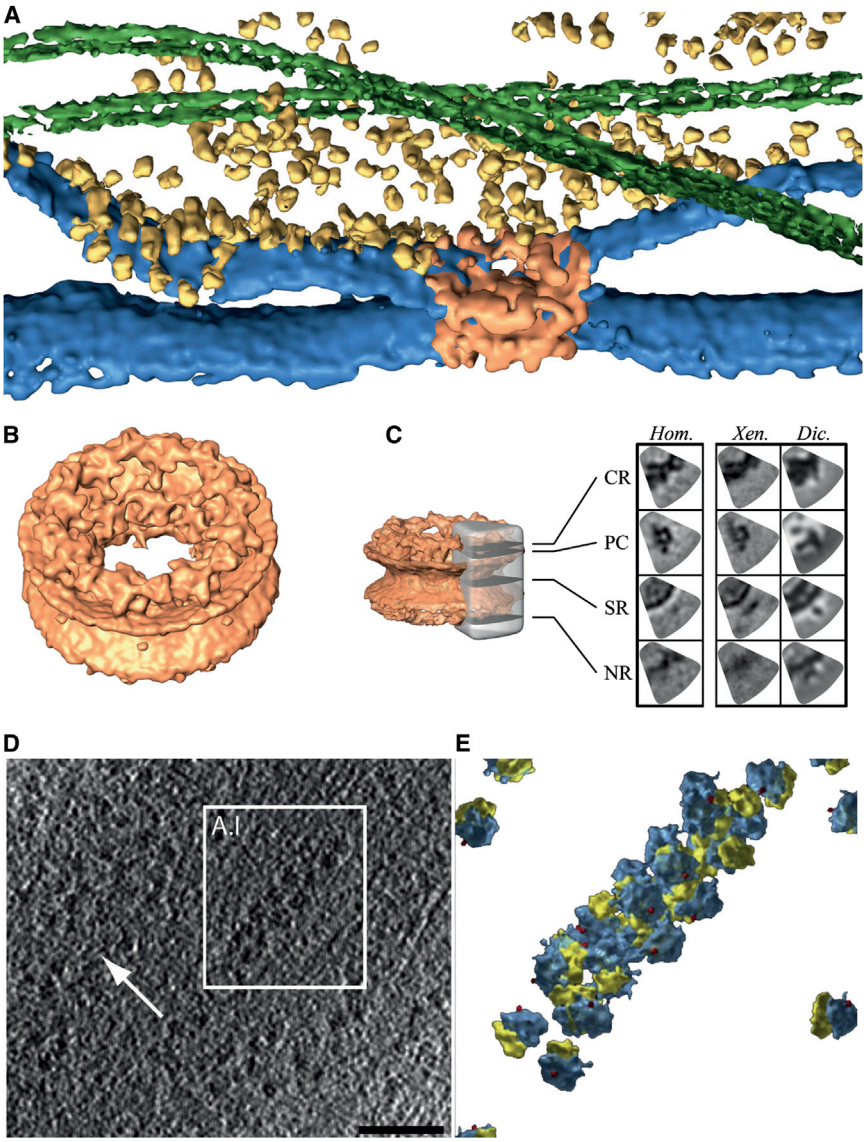

Figure 1. In Situ Subtomogram Averaging
(A) A surface-rendered view of a tomographic reconstruction showing the interior of a U2OS cell. Nuclear membranes (blue), NPCs (orange), microtubules (green) and ribosomes (yellow).
(B) The structure of the *Homo sapiens* NPC as derived by subtomogram averaging.
(C) Comparison of the cytoplasmic ring (CR), the peripheral channel (PC), the spoke ring (SR) and the nuclear ring (NR) in NPC protomer slices of *H. sapiens*, *X. laevis*, and *D. discoideum*.
(D) Tomographic slice showing polysomes from intact human cells (white box labeled with A.I indicates the area used for 3D visualization; white arrow indicates local accumulations of monosomes).
(E) 3D model of the polysome from box A.I. Figures 1A–1C reprinted from Maimon et al. (2012). Figures 1D and 1E reprinted with permission from Brandt et al. (2009).

lack of coverage in the high-tilt range (i.e., above −70° and +70°) produces an area of missing information termed ''missing wedge'' because of its appearance in Fourier space, leading to feature elongation and reduced resolution in the direction of the electron beam (Frank, 1992). The missing information can be reduced by acquiring a second tilt-series orthogonal to the first one, e.g., dual-axis tilting (Mastronarde, 1997), thus reducing the missing wedge to <10%. However, aligning the two perpendicular sets of projections remains a challenging task (Iancu et al., 2005).

Reconstructing the Structures of Macromolecular Complexes In Situ

A major advantage of cellular cryo-ET is that intracellular structures and protein complexes, e.g., the actin cytoskeleton, nuclear lamina, nuclear pore complexes (NPCs), and ribosomes, can be imaged in their native context, i.e., within an intact cell (Figures 1D, 2A, 4B, and 4C), and subsequently analyzed by specialized image processing methods (Frangakis and Förster, 2004).

Cellular tomograms containing macromolecular assemblies in multiple copies can be further processed by subtomogram averaging (Bartesaghi and Subramaniam, 2009; Briggs, 2013). The basic goal of this in silico procedure is to combine subtomograms (subvolumes of tomograms) that contain repeating structures, in order to produce a subtomogram average (final structure) with an enhanced resolution and signal-to-noise ratio (SNR) compared to the initial tomograms. The application of subtomogram averaging relies on the successful identification of a complex, structural homogeneity of a complex in the cellular environment, and occurrence of a complex in many different orientations.

In order to generate a subtomogram average with isotropic resolution, as first described by Förster et al. (2005), the missing wedge in the tomographic data has to be filled by orienting and subsequently averaging a sufficiently large number of different views of the macromolecular complex being investigated (Figure 3). The subtomograms are aligned with respect to a common reference, where the rotational part of the alignment is performed by an exhaustive search over a set of equally distributed Euler angles (Stölken et al., 2011). Thereby, the reference is rotated and convoluted with the experimentally realized missing wedge prior to a cross-correlation comparison with the subvolumes. These steps are performed successively for all desired angles. Subsequently, the maximum cross-correlation value indicates the orientation that maximizes the similarity between a subtomogram and the reference (Frangakis et al., 2002), whereas the translation between the volumes is given by the position of the cross-correlation peak (Frank, 2006). In this way a unique rotation and translation can be assigned to each subtomogram.

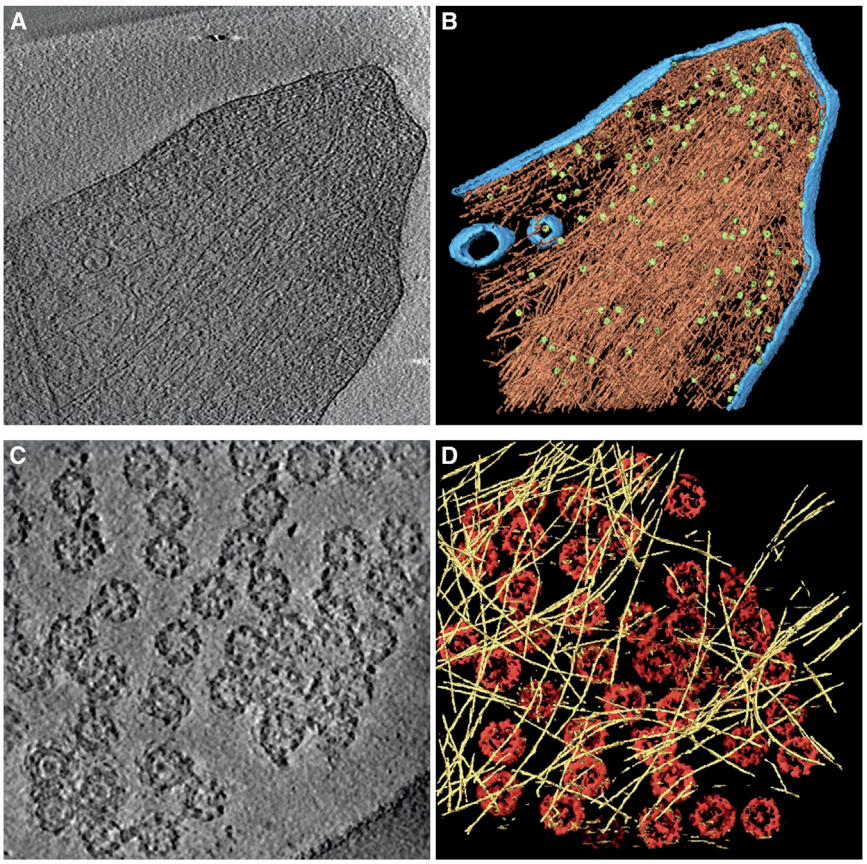

Figure 2. Cryo-ET of Cytoskeletal Elements
(A and B) A 10 nm tomographic slice through a focal adhesion site (A) and a corresponding rendered view of the cellular volume (B). Membranes (blue), actin (red) and adhesion-related particles (green).
(C and D) A 10 nm tomographic slice through a spread nuclear membrane of *X. laevis* ectopically expressing ce-lamins (C) and a corresponding rendered view of the tomographic volume (D). Lamin filaments (yellow), NPCs (red). Figures 2A and 2B reprinted from Patla et al. (2010); Figures 2C and 2D reprinted from Grossman et al. (2012b).

Next, the subtomograms are transformed according to the found parameters, and the aligned stack of volumes is averaged and serves as the reference for the next step. This iterative procedure is performed until the structure no longer changes with subsequent iterations. Finally, the iteratively refined transformations are used to generate the final subtomogram average (Walz et al., 1997). Obviously, the inverse of the calculated rotations describe the original orientations of the macromolecular complexes in the cellular environment. This information can be useful for unveiling the spatial relationship between macromolecules in a physiological assembly such as polysomes (Brandt et al., 2009, 2010) (Figures 1D and 1E). Because of a high value of defocus used in cellular cryo-ET, typically in the range of −6 to −15 μm, the maximal resolution of a subtomogram average is around 3–5 nm. In order to extend the information beyond the first destructive electron interference, a contrast transfer function (CTF) correction can be applied to the projection images, as it is routinely used in single-particle analysis electron microscopy (van Heel et al., 2000). Here, the resulting CTF-corrected tomograms serve as input data for subtomogram averaging.

Two major challenges in applying the CTF correction to tomographic data sets should be resolved. First, the effective value of defocus cannot be accurately determined in an image of thick cells, because of the low electron-dose used to obtain each individual projection. Second, the effective value of defocus varies throughout the entire projection, because of the tilting of the sample (Philippsen et al., 2007). In order to tackle these challenges, an approach called strip-based periodogram averaging was developed by Fernández et al. (2006). The problem of defocus determination can be solved by dividing a projection into subimages with constant values of defocus. These are located parallel to the tilt axis when the tilt-series is eucentric and no major jumps in the beam direction occur. Depending on the tilt angle, the target region for the extraction of the subimages has to be adjusted with a precision threshold. For example, one can use the entire 0° projection image because it has a constant value of defocus over the entire field of view. In contrast, only a small region parallel to the tilt axis of the projections acquired at the highest tilt angles can be used for strip-based periodogram averaging. Once all subimages with constant defocus from a tilt-series have been extracted, they can be averaged. The power spectrum of this periodogram average (Fernandez et al., 1997) has an improved SNR and the Thon rings become more clearly visible. The average defocus value of the tilt-series can now be determined from the periodogram average, using standard methods (Mindell and Grigorieff, 2003). Subsequently, the average defocus value can be used to calculate the defocus value of each pixel in the projections using geometrical parameters of the tilt-series (tilt angle and tilt axis orientation). Finally, the CTF gradient arising from the tilting of the sample can be corrected locally (Winkler et al., 2003).

Other approaches were recently developed that use advanced schemes to determine the effective value of defocus in a tilt-series and to perform proper CTF correction (Eibauer et al., 2012; Xiong et al., 2009; Zanetti et al., 2009). The CTF correction in combination with subtomogram averaging will allow the reconstruction of images of macromolecular complexes in situ, reaching resolutions close to 1 nm in the future.

In recent years additional algorithms were developed in order to tackle the challenge of subtomogram averaging, mainly in order to accelerate the angular part of the search. Examples include approaches that employ spherical harmonics for angular assignments (Bartesaghi et al., 2008; Chen et al., 2013; Xu et al., 2012) and maximum likelihood-based methods (Scheres et al., 2009; Stölken et al., 2011), as well as integrated open-source

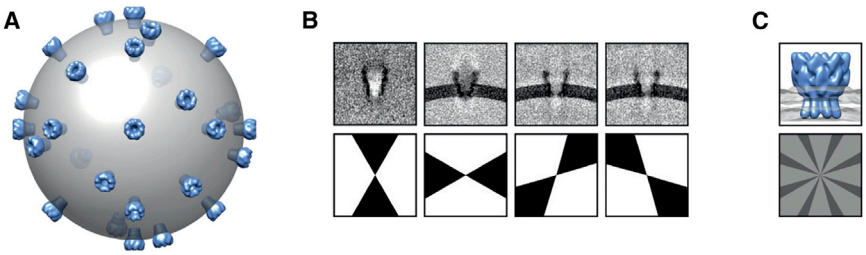

Figure 3. Principles of Subtomogram Averaging

(A–C) A cryo-ET analysis yields a 3D-reconstructed volume (A) (shown schematically). A stack of ***N*** subtomograms of a macromolecular assembly in different orientations is extracted from the cryo-tomograms. These subtomograms have a very low SNR (B, upper panel), and the protein complex is elongated in direction of the electron beam because of the missing wedge, which has the same orientation for all subtomograms. The subtomograms are aligned with respect to a common reference by an exhaustive angular search. The missing wedges of the aligned particles indicate which regions in Fourier space are sampled in the related subtomogram (B, lower panel). Finally, the aligned subtomogram stack is averaged, which improves the SNR by a factor of $\sqrt{N}$ (C, upper panel). Furthermore, the resolution is isotropic, because missing regions in Fourier space are filled (C, lower panel). Figure modified from Eibauer et al. (2012).

software packages for subtomogram averaging that will surely make the procedure more accessible to a wide audience (Castaño-Díez et al., 2012; Hrabe et al., 2012).

The Structure of the NPC as Resolved by Subtomogram Averaging

A successful application of subtomogram averaging, applied to tomograms from intact human cells, is the structural analysis of the NPC (Maimon et al., 2012). NPCs are composed of ~30 different proteins termed nucleoporins (Nups), which are arranged as multimers containing multiple copies (Alber et al., 2007; Cronshaw et al., 2002; Ori et al., 2013; Terry et al., 2007). The architecture of the NPC is largely conserved between lower and higher eukaryotes (Figure 1C), comprising a pseudo-8-fold symmetric central framework termed the spoke complex, a central pore of about 50 nm in diameter, and filamentous structures on the cytoplasmic and nuclear sides of the complex (Elad et al., 2009). On the nuclear face, the NPC is found in close interaction with the nuclear lamina, a meshwork of filamentous protein structures and other associated proteins (Burke and Stewart, 2013).

This humongous macromolecular assembly of over 120 MDa fuses the outer nuclear membrane and the inner nuclear membrane to form aqueous translocation channels. The NPC allows passive diffusion of small molecules and receptor-dependent translocation of large proteins and ribonucleoproteins (Adams and Wente, 2013; Grossman et al., 2012a). Macromolecular cargo usually harbors a specific nuclear localization signal (NLS) or nuclear export signal (NES) that are recognized by transport receptors, mediating cargo passage through the NPC. Receptors referred to as karyopherins chaperone cargo during transport across the NPC by means of hydrophobic interactions with phenylalanine-glycine-rich nucleoporin repeat domains (FG-repeats) (Stewart, 2006; Suntharalingam and Wente, 2003).

Over the last decade, cryo-ET has become a major tool for reconstructing the structure of the NPC by using intact nuclei and nuclear envelopes (NE) with minimal purification steps (Beck et al., 2004; Stoffler et al., 2003). However, variability within the complex and deviations from its 8-fold symmetrical structure limited the resolution to ~8.5 nm. Introducing symmetry-independent averaging procedures allowed computational compensation for the deviations of individual NPC protomers from their putative positions in an 8-fold rotational symmetric structure in both *Dictyostelium discoideum* and *Xenopus laevis* (Beck et al., 2007; Frenkiel-Krispin et al., 2010).

Recently, we have deployed a similar approach to reconstructing the human NPC, using intact cells (Maimon et al., 2012). Tomograms were acquired at thin nuclear regions within cells, ~700 nm, followed by subtomogram averaging analysis that used the symmetry-independent averaging approach (Beck et al., 2007). The result was a detailed structure of the human NPC at a resolution of 6.4 nm. NPCs from three different species were reconstructed using the very same approach at similar resolutions (Figure 1C). All three structures converged to a pseudo-8-fold rotational symmetric architecture with similar values for the outer diameter (~105 nm) and the central channel (~50 nm). However, they exhibited substantial structural differences in the cytoplasmic ring and the peripheral channels, especially between the NPCs of higher and lower eukaryotes (Figure 1C). The structure of the spoke ring shows overall structural similarity between the NPCs of *X. laevis* and *D. discoideum*. Furthermore, the density of the NPCs in the nuclear envelope differs widely across these species rising up to 50 NPCs/μm^2 in *X. laevis* and is significantly less in human cells (Maimon et al., 2012). A more detailed structure that allows for the fine interpretation of the spatial organization and protein composition of the NPCs will surely arise in the future. The combined approach of cryo-ET and 3D averaging over a data set sufficiently large, acquired on a thinner sample, should allow for a final resolution of ~2 nm and make possible the reliable fitting of individual Nup crystal structures into the final tomographic reconstruction.

Cellular Processes

Cryo-ET has been successfully applied to the study of cytoskeleton-based processes (Ben-Harush et al., 2010), allowing for a detailed description of cellular events, such as adhesion (Patla et al., 2010), virus infection (Ibiricu et al., 2013), endocytosis (Swulius et al., 2011), and cytokinesis (Elad et al., 2011). The exact architecture of the actin filaments and the macromolecular assembly of adhesion sites could not be seen using conventional electron microscopy sample preparation methods (Medalia and Geiger, 2010). The architecture of focal adhesions was described in great detail, clearly showing that the actin cytoskeleton is not directly connected to the membrane domain of the adhesion site, namely, the integrin (Figures 2A and 2B). Another example is the elucidation of the intricate organizational properties of the *Caenorhabditis elegans* lamin filaments assembled in *X. laevis* oocytes that show the wild-type filaments to be almost half the previously reported diameter (Grossman et al., 2012b) (Figure 2D).

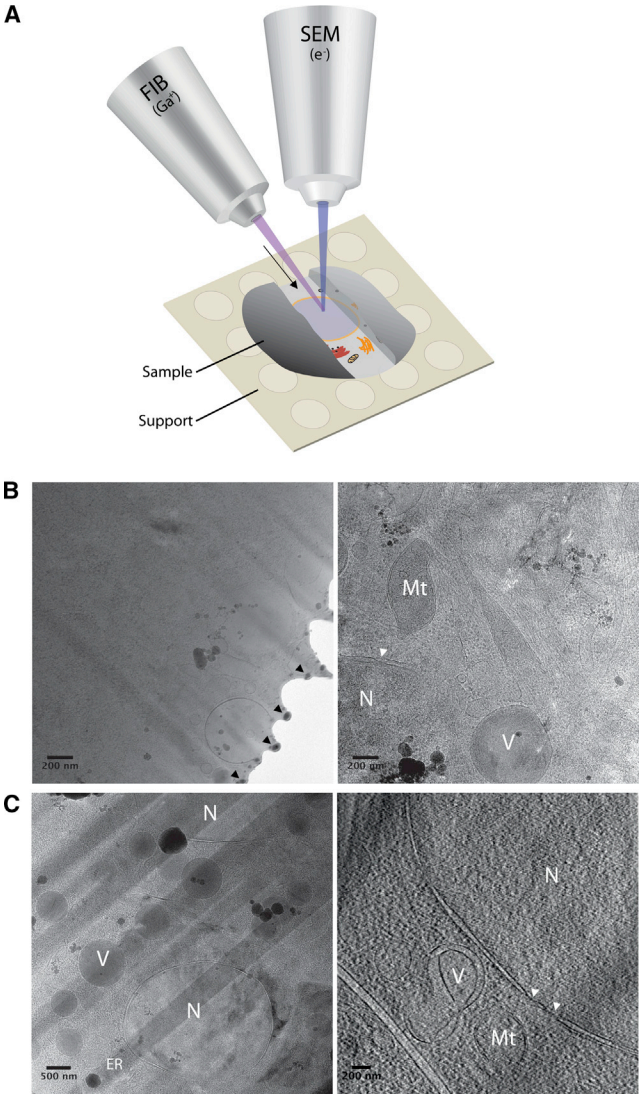

Figure 4. Focused Ion Beam Milling of Vitrified Eukaryotic Samples
(A) Schematic illustration of FIB milling of cells and the production of thin lamellas for subsequent cryo-ET analysis.
(B) Cryo-EM image of a 250 nm thick vitreous lamella produced by FIB milling of a U2Os cell (left) and a higher magnification TEM image indicating crowded cytoplasm.
(C) The application of cryo-FIB to a multicellular specimen is exemplified by imaging the 300 nm thick lamella produced in an early *C. elegans* embryo (left), and a 4 nm slice through a tomographic reconstruction of such a sample. N, nucleus; Mt, mitochondria; V, vesicles; ER, endoplasmatic reticulum; white arrowheads, Ga^+ ion deposits at the edges of the lamella; black arrows indicate, NPCs; black arrow, direction of FIB milling.

Cryo-ET has several fundamental limitations that warrant the use of additional methods in order to produce high-quality tomograms in which molecular complexes can be identified and localized. These issues arise mainly from limited resolution, low SNR, and a limited field of view (only covers 3–4 μm^2 of a cell) and can be overcome, for example, by a correlative light and electron microscopy approach (Lučić et al., 2008) (Fridman et al., 2012). In such a way, one can localize specific molecules with fluorescence-based microscopy and subsequently acquire cryo-tomograms to reveal the cellular ultrastructure at these sites (Jun et al., 2011; Patla et al., 2010; Swulius et al., 2011).

Another example of such limitations is the specimen thickness. Samples exceeding 1 μm in thickness can barely be studied in toto and require preprocessing, such as cryo-sectioning, before tomographic analysis. Several laboratories have devoted substantial efforts to establishing robust thinning procedures (Al-Amoudi et al., 2007; Bokstad et al., 2012; Marko et al., 2006). Cryo-electron microscopy of vitrified sections (CEMOVIS) was successfully applied to reconstructing 3D images of both prokaryotic and eukaryotic cells, as well as some tissues (Al-Amoudi et al., 2003, 2004, 2005, 2007; Hsieh et al., 2002; Pierson et al., 2011). However, the production of thick cryo-sections (300–500 nm) remains a challenging task, and the sections are riddled with sectioning-associated artifacts, such as physical compressions, knife marks, and other distortions. These perturbations are readily observed in the tomographic reconstructions and are keeping this approach from widespread use. In order to be able to apply cryo-ET to thick specimens, such as whole cells and tissues, one must be able to produce a vitrified area of suitable thickness (<500 nm). Thus, the need arose for a robust solution to conventional sample thinning procedures.

Focused Ion Beam Milling for Cryo-ET of Cells and Tissues

Focused ion beam (FIB) technology has already been routinely applied in the field of material sciences in order to manipulate sample thickness and gain insight into so far inaccessible interiors of complex materials (MoberlyChan and Schalek, 2007). In biology, this technique offers a broad range of applications for sequential imaging of plastic embedded samples at room temperature, allowing full-range structural reconstructions (Bennett et al., 2009; Bushby et al., 2011; Heymann et al., 2006). It provides highly resolved views on membranes, up to 5 nm (Kreshuk et al., 2011). However, a 3D structure of macromolecular complexes cannot be reconstructed in great detail because of fixation, dehydration, staining with heavy metal salts, and embedding of the specimen into resins (Bushby et al., 2011).

The application of FIB technology to biological samples under cryogenic conditions is an emerging technology for the production of thin, vitrified specimens for cryo-ET analysis (Marko et al., 2006, 2007; Rigort et al., 2012; Wang et al., 2012). Biological material applied to EM grids can be vitrified by plunge-freezing or high-pressure freezing (HPF) and directly transferred to the cryo-FIB without further processing or use of chemical fixatives and stains. The sample is then thinned by a Ga^+ ion beam at a velocity sufficiently high to overcome the surface binding energies of the sample, consequentially ejecting atoms and leaving a thinned surface (Giannuzzi, 2005). Thus, lamellas of various thicknesses, suitable for cryo-tomography, can be readily produced (Figure 4A). Finally, the EM grid is transferred into the transmission electron microscope for tomographic analysis. High-quality tomograms of biological samples (Rigort et al., 2012), regardless of the original cellular thickness, can be acquired, opening up a plethora of directions for studying the structural and functional organization of both cells and tissues, e.g., human cells and embryos of *C. elegans* (Figures 4B and 4C, respectively). The quality of these tomograms makes possible the application of subtomogram averaging techniques

(Rigort et al., 2012) to the reconstruction of macromolecular complexes in tissues within reach.

Several considerations have to be taken into account throughout the procedure. In order to avoid devitrification and surface contamination of the thinned area, the sample needs to be kept under high-vacuum and cryogenic conditions, as well as be physically shielded with a shutter during the transfer between the different devices used in this kind of a setup. Furthermore, the duration of the milling and the intensity of the ion beam should be kept at a minimum in order to ensure minimal heat transfer to the sample (Marko et al., 2007). The milling of biological samples is performed relatively fast (compared with plastic embedded samples) and at ''grazing'' angles. Thus, the effects of SEM imaging, used primarily for finding regions of interest, and the implantation of Ga+ ions can be considered negligible (Rigort et al., 2010). The straightforward control over the milling process, the possibility of choosing from a wide variety of acceleration voltages and doses of the FIB column, and the design of a milling strategy, depending on the topology of the vitrified biological sample, will ensure the widespread use of this procedure in the near future.

Future Perspectives

Cryo-ET is a pivotal tool for studying cellular architecture and macromolecules in their native environment. In conjunction with subtomogram averaging, it can describe the structural architecture of macromolecular complexes in situ. Extending the application of this method and developing novel image processing algorithms will surely provide an optimal interface for determining cellular structures and following biological processes at high resolution. Sample preparation techniques, such as the cryo-FIB, will eventually make the study of developmental processes from a structural perspective possible. Macromolecular complexes could then be reconstructed at specific stages of development. This will give exciting insight into the macromolecular remodeling within complex organisms.

The achievable resolution in cryo-tomography is hampered by the large sample thickness and the low SNR, resulting in a restricted resolution range (2–4 nm) compared to single-particle analysis reconstructions (Lučić et al., 2005). Thus, hardware developments and improvements in electron microscopy accessories will eventually make increasing the resolution and the SNR of cellular tomograms possible. In particular, introducing direct-electron detectors will allow the acquisition of higher quality data (McMullan et al., 2009). This will have profound effects on the sample integrity because higher quality data will decrease the amount of electrons required to obtain a given resolution, thus ensuring less irradiation of the sample. Data collection routines will be further optimized, leading to the acquisition of larger data sets from which critical parameters, such as defocus, can be reliably determined. Within such a body of data, striking the right balance of dose, focus, and geometry for the problem being addressed will become less demanding. More powerful and increasingly user-friendly software for tomographic reconstruction and subtomogram averaging is continuously being developed, making data analysis a routine task (Castaño-Díez et al., 2012; Chen et al., 2013; Hrabe et al., 2012; Meyerson et al., 2011).

A major challenge, at the current resolution of cellular tomograms, remains the identification of individual constituents within macromolecular complexes. This can be overcome by developing new labeling techniques that would enable the identification of specific molecules by cryo-ET. Several approaches have been described that use genetically encoded tags, such as metallothionein (Mercogliano and DeRosier, 2006; Nishino et al., 2007), ''miniSOG'' (Shu et al., 2011), and APEX (Martell et al., 2012). However, these approaches are not yet suitable for close-to-life cryo-ET of cells and tissues. Thus, there is a fundamental need for the design of a GFP analog for electron microscopy that would provide a general solution for the in situ identification of complexes whose structure is not yet determined or which intimately interact to form large assemblies. The development of novel labeling approaches, the improved resolution of cryo-electron microscopy, and the ability to reconstruct 3D volumes of tissues and cells in a hydrated state are likely to revolutionize cellular and molecular structural biology and our understanding of basic processes in biology.

ACKNOWLEDGMENTS

We thank Dr. Monika Zwerger and Dr. Tanuj K. Sapra for their critical reading of our manuscript. This work was supported by a European Research Council Starting Grant (243047 INCEL) and a Swiss National Science Foundation Grant (SNSF 31003A_141083/1).

REFERENCES

Abrusci, P., Vergara-Irigaray, M., Johnson, S., Beeby, M.D., Hendrixson, D.R., Roversi, P., Friede, M.E., Deane, J.E., Jensen, G.J., Tang, C.M., and Lea, S.M. (2013). Architecture of the major component of the type III secretion system export apparatus. Nat. Struct. Mol. Biol. *20*, 99–104.

Adams, R.L., and Wente, S.R. (2013). Uncovering nuclear pore complexity with innovation. Cell *152*, 1218–1221.

Adrian, M., Dubochet, J., Lepault, J., and McDowall, A.W. (1984). Cryo-electron microscopy of viruses. Nature *308*, 32–36.

Al-Amoudi, A., Dubochet, J., Gnaegi, H., Lüthi, W., and Studer, D. (2003). An oscillating cryo-knife reduces cutting-induced deformation of vitreous ultrathin sections. J. Microsc. *212*, 26–33.

Al-Amoudi, A., Chang, J.J., Leforestier, A., McDowall, A., Salamin, L.M., Norlén, L.P., Richter, K., Blanc, N.S., Studer, D., and Dubochet, J. (2004). Cryo-electron microscopy of vitreous sections. EMBO J. *23*, 3583–3588.

Al-Amoudi, A., Studer, D., and Dubochet, J. (2005). Cutting artefacts and cutting process in vitreous sections for cryo-electron microscopy. J. Struct. Biol. *150*, 109–121.

Al-Amoudi, A., Díez, D.C., Betts, M.J., and Frangakis, A.S. (2007). The molecular architecture of cadherins in native epidermal desmosomes. Nature *450*, 832–837.

Alber, F., Dokudovskaya, S., Veenhoff, L.M., Zhang, W., Kipper, J., Devos, D., Suprapto, A., Karni-Schmidt, O., Williams, R., Chait, B.T., et al. (2007). The molecular architecture of the nuclear pore complex. Nature *450*, 695–701.

Amat, F., Moussavi, F., Comolli, L.R., Elidan, G., Downing, K.H., and Horowitz, M. (2008). Markov random field based automatic image alignment for electron tomography. J. Struct. Biol. *161*, 260–275.

Bartesaghi, A., and Subramaniam, S. (2009). Membrane protein structure determination using cryo-electron tomography and 3D image averaging. Curr. Opin. Struct. Biol. *19*, 402–407.

Bartesaghi, A., Sprechmann, P., Liu, J., Randall, G., Sapiro, G., and Subramaniam, S. (2008). Classification and 3D averaging with missing wedge correction in biological electron tomography. J. Struct. Biol. *162*, 436–450.

Beck, M., Förster, F., Ecke, M., Plitzko, J.M., Melchior, F., Gerisch, G., Baumeister, W., and Medalia, O. (2004). Nuclear pore complex structure and dynamics revealed by cryoelectron tomography. Science *306*, 1387–1390.

Beck, M., Lucić, V., Förster, F., Baumeister, W., and Medalia, O. (2007). Snapshots of nuclear pore complexes in action captured by cryo-electron tomography. Nature *449*, 611–615.

Ben-Harush, K., Maimon, T., Patla, I., Villa, E., and Medalia, O. (2010). Visualizing cellular processes at the molecular level by cryo-electron tomography. J. Cell Sci. *123*, 7–12.

Bennett, A.E., Narayan, K., Shi, D., Hartnell, L.M., Gousset, K., He, H., Lowekamp, B.C., Yoo, T.S., Bliss, D., Freed, E.O., and Subramaniam, S. (2009). Ion-abrasion scanning electron microscopy reveals surface-connected tubular conduits in HIV-infected macrophages. PLoS Pathog. *5*, e1000591.

Bharat, T.A., Davey, N.E., Ulbrich, P., Riches, J.D., de Marco, A., Rumlova, M., Sachse, C., Ruml, T., and Briggs, J.A. (2012). Structure of the immature retroviral capsid at 8 Å resolution by cryo-electron microscopy. Nature *487*, 385–389.

Bokstad, M., Sabanay, H., Dahan, I., Geiger, B., and Medalia, O. (2012). Reconstructing adhesion structures in tissues by cryo-electron tomography of vitrified frozen sections. J. Struct. Biol. *178*, 76–83.

Brandt, F., Etchells, S.A., Ortiz, J.O., Elcock, A.H., Hartl, F.U., and Baumeister, W. (2009). The native 3D organization of bacterial polysomes. Cell *136*, 261–271.

Brandt, F., Carlson, L.A., Hartl, F.U., Baumeister, W., and Grünewald, K. (2010). The three-dimensional organization of polyribosomes in intact human cells. Mol. Cell *39*, 560–569.

Briegel, A., Li, X., Bilwes, A.M., Hughes, K.T., Jensen, G.J., and Crane, B.R. (2012). Bacterial chemoreceptor arrays are hexagonally packed trimers of receptor dimers networked by rings of kinase and coupling proteins. Proc. Natl. Acad. Sci. USA *109*, 3766–3771.

Briggs, J.A. (2013). Structural biology in situ—the potential of subtomogram averaging. Curr. Opin. Struct. Biol. *23*, 261–267.

Burke, B., and Stewart, C.L. (2013). The nuclear lamins: flexibility in function. Nat. Rev. Mol. Cell Biol. *14*, 13–24.

Bushby, A.J., P'ng, K.M., Young, R.D., Pinali, C., Knupp, C., and Quantock, A.J. (2011). Imaging three-dimensional tissue architectures by focused ion beam scanning electron microscopy. Nat. Protoc. *6*, 845–858.

Castaño-Díez, D., Scheffer, M., Al-Amoudi, A., and Frangakis, A.S. (2010). Alignator: a GPU powered software package for robust fiducial-less alignment of cryo tilt-series. J. Struct. Biol. *170*, 117–126.

Castaño-Díez, D., Kudryashev, M., Arheit, M., and Stahlberg, H. (2012). Dynamo: a flexible, user-friendly development tool for subtomogram averaging of cryo-EM data in high-performance computing environments. J. Struct. Biol. *178*, 139–151.

Chen, Y., Pfeffer, S., Hrabe, T., Schuller, J.M., and Förster, F. (2013). Fast and accurate reference-free alignment of subtomograms. J. Struct. Biol. *182*, 235–245.

Cronshaw, J.M., Krutchinsky, A.N., Zhang, W., Chait, B.T., and Matunis, M.J. (2002). Proteomic analysis of the mammalian nuclear pore complex. J. Cell Biol. *158*, 915–927.

Dierksen, K., Typke, D., Hegerl, R., Koster, A.J., and Baumeister, W. (1992). Towards automatic electron tomography. Ultramicroscopy *40*, 71–87.

Dierksen, K., Typke, D., Hegerl, R., and Baumeister, W. (1993). Towards automatic electron tomography II. Implementation of autofocus and low-dose procedures. Ultramicroscopy *49*, 109–120.

Diez, S., Gerisch, G., Anderson, K., Müller-Taubenberger, A., and Bretschneider, T. (2005). Subsecond reorganization of the actin network in cell motility and chemotaxis. Proc. Natl. Acad. Sci. USA *102*, 7601–7606.

Dobro, M.J., Samson, R.Y., Yu, Z., McCullough, J., Ding, H.J., Chong, P.L., Bell, S.D., and Jensen, G.J. (2013). Electron cryotomography of ESCRT assemblies and dividing Sulfolobus cells suggests that spiraling filaments are involved in membrane scission. Mol. Biol. Cell *24*, 2319–2327.

Dubochet, J., Adrian, M., Chang, J.J., Homo, J.C., Lepault, J., McDowall, A.W., and Schultz, P. (1988). Cryo-electron microscopy of vitrified specimens. Q. Rev. Biophys. *21*, 129–228.

Eibauer, M., Hoffmann, C., Plitzko, J.M., Baumeister, W., Nickell, S., and Engelhardt, H. (2012). Unraveling the structure of membrane proteins in situ by transfer function corrected cryo-electron tomography. J. Struct. Biol. *180*, 488–496.

Elad, N., Maimon, T., Frenkiel-Krispin, D., Lim, R.Y., and Medalia, O. (2009). Structural analysis of the nuclear pore complex by integrated approaches. Curr. Opin. Struct. Biol. *19*, 226–232.

Elad, N., Abramovitch, S., Sabanay, H., and Medalia, O. (2011). Microtubule organization in the final stages of cytokinesis as revealed by cryo-electron tomography. J. Cell Sci. *124*, 207–215.

Fernandez, J.J., Sanjurjo, J.R., and Carazo, J.M. (1997). A spectral estimation approach to contrast transfer function detection in electron microscopy. Ultramicroscopy *68*, 267–295.

Fernández, J.J., Li, S., and Crowther, R.A. (2006). CTF determination and correction in electron cryotomography. Ultramicroscopy *106*, 587–596.

Förster, F., Medalia, O., Zauberman, N., Baumeister, W., and Fass, D. (2005). Retrovirus envelope protein complex structure in situ studied by cryo-electron tomography. Proc. Natl. Acad. Sci. USA *102*, 4729–4734.

Frangakis, A.S., Böhm, J., Förster, F., Nickell, S., Nicastro, D., Typke, D., Hegerl, R., and Baumeister, W. (2002). Identification of macromolecular complexes in cryoelectron tomograms of phantom cells. Proc. Natl. Acad. Sci. USA *99*, 14153–14158.

Frangakis, A.S., and Förster, F. (2004). Computational exploration of structural information from cryo-electron tomograms. Curr. Opin. Struct. Biol. *14*, 325–331.

Frank, J. (1992). Electron Tomography: Three-Dimensional Imaging with the Transmission Electron Microscope (New York: Plenum Press).

Frank, J. (2006). Three-Dimensional Electron Microscopy of Macromolecular Assemblies: Visualization of Biological Molecules in Their Native State, Second Edition (Oxford: Oxford University Press).

Frenkiel-Krispin, D., Maco, B., Aebi, U., and Medalia, O. (2010). Structural analysis of a metazoan nuclear pore complex reveals a fused concentric ring architecture. J. Mol. Biol. *395*, 578–586.

Fridman, K., Mader, A., Zwerger, M., Elia, N., and Medalia, O. (2012). Advances in tomography: probing the molecular architecture of cells. Nat. Rev. Mol. Cell Biol. *13*, 736–742.

Giannuzzi, L.A. (2005). Introduction to Focused Ion Beams: Instrumentation, Theory, Techniques and Practice, Softcover Edition (New York: Springer).

Gilbert, P. (1972). Iterative methods for the three-dimensional reconstruction of an object from projections. J. Theor. Biol. *36*, 105–117.

Gordon, R.B., Bender, R., and Herman, G.T. (1970). Algebraic reconstruction techniques (ART) for three-dimensional electron microscopy and x-ray photography. J. Theor. Biol. *29*, 471–481.

Grossman, E., Medalia, O., and Zwerger, M. (2012a). Functional architecture of the nuclear pore complex. Annu. Rev. Biophys. *41*, 557–584.

Grossman, E., Dahan, I., Stick, R., Goldberg, M.W., Gruenbaum, Y., and Medalia, O. (2012b). Filaments assembly of ectopically expressed Caenorhabditis elegans lamin within Xenopus oocytes. J. Struct. Biol. *177*, 113–118.

Heymann, J.A., Hayles, M., Gestmann, I., Giannuzzi, L.A., Lich, B., and Subramaniam, S. (2006). Site-specific 3D imaging of cells and tissues with a dual beam microscope. J. Struct. Biol. *155*, 63–73.

Horowitz, R.A., Koster, A.J., Walz, J., and Woodcock, C.L. (1997). Automated electron microscope tomography of frozen-hydrated chromatin: the irregular three-dimensional zigzag architecture persists in compact, isolated fibers. J. Struct. Biol. *120*, 353–362.

Hrabe, T., Chen, Y., Pfeffer, S., Cuellar, L.K., Mangold, A.V., and Förster, F. (2012). PyTom: a python-based toolbox for localization of macromolecules in cryo-electron tomograms and subtomogram analysis. J. Struct. Biol. *178*, 177–188.

Hsieh, C.E., Marko, M., Frank, J., and Mannella, C.A. (2002). Electron tomographic analysis of frozen-hydrated tissue sections. J. Struct. Biol. *138*, 63–73.

Iancu, C.V., Wright, E.R., Benjamin, J., Tivol, W.F., Dias, D.P., Murphy, G.E., Morrison, R.C., Heymann, J.B., and Jensen, G.J. (2005). A "flip-flop" rotation stage for routine dual-axis electron cryotomography. J. Struct. Biol. *151*, 288–297.

Ibiricu, I., Maurer, U.E., and Grünewald, K. (2013). Characterization of herpes simplex virus type 1 L-particle assembly and egress in hippocampal neurones by electron cryo-tomography. Cell. Microbiol. *15*, 285–291.

Jun, S., Ke, D., Debiec, K., Zhao, G., Meng, X., Ambrose, Z., Gibson, G.A., Watkins, S.C., and Zhang, P. (2011). Direct visualization of HIV-1 with correlative live-cell microscopy and cryo-electron tomography. Structure *19*, 1573–1581.

Kreshuk, A., Straehle, C.N., Sommer, C., Koethe, U., Cantoni, M., Knott, G., and Hamprecht, F.A. (2011). Automated detection and segmentation of synaptic contacts in nearly isotropic serial electron microscopy images. PLoS ONE *6*, e24899.

Kürner, J., Frangakis, A.S., and Baumeister, W. (2005). Cryo-electron tomography reveals the cytoskeletal structure of Spiroplasma melliferum. Science *307*, 436–438.

Lieber, A., Leis, A., Kushmaro, A., Minsky, A., and Medalia, O. (2009). Chromatin organization and radio resistance in the bacterium Gemmata obscuriglobus. J. Bacteriol. *191*, 1439–1445.

Lučić, V., Förster, F., and Baumeister, W. (2005). Structural studies by electron tomography: from cells to molecules. Annu. Rev. Biochem. *74*, 833–865.

Lučić, V., Leis, A., and Baumeister, W. (2008). Cryo-electron tomography of cells: connecting structure and function. Histochem. Cell Biol. *130*, 185–196.

Maimon, T., Elad, N., Dahan, I., and Medalia, O. (2012). The human nuclear pore complex as revealed by cryo-electron tomography. Structure *20*, 998–1006.

Marko, M., Hsieh, C., Moberlychan, W., Mannella, C.A., and Frank, J. (2006). Focused ion beam milling of vitreous water: prospects for an alternative to cryo-ultramicrotomy of frozen-hydrated biological samples. J. Microsc. *222*, 42–47.

Marko, M., Hsieh, C., Schalek, R., Frank, J., and Mannella, C. (2007). Focused-ion-beam thinning of frozen-hydrated biological specimens for cryo-electron microscopy. Nat. Methods *4*, 215–217.

Martell, J.D., Deerinck, T.J., Sancak, Y., Poulos, T.L., Mootha, V.K., Sosinsky, G.E., Ellisman, M.H., and Ting, A.Y. (2012). Engineered ascorbate peroxidase as a genetically encoded reporter for electron microscopy. Nat. Biotechnol. *30*, 1143–1148.

Mastronarde, D.N. (1997). Dual-axis tomography: an approach with alignment methods that preserve resolution. J. Struct. Biol. *120*, 343–352.

McMullan, G., Chen, S., Henderson, R., and Faruqi, A.R. (2009). Detective quantum efficiency of electron area detectors in electron microscopy. Ultramicroscopy *109*, 1126–1143.

Medalia, O., and Geiger, B. (2010). Frontiers of microscopy-based research into cell-matrix adhesions. Curr. Opin. Cell Biol. *22*, 659–668.

Medalia, O., Weber, I., Frangakis, A.S., Nicastro, D., Gerisch, G., and Baumeister, W. (2002). Macromolecular architecture in eukaryotic cells visualized by cryoelectron tomography. Science *298*, 1209–1213.

Mercogliano, C.P., and DeRosier, D.J. (2006). Gold nanocluster formation using metallothionein: mass spectrometry and electron microscopy. J. Mol. Biol. *355*, 211–223.

Meyerson, J.R., White, T.A., Bliss, D., Moran, A., Bartesaghi, A., Borgnia, M.J., de la Cruz, M.J., Schauder, D., Hartnell, L.M., Nandwani, R., et al. (2011). Determination of molecular structures of HIV envelope glycoproteins using cryo-electron tomography and automated sub-tomogram averaging. J. Vis. Exp. Published online December 1, 2011. http://dx.doi.org/10.3791/2770.

Mindell, J.A., and Grigorieff, N. (2003). Accurate determination of local defocus and specimen tilt in electron microscopy. J. Struct. Biol. *142*, 334–347.

MoberlyChan W.J., and Schalek, R. (2007). Ion beam induced surface modulations from nano to pico: optimizing deposition during erosion and erosion during deposition. MRS Proceedings *1059*/2007.

Nishino, Y., Yasunaga, T., and Miyazawa, A. (2007). A genetically encoded metallothionein tag enabling efficient protein detection by electron microscopy. J. Electron Microsc. (Tokyo) *56*, 93–101.

Ori, A., Banterle, N., Iskar, M., Andrés-Pons, A., Escher, C., Khanh Bui, H., Sparks, L., Solis-Mezarino, V., Rinner, O., Bork, P., et al. (2013). Cell type-specific nuclear pores: a case in point for context-dependent stoichiometry of molecular machines. Mol. Syst. Biol. *9*, 648.

Patla, I., Volberg, T., Elad, N., Hirschfeld-Warneken, V., Grashoff, C., Fässler, R., Spatz, J.P., Geiger, B., and Medalia, O. (2010). Dissecting the molecular architecture of integrin adhesion sites by cryo-electron tomography. Nat. Cell Biol. *12*, 909–915.

Philippsen, A., Engel, H.A., and Engel, A. (2007). The contrast-imaging function for tilted specimens. Ultramicroscopy *107*, 202–212.

Pierson, J., Ziese, U., Sani, M., and Peters, P.J. (2011). Exploring vitreous cryosection-induced compression at the macromolecular level using electron cryo-tomography; 80S yeast ribosomes appear unaffected. J. Struct. Biol. *173*, 345–349.

Radermacher, M. (1988). Three-dimensional reconstruction of single particles from random and nonrandom tilt series. J. Electron Microsc. Tech. *9*, 359–394.

Rigort, A., Bäuerlein, F.J., Leis, A., Gruska, M., Hoffmann, C., Laugks, T., Böhm, U., Eibauer, M., Gnaegi, H., Baumeister, W., and Plitzko, J.M. (2010). Micromachining tools and correlative approaches for cellular cryo-electron tomography. J. Struct. Biol. *172*, 169–179.

Rigort, A., Bäuerlein, F.J., Villa, E., Eibauer, M., Laugks, T., Baumeister, W., and Plitzko, J.M. (2012). Focused ion beam micromachining of eukaryotic cells for cryoelectron tomography. Proc. Natl. Acad. Sci. USA *109*, 4449–4454.

Scheres, S.H., Melero, R., Valle, M., and Carazo, J.M. (2009). Averaging of electron subtomograms and random conical tilt reconstructions through likelihood optimization. Structure *17*, 1563–1572.

Schlimpert, S., Klein, E.A., Briegel, A., Hughes, V., Kahnt, J., Bolte, K., Maier, U.G., Brun, Y.V., Jensen, G.J., Gitai, Z., and Thanbichler, M. (2012). General protein diffusion barriers create compartments within bacterial cells. Cell *151*, 1270–1282.

Shu, X., Lev-Ram, V., Deerinck, T.J., Qi, Y., Ramko, E.B., Davidson, M.W., Jin, Y., Ellisman, M.H., and Tsien, R.Y. (2011). A genetically encoded tag for correlated light and electron microscopy of intact cells, tissues, and organisms. PLoS Biol. *9*, e1001041.

Sorzano, C.O., Messaoudi, C., Eibauer, M., Bilbao-Castro, J.R., Hegerl, R., Nickell, S., Marco, S., and Carazo, J.M. (2009). Marker-free image registration of electron tomography tilt-series. BMC Bioinformatics *10*, 124.

Stewart, M. (2006). Structural basis for the nuclear protein import cycle. Biochem. Soc. Trans. *34*, 701–704.

Stoffler, D., Feja, B., Fahrenkrog, B., Walz, J., Typke, D., and Aebi, U. (2003). Cryo-electron tomography provides novel insights into nuclear pore architecture: implications for nucleocytoplasmic transport. J. Mol. Biol. *328*, 119–130.

Stölken, M., Beck, F., Haller, T., Hegerl, R., Gutsche, I., Carazo, J.M., Baumeister, W., Scheres, S.H., and Nickell, S. (2011). Maximum likelihood based classification of electron tomographic data. J. Struct. Biol. *173*, 77–85.

Suntharalingam, M., and Wente, S.R. (2003). Peering through the pore: nuclear pore complex structure, assembly, and function. Dev. Cell *4*, 775–789.

Swulius, M.T., Chen, S., Jane Ding, H., Li, Z., Briegel, A., Pilhofer, M., Tocheva, E.I., Lybarger, S.R., Johnson, T.L., Sandkvist, M., and Jensen, G.J. (2011). Long helical filaments are not seen encircling cells in electron cryotomograms of rod-shaped bacteria. Biochem. Biophys. Res. Commun. *407*, 650–655.

Terry, L.J., Shows, E.B., and Wente, S.R. (2007). Crossing the nuclear envelope: hierarchical regulation of nucleocytoplasmic transport. Science *318*, 1412–1416.

van Heel, M., Gowen, B., Matadeen, R., Orlova, E.V., Finn, R., Pape, T., Cohen, D., Stark, H., Schmidt, R., Schatz, M., and Patwardhan, A. (2000).

Single-particle electron cryo-microscopy: towards atomic resolution. Q. Rev. Biophys. *33*, 307–369.

Walz, J., Typke, D., Nitsch, M., Koster, A.J., Hegerl, R., and Baumeister, W. (1997). Electron tomography of single ice-embedded macromolecules: three-dimensional alignment and classification. J. Struct. Biol. *120*, 387–395.

Wang, K., Strunk, K., Zhao, G., Gray, J.L., and Zhang, P. (2012). 3D structure determination of native mammalian cells using cryo-FIB and cryo-electron tomography. J. Struct. Biol. *180*, 318–326.

Winkler, H.H., Daugherty, R.M., and Audia, J.P. (2003). Cysteine-scanning mutagenesis and thiol modification of the Rickettsia prowazekii ATP/ADP translocase: evidence that TM VIII faces an aqueous channel. Biochemistry *42*, 12562–12569.

Xiong, Q., Morphew, M.K., Schwartz, C.L., Hoenger, A.H., and Mastronarde, D.N. (2009). CTF determination and correction for low dose tomographic tilt series. J. Struct. Biol. *168*, 378–387.

Xu, M., Beck, M., and Alber, F. (2012). High-throughput subtomogram alignment and classification by Fourier space constrained fast volumetric matching. J. Struct. Biol. *178*, 152–164.

Yahav, T., Maimon, T., Grossman, E., Dahan, I., and Medalia, O. (2011). Cryo-electron tomography: gaining insight into cellular processes by structural approaches. Curr. Opin. Struct. Biol. *21*, 670–677.

Zanetti, G., Riches, J.D., Fuller, S.D., and Briggs, J.A. (2009). Contrast transfer function correction applied to cryo-electron tomography and sub-tomogram averaging. J. Struct. Biol. *168*, 305–312.

Archives of Biochemistry and Biophysics 581 (2015) 78–85

Contents lists available at ScienceDirect

Archives of Biochemistry and Biophysics

journal homepage: www.elsevier.com/locate/yabbi

Review

Developments in cryo-electron tomography for *in situ* structural analysis

Anna Dubrovsky [a], Simona Sorrentino [a], Jan Harapin [a], K. Tanuj Sapra [a], Ohad Medalia [a,b,*]

[a] Department of Biochemistry, University of Zurich, Winterthurerstrasse 190, 8057 Zurich, Switzerland
[b] Department of Life Sciences and the National Institute for Biotechnology in the Negev, Ben-Gurion University, Beer-Sheva 84105, Israel

ARTICLE INFO

Article history:
Received 27 January 2015
and in revised form 14 April 2015
Available online 25 April 2015

Keywords:
Cryo-electron tomography
Cryo-focused-ion beam
Direct electron detector
Phase plate

ABSTRACT

Structural analysis of macromolecular assemblies and their remodeling during physiological processes is instrumental to defining the fundament of cellular and molecular biology. Recent advances in computational and analytical tools for cryo-electron tomography have enabled the study of macromolecular structures in their native environment, providing unprecedented insights into cell function. Moreover, the recent implementation of direct electron detectors has progressed cryo-electron tomography to a stage where it can now be applied to the reconstruction of macromolecular structures at high resolutions. Here, we discuss some of the recent technical developments in cryo-electron tomography to reveal structures of macromolecular complexes in their physiological medium, focusing mainly on eukaryotic cells.

Introduction

Structural analysis of macromolecular protein complexes is crucial for a comprehensive understanding of their function. However, protein complexes in cells reside in a crowded environment. In fact, almost all cellular activities rely on the concerted action of macromolecular complexes in a dynamic network. Therefore, retrieving three-dimensional (3D)[1] molecular structures in their physiological environment is of major importance for cellular and molecular structural biology.

Cryo-electron tomography (cryo-ET) is a promising approach for the 3D visualization of large pleomorphic structures [1] as well as macromolecules in their native environment [2–6]. Although not a new concept, ET has posed formidable technical problems hampering progress towards practical application for more than three decades. Recent, technological advances and evolving sample preparation methodologies, in particular the automation of ET and the application of an energy filter (Fig. 1), have led to successful use of cryo-ET for biological samples [7–9]. A range of biological samples such as isolated cellular compartments [10,11], isolated organelles [12], viruses [13,14], bacteria [15,16], eukaryotic cells [17], and tissue sections [4,18] have been successfully studied with cryo-ET. Owing to the cryo-techniques employed, cryo-ET can literally be used to capture high resolution structural snapshots of dynamic cellular processes in close to native conditions [19]. The remodeling of actin network during filopodium formation of *Dictyostelium discoideum* (*D. discoideum*) [20], virus assembly in human cells [21] as well as virus assembly intermediates inside infected bacteria [22] are a few examples of dynamic processes that have been studied by cryo-ET.

In this review we will discuss the main challenges in cryo-ET and the recent advances which have overcome some of those bottlenecks. State-of-the-art hardware and software developments that include phase plates, direct electron detectors (DEDs) and motion correction function will be discussed. We will further explore the application of cryo-ET on various types of samples, from large complexes and protein networks situated in their native medium, to whole eukaryotic cells and multicellular organisms. We will specifically focus on the power of cryo-ET for *in situ* applications. However, it is important to note that purified macromolecular assemblies have also been successfully studied with this technique [23,24].

Technical principles of cryo-electron tomography

Depending on its thickness, a sample is vitrified either by direct plunging into a liquid nitrogen cooled cryogen like ethane (for samples less than 20 μm in thickness [25,26]), or by high pressure freezing (for thicker samples, 20–200 μm [27]). The quick freezing fixes the biological material in a thin layer of amorphous ice, preserving

* Corresponding author at: Department of Biochemistry, University of Zurich, Winterthurerstrasse 190, 8057 Zurich, Switzerland.
E-mail address: omedalia@bioc.uzh.ch (O. Medalia).

[1] *Abbreviations used:* 3D, three-dimensional; cryo-ET, cryo-electron tomography; DEDs, direct electron detectors; cryo-EM, cryo-electron microscopy; SNR, signal-to-noise ratio; TEM, transmission electron microscope; CTF, contrast transfer function; ZPP, Zernike phase plate; VPP, Volta phase plate; CMOS, complementary metal-oxide-semiconductor; CCD, charge-coupled device; DQE, detective quantum efficiency; MTF, modulation transfer function; NE, nuclear envelope; NPCs, nuclear pore complexes; ECM, extracellular matrix; cryo-FIB-SEM, cryo focused ion beam scanning electron microscopy.

http://dx.doi.org/10.1016/j.abb.2015.04.006
0003-9861/

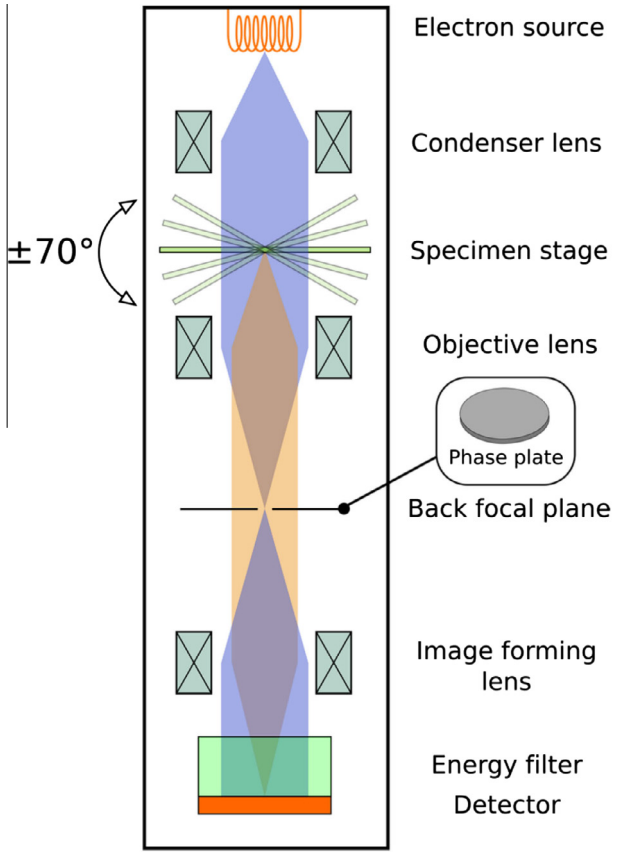

Fig. 1. Principle of data acquisition in cryo-ET. The electron beam emanated from the electron source is projected towards the vitrified specimen held by a cryo-stage. During the acquisition of a tilt series, the cryo-stage is rotated to successive tilt positions (maximal tilt range −70° to +70°) around a single axis perpendicular to the incident beam. An energy-filter, located between the specimen and the detector, filters electrons according to their energy. A thin-film phase plate can be placed in the back focal plane of the objective lens to increase the phase contrast of the sample.

it in a vitrified state [25], and avoiding the risk of artifacts associated with chemical fixation, staining, or dehydration. The molecular landscape of the cell is thus preserved [28], and ultrastructural analysis at the nanometer scale becomes attainable [29,30].

An electron micrograph is essentially a two-dimensional projection of 3D objects in the direction of the electron beam. The three-dimensionality of the specimen is retrieved by recording a series of projections at different tilt angles and then combining the tilt projections into a 3D density map, a so-called tomogram [31]. In practice, a series of projection images is collected by incrementally tilting the specimen usually around a single tilt-axis, perpendicular to the optical axis of the electron beam (Fig. 1). This tilt series is then aligned to a common frame of reference and synthesized to a tomogram, most commonly by using the 'weighted back projection' algorithm [32].

Due to the tilting geometry of the sample, there is an increase in sample thickness along the beam axis at high tilt angles, which leads to an excessive electron path through the sample. This phenomenon, along with the design of grid and specimen-holder [33,34], restricts the tilt range of the sample to a maximum of 120–140° (+60° to −60° or +70° to −70°; Fig. 1). Consequently, in the 3D Fourier space of the tomogram an area of missing information, known as the "missing wedge", is formed, leading to distortions in features along the electron beam axis (z direction) [1,35]. Thus, the resolution of a tomogram is not isotropic; the resolution in the z direction is lower compared to the resolution in the specimen plane (x–y plane). Other factors also influence the quality of a tomogram; e.g., the angular increment between two adjacent projections, the total number of projections [36,37], the total electron dose during data acquisition, and the accuracy of the alignment of the tilt series projections prior to reconstruction [38].

The interaction between the electron beam and the cryo-preserved specimen is fundamental to image formation in cryo-electron microscopy (cryo-EM). However, the high-energy incident electrons also cause degradation of the biological sample. Exposure to the electron beam can increase the thermal energy of the sample, cause ionization, and generate free radicals that break chemical bonds [1] detrimental to the sample structure [39]. Distortions in biological structures primarily lead to a loss of high resolution information [9,40]. Since the object is exposed multiple times to the electron beam during the acquisition of a tilt series, avoiding radiation damage is an exceptional challenge in cryo-ET. A straightforward solution is to keep the cumulative electron dose during data collection to a minimum, using the so-called 'low-dose imaging' [41]. However, imaging with a low electron dose results in micrographs with a low signal-to-noise ratio (SNR). Cryo-tomograms reconstructed from such low SNR micrographs show limited contrast and resolution. Nevertheless, the resolution of macromolecular complexes in a tomogram can be improved by applying image processing procedures like subtomogram averaging [42,43].

Improving contrast in cryo-ET

Hydrated biological materials act as phase contrast objects in cryo-EM; they mainly affect the phase and to a lesser extent the amplitude of the electron wave [44,45]. Hence, the structural information can be extracted from phase variations between the specimen and the vitrified buffer. However, due to the electron optics and the low dose imaging, images of vitrified biological specimens suffer from low contrast [46]. The low contrast is a limiting factor in the amount of structural information that can be extracted from cryo-ET data, and a predominant hindrance to the structural determination of small biological objects.

Defocus phase contrast

Close to Gaussian focus, cryo-fixed biological specimens generate weak contrast in the transmission electron microscope (TEM). The contrast transfer function (CTF) starts at zero (at the origin of the frequency-space) and remains low at low spatial frequencies. Thus, electron micrographs recorded close to focus suffer from poor contrast [31]. This introduces difficulties in identifying biological objects to be investigated. Imaging with an underfocus typically in the range of 5–10 μm can compensate for the low-frequency damping. This approach, called defocus phase contrast, is the most commonly applied phase contrast method in cryo-EM [6,47]. Although defocusing the objective lens improves the low frequency contrast transfer, a drawback of this approach is that the envelope function of the CTF shows a continuous attenuation of amplitudes towards higher spatial frequencies. This phenomenon leads to a loss in high resolution information [48]. Moreover, the CTF is a sinusoidal function, a fact that introduces two issues: (i) oscillations of the CTF between positive and negative contrast transfer bands, and (ii) formation of nodes (where the CTF passes zero) where there is no transfer of information and the data at those frequencies are lost [49]. The missing information at the nodes can be restored by combining images taken at different defocus values. Their CTFs will have nodes at different spatial frequencies and therefore a combination of these images will compensate for the lost information. To extract information

beyond the first destructive electron interference (typically referred as "the first zero"), a computational CTF correction can be applied to the electron micrographs [50,51]. However, it is challenging to apply CTF correction to tomographic data. The precise defocus value is often hard to determine because of the low electron-dose imaging and its variations throughout the entire projection due to the sample-tilting geometry [50,52–54]. Overall, adoption of the defocus phase contrast method imposes a compromise between contrast and resolution – higher defocus values increase image contrast but reduce the resolution, and vice versa.

Phase plate technology

An alternative approach, adopted from light microscopy [55], to enhance the contrast of low resolution information without sacrificing the high resolution information is by adding a phase contrast device to the optical system. There are several types of such devices, also referred to as "phase plates" [56]. Technical issues such as charging, contamination, phase plate design and production, and modifications of the microscope suited for phase plate operation, prevented the use of phase plates in transmission electron microscopy for many years [57,58]. To date, the thin-film carbon phase plates are the only phase plates successfully implemented in cryo-EM. The first phase plate to prove useful for cryo-ET is the Zernike phase plate (ZPP; Fig. 2) [46,47,59,60]. A ZPP is made of a thin amorphous carbon film (~20–30 nm) with a submicron hole (<1 μm) in its center, and is placed in the back focal plane of the TEM (Fig. 1). The unscattered electron beam passes unmodified through the central hole, while the diffracted beam, after interactions with the specimen, hits the carbon layer causing a phase shift usually by $\pi/2$ [47]. This phase shift converts the CTF from a sine to a cosine function that shows maximum contrast transfer at low frequencies, markedly enhancing the contrast of low resolution features (Fig. 2). Images can thus be recorded at zero (or close to zero) defocus, thereby avoiding loss of information due to CTF oscillations [59]. Moreover, there is no need to correct the CTF as the information is uniformly transferred over a wide range of spatial frequencies [49].

Initially, the use of ZPP was restricted to small specimens such as purified protein complexes and bacteriophages due to the size of the central hole that limited the recoverable low resolution information (attributed to the 'cut-on frequency' of the plate [61]) [49,59,62]. Recently, the fabrication of plates with a smaller central hole has expanded the application to large vitrified pleomorphic biological specimens like brain tissues and whole mount cells [60,63]. Wei Dai and colleagues have demonstrated the power of Zernike phase contrast in cryo-ET and proved this imaging modality to dramatically enhance image contrast over conventional cryo-ET (Fig. 2) [22,64]. Tomographic data of cyanobacteria infected with cyanophages illustrated different stages of infection, phage assembly intermediates, and the maturation of phage progenies inside the host cell.

ZPPs present a number of issues that have thus far prevented their widespread use. For instance, the rapid aging of the plate demands an exchange normally within a week after installation [61]. The central hole needs a precise centering in the unscattered beam path. In addition, the hole-edge introduces artifacts in images, e.g., fringes around high-contrast objects. As mentioned above, a smaller hole-size permits the imaging of large specimens, but becomes non-trivial to align and maintain the hole centered [63,65].

A new type of thin-film carbon phase plate, namely the Volta phase plate (VPP), offers solutions to the above mentioned issues. Similar to the ZPP, a VPP can be placed in the back focal plane of the objective lens (Fig. 1), and generates a phase shift of about $\pi/2$ (when operated in-plane) [56]. A key difference between the ZPP and the VPP is that the latter does not have a central hole. Instead of passing through a hole, the unscattered beam passes through the carbon film and generates the phase shifting area. Thus, the VPP offers a practical advantage over ZPP with easier operation circumventing the need of accurate positioning of the plate. Also, VPPs have a longer life-span overcoming the need for frequent replacements.

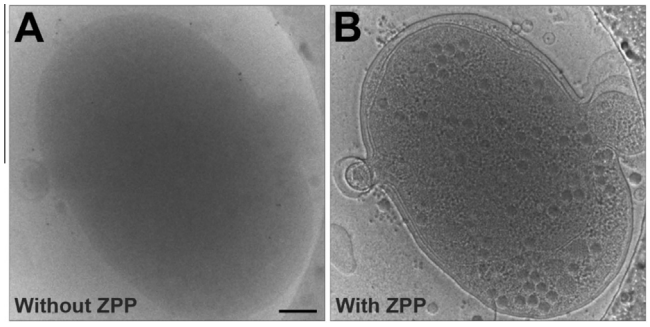

Fig. 2. ZPP improves contrast in cryo-micrographs. A cyanobacterium infected with cyanophages was imaged (A) with conventional cryo-TEM and (B) with ZPP-cryo-TEM, under the same imaging conditions. Scale bar, 200 nm. Modified with permission from [47].

Recently, cryo-ET with VPP was used to investigate the structure of 26S proteasomes within intact neurons [66]. Proteasomes were found in two different states: 80% of the proteasomes were found in the substrate-accepting ground state and 20% of the proteasomes were found in the substrate-processing state, when the cells were not under proteolytic stress. This work proved the potential of the VPP to enhance the contrast of data imaged in-focus. Furthermore, it was demonstrated how dynamic macromolecular assemblies can be investigated in their functional cellular environment without perturbation of the cell.

Revolutionizing cryo-ET with direct electron detectors

A novel type of detectors, namely the complementary metal-oxide-semiconductor (CMOS) technology based DEDs, is an attractive alternative to the commonly used charge-coupled device (CCD) detectors. Devoid of any scintillator or optical coupling, DEDs are designed to directly record the primary electrons, and thereby dramatically improve the sensitivity and the SNR [67]. A comparison between the CCD detectors and the DEDs [68–71] show that the DEDs exhibit substantially better detective quantum efficiency (DQE) and modulation transfer function (MTF), particularly at high spatial frequencies, mostly at an acceleration voltage of 300 keV [72].

Stage drift (due to instability of the sample holder) and beam induced motion (generated when the electron beam strikes the sample) cause blurring of the images, and are detrimental to resolution [73–75]. Owing to a fast frame rate (10–40 fps) and a fast readout rate, data acquired with the new CMOS–DEDs can be corrected for those motions. Instead of collecting one frame per exposure, as done with the CCD, the use of DED allows the collection of a stack of frames per exposure. The frames within the stack are then aligned with respect to each other and summed as one 'motion-corrected' image [74].

The so-called 'counting mode' in the commercially available K2 Summit™ DED from Gatan (Pleasanton, CA, USA) is an additional beneficial feature for cryo-EM. In this imaging mode, individual electron events are detected and recorded. Therefore, the Landau noise (noise arising from the statistical variations in the signal deposited by the incident electrons) and the readout noise are eliminated [74,76], elevating the DQE at low spatial frequencies [72].

Owing to its improved performance in both DQE and MTF, the direct detection approach has proven very useful for cryo-EM single-particle analysis [74,77,78] and in cryo-ET [66,79] for high-resolution reconstructions. The ability to correct for drift and beam induced movements [74,75] is a crucial feature for cryo-ET especially at high tilt angles when the exposure time increases and the stage drift is more significant. An example of the substantially better performance of the DED over CCD in cryo-ET of biological specimens is shown in Fig. 3. Volumes reconstructed from data collected with a DED show more details, such as the filamentous structures present at the nuclear envelope (NE; Fig. 3B). Moreover, with the DED the helical structure of actin filaments within cells could be clearly observed (Fig. 3C), which was not possible with a CCD.

In situ studies of macromolecular assemblies and protein networks at the nuclear envelope

To obtain a comprehensive insight into the structural organization of protein complexes, it is crucial to study them in the context of the cellular milieu. Here, we discuss the importance of such an approach using the cell nucleus as a model system.

Nuclear lamina

In eukaryotic cells, the NE, composed of an outer and an inner bilayer membrane, separates the nucleus from the cytoplasm. The two nuclear membranes fuse at the periphery of the nuclear pore complexes (NPCs) [80]. Metazoan NEs consist of an additional prominent structure – the lamina, a filamentous protein meshwork underlying the inner nuclear membrane, mainly composed of lamin intermediate filament proteins. The lamin proteins are classified as A-type or B-type lamins that form separate but interconnected networks [81,82]. Lamins and lamina-associated proteins are involved in diverse cellular and nuclear functions, and implicated in various human diseases termed laminopathies, affecting bones, nerves, muscles and other body tissues [83]. 3D structural analysis of the nuclear lamina is therefore an essential aspect in understanding how mutations in the lamin genes may alter the structural organization of the NE [84].

In vitro studies of reconstituted lamins have provided us with important structural insights about lamin assembly into filaments [23]. However, the absence of a lipid bilayer membrane, to which the lamins are attached *in vivo*, may alter the organization of the lamin filaments and the whole lamin network. Due to its location in a very dense environment, sandwiched in-between the inner nuclear membrane and heterochromatin [85,86], it has been extremely challenging to acquire high resolution cryo-tomograms of the lamina in somatic cells. The ectopic expression of lamins in a simpler environment – the *Xenopus laevis* (*X. laevis*) nucleus, in which the heterochromatin is not in contact with the nuclear periphery [87], allows access to lamin filaments assembled and organized in their native environment – the NE [88].

The approach was adopted by Grossman *et al.*; they expressed *Caenorhabditis elegans* (*C. elegans*) lamin proteins in *X. laevis* oocytes and elucidated the complex organization of the *C. elegans* lamin filaments in mechanically spread NEs (Fig. 4A) [89]. The *C. elegans* lamin filaments were shown to be thinner (5–6 nm) than previously suggested (~10 nm) [23,81], and to have diverse interactions with each other.

The nuclear pore complex

The NPC is the sole gateway of the nucleus, facilitating a bilateral transport of cargoes in and out of the nucleus. Molecules smaller than ~45 kDa passively diffuse through the pore while larger molecules are actively transported. The NPC is composed of multiple copies of about 30 different proteins arranged in a pseudo eightfold symmetry [90,91]. The enormous size of the NPC (~120 MDa for vertebrate NPC [92]) poses major challenges towards the structural elucidation of the whole complex by conventional crystallography techniques. NPCs in isolated NEs [93], intact nuclei [19] and even in intact cells [17] were studied by cryo-ET in combination with subtomogram averaging, a method adopted from single particle analysis [3,43]. Whereas in single particle analysis many copies of the object of interest are imaged after biochemical purification, in subtomogram averaging the 'purification' is done *in silico*; the required protein complexes are extracted from the tomograms within sub-volumes, the so-called subtomograms.

Since intact NPCs cannot be purified by biochemical means, subtomogram averaging is a well-designed approach to reconstruct a functional structure of NPC. Individual subtomograms containing single copies of the NPC were aligned to a common frame of reference and averaged to produce a high SNR structure. Because the NPCs are embedded in the NE in different orientations, the averaging procedure filled the missing wedge and yielded an isotropically sampled structure with an isotropic resolution [6,10,94]. The structure of NPCs from human cells [17,95], *D. discoideum* cells [10,19], and *X. laevis* oocytes [93,96] were reconstructed at resolutions of ~6.6, ~5.8, and ~6.4 nm, respectively. Those studies essentially demonstrate that NPCs from different organisms have a similar basic architecture comprising three fundamental key elements: a cytoplasmic ring, a central spoke ring, and a nucleoplasmic ring capped with a distal ring termed the nuclear basket [97]. Despite sharing a consensus structure, NPCs from different organisms vary in their dimensions [28]. For example, NPCs from *D. discoideum* and from human fibroblasts have similar diameters of the nuclear and cytoplasmic rings (~120 nm) and of the spoke ring (~50 nm), but differ in heights and in protein density distribution, suggesting different positioning of the proteins in the complex. Furthermore, cryo-ET analysis of NPCs embedded in intact nuclei of *D. discoideum* have provided us with an extraordinary visualization of cargo import trajectories through the NPC [19]. However, to gain further insights into the structure and function of the NPC, the organization of its gating mechanism needs to be obtained. This will be possible by reconstructing the NPC at a resolution of at least 1–2 nm.

Actin networks within intact cells

The cytokseletal network, especially polymerized actin network, represent a pressing example of cryo-ET studies on intact cells (Fig. 4B and C). For instance, the anchorage of actin to the plasma membrane is an important process for cellular function, as illustrated by the formation of focal adhesions. Focal adhesions are highly dynamic multiprotein complexes, establishing a mechanical link between the extracellular matrix (ECM) and the F-actin within the cytosol of a cell [98,99]. The structural integrity of the adhesion site is maintained by actin stress fibers [100,101]. It is impossible to accurately elucidate the organization of actin filaments and other macromolecular assemblies at focal adhesion sites with conventional EM [102]. 3D cryo-reconstructions of focal adhesions showed that actin filaments do not interact directly with the plasma membrane adhesion receptors (the integrins), and revealed a large number of previously unidentified doughnut-shaped particles at the membrane-stress fibers interface (Fig. 4B) [103,104].

Filopodia are thin protrusions of the plasma membrane, rich in F-actin. Their formation is important for various cellular processes such as sensing the environment and cell migration [105].

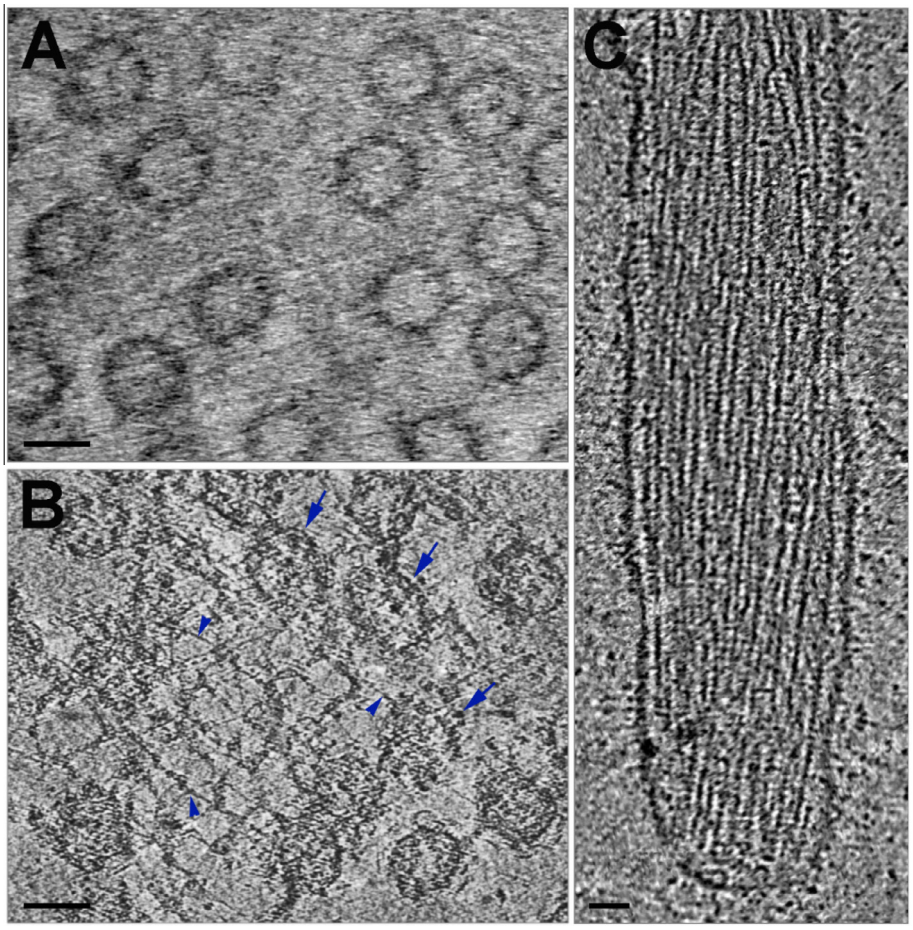

Fig. 3. DEDs improve the quality of cryo-ET data. (A and B) *x*–*y* slices through cryo-tomograms, 1.4 nm in thickness, of spread nuclear envelopes isolated from *X. laevis* oocytes. The tomograms were recorded using (A) a CCD, or (B) a DED, under the same imaging conditions. NPCs are shown with blue arrows, and filaments are shown with blue arrowheads. (C) An *x*–*y* slice, 1.4 nm in thickness, through a cryo-tomogram of a platelet filopodium recorded with a DED. The helical symmetry of actin filaments is clearly detected. Scale bars, 100 nm.

Studying the 3D architecture of the filopodium and in particular the organization of F-actin within the filopodium is meaningful only in intact cells, where the membrane, the actin, and all other participating molecules are present. Cryo-ET of intact *D. discoideum* cells showed the actin filaments to be discontinuous throughout the entire protrusion [20]. The organization and length of the filaments is divergent at different areas of the filopodium; short filaments were found at the tip of the filopodium protrusion and assumed to be the driving force pushing the plasma-membrane forward.

Platelets, which are small anucleated cells in the blood stream, can effectively be studied by means of cryo-ET (Fig. 4C) [106]. Platelets are crucial elements in thrombosis and arrest bleeding after blood vessel damage, functions that rely on their ability to modify actin organization and adhesion to the ECM surface [107]. Actin network in platelets has been traditionally imaged by means of EM after stripping platelets of plasma-membrane and soluble proteins using detergents [108]. Cryo-ET of intact platelets (Fig. 4C) can be instrumental for the study of actin network during activation. Platelet membranes also harbor integrin receptors that participate in the adhesion to ECM via their extracellular domain. These receptors interact with focal adhesion complexes that bridge the receptors to F-actin in the filopodium [109,110]. 3D structural data of platelets on an ECM-coated surface can divulge the changes in actin organization and the conformational shifts of the adhesion receptors during spreading and activation processes of platelets.

Focused ion beam milling as a tool for sample preparation

Cryo-ET has gained popularity for imaging protein assemblies and thin cellular regions. However, a major scientific advance lies in obtaining structural snapshots of macromolecular complexes in different cell types, tissues or even an entire organism. Although whole cells and small organisms can be cryo-preserved, samples thicker than 1 μm cannot be studied *in toto* due to the mean free path of an electron (200 nm and 350 nm for acceleration voltages of 120 keV and 300 keV, respectively). The frequency of multi-scattering events of the electrons within the sample increases above this thickness threshold and can considerably degrade data quality [33]. Therefore, thinning methods such as sectioning with diamond knives and focused ion beam milling are beginning to be routinely applied for cryo-ET of biological organisms [6].

Cryo focused ion beam scanning electron microscopy – cryo-FIB-SEM – is a hybrid method used to selectively produce thin lamellae of regions of interest within an otherwise thick, fully vitrified biological sample [111–115]. The basic principle of this approach is to iteratively thin the sample using a focused beam of Ga^+ ions, resulting in a thin cryo-lamella of the desired dimensions [116]. Cryo-FIB-SEM, cryo-ET, and feature tracking-based alignment procedures have successfully converged to produce pictures of the intracellular organization of both single cell eukaryotes [112,115] and multi-cellular eukaryotes [6,113,114].

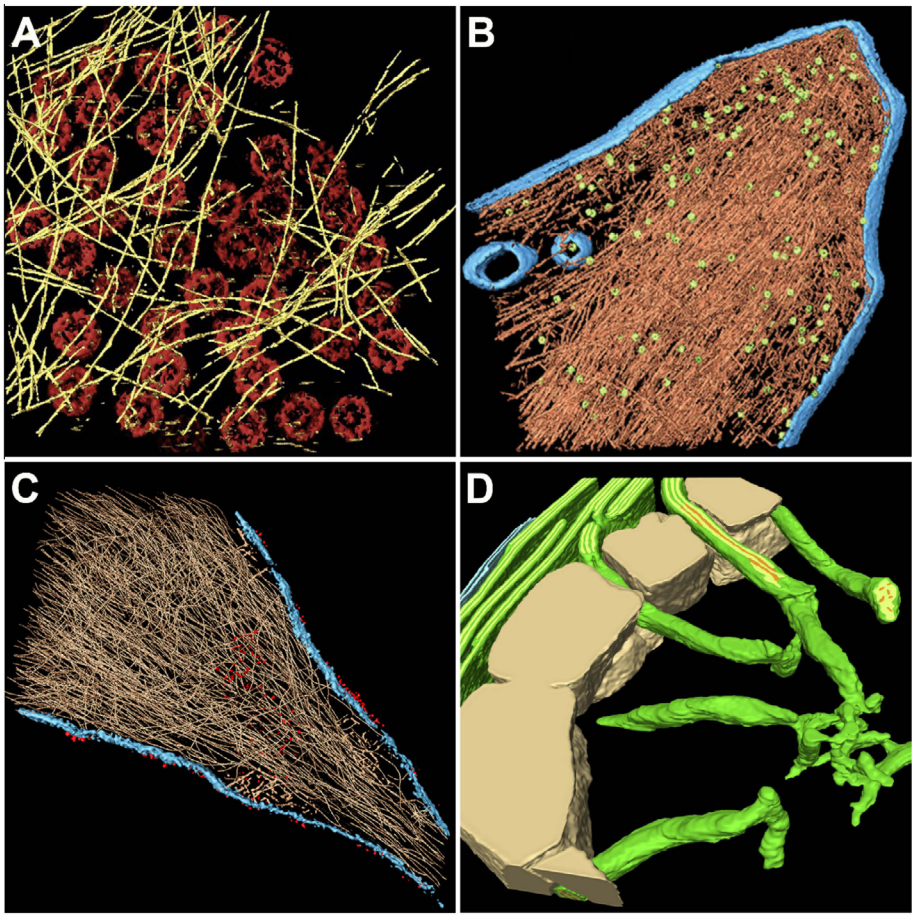

Fig. 4. Examples of samples studied *in situ* by cryo-ET. (A) Lamin filaments formed from ectopically expressed *C. elegans* lamins in *X. laevis* NE. Lamin filaments are shown in yellow and NPCs in red. Reprinted with permission from [89], copyright Elsevier. (B) A focal adhesion site of an intact mammalian cell indicating the complex protein network of these mechanosensing assemblies. Actin is shown in orange, cell membrane in blue, and adhesion-related particles in green. Reprinted with permission from [103]. (C) An adherent protrusion of a spreading human platelet. Actin is shown in brown, membrane in blue, and integrin receptors in red. Modified with permission from [106], copyright Elsevier. (D) Cylindrical tubes (minitubules shown in orange) connect the pyrenoid (tan) to the thylakoid (membrane shown in dark green and lumina in light green) in the chloroplast of a *Chlamydomonas* cell. The chloroplast envelope is shown in blue (top left). Modified with permission from [115].

The great potential of cryo-FIB-SEM in combination with cryo-ET is exemplified in the work of Engel *et al.*, who acquired the first *in situ* 3D structures of the algal chloroplast [115]. This work has provided many insights into the structural arrangement of the chloroplast, the site of eukaryotic photosynthesis and carbon fixation. The tomographic reconstructions show tubes that connect the thylakoids, where the light dependent steps of photosynthesis occur, to the site of light independent reactions – the pyrenoid (Fig. 4D). This observation is important as it can explain the synchronization between those two regions that are physically separated from each other in the chloroplast. Furthermore, the studies by Engel *et al.* [115] and Rigort *et al.* [112] demonstrate that subtomogram averaging can be performed on cryo-ET data from cryo-FIB-SEM-milled single cell eukaryotes by successfully reconstructing the structure of the algal RuBisCO enzyme and the *D. discoideum* NPC, respectively.

Summary and outlook

Cryo-ET is fast gaining importance as a central methodology for structural investigation of cellular architecture and macromolecular assemblies *in situ* (Fig. 4). The introduction of novel developments (phase plates, DED) is expected to have a profound effect on biological research, and is likely to increase the specimens amenable for cryo-ET studies. DEDs with motion correction function are proven to generate data with superior contrast and resolution. Since DEDs permit the use of lower electron dose, the integrity of the sample is better preserved, and data of higher quality can be acquired. Using less exposure per tilt series also makes it possible to acquire dual-axis tilt series without damaging the specimen. This will significantly reduce the missing information in Fourier space, from a wedge to a pyramid, which will in turn improve the overall quality and resolution of the tomograms in the *z* direction [117,118].

Thin-film phase plates can be tremendously beneficial for cellular cryo-ET by significantly improving the contrast of intracellular components and assemblies (Fig. 2). Furthermore, this technology can be applied to small proteins and complexes, which have inherently low contrast. However, there are still some technical challenges, including microscope modifications and maintenance of the phase plates, which need to be resolved before the technology can be applied for routine use [56,61]. In addition, many efforts are being invested in designing other phase plates, such as electrostatic phase plates [119], suitable for cryo-EM applications.

Cells and subcellular regions are crowded environments populated with a large assortment of molecular complexes. The identification of a protein complex of interest in a soup of proteins is not a trivial task. This can be solved with the help of pattern recognition methods based on matching known structures onto tomograms [120,121]. Nevertheless, these methods often cannot be implemented because of a lack of structural information on the majority of the cellular complexes [122]. Alternative labeling

approaches have been developed, e.g., electron dense markers like metallothionein [123] and genetically encoded tags like APEX [124]. Those however are not yet suitable to be used in intact cells or in close-to-life cryo preservation. Lately, a labeling method for ligand-binding membrane protein complexes named STAMP, suitable for *in situ* application and cryo preservation, has been developed [125]. However, this method is limited to proteins in their active state. Additionally, the electron-dense labeling molecule is situated a few nm away from the labeled protein complex making an unambiguous identification of the protein of interest difficult in a crowded environment. Still, the fundamental drawback in cryo-ET is a lack of applicable techniques for *in situ* labeling that would enable the direct identification of proteins. Therefore, the development of an electron dense tag that can be genetically conjugated to the protein of interest is necessary. A GFP analogue for cryo-EM would make it possible to unambiguously identify proteins whose structures are not yet resolved or which participate in larger assemblies [126].

Acknowledgments

This work was supported by a European Research Council (ERC) Starting Grant (243047 INCEL) and the Swiss National Science Foundation Grant (SNSF 31003A_159706/1).

KTS was supported by the Forschungskredit of the University of Zurich, [FK-13-049].

References

[1] V. Lucic, F. Forster, W. Baumeister, Annu. Rev. Biochem. 74 (2005) 833–865.
[2] O. Medalia et al., Science 298 (5596) (2002) 1209–1213.
[3] A. Bartesaghi, S. Subramaniam, Curr. Opin. Struct. Biol. 19 (4) (2009) 402–407.
[4] M. Bokstad et al., J. Struct. Biol. 178 (2) (2012) 76–83.
[5] M. Faini et al., Science 336 (6087) (2012) 1451–1454.
[6] J. Harapin, M. Eibauer, O. Medalia, Structure 21 (9) (2013) 1522–1530.
[7] R. Grimm et al., J. Microsc. 183 (1) (1996) 60–68.
[8] R. Grimm et al., Biophys. J. 72 (1) (1997) 482–489.
[9] K. Dierksen et al., Ultramicroscopy 49 (1–4) (1993) 109–120.
[10] M. Beck et al., Science 306 (5700) (2004) 1387–1390.
[11] N. Elad et al., J. Cell Sci. 124 (Pt 2) (2011) 207–215.
[12] D. Nicastro et al., J. Struct. Biol. 129 (1) (2000) 48–56.
[13] K. Grunewald et al., Science 302 (5649) (2003) 1396–1398.
[14] F.K. Schur et al., Nature 517 (7535) (2015) 505–508.
[15] J. Kurner, A.S. Frangakis, W. Baumeister, Science 307 (5708) (2005) 436–438.
[16] E.I. Tocheva et al., Mol. Microbiol. 88 (4) (2013) 673–686.
[17] T. Maimon et al., Structure 20 (6) (2012) 998–1006.
[18] P. Sarkar et al., PLoS One 9 (9) (2014) e106928.
[19] M. Beck et al., Nature 449 (7162) (2007) 611–615.
[20] O. Medalia et al., Curr. Biol. 17 (1) (2007) 79–84.
[21] C.L. Woodward, S.N. Cheng, G.J. Jensen, J. Virol. 89 (2) (2015) 1267–1277.
[22] W. Dai et al., Nature 502 (7473) (2013) 707–710.
[23] K. Ben-Harush et al., J. Mol. Biol. 386 (5) (2009) 1392–1402.
[24] F.M. Coquelle et al., Methods Mol. Biol. 777 (2011) 193–208.
[25] J. Dubochet et al., Q. Rev. Biophys. 21 (2) (1988) 129–228.
[26] J. Dubochet et al., J. Bacteriol. 155 (1) (1983) 381–390.
[27] D. Studer, B.M. Humbel, M. Chiquet, Histochem. Cell Biol. 130 (5) (2008) 877–889.
[28] K. Ben-Harush et al., J. Cell Sci. 123 (Pt. 1) (2010) 7–12.
[29] V. Lucic, A. Rigort, W. Baumeister, J. Cell Biol. 202 (3) (2013) 407–419.
[30] E.I. Tocheva, Z. Li, G.J. Jensen, Cold Spring Harbor Perspect. Biol. 2 (6) (2010) a003442.
[31] J. Frank, Electron Tomography: Methods for Three-Dimensional Visualization of Structures in the Cell, second ed., Springer, 2006.
[32] M. Radermacher, J. Electron Microsc. Tech. 9 (4) (1988) 359–394.
[33] R. Grimm et al., Biophys. J. 74 (2 Pt. 1) (1998) 1031–1042.
[34] R.A. Crowther, D.J. Derosier, A. Klug, Proc. R. Soc. London A 317 (1970) 319–340.
[35] J. Frank et al., J. Struct. Biol. 138 (1–2) (2002) 85–91.
[36] A.J. Koster et al., J. Struct. Biol. 120 (3) (1997) 276–308.
[37] R.A. Horowitz et al., J. Struct. Biol. 120 (3) (1997) 353–362.
[38] R. McIntosh, D. Nicastro, D. Mastronarde, Trends Cell Biol. 15 (1) (2005) 43–51.
[39] Y. Talmon, in: R.A. Steinbrecht, K. Zierold (Eds.), Cryotechniques in Biological Electron Microscopy, Springer, 1987, pp. 64–86.
[40] S. Subramaniam et al., ASM News 69 (5) (2003) 240–245.
[41] D.B. Carlson, J.E. Evans, in: K. Maaz (Ed.), The Transmission Electron Microscope, InTech, 2012, pp. 85–98.
[42] F. Forster, R. Hegerl, Methods Cell Biol. 79 (2007) 741–767.
[43] J.A. Briggs, Curr. Opin. Struct. Biol. 23 (2) (2013) 261–267.
[44] C. Toyoshima, N. Unwin, Ultramicroscopy 25 (4) (1988) 279–291.
[45] K. Nagayama, in: G.C.K. Roberts (Ed.), Encyclopedia of Biophysics, Springer, 2013, pp. 1837–1841.
[46] K. Nagayama, R. Danev, Philos. Trans. R. Soc. Lond. B: Biol. Sci. 363 (1500) (2008) 2153–2162.
[47] W. Dai et al., Nat. Protoc. 9 (11) (2014) 2630–2642.
[48] P.A. Penczek et al., Scan. Microsc. Suppl. 11 (1997) 147–154 (special issue on signal and image processing).
[49] R. Danev et al., J. Struct. Biol. 171 (2) (2010) 174–181.
[50] G. Zanetti et al., J. Struct. Biol. 168 (2) (2009) 305–312.
[51] J.J. Fernandez, S. Li, R.A. Crowther, Ultramicroscopy 106 (7) (2006) 587–596.
[52] A. Philippsen, H.A. Engel, A. Engel, Ultramicroscopy 107 (2–3) (2007) 202–212.
[53] M. Eibauer et al., J. Struct. Biol. 180 (3) (2012) 488–496.
[54] H. Winkler, K.A. Taylor, J. Struct. Biol. 143 (1) (2003) 24–32.
[55] F. Zernike, Physica 9 (7) (1942) 686–698.
[56] R. Danev et al., Proc. Natl. Acad. Sci. USA 111 (44) (2014) 15635–15640.
[57] K. Nagayama, J. Electron. Microsc. (Tokyo) 60 (Suppl. 1) (2011) S43–S62.
[58] R. Danev, K. Nagayama, in: G. Jensen (Ed.), Methods Enzymol, Academic Press, 2010, pp. 343–369.
[59] K. Murata et al., Structure 18 (8) (2010) 903–912.
[60] Y. Fukuda, K. Nagayama, J. Struct. Biol. 177 (2) (2012) 484–489.
[61] R. Danev, R.M. Glaeser, K. Nagayama, Ultramicroscopy 109 (4) (2009) 312–325.
[62] K. Nagayama, R. Danev, Biophys. Rev. 1 (1) (2009) 37–42.
[63] Y. Fukuda et al., J. Struct. Biol. 168 (3) (2009) 476–484.
[64] W. Dai et al., Microb. Cell 1 (1) (2014) 45–47.
[65] R. Danev, K. Nagayama, Ultramicroscopy 111 (8) (2011) 1305–1315.
[66] S. Asano et al., Science 347 (6220) (2015) 439–442.
[67] A.R. Faruqi, R. Henderson, Curr. Opin. Struct. Biol. 17 (5) (2007) 549–555.
[68] R.N. Clough, G. Moldovan, A.I. Kirkland, J. Phys: Conf. Ser. 522 (2014) 1–4.
[69] R.S. Ruskin, Z. Yu, N. Grigorieff, J. Struct. Biol. 184 (3) (2013) 385–393.
[70] L. Jin et al., J. Struct. Biol. 161 (3) (2008) 352–358.
[71] B.E. Bammes et al., J. Struct. Biol. 177 (3) (2012) 589–601.
[72] G. McMullan et al., Ultramicroscopy 147 (2014) 156–163.
[73] A.F. Brilot et al., J. Struct. Biol. 177 (3) (2012) 630–637.
[74] X. Li et al., Nat. Methods 10 (6) (2013) 584–590.
[75] R. Ramachandra et al., Microsc. Microanal. 20 (3) (2014) 706–714.
[76] X. Li et al., J. Struct. Biol. 184 (2) (2013) 251–260.
[77] S.H. Scheres, Elife 3 (2014) e03665.
[78] X.C. Bai et al., Elife 2 (2013) e00461.
[79] S. Pfeffer et al., Nat. Commun. 6 (2015) 6019.
[80] C.L. Stewart, K.J. Roux, B. Burke, Science 318 (5855) (2007) 1408–1412.
[81] U. Aebi et al., Nature 323 (6088) (1986) 560–564.
[82] Y. Gruenbaum, O. Medalia, Curr. Opin. Cell Biol. 32C (2015) 7–12.
[83] C.Y. Ho, J. Lammerding, J. Cell Sci. 125 (Pt 9) (2012) 2087–2093.
[84] M. Zwerger, O. Medalia, Histochem. Cell Biol. 140 (1) (2013) 3–12.
[85] A.E. Goldman et al., Proc. Natl. Acad. Sci. USA 83 (11) (1986) 3839–3843.
[86] D.W. Fawcett, Am. J. Anat. 119 (1) (1966) 129–145.
[87] J.G. Gall et al., Exp. Cell Res. 296 (1) (2004) 28–34.
[88] R. Stick, M.W. Goldberg, Methods 51 (1) (2010) 170–176.
[89] E. Grossman et al., J. Struct. Biol. 177 (1) (2012) 113–118.
[90] E. Grossman, O. Medalia, M. Zwerger, Annu. Rev. Biophys. 41 (2012) 557–584.
[91] N. Elad et al., Curr. Opin. Struct. Biol. 19 (2) (2009) 226–232.
[92] R. Reichelt et al., J. Cell Biol. 110 (4) (1990) 883–894.
[93] D. Frenkiel-Krispin et al., J. Mol. Biol. 395 (3) (2010) 578–586.
[94] F. Forster et al., Proc. Natl. Acad. Sci. U.S.A. 102 (13) (2005) 4729–4734.
[95] K.H. Bui et al., Cell 155 (6) (2013) 1233–1243.
[96] D. Stoffler et al., J. Mol. Biol. 328 (1) (2003) 119–130.
[97] B. Fahrenkrog, U. Aebi, Nat. Rev. Mol. Cell Biol. 4 (10) (2003) 757–766.
[98] S. Wiesner, A. Lange, R. Fassler, Trends Cell Biol. 16 (7) (2006) 327–329.
[99] K. Burridge et al., Annu. Rev. Cell Biol. 4 (1988) 487–525.
[100] V. Vogel, M. Sheetz, Nat. Rev. Mol. Cell Biol. 7 (4) (2006) 265–275.
[101] M. Chrzanowska-Wodnicka, K. Burridge, J. Cell Biol. 133 (6) (1996) 1403–1415.
[102] O. Medalia, B. Geiger, Curr. Opin. Cell Biol. 22 (5) (2010) 659–668.
[103] I. Patla et al., Nat. Cell Biol. 12 (9) (2010) 909–915.
[104] N. Elad et al., J. Cell Sci. 126 (Pt. 18) (2013) 4099–4107.
[105] P.K. Mattila, P. Lappalainen, Nat. Rev. Mol. Cell Biol. 9 (6) (2008) 446–454.
[106] S. Sorrentino et al., Eur. J. Cell Biol. 94 (3–4) (2015) 129–138.
[107] A.D. Michelson, Platelets, third ed., Academic Press, 2012. p. 1398.
[108] J.H. Hartwig, M. DeSisto, J. Cell Biol. 112 (3) (1991) 407–425.
[109] J.S. Bennett, B.W. Berger, P.C. Billings, J. Thromb. Haemost. 7 (Suppl. 1) (2009) 200–205.
[110] B. Nieswandt, D. Varga-Szabo, M. Elvers, J. Thromb. Haemost. 7 (Suppl. 1) (2009) 206–209.
[111] M. Marko et al., Nat. Methods 4 (3) (2007) 215–217.
[112] A. Rigort et al., Proc. Natl. Acad. Sci. USA 109 (12) (2012) 4449–4454.
[113] K. Wang et al., J. Struct. Biol. 180 (2) (2012) 318–326.
[114] C. Hsieh et al., J. Struct. Biol. 185 (1) (2014) 32–41.
[115] B.D. Engel et al., Elife 4 (2015) e04889.
[116] L.A. Giannuzzi, F.A. Stevie, Introduction to Focused Ion Beams: Instrumentation, Theory, Techniques and Practice, Springer, 2005.
[117] A. Guesdon et al., J. Struct. Biol. 181 (2) (2013) 169–178.

[118] D.N. Mastronarde, J. Struct. Biol. 120 (3) (1997) 343–352.
[119] A. Walter et al., Ultramicroscopy 153C (2015) 22–31.
[120] C. Best, S. Nickell, W. Baumeister, Methods Cell Biol. 79 (2007) 615–638.
[121] A.S. Frangakis et al., Proc. Natl. Acad. Sci. USA 99 (22) (2002) 14153–14158.
[122] M. Xu, M. Beck, F. Alber, Bioinformatics 27 (13) (2011) i69–i76.
[123] C.P. Mercogliano, D.J. DeRosier, J. Mol. Biol. 355 (2) (2006) 211–223.
[124] S.S. Lam et al., Nat. Methods 12 (1) (2015) 51–54.
[125] V.A. Gold et al., Nat. Commun. 5 (2014) 4129.
[126] T. Yahav et al., Curr. Opin. Struct. Biol. 21 (5) (2011) 670–677.

JOURNAL OF THE MECHANICAL BEHAVIOR OF BIOMEDICAL MATERIALS 63 (2016) 35–43

Available online at www.sciencedirect.com

ScienceDirect

www.elsevier.com/locate/jmbbm

Short Communication

The assembly of *C. elegans* lamins into macroscopic fibers

Irena Zingerman-Koladko[a], *Maayan Khayat*[b], *Jan Harapin*[c], *Oded Shoseyov*[d], *Yosef Gruenbaum*[e], *Ahmad Salman*[f], *Ohad Medalia*[a,c], *Kfir Ben-Harush*[b,*]

[a]*Department of Life Sciences and the National Institute for Biotechnology in the Negev, Ben-Gurion University of the Negev, Ben-Gurion Av. 1, 8410501 Beer-Sheva, Israel*
[b]*Department of Chemical Engineering, SCE – Shamoon College of Engineering, Jabotinsky 84, 77245 Ashdod, Israel*
[c]*Department of Biochemistry, University of Zurich, Winterthurerstrasse 190, 8057 Zurich, Switzerland*
[d]*The Robert H. Smith Institute of Plant Science and Genetics in Agriculture, The Robert H. Smith Faculty of Agriculture, Food and Environment, The Hebrew University of Jerusalem, P.O. Box 12, 7612001 Rehovot, Israel*
[e]*Department of Genetics, The Alexander Silberman Institute of Life Sciences, The Hebrew University of Jerusalem, The Edmond J. Safra Campus – Givat Ram, 9190401 Jerusalem, Israel*
[f]*Department of Physiscs, SCE – Shamoon College of Engineering, Bialik, 84100 Beer-Sheva, Israel*

ARTICLE INFO

Article history:
Received 9 March 2016
Received in revised form
23 April 2016
Accepted 28 May 2016
Available online 4 June 2016

Keywords:
Nuclear lamins
Intermediate filaments
Biological fibers
Electron cryo-tomography
Stress–strain properties

ABSTRACT

Intermediate filament (IF) proteins are known mainly by their propensity to form viscoelastic filamentous networks within cells. In addition, IF-proteins are essential parts of various biological materials, such as horn and hagfish slime threads, which exhibit a range of mechanical properties from hard to elastic. These properties and their self-assembly nature made IF-proteins attractive building blocks for biomimetic and biological materials in diverse applications. Here we show that a type V IF-protein, the *Caenorhabditis elegans* nuclear lamin (Ce-lamin), is a promising building block for protein-based fibers. Electron cryo-tomography of vitrified sections enabled us to depict the higher ordered assembly of the Ce-lamin into macroscopic fibers through the creation of paracrystalline fibers, which are prominent in vitro structures of lamins. The lamin fibers respond to tensile force as other IF-protein-based fibers, i.e., hagfish slime threads, and possess unique mechanical properties that may potentially be used in certain applications. The self-assembly nature of lamin proteins into a filamentous structure, which is further assembled into a complex network, can be easily modulated. This knowledge may lead to a better understanding of the relationship in IF-proteins-based fibers and materials, between their hierarchical structures and their mechanical properties.

*Corresponding author.
E-mail address: kfirb@sce.ac.il (K. Ben-Harush).

http://dx.doi.org/10.1016/j.jmbbm.2016.05.037
1751-6161/

1. Introduction

Biological materials execute diverse mechanical tasks in nature (Chen et al., 2008). Through evolution, their building blocks and structural design have been optimized in order to cope with a variety of environmental factors and tasks. The study of biological materials and biomimetic materials has gained interest, particularly for their potential use as alternatives for a variety of materials required by humans, especially in regenerative medicine and medical devices (Miserez et al., 2015). Among biological materials, protein-based fibers are under intense scrutiny for their exceptional mechanical properties, which combine elasticity and toughness (Gosline et al., 2002; Miserez and Guerette, 2013). Biological fibers such as spider and cocoon silks are widely used as biological materials in diverse applications (Omenetto and Kaplan, 2010). They have been elucidated in great detail in terms of structure and mechanical properties (Lintz and Scheibel, 2013). However, a complete description of their hierarchical structure and assembly pathway is still underway (van Beek et al., 2002). Another example is the native hagfish slime threads (Winegard et al., 2014), which have been shown to possess mechanical properties that are comparable to spider silk fibers (Negishi et al., 2012). The micrometer-sized slime threads are built from two intermediate filament (IF) proteins (α and γ) that are homologous to epidermal keratin (Koch et al., 1995). Due to the combination of impressive mechanical performance and the self-assembly nature of IF-proteins (Herrmann and Aebi, 2004), the slime threads have been proposed as biomimetic models for creating protein fibers and biomaterials with remarkable mechanics (Fudge et al., 2010). Thus, a study on vimentin, a type III cytoplasmic IF protein, showed that it can be assembled into tough fibers (Pinto et al., 2014) that, with further optimization, can reach the extraordinary mechanical properties of native hagfish threads. An improvement in fiber strength was achieved by self-assembly of recombinant vimentin into native-like 10-nm filaments, a prominent structure formed by cytoplasmic IF-proteins. It was suggested that a secondary structure transition of α-helix to β-sheets is a major contributor to strength in IF native fibers, similar to slime threads and keratin fibers (Fudge et al., 2003; Kreplak et al., 2004). In this study, we used the *Caenorhabditis elegans* lamin (Ce-lamin) as a potential building block for new macroscopic protein-based fibers (Karabinos et al., 2003).

Lamins are classified as being either A or B type (Dittmer and Misteli, 2011). Together they form a composite filaments network at the periphery of the nucleus, the nuclear lamina (Aebi et al., 1986; Shimi et al., 2008), which functions as an elastic shell (Dahl et al., 2004; Rowat et al., 2005). In vitro studies show that lamins, like all IF-proteins, consist of a central α-helical coiled-coil domain flanked by a non-α-helix 'head' and 'tail' domain. Two central α-helical domains interact to form a lamin dimer (Stuurman et al., 1998). Furthermore, lamin dimers from diverse organisms tend to form paracrystalline fibers in vitro (Heitlinger et al., 1991; Moir et al., 1991; Sasse et al., 1998). Interestingly, Ce-lamin, similar to that of mammalian lamins, forms paracrystalline fibers. In general, paracrystalline arrays have been observed in other assemblies of fibrous proteins such as collagen (Kadler et al., 1996). The variety of banding patterns that have been observed in these assemblies is mainly dependent on protein sequence, structural domains, and assembly pathways. Paracrystalline fibers assembled from lamins have been studied intensively using electron cryo-tomography (Bank et al., 2011; Ben-Harush et al., 2009; Taimen et al., 2009). These studies suggest that paracrystalline fibers are assembled in four hierarchical assembly steps (Fig. 5). First, lamin monomers coiled around each other to form a coiled-coil dimer, which is ~55 nm in length and ~2 nm thick. These dimers associate in head-to-tail fashion, with a short overlap, to form a head-to-tail polymer of dimers. Along the head-to-tail polymer axis, the distance between dimeric tails is around 48 nm (Ben-Harush et al., 2009; Stuurman et al., 1998). Next, two head-to-tail polymers interact laterally and in antiparallel fashion to form tetrameric protofilaments, ~4 nm diameter in cross-section. The distance between dimeric tails along the protofilament alternates between 21 and 27 nm, which is the result of staggered association between two head-to-tail polymers of dimers. The last step is the lateral association of protofilaments into Ce-lamin filaments or paracrystalline fibers. Therefore, the banding pattern along the paracrystalline fibers represents the distance between the C-terminus tail domains.

Ce-lamin forms stable 10-nm IF-native-like filaments, in which the proteins arrange similarly as in paracrystalline fibers. Hence, structural elements of paracrystalline fibers assemblies might keep one of the native-like structures of lamin filaments. Here, we used conditions favoring the self-assembly of Ce-lamin into paracrystalline fibers to create a network of microfibers, which then were mechanically spun into tough macroscopic fibers. Paracrystalline lamin fibers were further assembled into macroscopic fibers that resembled vimentin fibers and native hagfish threads in their response to tensile force. Therefore, simple Ce-lamin preparation might serve as a platform to better understand the relationship between hierarchical structure and mechanical properties in IF-based materials.

2. Material and methods

2.1. *Ce-lamin expression and purification*

Ce-lamin was expressed using BL21DE3 Rosetta plysS bacteria containing plasmid encoding *lmn-1* (NC_003279.8), and was induced using IPTG. Three hours after induction, bacteria were harvested by centrifugation. The resulting pellet was suspended in a re-suspension buffer (20 mM Tris–HCl pH=7.6, 200 mM NaCl, 1 mM EDTA, 1% v/v Triton and 1:10,000 v/v Calbiochem Protease Inhibitor Cocktail Set III). The bacterial suspension was sonicated, inclusion bodies were washed twice with the re-suspension buffer, and then incubated with 20 unit/mL Benzonaze Nuclease (Novagen, Denmark) for 30 min. Inclusion bodies were centrifuged again at 8000 g for 10 min, then dissolved in a urea buffer (20 mM Tris–HCl pH=7.6, 50 mM NaCl, 6 M urea). Lastly, the suspension was centrifuged at 16,000 g, for 1 h at 4 °C and the supernatant was kept for SDS-PAGE analysis and further use.

2.2. Protein assembly and preparation of lamin fibers

Ce-lamin (1.0 mg/ml) in a 6 M urea-containing buffer was dialyzed against 15 mM Tris–HCl, pH 7.6, 1 mM DTT for 2 h at room temperature, followed by a 3 h dialysis against 25 mM Tris–HCl, pH 9.0, 20 mM $CaCl_2$, 1 mM DTT. Throughout the dialysis process the orientation of the dialysis bags was kept in the vertical position, which was a crucial matter for the creation of a long microfibers network that facilitates fiber spinning (when the dialysis bag is horizontal, aggregation of paracrystalline fibers is formed at the second dialysis step). Next, the dialysis bags were exposed to isopropanol for 5 min, while the macroscopic fibers were spun out of the solution in a rotating manner and kept in the dialysis buffer (non-drawn fibers). For cryo-sectioning, the microfibers were spun down at the end of the second dialysis stage at 4000 g, for 10 min.

2.3. Mechanical characterization of Ce-lamin fibers

Fibers were mounted onto a cardstock paper frame and glued at both ends using super glue (Scotch). Fiber length was measured using a standard ruler. Tensile testing was performed using an Instron single column universal testing machine (Instron model 3345) with a 100 N load cell, at room temperature, 50% humidity, and a crosshead speed of 0.3 mm/min. All wet fibers ($n=8$) were dried by pulling during testing until an elevation in stress was observed. Fiber diameters were measured using SEM images of post-testing fibers. Therefore, breaking stress was calculated as the engineering stress at failure, and breaking strain was calculated as the strain (d_L/L_0) at failure. Young's modulus was calculated as the slope of the stress–strain curve at the elastic region of the curve prior to the yield point. Toughness at failure was calculated by measuring the area under the stress–strain curve.

2.4. FTIR measurements

Nicolet spectrometer with MCT detector (nitrogen cooled detector) was used. The fibers were mounted on zinc selenide crystals that are transparent to infrared radiation. Using the microscope attached to the infrared spectrometer, we carefully choose the measured areas, which were not in the edge sites. The measured spot has a square shape with side length of 100 μm. The measurements were performed in the transmission mode in the spectral range of 650–4000 cm^{-1}. Each spectrum was measured for 45 s resulting on 128 co-added scans for each individual spectrum.

In order to compare among the spectra measured from different fibers, sited and days all the spectra were manipulated using OPUS 7 software (BRUKER Germany). All the spectra were smoothed using Savitzky–Golay algorithm 13 points. The smoothed spectra were cut in the amide I region 1600–1720 cm^{-1}; baseline corrected using "concave rubberband" method with 5 sections and 2 iterations. Using rubberband method the spectrum was divided into 5 regions, a polynomial fit was performed using the minima in all the sections and then subtracted from the original spectrum. This procedure was repeated as the number of iteration (2 times in our case). The baseline corrected spectra were normalized using min-max normalization. Using min-max normalization the minimum y-value becomes zero and the maximum y-value in the specific range is expanded in the y-direction to 2 absorbance units.

2.5. Optical polarization microscopy

Fibers were deposited onto a clean glass microscope slide. Samples were viewed on an Olympus SZX9 microscope at $\times 10$ magnification.

2.6. Scanning electron microscope (SEM)

Electron microscope images were acquired using a Zeiss Ultra55 high resolution scanning electron microscope (HRSEM). Samples were mounted on the SEM holder using double-sided carbon tape. In order to avoid charging, low voltage (1 kV) and low current were set as the working conditions.

2.7. Cryo-sectioning of Ce-lamin microfibers

Lamin microfibers were spun down to the bottom of a 2.0 ml tube. Samples were gently dislodged from the bottom of the tube with a toothpick and the preparation buffer (second dialysis buffer) was exchanged for the fixative mixture. The mixture included 2% formaldehyde and 2.5% glutaraldehyde; the samples were left in the mixture for 2 h. The time and composition were adjusted to the thickness of the sample. Both fixatives were prepared in the preparation buffer. Post fixation, the hardened pellets were chopped into small cubes of approximately 1 mm^3 and transferred into a new tube with 2.5 M sucrose, in water. Samples were infiltrated with sucrose overnight at 4 °C with gentle rotation. A single sample cube was subsequently frozen on a cryo-ultramicrotome aluminum pin by immersion into liquid nitrogen. This was repeated several times in order to produce several samples for cryo-sectioning. Trimming was carried out at −75 °C with a 100 nm feed at a speed of 40 mm/s, using a trimming knife (Cryo trim 45°, Diatome). Cryo-sectioning was carried out at a speed of 0.4-0.6 mm/s at −105 °C using a sectioning knife (Cryo immuno 35°, Diatome). Sections of 200 nm were collected from the cutting knife as five-section ribbons, picked up with a droplet of 2.3 M sucrose, applied to plasma-cleaned holey carbon-coated copper grids (Quantifoil), and left rehydrating in a pool of water for 2 h. Standard gold markers (BSA gold tracers, 10 nm, Aurion, EMS) were applied to the grids, followed by plunging them into liquid-nitrogen-cooled liquid ethane and transferring them to be stored (Bokstad et al., 2012).

2.8. Electron cryo-tomography

Five cryo-tomograms were acquired using a 300 kV Titan Kryos transmission electron microscope (FEI) equipped with a Gatan post-column energy filter and a K2 summit director electron detector. Tilt series were acquired, covering an angular range of −60–60°; with 2° tilt increments and a defocus of −6 μm, resulting in a pixel size of 0.34 nm at the specimen level. Projection images were aligned to a common origin using fiducial gold markers, and reconstructed by means of weighted

back-projection, as implemented by the TOM toolbox software package (Nickell et al., 2005).

3. Results and discussion

3.1. *Ce-lamin fiber formation*

Purification of the Ce-lamin protein from bacteria requires isolation under denaturing conditions. Thus, recombinant lamins expressed in *Escherichia coli* are deposited in 'inclusion bodies' and are isolated by high molar concentrations of chaotropic substances, e.g., urea. Therefore, the formation of Ce-lamin paracrystalline fibers is promoted by two assembly dialysis steps, in which divalent ions ($CaCl_2$) are used in the second step to yield paracrystalline fibers. Here, a network of microfibers was detected 15 min after lamins were introduced to the divalent ions, and as the dialysis proceeded the network of microfibers was organized into a hollow cylinder-like structure (Fig. 1A and Fig. S1). Namely, the network of microfibers grew longitudinally with a defined thickness. The assembly mechanism by which Ce-lamin assembles into paracrystalline fibers that grow along the long axis of the dialysis bag and not inward is not clear. It might that the dialysis bag supports, at first, the buildup of the network.

In order to verify that a network of lamin microfibers was assembled from paracrystalline fibers, electron cryo-tomography of a vitrified section was applied to such preparations (Fig. 1A), demonstrating that, indeed, a lamin microfibers network is built from non-uniform paracrystalline assemblies that are interconnected at random orientations. This was also demonstrated by birefringence analysis of the dry non-drawn fibers (Fig. 2B). The lengths of the paracrystalline fibers vary from 350 to 1500 nm and their diameters vary from 30–200 nm. At the assembly conditions used here, it might that shorter and longer fibers exist, but it seems that the majority of the lengths and diameters of paracrystalline fibers lie at that range. The reason for the size limitation is not clear, although it is probably due the kinetics of the dimers assembly at the assembly condition that was used in this study. Other assembly conditions may lead to different organization and sizes of paracrystalline fibers within the microfibers network. Moreover, the banding pattern along the paracrystalline fibers alternates, on average, between 21 and 27 nm, which is identical to the banding pattern observed in individual paracrystalline fibers (Ben-Harush et al., 2009).

Next, we pull the network using a rotational movement to form the macroscopic Ce-lamin fiber (Fig. 1B), indicating that lamin wet macroscopic fibers are assembled from paracrystalline fibers. Hence, we conclude that the Ce-lamin macroscopic fibers are built from coiled-coil dimers that are assembled into higher-order structures that self-organized into paracrystalline fibers and eventually into a network of microfibers, suggesting that Ce-lamin wet fibers keep the structural integrity of lamins filaments, which probably retain the special mechanoelastic properties of intermediate filament proteins.

3.2. *The structural organization of Ce-lamin macroscopic fibers*

To learn about the mechanical properties of the macrofibers, Ce-lamin macroscopic fibers went through three pull procedures, with the first pull designed to dry the fiber (non-drawn

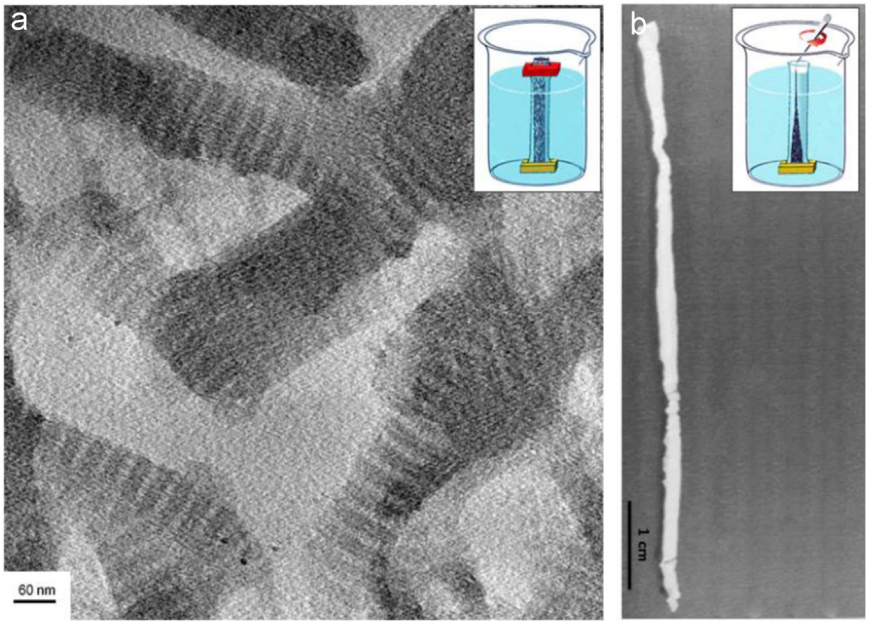

Fig. 1 – Ce-lamin macroscopic fiber and cryo-section of a microfibers network. (a) An electron micrograph projection from a tomographic reconstructed volume of a cryo-sectioned sample of a Ce-lamin microfibers network. Ce-lamin microfibers are comprised from paracrystalline fibers. Inset: Drawing of the Ce-lamin microfibers network inside the dialysis bag. (b) Ce-lamin wet macroscopic fiber produced from a mechanically spun microfibers network. Inset: Drawing of the step showing the spinning of Ce-lamin microfibers into wet fiber.

fibers) under a relatively constant tension force in order to avoid contraction (pre-drawn fibers). Fig. 2A shows that the fiber surface was relatively rough after the first pull and that it is built from straight microfibers. These results could indicate that the low force (Fig. 4) applied to the non-drawn fibers during the drying process only aligns the microfibers along the long axis of the macroscopic fiber. In addition, birefringence analysis demonstrates the lack of orientation within pre-drawn fibers. This might mean that while the microfibers are relatively aligned along the long axis of the fiber, the paracrystalline fibers within it are still randomly oriented.

The second pull was applied to the pre-drawn fibers until their breakage (single drawn fibers). The morphology of the single drawn fibers was smoother than the pre-drawn fibers and their birefringence was larger than that of the pre-drawn fibers, which could stem from additional compaction of the microfibers, and the reorientation and slippage of paracrystalline fibers within the microfibers. Other possible structural rearrangement may be focused on the slippage and compaction of protofilaments within paracrystalline fibers. Possible sliding of protofilaments may lead to intermolecular cross-link breakage. The divalent ion is known to prompt the assembly of paracrystalline fibers, probably by the lateral association of protofilaments. Therefore, sliding of protofilaments within paracrystalline fibers may lead to irreversible deformation of the paracrystalline fibers, and thus the fiber.

The third pull was applied to the single drawn fibers until breakage (double drawn fibers). The morphology of the double drawn fibers was a nanofibril-like structure (Fig. 2A), and their birefringence was larger than that of the single drawn fibers (Fig. 2B). It might be that additional structural arrangement, such as slippage of head-to tail polymers within protofilaments, which is associated with coiled-coil dimers sliding along the long axis of the protofilaments. Moreover, infrared absorption spectra of non- and double drawn fibers in the amide I region 1600–1720 cm^{-1} (Fig. 3), which is sensitive to secondary structure of proteins, demonstrate that the amide I absorption bands are larger in the double drawn fiber and has a clear shoulder in the 1670–1715 region. This shoulder may be due to high frequency vibrations of an antiparallel β sheets of amide I (Eckel, 2001). This analysis may suggest that uncoiling of the coiled-coil dimer has taken place concurrently with transition of the secondary structure to exhibit a more uniform surface. Such behavior has been previously shown for other IF-protein-based fibers.

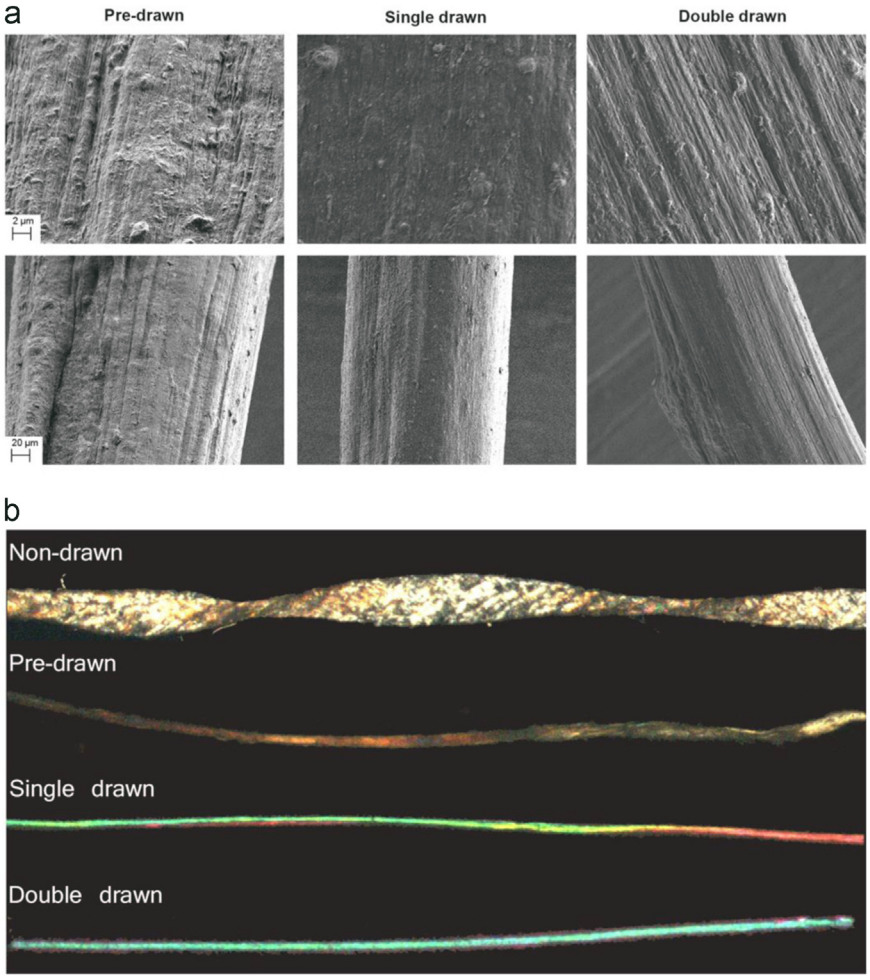

Fig. 2 – Structural organization of Ce-lamin fibers. (a) SEM images of Ce-lamin macroscopic fibers: pre-drawn, single drawn, and double drawn. Upper panel: higher magnification of lower panel. (b) Optical polarized microscopy of Ce-lamin macroscopic fibers: non-drawn, pre-drawn, single drawn and double drawn.

During the three pulling procedures, the possible compaction and slippage of paracrystalline fibers, protofilaments, and head-to tail polymers of dimers, is the main reason for the shrinkage in the diameters of the fibers (Table 1).

3.3. *Stress–strain properties of Ce-lamin fibers*

Stress–strain curves of single and double drawn fibers show mechanical behavior similar to dry vimentin fibers and native hagfish slime thread (Fig. 4). This demonstrates a common response of IF-protein assemblies to tensile force, where the elastic range of the single drawn dry fibers is relatively short (~5% strain) with modulus of resilience of ~1 MPa, and continues with long (~100% strain) plastic deformation until breakage (Table 1). The structural rearrangements described above were probably the major contributors to the long plastic deformation of the single drawn fibers, where cross-link bonds between building blocks were probably breaking. In addition, these structural rearrangements may be the reason that the length and mechanics of the dry fibers have not been recovered Fig. 5.

The stiffness of single drawn fibers (~1 GPa) was lower than in the double drawn fibers (~1.5 GPa), which can be attributed to the direct stretching of the relatively aligned and strained protofilaments/paracrystalline fibers in the single drawn fibers, when compared to direct stretching of the non-oriented paracrystalline within pre-drawn fibers. In addition to the first modulus, two other distinct moduli were observed

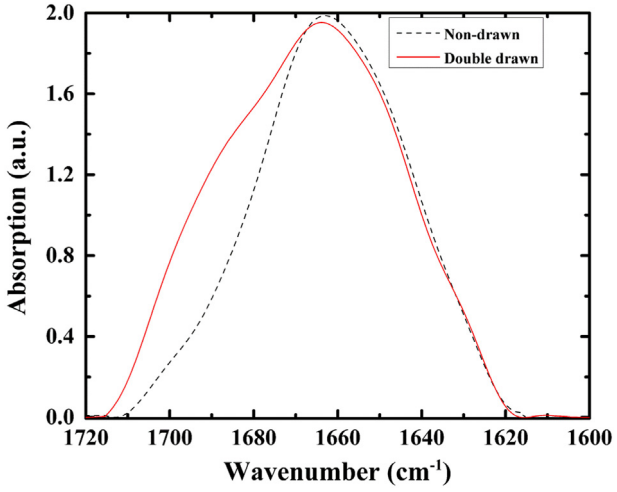

Fig. 3 – Infrared absorption spectra of non-drawn (dash line) and double drawn (solid line) fibers in the amide I region. Each spectrum is an average of at least 15 measurements performed from different fibers and different sites along the fibers.

in all double drawn fiber curves, which is similar to the behavior of the human patellar tendon (Svensson et al., 2013). Together, these three distinct regions might correspond to the structural arrangements of the fiber during stretching. Namely, the modulus (~1.5 GPa) of the first region (0–4% strain) may describe the direct pulling of protofilaments/paracrystalline fibers. The second region (4–11% strain) modulus (~0.6 GPa) may describe the compaction and sliding of head to tail polymers along the protofilaments. The third region (11–21% strain) modulus (~0.3 GPa) may describe the uncoiling of the coiled coil dimers. This mechanical behavior can explain the reason for the limited extensibility (~20%) and higher breaking strength of the double drawn fibers (~120 Mpa) when compared to single drawn fibers (100% and ~80 MPa). Overall, single drawn fibers (~55 MJ/m^3) are tougher than double drawn fibers (~17 MJ/m^3). The structural rearrangements in the second pull (single drawn fibers) are mainly the compaction and slippage of the paracrystalline fibers and protofilaments. These rearrangements are probably the major reason for the higher breaking strain, and thus to higher toughness. Finally, the mechanical response of the wet fiber to tensile force leads us to predict that lamin wet fibers behave in a manner similar to soft and elastic fibers. It should be emphasized that the first pull started with wet fiber and ended when the fiber became dry, resulting in a force elevation. Generally, the wet fibers reached ~100% strain, which could attribute to the alignment and rearrangement of the microfibers network.

The mechanical properties of Ce-lamin macroscopic fibers are similar to other protein-based fibers that show hierarchical self-assembly of coiled coil protein (Table 2), such as, other IF-proteins and collagen. The properties of such materials can reach the excellent mechanical properties of spider silk fibers, as in the case of hagfish slime threads. The high strength and toughness of spider silk fiber arises from two repetitive alanine- and glycine-rich areas leading to crystalline (β-sheet) and amorphous (3_{10}-helices and β-turn spirals) structures (Heidebrecht and Scheibel, 2013), which contribute to the high stiffness and flexibility, respectively. Therefore, understanding the mechanism of secondary structure transition taking place in IF-protein-based fibers, which might contribute to the high strength, is highly important. To be precise, we need to understand how the difference in amino acids sequence between the proteins that built the hagfish slime threads and other IF protein-based fibers, such as lamin fibers, affects the hierarchical structure and thus the secondary structural transition mechanism.

Table 1 – Average mechanical properties of Ce-lamin macroscopic fibers. The properties of pre-drawn, single, and double drawn fibers are displayed.

	Diameter (μm)	young's modulus (GPa)	break strain (d_I/L_0)	break stress (MPa)	Toughness (MJ/m^3)
Pre-drawn fibers	240±19.3	0.003±0.0001	1.05±0.04	2.8±0.26	1.71±0.13
Single drawn fibers	217±41.1	0.89±0.32	1.01±0.04	80.28±11.73	54.83±5.21
Double drawn fibers	185±39.9	1.57±0.17	0.21±0.04	120.29±26.46	16.73±4.87

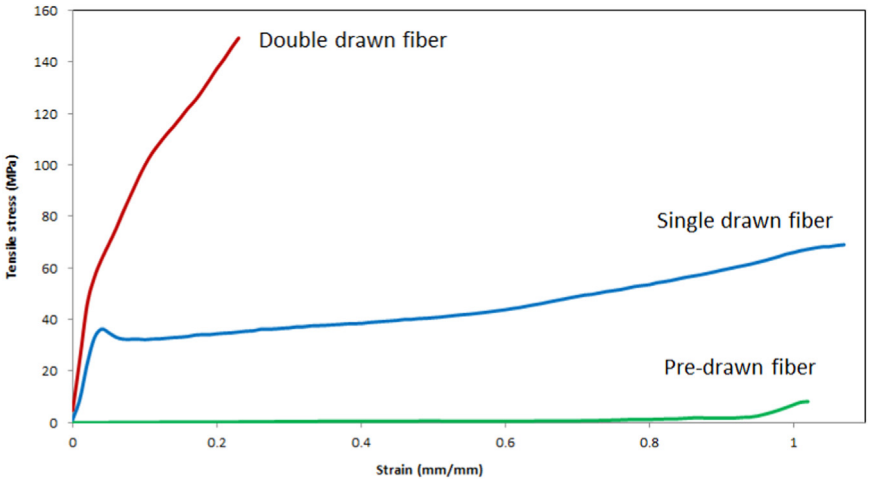

Fig. 4 – Stress–strain curves of pre-drawn (green), single (blue), and double drawn (red) Ce-lamin fibers. All curves represent one fiber sample of the 8 fibers tested. Pre-drawn fiber test was stopped when the fibers became dry and force elevation was observed. Single and double drawn fibers showed a typical IF-response to tensile force. In general, double drawn fibers are stiffer but much less extensible. (For interpretation of the references to color in this figure legend, the reader is referred to the web version of this article.)

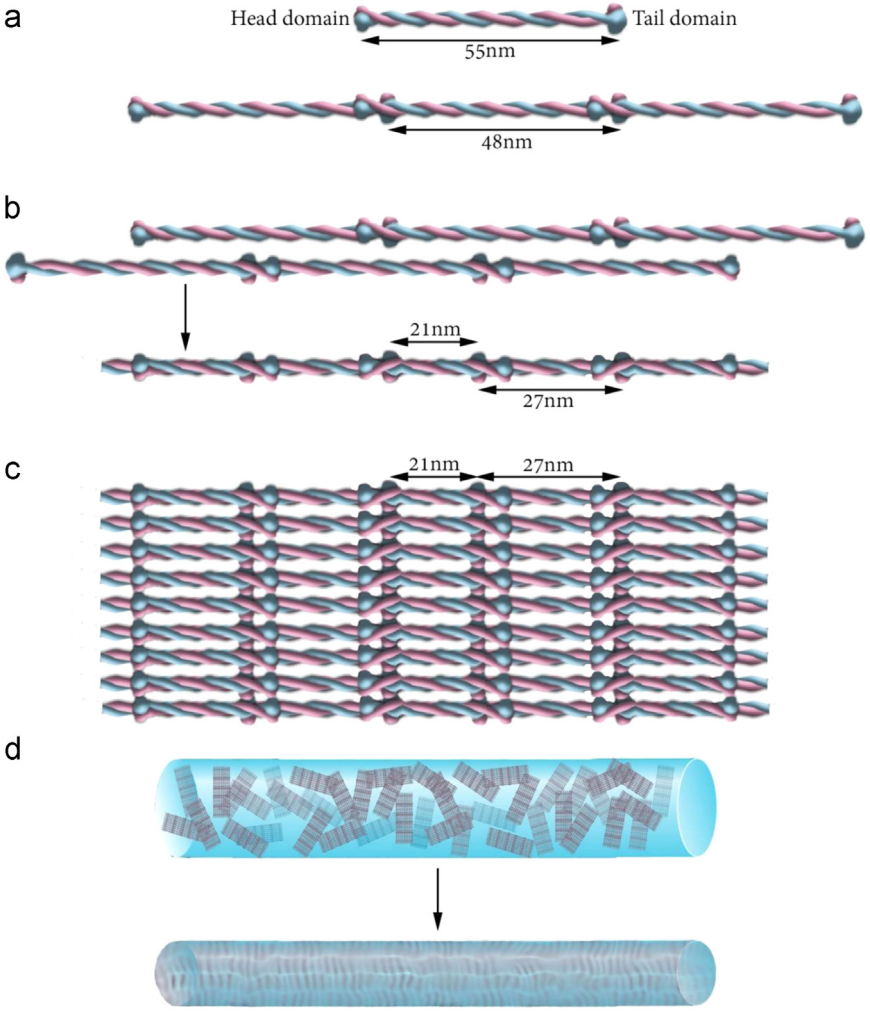

Fig. 5 – An assembly model of Ce-lamin dimers into macroscopic fibers. (a) Ce-lamin dimer and head-to-tail polymer of dimers. (b) Lateral association of two head-to-tail polymers into protofilament. (c) Lateral association of protofilaments into paracrystalline fibers. (d) A network of microfibers assembled from interconnected paracrystalline fibers spun into fiber. After stretching procedures, the paracrystalline fibers are oriented within Ce-lamin fibers.

Table 2 – Average mechanical properties of various biological fibers including the fibers tested in this study.

Protein	Break stress (MPa)	Young's modulus (GPa)	Break strain (d_I/L_0)
Keratin (wool) [1]	150	3	0.45
Hagfish slime (wet) [1]	180	0.006	2.2
Hagfish slime (dry) [1]	530	7.7	1
Hagfish (single drawn, dry)[2]	706	7.99	0.36
Vimentin + Mg^{2+} (single drawn) [3]	42	1.6	1.1
Vimentin + Mg^{2+} (double drawn) [3]	96	2.2	0.4
Dragline silk [4]	544–1469	4.5–22.1	0.17–0.36
Silkworm Silk [5]	165–248	3.82–6.10	0.19–0.33
Recombinant spider silk (96-mer) [6]	508	21	0.15
Human pataellar tendon (HPT) [7]	65	0.66	0.14
Ce lamin single drawn	80.3	0.89	1.01
Ce lamin double drawn	120	1.57	0.21

[1] Ref. (Fudge and Gosline, 2004) [2] Ref. (Fudge et al., 2010) [3] Ref. (Fudge et al., 2010) [4] Ref. (Swanson et al., 2006) [5] Ref. (Cheung et al., 2009) [6] Ref. (Xia et al., 2010) [7] Ref. (Johnson et al., 1994).

4. Conclusions

In this study we have demonstrated that Ce-lamin assembles into tough macroscopic fibers with tensile properties similar to vimentin-based fibers, especially in their response to increased tensile force. Overall, lamins have shown a tendency to self-assemble into a dense fibrous structure that is utilized to produce materials with unique mechanical properties. These materials may render lamins into a good biomaterial in a variety of applications. Additionally, lamins play a major role in providing mechanoelastic protection to our genome by forming a composite filamentous network, the structure and mechanics of which are still unknown. In vitro, Ce-lamins assemble into native-like 10-nm filaments that are assembled from protofilaments. These filamentous structures are thought to exist within the nucleus (Harapin et al., 2015; Mahamid et al., 2016). Paracrystalline fibers, which are the major building blocks of the macroscopic fiber, are organized similarly to Ce-lamin 10-nm filaments. Thus, the experimental setup described here can be utilized to study, in vitro, the mechanics of all lamin assemblies from different sources. In addition, this setup may produce another tool to investigate the structural-mechanical properties relationship in IF protein-based fibers by introduction of human disease-linked mutations (Worman and Bonne, 2007), which are known to deform the structure and mechanics of the cell nucleus and alter the structure of paracrystalline fibers in vitro (Taimen et al., 2009; Wiesel et al., 2008).

Acknowledgments

This work was supported by an internal funding program of SCE – Shamoon College of Engineering to K.B-H and A.S, a Swiss National Science Foundation Grant (SNSF 31003A 159706/1), the Mäxi Foundation to O.M and GIF I-1289-412.13/2015 to Y.G. and O.M. We also thank the Center for Microscopy and Image Analysis of the University of Zurich. We also thank Yael Diskin Posner from the Chemical Support Unit at the Weizmann Institute of Science, for her help with the optical microscopy.

Appendix A. Supplementary material

Supplementary data associated with this article can be found in the online version at http://dx.doi.org/10.1016/j.jmbbm.2016.05.037.

REFERENCES

Aebi, U., Cohn, J., Buhle, L., Gerace, L., 1986. The nuclear lamina is a meshwork of intermediate-type filaments. Nature 323, 560–564, http://dx.doi.org/10.1038/323560a0.

Bank, E.M., Ben-Harush, K., Wiesel-Motiuk, N., Barkan, R., Feinstein, N., Lotan, O., Medalia, O., Gruenbaum, Y., 2011. A laminopathic mutation disrupting lamin filament assembly causes disease-like phenotypes in *Caenorhabditis elegans*. Mol. Biol. Cell 22, 2716–2728.

Ben-Harush, K., Wiesel, N., Frenkiel-Krispin, D., Moeller, D., Soreq, E., Aebi, U., Herrmann, H., Gruenbaum, Y., Medalia, O., 2009. The supramolecular organization of the *C. elegans* nuclear lamin filament. J. Mol. Biol. 386, 1392–1402.

Bokstad, M., Sabanay, H., Dahan, I., Geiger, B., Medalia, O., 2012. Reconstructing adhesion structures in tissues by cryo-electron tomography of vitrified frozen sections. J. Struct. Biol. 178, 76–83, http://dx.doi.org/10.1016/j.jsb.2011.10.013.

Chen, P.P.P.-Y., Lin, A.Y.-M.A., Meyers, M.A., Seki, Y., 2008. Biological materials: structure and mechanical properties. Prog. Mater. Sci. 53, 1–206, http://dx.doi.org/10.1016/j.pmatsci.2007.05.002.

Cheung, H.-Y., Lau, K.-T., Ho, M.-P., Mosallam, A., 2009. Study on the mechanical properties of different silkworm silk fibers. J. Compos. Mater. 43, 2521–2531, http://dx.doi.org/10.1177/0021998309345347.

Dahl, K.N., Kahn, S.M., Wilson, K.L., Discher, D.E., 2004. The nuclear envelope lamina network has elasticity and a compressibility limit suggestive of a molecular shock absorber. J. Cell Sci. 117, 4779–4786, http://dx.doi.org/10.1242/jcs.01357.

Dittmer, T., Misteli, T., 2011. The lamin protein family. Genome Biol. 12, 222, http://dx.doi.org/10.1186/gb-2011-12-5-222.

Eckel, R., 2001. Characteristic infrared spectroscopic patterns in the protein bands of human breast cancer tissue. Vib. Spectrosc. 27, 165–173, http://dx.doi.org/10.1016/S0924-2031(01)00134-5.

Fudge, D.S., Gosline, J.M., 2004. Molecular design of the alpha-keratin composite: insights from a matrix-free model, hagfish slime threads. Proc. R. Soc. London B Biol. Sci. 271, 291–299, http://dx.doi.org/10.1098/rspb.2003.2591.

Fudge, D.S., Hillis, S., Levy, N., Gosline, J.M., 2010. Hagfish slime threads as a biomimetic model for high performance protein fibres. Bioinspir. Biomim. 5, 035002, http://dx.doi.org/10.1088/1748-3182/5/3/035002.

Fudge, D.S., Gardner, K.H., Forsyth, V.T., Riekel, C., Gosline, J.M., 2003. The mechanical properties of hydrated intermediate filaments: insights from hagfish slime threads. Biophys. J. 85, 2015–2027, http://dx.doi.org/10.1016/S0006-3495(03)74629-3.

Gosline, J., Lillie, M., Carrington, E., Guerette, P., Ortlepp, C., Savage, K., 2002. Elastic proteins: biological roles and mechanical properties. Philos. Trans. R. Soc. Lond. B. Biol. Sci. 357, 121–132, http://dx.doi.org/10.1098/rstb.2001.1022.

Harapin, J., Börmel, M., Sapra, K.T., Brunner, D., Kaech, A., Medalia, O., 2015. Structural analysis of multicellular organisms with cryo-electron tomography. Nat. Methods 12, 634–636, http://dx.doi.org/10.1038/nmeth.3401.

Heidebrecht, A., Scheibel, T., 2013. Recombinant production of spider silk proteinsAdv. Appl. Microbiol.http://dxdoi.org/10.1016/B978-0-12-407679-2.00004-1.

Heitlinger, E., Peter, M., Lustig, A., Nigg, E.A., 1991. Expression of chicken lamin B2. Cell 113, 485–495.

Herrmann, H., Aebi, U., 2004. Intermediate filaments: molecular structure, assembly mechanism, and integration into functionally distinct intracellular scaffolds. Annu. Rev. Biochem. 73, 749–789, http://dx.doi.org/10.1146/annurev.biochem.73.011303.073823.

Johnson, G.A., Tramaglini, D.M., Levine, R.E., Ohno, K., Choi, N.Y., Woo, S.L.Y., 1994. Tensile and viscoelastic properties of human patellar tendon. J. Orthop. Res. 12, 796–803, http://dx.doi.org/10.1002/jor.1100120607.

Kadler, K.E., Holmes, D.F., Trotter, J.A., Chapman, J.A., 1996. Collagen fibril formation. J. Biochem. 316, 1–11, http://dx.doi.org/10.1042/bj3160001.

Karabinos, A., Schünemann, J., Meyer, M., Aebi, U., Weber, K., 2003. The single nuclear lamin of Caenorhabditis elegans forms in vitro stable intermediate filaments and paracrystals with a reduced axial periodicity. J. Mol. Biol. 325, 241–247, http://dx.doi.org/10.1016/S0022-2836(02)01240-8.

Koch, E.A., Spitzer, R.H., Pithawalla, R.B., Castillos, F.A., Parry, D.A. D., 1995. Hagfish biopolymer: a type I/type II homologue of epidermal keratin intermediate filaments. Int. J. Biol. Macromol. 17, 283–292, http://dx.doi.org/10.1016/0141-8130(95)98156-S.

Kreplak, L., Doucet, J., Dumas, P., Briki, F., 2004. New aspects of the alpha-helix to beta-sheet transition in stretched hard alpha-keratin fibers. Biophys. J. 87, 640–647, http://dx.doi.org/10.1529/biophysj.103.036749.

Lintz, E.S., Scheibel, T.R., 2013. Dragline, egg stalk and byssus: a comparison of outstanding protein fibers and their potential for developing new materials. Adv. Funct. Mater. 23, 4467–4482, http://dx.doi.org/10.1002/adfm.201300589.

Mahamid, J., Pfeffer, S., Schaffer, M., Villa, E., Danev, R., Kuhn Cuellar, L., Forster, F., Hyman, A.A., Plitzko, J.M., Baumeister, W., 2016. Visualizing the molecular sociology at the HeLa cell nuclear periphery. Science 351, 969–972, http://dx.doi.org/10.1126/science.aad8857.

Miserez, A., Guerette, P. a, 2013. Phase transition-induced elasticity of α-helical bioelastomeric fibres and networks. Chem. Soc. Rev. 42, 1973–1995, http://dx.doi.org/10.1039/c2cs35294j.

Miserez, A., Weaver, J.C., Chaudhuri, O., 2015. Biological materials and molecular biomimetics – filling up the empty soft materials space for tissue engineering applications. J. Mater. Chem. B 3, 13–24, http://dx.doi.org/10.1039/C4TB01267D.

Moir, R.D., Donaldson, A.D., Stewart, M., 1991. Expression in Escherichia coli of human lamins A and C: influence of head and tail domains on assembly properties and paracrystal formation. J. Cell Sci. 99, 363–372.

Negishi, A., Armstrong, C.L., Kreplak, L., Rheinstadter, M.C., Lim, L.T., Gillis, T.E., Fudge, D.S., 2012. The production of fibers and films from solubilized hagfish slime thread proteins. Biomacromolecules 13, 3475–3482, http://dx.doi.org/10.1021/bm3011837.

Nickell, S., Förster, F., Linaroudis, A., Del Net, W., Beck, F., Hegerl, R., Baumeister, W., Plitzko, J.M., 2005. TOM software toolbox: acquisition and analysis for electron tomography. J. Struct. Biol. 149, 227–234, http://dx.doi.org/10.1016/j.jsb.2004.10.006.

Omenetto, F.G., Kaplan, D.L., 2010. New opportunities for an ancient material. Science 329, 528–531, http://dx.doi.org/10.1126/science.1188936.

Pinto, N., Yang, F.C., Negishi, A., Rheinst??dter, M.C., Gillis, T.E., Fudge, D.S., 2014. Self-assembly enhances the strength of fibers made from vimentin intermediate filament proteins. Biomacromolecules 15, 574–581, http://dx.doi.org/10.1021/bm401600a.

Rowat, A.C., Foster, L.J., Nielsen, M.M., Weiss, M., Ipsen, J.H., 2005. Characterization of the elastic properties of the nuclear envelope. J. R. Soc. Interface, 63–69, http://dx.doi.org/10.1098/rsif.2004.0022.

Sasse, B., Aebi, U., Stuurman, N., 1998. A tailless Drosophila lamin Dm0 fragment reveals lateral associations of dimers. J. Struct. Biol. 123, 56–66, http://dx.doi.org/10.1006/jsbi.1998.4006.

Shimi, T., Pfleghaar, K., Kojima, S.I., Pack, C.G., Solovei, I., Goldman, A.E., Adam, S.A., Shumaker, D.K., Kinjo, M., Cremer, T., Goldman, R.D., 2008. The A- and B-type nuclear lamin networks: microdomains involved in chromatin organization and transcription. Genes Dev. 22, 3409–3421, http://dx.doi.org/10.1101/gad.1735208.

Stuurman, N., Heins, S., Aebi, U., 1998. Nuclear lamins: their structure, assembly, and interactions. J. Struct. Biol. 122, 42–66, http://dx.doi.org/10.1006/jsbi.1998.3987.

Svensson, R.B., Mulder, H., Kovanen, V., Magnusson, S.P., 2013. Fracture mechanics of collagen fibrils: influence of natural cross-links. Biophys. J. 104, 2476–2484, http://dx.doi.org/10.1016/j.bpj.2013.04.033.

Swanson, B.O., Blackledge, T.A., Summers, A.P., Hayashi, C.Y., Wanson, B.R.O.S., Lackledge, T.O.D.D.A.B., Ummers, A.D.A.M.P. S., 2006. Spider dragline silk : correlated and mosaic evolution in high-performance biological materials. Evolution 60, 2539–2551, http://dx.doi.org/10.1554/06-267.1.

Taimen, P., Pfleghaar, K., Shimi, T., Möller, D., Ben-Harush, K., Erdos, M.R., Adam, S. a, Herrmann, H., Medalia, O., Collins, F. S., Goldman, A.E., Goldman, R.D., 2009. A progeria mutation reveals functions for lamin A in nuclear assembly, architecture, and chromosome organization. Proc. Natl. Acad. Sci. USA 106, 20788–20793.

van Beek, J.D., Hess, S., Vollrath, F., Meier, B.H., 2002. The molecular structure of spider dragline silk: folding and orientation of the protein backbone. Proc. Natl. Acad. Sci. 99, 10266–10271, http://dx.doi.org/10.1073/pnas.152162299.

Wiesel, N., Mattout, A., Melcer, S., Melamed-Book, N., Herrmann, H., Medalia, O., Aebi, U., Gruenbaum, Y., 2008. Laminopathic mutations interfere with the assembly, localization, and dynamics of nuclear lamins. Proc. Natl. Acad. Sci. USA 105, 180–185, http://dx.doi.org/10.1073/pnas.0708974105.

Winegard, T., Herr, J., Mena, C., Lee, B., Dinov, I., Bird, D., Bernards, M., Hobel, S., Van Valkenburgh, B., Toga, A., Fudge, D., 2014. Coiling and maturation of a high-performance fibre in hagfish slime gland thread cells. Nat. Commun. 5, 1–5, http://dx.doi.org/10.1038/ncomms4534.

Worman, H.J., Bonne, G., 2007. Laminopathies: a wide spectrum of human diseases. Exp. Cell Res. 313, 2121–2133, http://dx.doi.org/10.1016/j.yexcr.2007.03.028.

Xia, X.-X., Qian, Z.-G., Ki, C.S., Park, Y.H., Kaplan, D.L., Lee, S.Y., 2010. Native-sized recombinant spider silk protein produced in metabolically engineered Escherichia coli results in a strong fiber. Proc. Natl. Acad. Sci. USA 107, 14059–14063, http://dx.doi.org/10.1073/pnas.1003366107.

Biophysical Journal
Article

Biophysical Society

Phosphorylation-Induced Mechanical Regulation of Intrinsically Disordered Neurofilament Proteins

Eti Malka-Gibor,[1] Micha Kornreich,[1] Adi Laser-Azogui,[1] Ofer Doron,[1] Irena Zingerman-Koladko,[2] Jan Harapin,[3] Ohad Medalia,[2,3] and Roy Beck[1,*]

[1]Raymond and Beverly Sackler School of Physics and Astronomy, Tel Aviv University, Tel Aviv, Israel; [2]Department of Life Sciences and the National Institute for Biotechnology in the Negev, Ben-Gurion University, Beer-Sheva, Israel; and [3]Department of Biochemistry, University of Zurich, Zurich, Switzerland

ABSTRACT The biological function of protein assemblies has been conventionally equated with a unique three-dimensional protein structure and protein-specific interactions. However, in the past 20 years it has been found that some assemblies contain long flexible regions that adopt multiple structural conformations. These include neurofilament proteins that constitute the stress-responsive supportive network of neurons. Herein, we show that the macroscopic properties of neurofilament networks are tuned by enzymatic regulation of the charge found on the flexible protein regions. The results reveal an enzymatic (phosphorylation) regulation of macroscopic properties such as orientation, stress response, and expansion in flexible protein assemblies. Using a model that explains the attractive electrostatic interactions induced by enzymatically added charges, we demonstrate that phosphorylation regulation is far richer and versatile than previously considered.

INTRODUCTION

In the past two decades it has been discovered that ~50% of human proteins are intrinsically disordered, i.e., they contain long peptide regions that do not fold into secondary or tertiary structures. The disordered regions contain a disproportionate number of phosphorylation sites, which are functionally crucial (1). In particular, assemblies of phosphorylation-rich intrinsically disordered proteins (IDPs) are associated with neurodegenerative diseases including amyotrophic lateral sclerosis and Alzheimer's, Parkinson's, and Charcot-Marie-Tooth diseases (2–4). Despite the significance of IDP *assemblies*, little is known about the phosphorylation regulation of their structural and mechanical properties.

Neurofilaments (NFs) make a valuable model system for the exploration of phosphorylation-driven interactions in IDP assemblies due to their high modularity in protein content and phosphorylation levels. In axons, NF proteins hierarchically form a filamentous network whose main roles are to provide the cell with its mechanical support and structure (5). Protein subunits co-assemble into 10 nm bottlebrush-like filaments (Fig. 1, *A* and *B*), where the filament backbone consists of the N-terminal domains. The long disordered C-terminal tail domains protrude outward and mediate inter-filament interactions and neuronal cytoskeletal organization (6,7).

The expression levels of NF proteins are modified during nerve growth or trauma, where changes in protein ratios are thought to accommodate the changing mechanical and structural needs of the nervous system. This modularity is enabled by three of the NF proteins, NF-L, NF-M, and NF-H, which are expressed in both the central and peripheral nervous systems (8,9). Their disordered tails, which govern the network organization, differ considerably in sequence, length, net charge, and charge distribution (Fig. 1, *C–F*; Table S1 in the Supporting Material).

Additional functional versatility is achieved by enzymatic regulation of tail charge distribution through phosphorylation and de-phosphorylation. The majority of the phosphorylation sites correspond to the serine residues of the Lys-Ser-Pro (KSP) repeat motifs. These repeats abound in the tail domains of NF-M and NF-H subunits and significantly alter their charges (10). For example, de-phosphorylation of the NF-H tail changes its total charge from −97 to −7 e, and its charge density from −0.14 to −0.01 e/amino acid (Fig. 1; Table S1). Given this significant charge difference, NF-M and NF-H phosphorylation is thought to govern the lateral extensions of NF tails, thereby regulating NF spacing, axonal caliber, and protein transport (7,11–14).

Submitted July 29, 2016, and accepted for publication December 29, 2016.

*Correspondence: roy@post.tau.ac.il

Eti Malka-Gibor and Micha Kornreich contributed equally to this work.

Editor: Jennifer Ross.

http://dx.doi.org/10.1016/j.bpj.2016.12.050

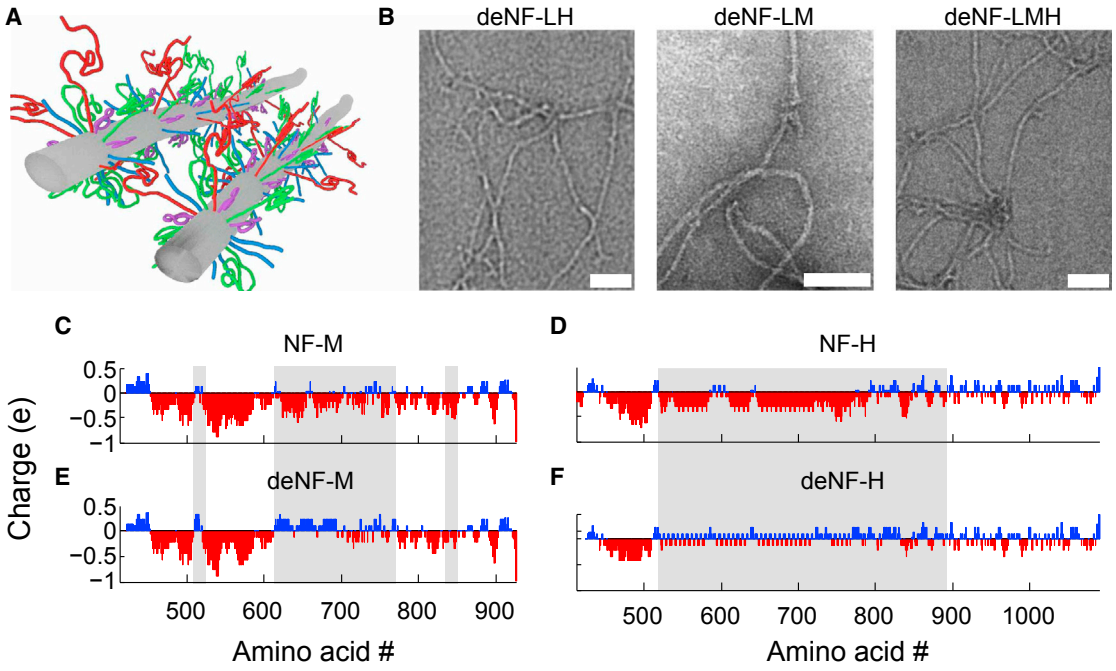

FIGURE 1 Structure of bottlebrush NF filaments. (*A*) A schematic of two neighboring interacting filaments. Each filament consists of three different subunit proteins whose protruding tails are shown in color (*red*, *blue* and *green*). (*B*) Transmission electron microscopy images of de-phosphorylated filaments (from *left* to *right*) NF-LH, NF-LM, and NF-LMH. Scale bar, 100 nm. (*C–F*) Tail charge distributions of (*C*) phosphorylated NF-M, (*D*) phosphorylated NF-H, (*E*) de-phosphorylated NF-M, and (*F*) de-phosphorylated NF-H. The charge distributions were calculated at pH 6.8 and averaged over a five-amino-acid window (see Materials and Methods). The gray-shaded areas highlight the protein segments that are most affected by the phosphate charge removal. To see this figure in color, go online.

These structural roles are the focus of a recent debate, after publication of a study that found no dependence of axonal caliber on the phosphorylation of NF-M (14,15).

Two seemingly contradictory effects can be attributed to the phosphorylation-induced charge regulation. On the one hand, phosphorylation enhances the electrostatic repulsion due to its excess charge. On the other hand, phosphorylation can promote short-range attractive cross-bridging between the disordered tails, as has been affirmed in cell-free experiments, cultured neurons, and in situ studies (16–24). Here, we address the structural and mechanical aspects of these two opposing phosphorylation effects. We show that NF assemblies have a distinctive phosphorylation-induced regulation of network properties, such as compression resistance and orientation. The regulation stems from the structural plasticity of the disordered tails and therefore differentiates between IDPs and structured-protein assemblies.

MATERIALS AND METHODS

Calculation of basic sequence-based properties

Protein sequences are imported from the UniProt database (25), and their identifiers are P02548 (NF-L), O77788 (NF-M), and P19246 (NF-H). Since there is not yet a UniProt-verified bovine NF-H sequence, the mouse NF-H sequence is used instead. Sequence-based calculations of NF tail charge are performed at pH 6.8 using the EMBOSS amino acid *p*Ka table (26). The average amino acid volume ($V_a = 0.134\ \mathrm{nm}^3$) is calculated using the values tabulated in (27). The phosphoserine sites are determined using the UniProt database, and the phosphoserine $p\mathrm{Ka}_2$ is set to 6.2 for charge calculations. Average tail charges and tail fraction charges appear in Table S1.

Protein purification

NF subunits (NF-L, NF-M, and NF-H) are purified from bovine spinal cord using a modification of an earlier protocol (28,29). Spinal cords are homogenized in an equal volume of buffer A (0.1 M MES, 1 mM EGTA, 1 mM $MgCl_2$, 0.02% (w/v) sodium azide, and 7 mM β-mercaptoethanol (pH 6.8 with NaOH) with 1% (w/v) Triton X-100 and 1 mM phenylmethylsulfonyl fluoride. The homogenates are centrifuged at 30,000 rpm (Beckman rotor type 45-Ti, Beckman Coulter, Brea, CA) for 70 min at 4°C. An equal volume of glycerol is added to the supernatant and incubated overnight. A pellet of NFs is recovered from the glycerol solution by precipitation at 40,000 rpm (Beckman rotor type 45-Ti) for 90 min at 4°C. The pellet is homogenized in buffer A with 0.8 M sucrose and clarified by spinning through a step gradient of 0.8 M sucrose buffer (0.8 M sucrose in buffer A) layered on top of 1.5 M sucrose buffer (1.5 M sucrose in buffer A) for 4 h at 55,000 rpm (Beckman rotor type 70-Ti). The pellet is homogenized in buffer B (0.1 M potassium phosphate and 0.1% (v/v) β-mercaptoethanol in 8 M urea (pH 6.5)), and applied to a DEAE sepharose column (DEAE Sepharose fast-flow column, GE Healthcare, Little Chalfont, United Kingdom). The column is rinsed with buffer B containing 55 mM NaCl, which elutes NF-H and protein contaminates. The next elution step, performed with buffer B at pH 7 containing 200 mM NaCl, elutes NF-L and NF-M. Using hydroxylapatite (HT) column chromatography

(hydroxylapatite biogel HT, Bio-Rad, Hercules, CA), the contaminants are removed from the NF-H fractions. NF-L and NF-M are separated by the HT column with a gradient of 0.1–0.4 M potassium phosphate (pH 7.0). The purity and separation of the NF-H, NF-M, and NF-L subunit proteins are verified by SDS-PAGE (Fig. S1).

Protein de-phosphorylation

For de-phosphorylated networks, purified proteins are dialyzed against de-phosphorylation buffer (50 mM Tris (pH 8), 100 mM NaCl, and 10 mM $MgCl_2$) and then incubated overnight with 50 units alkaline phosphatase (CIP, New England Biolabs, Ipswich, MA) per 0.1 mg protein at 37°C. The process is monitored by the decreased mobility of de-phosphorylated NF-M and NF-H in SDS-PAGE (30,31) (Fig. S1).

De-phosphorylation of NF-M is further supported by liquid chromatography-mass spectrometry performed at the Biological Services Department of the Weizmann Institute (Rehovot, Israel). Technical details are found in the Supporting Material.

We compare our results against the listed NF-M phosphosites in the UniProt database. We identified 7 of the 22 experimentally verified NF-M phosphosites, as well as seven of eight of the predicted phosphosites (25). None of the sites were phosphorylated (Table S2). Notably, since bovine NF-L tails contain only a few (1–3) phosphorylation sites (10), networks composed of recombinant and native NF-L proteins do not differ in inter-filament spacing, orientation, or compression response (32).

Filament self-assembly and hydrogel formation

After protein purification and de-phosphorylation, protein subunits are mixed in denaturing conditions at the desired composition. The protein solution is dialyzed against an MES buffer (100 mM MES (pH 6.8), 1 mM EGTA, 1 mM $MgCl_2$, 0.02% (w/v) sodium azide, 7 mM β-mercaptoethanol, and a total of 150 mM of NaCl and NaOH salts) at 37°C for 48 h.

For optical microscopy and small-angle x-ray scattering (SAXS), the reassembled filaments solution is centrifuged for 1 h at 50,000 RPM using a TLA100 rotor in a Beckman Coulter Optima TLX ultracentrifuge, and the supernatant is immediately removed from the pellet. The NF pellet is transferred to 1.5 mm quartz capillaries, overlaid with $\approx$ 100 μL MES buffer solution, and sealed with epoxy glue to prevent dehydration. To ensure that filaments remain intact after the centrifugation, we imaged a representative NF-L hydrogel using cryo-electron tomography (see Fig. S2 and Movie S1). In agreement with previous electron microscopy studies of the centrifuged hydrogels, we find a filamentous intertwined network (33).

To osmotically pressurize the network, the overlying MES buffer solution is supplemented with 20,000 g/mol polyethylene glycol (PEG) (34). The resultant PEG-induced osmotic pressure Π is determined by the PEG weight percentage (PEG_{wt}) and follows the formula $\log_{10}\Pi = 1.57 + 2.75(PEG_{wt})^{0.21}$. Samples that do not include PEG are diluted to the point that further buffer addition does not affect their inter-filament spacing (28,33). To overrule osmolyte interference with the NF network, we produce control hydrogels with the smaller 6000 g/mol PEG (35,36) (Fig. S3). At low osmotic pressure, the curves are in excellent agreement. At higher osmotic pressure, there are some discrepancies, but the general trend is unaltered.

To determine the protein molar ratios in the assembled hydrogel, control samples are analyzed by SDS-PAGE as described in (28,32). The protein molar ratios of the different hetero-filaments are 4:1 for NF-L/NF-H (denoted NF-LH), 7:3 for NF-L/NF-M (denoted NF-LM) and 10:3:2 for NF-L/NF-M/NF-H (denoted NF-LMH).

The NF-LM and NF-LH ratios used here follow previous works on NF hydrogels, which ensured that the preparation is well characterized for maximal reproducibility (for NF compositions given in weight percentages, see (32,37)). This makes it possible to compare the binary phosphorylated and de-phosphorylated networks to previous works.

Transmission electron microscopy

For transmission electron microscopy, a sample of 10 μL is laid on a formvar-coated 400 mesh grid (cat. no. 3440c-FA, SPI Supplies, West Chester, PA) and then fixed and negatively stained as in (38). Images of filaments composed of de-phosphorylated subunits are shown in Fig. 1 *B*, and resemble images of phosphorylated protein filaments (32,37).

Cryo-sectioning of NF-L hydrogel

Immediately before fixation, an NF-L hydrogel is spun down in a tabletop centrifuge (Eppendorf, Hamburg, Germany) at 14,000 rpm in 37°C for 30 min. The sample is then fixed for 30 min with 2% paraformaldehyde prepared in the filament assembly buffer and the fixative is removed and replaced by 2.5 M sucrose for overnight infiltration. The transparent gel is recovered with a pipette tip, cut into ~1 mm^3 cubes, glued onto cryo-sectioning pins with a small droplet of 2.5 M sucrose, and flash-frozen in liquid nitrogen.

Subsequent trimming is carried out at −75°C with a 100 nm feed and a speed of 40 mm/s using a trimming knife (Cryo trim 45, Diatome, Nidau, Switzerland). Cryo-sectioning is carried out at a speed of 0.4–0.6 mm/s at −105°C using a sectioning knife (Cryo immuno 35, Diatome). Sections of 200 nm are collected from the cutting knife as five-section ribbons, picked up with a droplet of 2.3 M sucrose, applied to plasma-cleaned holey carbon-coated copper grids (Quantifoil, Jena, Germany), and left rehydrating in a pool of double-distilled water for 2 h. Standard gold markers (bovine serum albumin gold tracers, 10 nm, Aurion, EMS, Wageningen, The Netherlands) are diluted 1:3 with the filament assembly buffer and applied to the grids. Grids carrying rehydrated sections and gold markers are frozen by plunging into liquid-nitrogen-cooled liquid ethane and stored.

Cryo-electron tomography

Data acquisition is carried out using a 300 keV FEI Polara (FEI, Eindhoven, The Netherlands) equipped with an energy filter (slit with 20 eV) and a direct electron detector (K2 summit, Gatan, Pleasanton, CA). Projection images are collected every 2°, covering a range from −60 to +60°, at a nominal magnification of 50,000× and de-focus of −6 μm, yielding a pixel size of 0.4221 nm at specimen level. Projection images are collected on the direct electron detector operated in counting mode (flux of 10 e/pixel/s) with individual exposures of 1.4 s per projection image that are then drift-corrected to yield the final image. Three-dimensional volumes are reconstructed using the Tomtoolbox package, and the data are binned two times, yielding a final pixel size of 1.68 nm at image data level.

Cross polarizing microscopy

The hydrogel orientation (isotropic or birefringent nematic) is characterized by cross-polarized light microscopy (Fig. 2). Sedimented NFs are observed in 1.5 mm quartz capillaries using a Nikon (Tokyo, Japan) Eclipse LV 100 POL microscope fitted with 5−20× objectives. Micrographs are taken with a Nikon D90 camera.

SAXS

NF hydrogel two-dimensional diffraction data were integrated azimuthally, and the intensity was plotted versus reciprocal distance q. The intensity, in arbitrary units, showed a broad peak with a maximum in the range $q = 0.1$–0.2 nm^{-1}. The peak location relates to the inter-filament spacing ($d = 2\pi/q$). Broadening of this peak is observed due to density fluctuations and the semi-flexible nature of the individual filaments. Baseline background of the form $A \times q^{-B} + C$, where $B = 2$–3, is subtracted from the

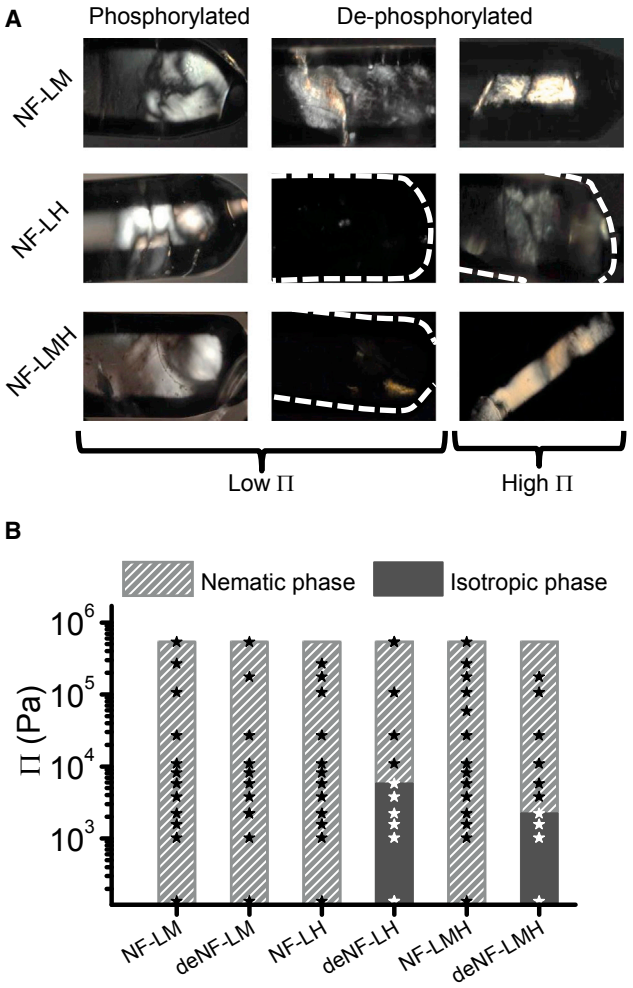

FIGURE 2 NF network phase behavior, as determined by cross-polarized microscopy. (*A*) Bright field and cross-polarized microscopy images of phosphorylated and de-phosphorylated networks at low (10^2–10^3 Pa) and high (10^5 to 2×10^5 Pa) osmotic pressure in quartz capillaries. White dashed lines demarcate the capillary boundaries, as observed with bright field (see Fig. S4). The filaments in all networks are aligned (nematic), except in the case of deNF-LM and deNF-LMH, where they are isotropic (i.e., un-oriented) at low Π. Each capillary is ~1.5 mm wide. (*B*) Phase diagram showing the network phase behavior at different osmotic pressures (Π). Each star denotes a measurement point. To see this figure in color, go online.

integrated data, and the resultant peak is fitted with a Lorentzian function using MATLAB (The MathWorks, Natick, MA) routines (37).

Preliminary experiments were performed at our home lab using a Pilatus (Stans, Switzerland) 300K detector and a Xenocs (Sassenage, France) GeniX low-divergence CuKα radiation source setup with scatterless slits (39). Subsequent measurements were performed with 10 keV at the following synchrotron facilities: the Diamond Light Source I22 beamline, United Kingdom; the Soleil SWING beamline, France; and the MAX-lab I911 SAXS beamline, Sweden.

Bulk modulus calculations

For these calculations, we treat filaments as infinitely long impenetrable cylinders of radius $R_{cyl} = 5$ nm set in a hexagonal lattice (Fig. S5; (40)). We define a prism-shaped unit cell whose base is an equilateral triangle with side length d, which is the inter-filament distance. The prism height is $l = 45$ nm, which is the NF protein's rod length. As 32 tails emanate from each filament backbone every 45 nm (41), the unit cell contains a total of $32/6 \times 3 = 16$ tails. The surface of the equilateral triangle found in the hexagonal model is $S(d) = \sqrt{3}d^2/4 - \pi R_{cyl}^2/2$, and therefore, the unit cell volume holds $V(d) = S(d) \times 45$ nm. The volume fraction is given by $\phi = NV_a/V$, where N is the number of tail amino acids in V. The Π -versus-d compression curves are fitted with smoothing splines (Fig. 3), and then used for the B_T calculation:

$$B_T = -V\frac{d\Pi}{dV} = -S(d)d\frac{d\Pi}{dd}\left(\frac{dV(d)}{dd}\right)^{-1}. \quad (1)$$

RESULTS AND DISCUSSION

We investigate the mechanical and structural roles of tail phosphorylation by reconstituting filaments from purified NF protein subunits at desired subunit compositions. To produce de-phosphorylated filaments, the natively phosphorylated proteins are enzymatically treated with alkaline phosphatase. Composite filaments include NF-L with either NF-M (NF-LM), NF-H (NF-LH), or both (NF-LMH). Formation of 10 nm wide filaments is verified by transmission electron microscopy (Fig. 1 *B*), as reported for native NFs (17,42). For simplicity, we refer to the de-phosphorylated filaments using a "de" prefix (i.e., deNF-LM, deNF-LH, or deNF-LMH).

At high concentrations, filaments condense into a hydrogel network that phase separates from the supernatant. To characterize the mechanical response of the network, we vary the osmotic pressure (Π) using a PEG osmolyte. All phosphorylated filaments, as well as deNF-LM filaments, form large oriented (nematic) domains, either at low or high osmotic pressures, as determined by cross-polarized microscopy. At low osmotic pressure, deNF-LH and deNF-LMH are isotropic and transition to a nematic phase at elevated osmotic pressure. Hence, NF-H phosphorylation regulates the macroscopic orientation of the hydrogel networks. (Fig. 2).

Although bottlebrush molecules rarely order in anisotropic phases (43), NF networks are nematic even without external pressure. This suggests that the NF tails promote anisotropic ordering, perhaps via attractive tail-tail interactions. Although it is clear that deNF-H hinders nematic organization, we find two results that suggest that deNF-M promotes such organization, similar to other NF tails. First, the low-osmotic-pressure deNF-LM networks are nematic. Second, the nematic transition of deNF-LMH occurs at a lower osmotic pressure than the transition of deNF-LH, despite the lower NF-L molar ratio in deNF-LMH.

Notably, the liquid crystalline behavior may also be affected by the persistence length of filaments, which was not measured due to the tendency of the long NFs produced in this study to interact and cluster (see Fig. 2). A

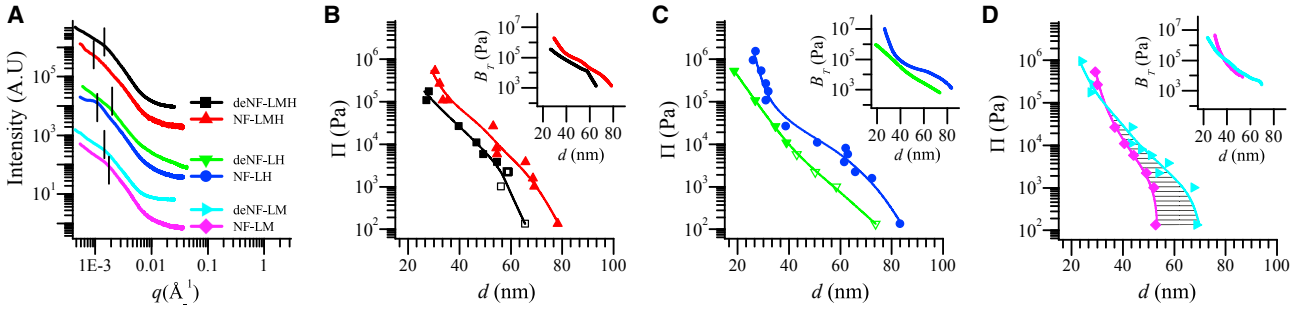

FIGURE 3 Comparison of native and de-phosphorylated networks using SAXS and osmotic pressure. (*A*) Intensity curves of NF-LH, NF-LM, and NF-LMH native and de-phosphorylated networks at 1% (w/w) PEG ($\Pi = 2.2 \times 10^3$ Pa). (*B–D*) Semi-log plot of osmotic pressure, Π, versus inter-filament distance, *d*, for different network compositions: (*B*) NF-LMH, (*C*) NF-LH, and (*D*) NF-LM. For calculation of *E* in Eq. 2, we integrate over the textured area in (*D*). The osmotic bulk modulus, B_T, is shown in the insets. The data are fitted with smoothing splines, which are then used to calculate B_T. Isotropic and nematic samples are denoted by solid and open symbols, respectively. Subunit molar ratios for native and de-phosphorylated NF-LM, NF-LH, and NF-LMH filaments are 7:3 (NF-L/NF-M), 4:1 (NF-L/NF-H) and 10:3:2 (NF-L/NF-M/NF-H). To see this figure in color, go online.

previous study, which focused on isolated short natively phosphorylated NF-LM and NF-LH filaments, reported 50- to 200-nm persistence lengths (42), which was a few times shorter than the typical filament length observed here (Fig. 1 *B*).

To study the nanoscopic structural organization and mechanics of the hydrogel, we measure the inter-filament spacing, *d*, using small-angle x-ray scattering (32,37,44). Azimuthally averaged intensity curves of phosphorylated (i.e., native) and de-phosphorylated networks at $\Pi = 2200$ Pa are shown in Fig. 3 *A*. For each intensity curve, the correlation peak position (q_0), denoted by a vertical line, is related to the inter-filament distance by $d = 2\pi/q_0$. At this given osmotic pressure, de-phosphorylation of NF-LMH and NF-LH results in a decrease of the inter-filament spacing from 70 to 58 nm and 67 to 50 nm, respectively. Therefore, native phosphorylation of NF-LH and NF-LMH results in network expansion. This agrees with the conventionally considered roles of NF phosphorylation, where the substantial addition of charged phosphate groups is naively expected to stretch the NF tails and consequently increase the inter-filament spacing. The Π -versus-*d* curves of NF-LH and NF-LMH exhibit the same phosphorylation-dependent effect over a wider range of osmotic pressures (Fig. 3, *B* and *C*).

In contrast, the correlation peak of deNF-LM shifts to lower *q*-values, in comparison to the NF-LM peak (Fig. 3 *A*). This indicates that the spacing actually increases from 48 to 60 nm due to de-phosphorylation. The result is atypical of charged polymers, as de-phosphorylation reduces the net charge by $\sim 50\%$, and thus, the electrostatic repulsion between adjacent filaments is expected to decrease. This behavior indicates an attractive interaction between phosphorylated tails, which opposes the trend observed in NF-LH and NF-LMH networks (Fig. 3, *B* and *C*). Notably, the expansion of deNF-LM in comparison to NF-LM is reversed only at high osmotic pressures, $\Pi \gtrsim 10^5$ Pa (Fig. 3 *D*).

The protein-dependent regulation of network expansion, alignment, and osmotic stress response is schematically summarized in Fig. 4, together with conjectured tails microscopic organization (Fig. 4, *C*, *D*, and *F*). Phosphorylation of the NF-H tail aligns the network and increases the inter-filament distance (Fig. 4 *A*). In contrast, NF-M phosphorylation has little effect on network alignment, and surprisingly, it *reduces* the inter-filament distance (Fig. 4 *B*). This indicates that NF-LM and NF-LH tails are organized differently.

At low osmotic pressures, tails are expected to form two distinctive layers, known as the flower conformation (Fig. 4 *C*). The inner-layer corona is composed of the short NF-L tails, whereas NF-H tails are repelled farther away from the corona into the outer layer. Since the tails within the outer layer are less dense, they assume a flower-like conformation (32,45,46). However, this picture does not agree with the NF-LM tail organization. The inter-filament spacing is very similar for NF-LM and NF-L networks (32,37), suggesting that the long NF-M tails are hidden within the NF-L inner coronas (termed the "truffle" regime) (32,40). Under significant osmotic pressure, all filament types align and compress, whereas opposite tails increasingly interpenetrate (Fig. 4, *E* and *F*).

In living cells, the osmotic pressure is induced by the crowded environment. We note that the effect of phosphorylation on the compression response is much more pronounced than its effect on NF expansion. In particular, phosphorylation at a given osmotic pressure, does not change the inter-filament spacing by more than 25%. However, to maintain the same spacing at the phosphorylated state, the osmotic pressure needs to increase by up to two orders of magnitude.

To further characterize this mechanical response, we calculate the osmotic bulk modulus, B_T, which quantifies the network's resistance to compression (Eq. 1; Fig. 3, *B–D*, *insets*). Similar to the phosphorylation-dependent network expansion and collapse, we find that changes to

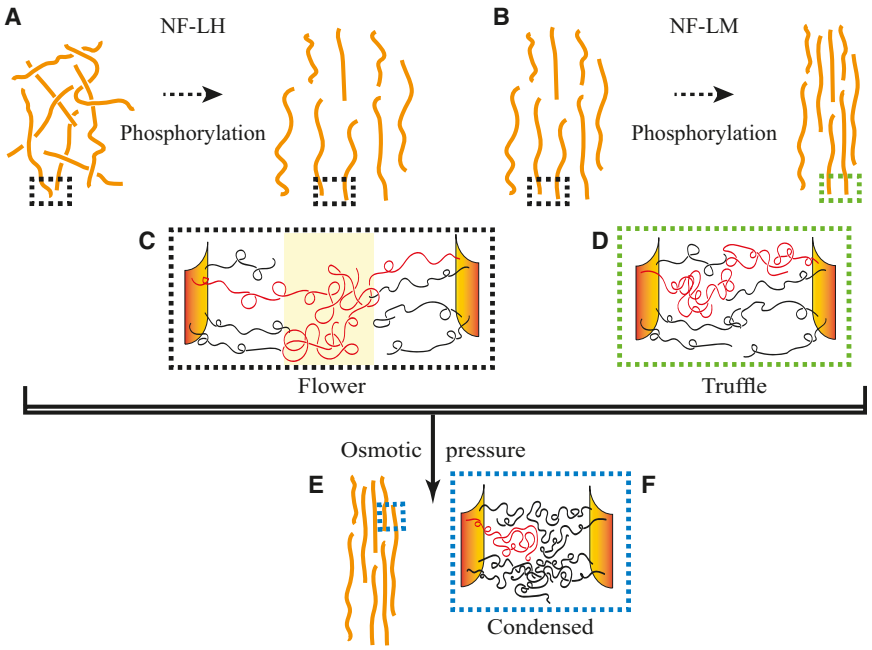

FIGURE 4 Schematic of phosphorylation regulation of NF network expansion, alignment, and osmotic stress response, together with the conjectured tail configuration. (*A* and *B*) NF-H phosphorylation aligns the isotropic deNF-LH network and increases the inter-filament distance (*A*), whereas NF-M phosphorylation collapses the nematic deNF-LM network (*B*). (*C* and *D*) Except for NF-LM networks, all protruding tails organize in two corona layers at low osmotic pressure. The outer layer is formed by the long tails (either NF-H or NF-M) and is denoted by yellow shading. Upon phosphorylation, deNF-LM tails transition from a flower (*C*) to a truffle conformation (*D*). (*E* and *F*) Under significant osmotic compression, filaments align and compress (*E*), whereas opposite tails increasingly inter-penetrate (*F*). To see this figure in color, go online.

the mechanical response are also protein specific. However, the effect of phosphorylation on the mechanical response is more pronounced, and B_T is altered by as much as an order of magnitude. For NF-LH and NF-LMH, de-phosphorylation of the tails reduces B_T at all values of d. In contrast, de-phosphorylation of NF-LM increases the network's resistance to compression (i.e., larger B_T) at low osmotic pressure. The latter occurs despite the reduced repulsive electrostatic forces and suggests that the charged phosphates also take part in attractive interactions (16,37). Further support for the excess electrostatic repulsion at high and low osmotic pressures is given by comparison to polymer scaling theories (Fig. S6).

Previous mechanical studies of various cytoskeletal elements (such as actin, vimentin, and NFs) used rheological tools to measure the shear moduli and viscosity (18,47–49). These studies focused on dilute isotropic solutions, whose elasticity arose from the constituting semiflexible cross-linked filament backbones (49,50). Our measurements, using the osmotic stress technique, enable us to measure the bulk modulus of composite NF networks. In contrast to the rheological studies, we investigate higher filament concentrations, where the NF hydrogels are typically anisotropic and biologically relevant (6,51). We show that the compression response of NFs arises from the disordered tails, whereas the shear moduli originate from the filament properties, such as their thermal motions. Nonetheless, both mechanical probes (shear and osmotic compression) are indeed affected by tail-mediated cross-linking interactions.

To estimate the attractive bridging energy per NF-LM phosphosite, we follow the calculation performed to quantify the attractive hydration energy between DNA double helices (52). The free energy is derived from the Π-d diagram under the hexagonal approximation. To evaluate the average energy per phosphosite (ϵ), we integrate over the free-energy difference between the two phosphorylation states and divide by the number of phosphosites in the volume (N_p):

$$\epsilon = -\frac{1}{N_p}\int_0^{\Pi_{int}} (V_{deNF-LM} - V_{NF-LM})d\Pi. \qquad (2)$$

The integration is performed on the fitted smoothing-spline curves from $\Pi = 0$ to the intersection of the curves at $\Pi_{int} \sim 10^5$ Pa (see the textured area in Fig. 3 *D*), and it yields approximately $\epsilon = -8\, k_B T$ per phosphosite. This is comparable to the free energy of protein salt bridges (53). Notably, the integration also includes contributions from repulsive interactions, and therefore, ϵ provides a lower limit for the attractive average energy per phosphosite.

Since these attractive interactions are sequence dependent, they may account for the opposite phosphorylation expansion trends of NF-LM and NF-LH. To identify the polypeptide segments involved in such attraction, we employ a coarse-grained "handshake" calculation aimed at locating pairs of amino acid segments that interact via electrostatic bridges (37). We calculate the unscreened Coulomb energy of two interacting segments, where each segment is centered at a specific tail amino acid and the segment length is on the order of the polypeptide persistence length (~3 nm (54)). We thus obtain a 2D matrix that points at the most electrostatically viable cross-linking pairs (Fig. 5 *A*).

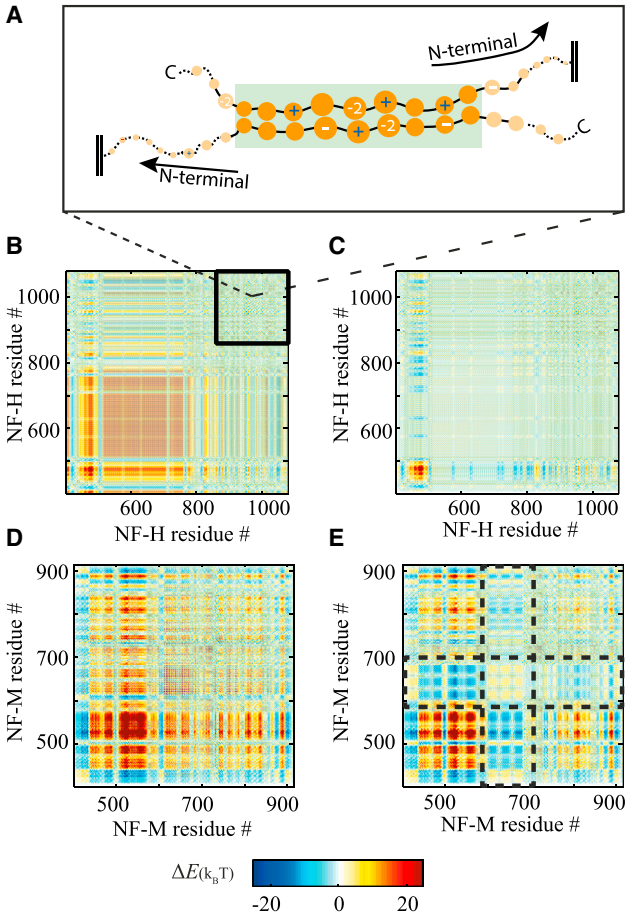

FIGURE 5 Handshake analysis of short-range electrostatic interactions between NF tail regions. (*A*) Two opposite nine-amino-acid-long segments interacting. Details of the electrostatic interaction energy calculations are found in (32,37). (*B–E*) Energy matrices for all possible segment pairs for two opposing NF-H (*B*), deNF-H (*C*), NF-M (*D*), or deNF-M (*E*) tails. Interactions between two oppositely charged segments, which are more electrostatically viable, are denoted in blue in the interaction matrices. The solid box in (*B*) marks the last 200 amino acids that are known to engage in attractive interactions. Dashed boxes in (*E*) denote phosphosite-rich segments (see also Fig. 1). Comparison of (*D*) with (*E*) reveals that de-phosphorylation forms new negative energy pairs between segments found farther away from the filament backbone. To see this figure in color, go online.

Handshake analysis of the natively phosphorylated NF-H tail reveals multiple potential attractive sites located among its last 200 amino acids (Fig. 5 *B*). This has also been described by a more elaborate theoretical calculation (19) and agrees with previous experiments (55). Upon de-phosphorylation, new attractive sites are predicted near the filament backbone (Fig. 5 *B*). These could participate in intra-filament attractive interactions, in agreement with the de-phosphorylated NF-H tail collapsed conformation (Fig. 3).

The unexpectedly collapsed conformation of phosphorylated NF-LM may involve interactions between NF-M segments and either NF-L or NF-M segments, as recently shown (32,40). Here, upon de-phosphorylation, new NF-M attractive binding sites are formed farther away from the filament backbone (Fig. 5, *D* and *E*). Consequently, the loss of the excess phosphate charge actually *expands* the NF-M tail, as shown in Fig. 3 *D*.

CONCLUSIONS

We demonstrate the roles of phosphorylation in regulating the structural and mechanical properties of NF networks. The phosphorylation-induced modifications strongly depend on the NF subunit composition and can result in either network expansion or collapse (Fig. 4). This versatility originates from the dual nature of the induced interactions, which are both repulsive and attractive and are protein-sequence dependent.

The attractive interactions are clearly manifested in the deNF-LM network, where the removal of the excess phosphate charges unexpectedly results in network expansion. This trend relates to previous studies suggesting that phosphorylation can promote NF binding either by associated proteins, by exposing hydrophobic residues, or by direct involvement in electrostatic bridging (16,18,19,21,22,24). Of these possibilities, our results affirm the direct involvement of NF-M phosphosites in attractive interactions, which is justified by the stronger ionic bridging formed between the divalent phosphate group and basic amino acids (Fig. 5).

The repulsive interactions govern the NF-LH and NF-LMH compression response. Here, phosphorylation moderately increases the inter-filament distance and considerably enhances the osmotic compression resistance, characterized by the bulk modulus (Fig. 3). Similarly, previous rheological studies of NF viscosity and shear modulus also found it to be highly phospho-dependent (18,21). This calls into question the hypothesized main structural role of tail phosphorylation, i.e., to expand the NF network, and suggests a primarily *mechanical* role for NF phosphorylation.

The individual roles of NF-M and NF-H phosphorylation, as demonstrated here, significantly increase opportunities to regulate NF network physical properties. Therefore, the roles of NF expansion (Fig. 3), mechanics (21) (Fig. 3) and orientation (51,56) (Fig. 2) must be considered where simultaneous changes in composition and tail phosphorylation levels are observed. Such changes occur, for example, during neuronal growth and development, after injury, and in neurodegenerative diseases (8,11,57). Specifically, our results indicate a close relation between phosphorylation and NF compression response and orientation. The latter has been considered only briefly in a previous review (6).

The relation between phosphorylation and orientation is closely associated with the noticeable bundling of NFs in axons, which is accompanied by increased cross-bridging and transport rate modification (5,24). Although these phenomena are commonly attributed to NF-H phospho-dependent interactions, we demonstrate how NF-M phosphorylation modulates NF associations. Interestingly,

NF-H knockout mice do not exhibit any NF transport defects, despite the well-established role of NF-H tail phospho-dependent interactions in NF transport. This surprising trend can be partially explained by our findings. We found that NF-M tail phosphorylation also modulates NF-NF association and may therefore compensate the NF-H deficiency, as previously suggested (58,59).

Additional assemblies of hyper-phosphorylated disordered proteins are typically involved in neurodegenerative diseases. These include the disordered τ and α-synuclein proteins, which are hyper-phosphorylated in pathological inclusions (2,3). Their aggregation is commonly attributed to an indirect process, where phosphorylation-driven conformational changes expose new segments for attractive interactions. However, the electrostatic attraction observed in phosphorylated NF-M tails demonstrates that phosphates in disordered protein assemblies *directly* engage in significant attractive interactions. This suggests that more attention should be drawn to the role of phosphorylation-driven attractive electrostatics in the study of disordered assemblies.

SUPPORTING MATERIAL

Seven figures, two tables, and one movie are available at http://www.biophysj.org/biophysj/supplemental/S0006-3495(17)30150-9.

AUTHOR CONTRIBUTIONS

R.B., A.L.A., E.M.-G., and M.K. planned and initiated the project. E.M.-G., M.K., A.L.A., O.D., I.Z.-K., J.H., and O.M. conducted the experiments. E.M.-G. and M.K. prepared the samples and analyzed the data. E.M.-G., M.K., and R.B. wrote the article.

ACKNOWLEDGMENTS

We are grateful to Dr. Geraisy Wassim of Beit Shean abattoirs Tnuva for kindly providing us with the spinal cords. We thank Ekaterina Zhulina for useful discussions and suggestions. We thank the following beamlines for SAXS measurements: the I911-SAXS at MAX IV Laboratory, Sweden; SWING at SOLEIL synchrotron, France; and the I-22 beamline at Diamond, United Kingdom.

This work was supported by the Israeli Scientific Foundation (571/11, 550/15), the Tel Aviv University Center for Nanoscience, Nanotechnology, the Abramson Center for Medical Physics,and the Scakler Institute for Biophysics at Tel Aviv University. Travel grants to synchrotron facilities were provided by BioStruct-X.

REFERENCES

1. Uversky, V. N. 2011. Intrinsically disordered proteins from A to Z. *Int. J. Biochem. Cell Biol.* 43:1090–1103.
2. Chen, L., and M. B. Feany. 2005. α-Synuclein phosphorylation controls neurotoxicity and inclusion formation in a *Drosophila* model of Parkinson disease. *Nat. Neurosci.* 8:657–663.
3. Stoothoff, W. H., and G. V. W. Johnson. 2005. Tau phosphorylation: physiological and pathological consequences. *Biochim. Biophys. Acta.* 1739:280–297.
4. Liu, Q., F. Xie, …, G. Perry. 2011. Neurofilamentopathy in neurodegenerative diseases. *Open Neurol. J.* 5:58–62.
5. Hirokawa, N., M. A. Glicksman, and M. B. Willard. 1984. Organization of mammalian neurofilament polypeptides within the neuronal cytoskeleton. *J. Cell Biol.* 98:1523–1536.
6. Safinya, C. R., J. Deek, …, Y. Li. 2015. Assembly of biological nanostructures: isotropic and liquid crystalline phases of neurofilament hydrogels. *Annu. Rev. Condens. Matter Phys.* 6:113–136.
7. Sihag, R. K., M. Inagaki, …, H. C. Pant. 2007. Role of phosphorylation on the structural dynamics and function of types III and IV intermediate filaments. *Exp. Cell Res.* 313:2098–2109.
8. Laser-Azogui, A., M. Kornreich, …, R. Beck. 2015. Neurofilament assembly and function during neuronal development. *Curr. Opin. Cell Biol.* 32:92–101.
9. Yuan, A., M. V. Rao, …, R. A. Nixon. 2012. Neurofilaments at a glance. *J. Cell Sci.* 125:3257–3263.
10. Trimpin, S., A. E. Mixon, …, M. L. Deinzer. 2004. Identification of endogenous phosphorylation sites of bovine medium and low molecular weight neurofilament proteins by tandem mass spectrometry. *Biochemistry.* 43:2091–2105.
11. Dale, J. M., and M. L. Garcia. 2012. Neurofilament phosphorylation during development and disease: which came first, the phosphorylation or the accumulation? *J. Amino Acids.* 2012:382107.
12. Kriz, J., Q. Zhu, …, A. L. Padjen. 2000. Electrophysiological properties of axons in mice lacking neurofilament subunit genes: disparity between conduction velocity and axon diameter in absence of NF-H. *Brain Res.* 885:32–44.
13. Ackerley, S., P. Thornhill, …, C. C. Miller. 2003. Neurofilament heavy chain side arm phosphorylation regulates axonal transport of neurofilaments. *J. Cell Biol.* 161:489–495.
14. Shea, T. B., C. Jung, and H. C. Pant. 2003. Does neurofilament phosphorylation regulate axonal transport? *Trends Neurosci.* 26:397–400.
15. Barry, D. M., W. Stevenson, …, M. L. Garcia. 2012. Expansion of neurofilament medium C terminus increases axonal diameter independent of increases in conduction velocity or myelin thickness. *J. Neurosci.* 32:6209–6219.
16. Aranda-Espinoza, H., P. Carl, …, D. E. Discher. 2002. Domain unfolding in neurofilament sidearms: effects of phosphorylation and ATP. *FEBS Lett.* 531:397–401.
17. Hisanaga, S., and N. Hirokawa. 1989. The effects of dephosphorylation on the structure of the projections of neurofilament. *J. Neurosci.* 9:959–966.
18. Gou, J. P., T. Gotow, …, J. F. Leterrier. 1998. Regulation of neurofilament interactions in vitro by natural and synthetic polypeptides sharing Lys-Ser-Pro sequences with the heavy neurofilament subunit NF-H: neurofilament crossbridging by antiparallel sidearm overlapping. *Med. Biol. Eng. Comput.* 36:371–387.
19. Leermakers, F. A. M., and E. B. Zhulina. 2008. Self-consistent field modeling of the neurofilament network. *Biophys. Rev. Lett.* 3:459–489.
20. Jeong, S., X. Zhou, …, Y. Jho. 2016. Monte carlo simulation of the neurofilament brush. *Isr. J. Chem.* 56:599–606.
21. Eyer, J., and J. F. Leterrier. 1988. Influence of the phosphorylation state of neurofilament proteins on the interactions between purified filaments in vitro. *Biochem. J.* 252:655–660.
22. Yabe, J. T., C. Jung, …, T. B. Shea. 2000. Phospho-dependent association of neurofilament proteins with kinesin in situ. *Cell Motil. Cytoskeleton.* 45:249–262.
23. Lee, S., N. Sunil, and T. B. Shea. 2011. C-terminal neurofilament phosphorylation fosters neurofilament-neurofilament associations that compete with axonal transport. *Cytoskeleton.* 68:8–17.
24. Lee, S., H. C. Pant, and T. B. Shea. 2014. Divergent and convergent roles for kinases and phosphatases in neurofilament dynamics. *J. Cell Sci.* 127:4064–4077.

25. UniProt Consortium. 2015. UniProt: a hub for protein information. *Nucleic Acids Res.* 43:D204–D212.
26. Hancock, J. M., and M. J. Bishop. 2004. EMBOSS (The european molecular biology open software suite). *In* Dictionary of Bioinformatics and Computational Biology. J. M. Hancock and M. J. Zvelebil, editors. John Wiley & Sons, Hoboken, NJ.
27. Harpaz, Y., M. Gerstein, and C. Chothia. 1994. Volume changes on protein folding. *Structure.* 2:641–649.
28. Jones, J. B., and C. R. Safinya. 2008. Interplay between liquid crystalline and isotropic gels in self-assembled neurofilament networks. *Biophys. J.* 95:823–835.
29. Leterrier, J. F., J. Käs, …, P. A. Janmey. 1996. Mechanical effects of neurofilament cross-bridges. Modulation by phosphorylation, lipids, and interactions with F-actin. *J. Biol. Chem.* 271:15687–15694.
30. Carden, M. J., W. W. Schlaepfer, and V. M. Lee. 1985. The structure, biochemical properties, and immunogenicity of neurofilament peripheral regions are determined by phosphorylation state. *J. Biol. Chem.* 260:9805–9817.
31. Pant, H. C. 1988. Dephosphorylation of neurofilament proteins enhances their susceptibility to degradation by calpain. *Biochem. J.* 256:665–668.
32. Kornreich, M., E. Malka-Gibor, …, R. Beck. 2015. Composite bottlebrush mechanics: α-internexin fine-tunes neurofilament network properties. *Soft Matter.* 11:5839–5849.
33. Jones, J. B. 2007. Structure and Interactions in Isotropic and Liquid Crystalline Neurofilament Networks. Ph.D. thesis, University of California, Santa Barbara.
34. Parsegian, V. A., R. P. Rand, …, D. C. Rau. 1986. Osmotic stress for the direct measurement of intermolecular forces. *Methods Enzymol.* 127:400–416.
35. Rau, D. C., B. Lee, and V. A. Parsegian. 1984. Measurement of the repulsive force between polyelectrolyte molecules in ionic solution: hydration forces between parallel DNA double helices. *Proc. Natl. Acad. Sci. USA.* 81:2621–2625.
36. Money, N. P. 1989. Osmotic pressure of aqueous polyethylene glycols: relationship between molecular weight and vapor pressure deficit. *Plant Physiol.* 91:766–769.
37. Beck, R., J. Deek, …, C. R. Safinya. 2010. Gel-expanded to gel-condensed transition in neurofilament networks revealed by direct force measurements. *Nat. Mater.* 9:40–46.
38. Mücke, N., L. Kreplak, …, J. Langowski. 2004. Assessing the flexibility of intermediate filaments by atomic force microscopy. *J. Mol. Biol.* 335:1241–1250.
39. Li, Y., R. Beck, …, M. Divinagracia. 2008. Scatterless hybrid metal-single-crystal slit for small-angle x-ray scattering and high-resolution x-ray diffraction. *J. Appl. Cryst.* 41:1134–1139.
40. Kornreich, M., E. Malka-Gibor, …, R. Beck. 2016. Neurofilaments function as shock absorbers: compression response arising from disordered proteins. *Phys. Rev. Lett.* 117:148101.
41. Herrmann, H., L. Kreplak, and U. Aebi. 2004. Isolation, characterization, and in vitro assembly of intermediate filaments. *Methods Cell Biol.* 78:3–24.
42. Beck, R., J. Deek, …, C. R. Safinya. 2010. Unconventional salt trend from soft to stiff in single neurofilament biopolymers. *Langmuir.* 26:18595–18599.
43. Storm, I. M., M. Kornreich, …, F. A. M. Leermakers. 2016. Loss of bottlebrush stiffness due to free polymers. *Soft Matter.* 12:8004–8014.
44. Kornreich, M., R. Avinery, and R. Beck. 2013. Modern x-ray scattering studies of complex biological systems. *Curr. Opin. Biotechnol.* 24:716–723.
45. Leermakers, F. A. M., and E. B. Zhulina. 2010. How the projection domains of NF-L and α-internexin determine the conformations of NF-M and NF-H in neurofilaments. *Eur. Biophys. J.* 39:1323–1334.
46. Jayanthi, L., W. Stevenson, …, Y. Gebremichael. 2013. Conformational properties of interacting neurofilaments: Monte Carlo simulations of cylindrically grafted apposing neurofilament brushes. *J. Biol. Phys.* 39:343–362.
47. Rammensee, S., P. A. Janmey, and A. R. Bausch. 2007. Mechanical and structural properties of in vitro neurofilament hydrogels. *Eur. Biophys. J.* 36:661–668.
48. Yao, N. Y., C. P. Broedersz, …, D. A. Weitz. 2010. Elasticity in ionically cross-linked neurofilament networks. *Biophys. J.* 98:2147–2153.
49. Lin, Y.-C. C., N. Y. Yao, …, D. A. Weitz. 2010. Origins of elasticity in intermediate filament networks. *Phys. Rev. Lett.* 104:058101.
50. MacKintosh, F. C., J. Käs, and P. A. Janmey. 1995. Elasticity of semiflexible biopolymer networks. *Phys. Rev. Lett.* 75:4425–4428.
51. Deek, J., P. J. Chung, …, C. R. Safinya. 2013. Neurofilament sidearms modulate parallel and crossed-filament orientations inducing nematic to isotropic and re-entrant birefringent hydrogels. *Nat. Commun.* 4:2224.
52. Rau, D. C., and V. A. Parsegian. 1992. Direct measurement of the intermolecular forces between counterion-condensed DNA double helices. Evidence for long range attractive hydration forces. *Biophys. J.* 61:246–259.
53. Kumar, S., and R. Nussinov. 1999. Salt bridge stability in monomeric proteins. *J. Mol. Biol.* 293:1241–1255.
54. Bright, J. N., T. B. Woolf, and J. H. Hoh. 2001. Predicting properties of intrinsically unstructured proteins. *Prog. Biophys. Mol. Biol.* 76:131–173.
55. Chen, J., T. Nakata, …, N. Hirokawa. 2000. The C-terminal tail domain of neurofilament protein-H (NF-H) forms the crossbridges and regulates neurofilament bundle formation. *J. Cell Sci.* 113:3861–3869.
56. Storm, I. M., M. Kornreich, …, R. de Vries. 2015. Liquid crystals of self-assembled DNA bottlebrushes. *J. Phys. Chem. B.* 119:4084–4092.
57. Toman, E., S. Harrisson, and T. Belli. 2016. Biomarkers in traumatic brain injury: a review. *J. R. Army Med. Corps.* 162:103–108.
58. Holmgren, A., D. Bouhy, and V. Timmerman. 2012. Neurofilament phosphorylation and their proline-directed kinases in health and disease. *J. Peripher. Nerv. Syst.* 17:365–376.
59. Shea, T. B., and W. K.-H. Chan. 2008. Regulation of neurofilament dynamics by phosphorylation. *Eur. J. Neurosci.* 27:1893–1901.